



**HAL**  
open science

# Search for transient sources with the ANTARES and KM3NeT neutrino telescopes in the multi-messenger astronomy era

Marta Colomer Molla

## ► To cite this version:

Marta Colomer Molla. Search for transient sources with the ANTARES and KM3NeT neutrino telescopes in the multi-messenger astronomy era. Physics [physics]. Université Paris Cité; Universitat de Valencia (Espagne), 2020. English. NNT : 2020UNIP7005 . tel-03153248

**HAL Id: tel-03153248**

**<https://theses.hal.science/tel-03153248>**

Submitted on 26 Feb 2021

**HAL** is a multi-disciplinary open access archive for the deposit and dissemination of scientific research documents, whether they are published or not. The documents may come from teaching and research institutions in France or abroad, or from public or private research centers.

L'archive ouverte pluridisciplinaire **HAL**, est destinée au dépôt et à la diffusion de documents scientifiques de niveau recherche, publiés ou non, émanant des établissements d'enseignement et de recherche français ou étrangers, des laboratoires publics ou privés.



Thèse de doctorat en "Physique de l'Univers" préparée  
en cotutelle à l'Université de Paris et la Universidad de Valencia  
Ecole doctorale STEP'UP – ED N°560 Laboratoire AstroParticule et Cosmologie (APC)  
Instituto de Física Corpuscular (IFIC)

sous la direction de  
Antoine KOUCHNER et Juan de Dios ZORNOZA GÓMEZ

---

# Search for transient sources with the ANTARES and KM3NeT neutrino telescopes in the multi-messenger astronomy era

---

Soutenue le 29 Septembre 2020 par  
Marta COLOMER MOLLA

Pr. Kate SCHOLBERG	Duke University	Présidente du jury
Pr. Antoine KOUCHNER	Université de Paris	Directeur de thèse
Pr. Juan de Dios ZORNOZA	Universidad de Valencia	Directeur de thèse
Dr. Alexis COLEIRO	Université de Paris	Co-encadrant de thèse
Pr. Imre BARTOS	University of Florida	Rapporteur
Pr. Jürgen BRUNER	Aix Marseille Université	Rapporteur
Pr. Alessandra TONAZZO	Université de Paris	Examineur
Pr. Manuel PERUCHO	Universidad de Valencia	Examineur



UNIVERSITÉ DE PARIS

*Abstract*

Université de Paris, UFR Physique  
Universitat de Valencia, CSIC  
Laboratoire APC (AstroParticule et Cosmologie)  
Instituto de Física Corpuscular (IFIC)

PhD Thesis

**Search for transient sources with the ANTARES and KM3NeT neutrino telescopes in the multi-messenger astronomy era**

by Marta COLOMER MOLLA

Two analyses are detailed in this thesis related to neutrino and multi-messenger astronomy with Cherenkov telescopes in the Mediterranean Sea.

The first analysis explores the capabilities of the KM3NeT neutrino telescopes to detect the signal from a Galactic core-collapse supernova (CCSN), as well as the physical constraints that could be extracted from such a detection. Together with the Sun, CCSNe are the only confirmed sources of astrophysical neutrinos. A search method for these astrophysical neutrino sources with KM3NeT has been developed during this thesis, based on the analysis of the first data which has allowed for a good characterisation of the background and the detector performance. The results show that the KM3NeT detector might be sensitive to this MeV neutrino flux, with a coverage at  $5\sigma$  discovery potential of more than 95% of Galactic CCSN progenitors. Therefore, KM3NeT will contribute to the observation of the next Galactic explosion. The CCSN analysis has been implemented in a real-time trigger, that is active since summer 2019. Moreover, it has yielded the first KM3NeT real-time results with the follow-up of the unmodelled candidate gravitational-wave (GW) events. These results have allowed the KM3NeT experiment to join the SNEWS network, to which all detectors sensitive to CCSN neutrino send their alerts.

The second analysis exploits the data of the ANTARES neutrino telescope to search for high-energy neutrinos (TeV-PeV) in time and space coincidence with gravitational-wave sources and very-high energy gamma-ray bursts (GRBs). In fact, compact binary mergers and gamma-ray bursts have long been suggested as potential high-energy neutrino emitters. Typically, these searches look for muon neutrinos coming through the Earth (upgoing tracks). For the first time, all-flavors (including the so-called shower events) were included in this kind of searches. Moreover, these analyses have been applied to sources both below the ANTARES horizon (seen as upgoing events), and above the horizon of the ANTARES telescope (downgoing). This has led to an improvement of *sim*15-30% for upgoing events and up to a 200% for searches above the horizon. The analyses carried out during the thesis yielded no neutrino in coincidence with any of the gravitational-wave sources from the first GW catalog, neither with the first GRBs detected at very high energies.

**Keywords:** astroparticles, neutrinos, multi-messenger, high-energy, astrophysics, supernova, gravitational waves



# Contents

<b>Abstract</b>	<b>iii</b>
<b>I Neutrino astronomy</b>	<b>13</b>
<b>1 An introduction to neutrino astronomy</b>	<b>15</b>
1.1 Historical introduction . . . . .	15
1.2 Cosmic Rays . . . . .	16
1.3 Neutrinos: a new window to the universe . . . . .	18
1.3.1 Neutrino oscillations . . . . .	20
1.3.2 Recent results by the IceCube Neutrino Observatory . . . . .	23
1.4 Multi-messenger connections and neutrino production . . . . .	25
1.4.1 Multi-messenger results . . . . .	27
The binary neutron star merger: GW170817 . . . . .	27
The case of blazar TXS 0506+506 . . . . .	32
1.5 Candidate neutrino sources . . . . .	34
1.5.1 Extra-Galactic neutrino potential emitters . . . . .	34
1.5.2 Neutrino source candidates in our Galaxy . . . . .	38
<b>2 Neutrino telescopes</b>	<b>41</b>
2.1 Detection principle . . . . .	41
2.1.1 Cherenkov radiation . . . . .	41
2.1.2 Neutrino interactions and event topologies in underwater Cherenkov detectors . . . . .	42
2.2 The ANTARES neutrino telescope . . . . .	43
2.2.1 Optical Module, Storey and Line . . . . .	44
2.2.2 The Data Acquisition System . . . . .	45
2.3 The KM3NeT neutrino detectors . . . . .	46
2.3.1 The Digital Optical Module and the Detection Unit . . . . .	47
2.3.2 The Data AcQuisition System . . . . .	48
2.3.3 The deployment . . . . .	49
2.4 Other Cherenkov neutrino detectors . . . . .	50
2.4.1 The IceCube Neutrino Observatory . . . . .	50
2.4.2 The Baikal Neutrino Telescope and the Gigaton Volume Detector . . . . .	52
2.4.3 From Kamiokande to Hyper-Kamiokande . . . . .	52

<b>3</b>	<b>From the detected photons to the physics results: analysis tools</b>	<b>55</b>
3.1	Sources of background in the Mediterranean Sea	55
3.2	Detector calibration	56
3.2.1	Time calibration	56
3.2.2	Position calibration	57
3.2.3	Charge calibration	57
3.3	Physics triggers	58
3.3.1	ANTARES	58
	TAToO triggers	58
3.3.2	KM3NeT	59
3.4	The simulation chain in ANTARES and KM3NeT	59
3.4.1	Event generation	59
3.4.2	Particle and light propagation	61
3.4.3	Detector response	62
3.4.4	Event reconstruction	62
3.4.5	Effective area and detector acceptance	64
3.5	Statistical concepts used in particle and astro-physics	67
3.5.1	Test statistic, p-value and significance	67
	Combining p-values	68
3.5.2	The sensitivity, discovery potential and upper limit	69
	Upper limit	70
	Sensitivity	70
	Discovery potential	70
<b>II</b>	<b>Detecting Galactic core-collapse supernova neutrinos with KM3NeT</b>	<b>71</b>
<b>4</b>	<b>Core Collapse SuperNova neutrinos: What we know today.</b>	<b>73</b>
4.1	Historical introduction to CCSN neutrinos	73
4.2	Phases of a Core-Collapse Supernova: the explosion mechanism	75
4.3	Prompt SN neutrino fluxes and spectra	78
4.3.1	Neutrino flavor conversion models in CCSN	82
4.4	Towards a multi-messenger detection of the next Core-Collapse Supernova: the SNEWS network	83
<b>5</b>	<b>CCSN neutrino simulation in KM3NeT</b>	<b>87</b>
5.1	General context	87
5.2	MeV neutrino interactions in sea water	88
5.2.1	Computing the interaction rates	88
5.2.2	Simulation of the neutrino interactions in the KM3NeT detector	90
5.2.3	Optimisation of the generation volume $V_{gen}$	92
5.3	Lightcurve simulations of background and CCSN neutrinos	93
5.3.1	Run-by-run MC simulation of background single rates from raw data	93
5.3.2	CCSN neutrino lightcurve using L1 data	94
5.4	Parametrisation of the detector response and SNOwGLOBES	94
<b>6</b>	<b>Detecting CCSN neutrinos with KM3NeT</b>	<b>99</b>
6.1	Signal and background	99
6.2	Background rejection	100
6.2.1	Muon rejection: coincidence correlation	101
6.2.2	Muon rejection: triggered events veto	102

6.3	Optical background characterisation: Bioluminescence impact on detector efficiency . .	104
6.4	Background stability . . . . .	105
6.5	Study of the systematic uncertainties . . . . .	106
	Detector response . . . . .	106
	Flux model . . . . .	108
6.6	Sensitivity of KM3NeT detectors to a CCSN neutrino signal . . . . .	108
6.6.1	Sensitivity definition . . . . .	109
6.6.2	Combined sensitivity . . . . .	109
6.6.3	Multiplicity selection . . . . .	110
6.6.4	Sensitivity results . . . . .	111
6.7	Online supernova trigger in KM3NeT . . . . .	114
6.8	Inter-DOM coincidences from a CCSN signal. . . . .	116
<b>7</b>	<b>Constraining the CCSN mechanism with KM3NeT</b>	<b>119</b>
7.1	First multi-messenger results with KM3NeT data and the CCSN trigger . . . . .	119
7.1.1	Procedure of the follow-up . . . . .	119
7.1.2	Gravitational wave trigger S191110af: results . . . . .	120
	Lower limit on the Core Collapse Supernova distance . . . . .	120
	Upper limit on the total energy emitted in neutrinos . . . . .	123
7.1.3	Gravitational wave trigger S200114f: results . . . . .	124
7.2	Determining the mean neutrino energy of CCSN neutrinos . . . . .	125
7.3	Sensitivity to fast time variations in the neutrino lightcurve. . . . .	130
7.3.1	Event selection . . . . .	130
7.3.2	Analysis method . . . . .	131
7.3.3	Sensitivity to fast time variation: frequency (model) independent approach . . . .	133
7.3.4	Sensitivity to fast time variation: frequency (model) dependent approach . . . .	134
7.3.5	Summary of the results . . . . .	136
<b>8</b>	<b>Timing and pointing the CCSN neutrino signal</b>	<b>137</b>
8.1	Combining experimental lightcurves for timing the CCSN neutrino signal . . . . .	137
8.1.1	Simulation . . . . .	138
8.1.2	Supernova neutrino fluxes . . . . .	138
	CCSN neutrino detection rates . . . . .	139
	Simplified detector model . . . . .	140
8.1.3	Method . . . . .	141
	Chi-square method . . . . .	142
	Normalised cross-correlation . . . . .	143
	Estimating the performance of the lightcurve matching . . . . .	144
	Tuning the parameters using a bootstrapping . . . . .	144
	The triangulation method . . . . .	145
	Procedure for the triangulation performance estimation . . . . .	146
8.1.4	Results . . . . .	146
	Time uncertainty results . . . . .	146
	Results of the triangulation: localisation skymaps . . . . .	148
8.2	Preliminary study of the sensitivity to the direction of the source using the multi-PMT DOM design of KM3NeT . . . . .	153

<b>III Searching for high-energy neutrino emission from TeV gamma-ray bursts and gravitational wave sources with ANTARES</b>	<b>159</b>
<b>9 Gamma-ray bursts as multi-messenger sources</b>	<b>161</b>
9.1 Introduction to gamma-ray bursts	161
9.2 Multi-messenger emission from GRBs	163
9.2.1 The case of long and late very high-energy gamma-ray emission	164
9.2.2 Neutrinos and GWs from compact binary mergers	166
Neutrinos and GWs from binary black hole mergers	166
Neutrinos from binary neutron stars (or short GRBs)	167
Neutrinos and GWs from NSBH systems	169
9.2.3 Observational results	169
<b>10 Neutrino follow-up of gravitational-wave sources</b>	<b>171</b>
10.1 Gravitational-wave interferometers	171
10.1.1 Gravitational-wave searches	172
10.1.2 State-of-the-art of gravitational-wave astronomy	173
10.2 GW events under study	173
10.3 Neutrino follow-up	175
10.3.1 Dataset and Monte Carlo simulations	175
10.3.2 Localisation of the GW events and ANTARES visibility	176
10.4 Analysis method	176
10.4.1 Optimization of the track event selection	180
10.4.2 Optimization of the shower event selection	181
10.5 Event selection	181
10.5.1 Finding the optimal cuts: example of GW170814	182
10.5.2 Finding the optimal cuts: example of GW170818	183
10.5.3 Summary	184
10.6 Analysis results	185
10.6.1 Constraints on the neutrino spectral fluence	185
10.6.2 Constraints on the total energy	188
<b>11 Follow-up of very high-energy gamma-ray bursts with ANTARES</b>	<b>191</b>
11.1 Introduction to the GRBs under study	191
11.1.1 GRB 180720B	191
11.1.2 GRB 190114C	192
11.1.3 GRB 190829A	193
11.2 Analysis method	193
11.2.1 Track selection	194
11.2.2 Shower optimization	194
11.3 Data and Monte Carlo samples	197
11.4 Neutrino follow-up and event selection	197
11.4.1 GRB 180720B	197
Track selection	198
Shower optimisation	199
11.4.2 GRB 190114C	200
Track optimization	201
Shower optimization	202
11.4.3 GRB 190829A	202
Track selection	202
Shower selection	203

---

11.5 Results of the ANTARES search . . . . .	204
<b>12 Summary, conclusions and outlook</b>	<b>209</b>
12.1 Detection of CCSN neutrinos with KM3NeT . . . . .	210
12.1.1 Real-time monitoring and first results . . . . .	211
12.1.2 Study of the properties of the CCSN neutrino flux . . . . .	211
12.1.3 Comparison with other experiments . . . . .	212
12.1.4 Outlook and perspectives . . . . .	213
12.2 ANTARES search for high-energy neutrinos in coincidence with GW events and GRBs detected at TeV energies . . . . .	214
12.2.1 Outlook and perspectives . . . . .	215



# Résumé

Dans le présent manuscrit s'expose le travail réalisé au sein de la Collaboration ANTARES-KM3NeT, dont le cadre général est l'astronomie multi-messagers avec des télescopes à neutrinos. Le travail a porté sur deux axes: la détection de neutrinos de supernova à effondrement de coeur à basse énergie avec KM3NeT (MeV), et la recherche de neutrinos de haute énergie (TeV-PeV) dans les données d'ANTARES associés à une source transitoire associée, détectée en ondes gravitationnelles ou via le rayonnement gamma de haute énergie.

## Astronomie des neutrinos

L'astronomie de neutrinos est une discipline jeune qui mélange la physique des particules et l'astrophysique. Elle est née avec les observations des neutrinos provenant du Soleil ainsi que d'une explosion de supernova (SN1987A). Plus récemment, les premières détections de neutrinos cosmiques à haute énergie et les premières sources astrophysiques détectées simultanément à travers différents messagers cosmiques ont conduit à une nouvelle perception qui va au delà de l'astronomie conventionnelle : l'astronomie multi-messagers.

Neutrinos, rayons cosmiques et rayons gamma peuvent être produits ensemble à proximité des sources astrophysiques où l'accélération de particules à très haute énergie est possible. Néanmoins, la production des rayons gamma peut aussi avoir lieu par des processus leptoniques. Pour cette raison, la détection des neutrinos provenant d'une source identifiée serait une preuve irréfutable d'un site d'accélération hadronique.

Puisque les neutrinos interagissent très faiblement, leur détection constitue un défi, mais cette même propriété fait des neutrinos des messagers cosmiques très utiles. Leur détection apporte des éléments uniques sur les mécanismes astrophysiques en jeu dans les phénomènes explosifs de l'Univers. Jusqu'à présent, une seule source de neutrinos de haute énergie a été identifiée : le blazar TXS 0506+056. A cela s'ajoute la détection d'un flux diffus de neutrinos cosmiques avec des énergies de l'ordre du TeV-PeV, qui se répartit de façon isotrope dans le ciel et dont l'origine est encore inconnue.

La détection des neutrinos se fait de façon indirecte. C'est à dire, à travers l'observation des particules produites lors de leur interactions. Le principe de détection des télescopes à neutrinos est basé sur la détection des particules chargées produites lors que les neutrinos interagissent avec la matière. Dans le cas des détecteurs ANTARES et KM3NeT, ces interactions ont lieu dans l'eau saline et elles peuvent être observées en collectant la lumière de Tcherenkov induite par le passage d'une particule chargée à vitesse relativiste grâce aux divers photomultiplicateurs (PMTs) qui constituent le détecteur. Les PMTs sont disposés sur des lignes verticales pour former l'ensemble de l'instrument. En suivant la quantité de lumière déposée et le temps auquel les photons sont détectés dans les PMTs, la trajectoire

des particules peut être reconstruite.

Il existe trois sources de bruit de fond dans la mer pour ce type de détecteurs Tcherenkov: la bioluminescence, les isotopes radioactifs présents dans l'eau de mer, et des leptons chargés qui sont produits dans des interactions des rayons cosmiques dans l'atmosphère, qui arrivent dans l'eau et produisent de la lumière qui peut être observée. Dans ce dernier cas, on inclut les neutrinos et les muons atmosphériques.

KM3NeT est un télescope à neutrinos qui est en cours de déploiement dans la mer Méditerranée. Il est composé de deux détecteurs: ORCA et ARCA. Le premier (ORCA) est situé au large de la côte française (Toulon), et il a comme objectif l'étude des oscillations des neutrinos et la détermination de l'hierarchie de masse des neutrinos. Le deuxième (ARCA), est placé au large de la Sicile (Cappo Passero) et est consacré à la recherche des sources astrophysiques de neutrinos de haute énergie, comme son prédécesseur ANTARES et le détecteur plus grand de ce type qui existe actuellement, IceCube. La nouveauté des détecteurs KM3NeT réside dans le fait qu'ils sont formés par des sphères qui disposent de 31 PMTs chacune, appelées DOMs, tandis qu'ANTARES et IceCube ont un seul PMT de grande photocathode. Ces détecteurs se situent à une profondeur d'environ 2500 m (ORCA, ANTARES) et 3500 m (ARCA). Ceci permet de réduire la quantité de bruit de fond atmosphérique qui est détectée. ORCA est un détecteur plus dense avec 115 lignes instrumentées, contrairement à ARCA qui lui est plus grand ( $\sim 1 \text{ km}^3$ ), avec 230 lignes de détection.

Dans la suite, les analyses menées pendant cette thèse et les résultats obtenus sont résumés.

## Detection des neutrinos de supernova avec KM3NeT

Dans une première partie, le potentiel des télescopes KM3NeT pour observer un flux de neutrinos d'une explosion supernova est étudié. Les supernovae sont la deuxième source de neutrinos astrophysiques confirmée après le Soleil. La seule détection des neutrinos provenant d'un événement supernova a permis de consolider les bases théoriques du mécanisme astrophysique sous-jacent des explosions de supernova. Par contre, une seule détection n'a pas suffi pour contraindre tous les paramètres qui permettent de décrire en détail les différents phénomènes qui ont lieu au cours de l'explosion. Cela constitue une motivation forte pour réaliser ce type d'études pour une prochaine détection.

Les détecteurs KM3NeT ne sont pas optimisés pour détecter des neutrinos à basse énergie (MeV). Néanmoins, le signal supernova peut être identifiée comme une hausse du taux d'événements détectés au dessus du bruit de fond. De fait, l'énorme quantité de neutrinos émise lors de l'explosion va produire une hausse pas seulement du taux d'événements détectés, mais aussi du taux d'événements détectés en coïncidence par les différents PMTs du même DOM.

Les détecteurs KM3NeT sont principalement sensibles au flux de  $\bar{\nu}_e$  qui interagissent avec les protons présents dans l'eau. Le nombre de PMTs sur un même DOM qui détectent des photons en coïncidence (multiplicité) est utilisé pour réduire de façon radicale le bruit de fond provenant de la bioluminescence et la radioactivité. D'autre part, les corrélations spatio-temporelles sont exploitées pour filtrer des événements de bruit de fond atmosphérique, qui vont produire des signatures caractéristiques que l'on peut identifier. Ces techniques permettent d'optimiser le potentiel de KM3NeT pour la détection d'un flux de neutrinos au MeV.

Une simulation détaillée de la réponse des détecteurs KM3NeT à un flux de neutrinos de supernova a été développée pendant cette thèse, et elle a permis d'évaluer sa sensibilité. Avec cette simulation, la masse effective de KM3NeT pour des recherches à basse énergie a été estimée. Les 115 lignes d'un

block de détection sont équivalentes à un détecteur de neutrinos au MeV de 50 kton. Avec la coupure en multiplicité optimisée pour la recherche de neutrinos de supernova, cette masse effective est réduite à  $\sim 1$  kton. Cette simulation a permis de caractériser la réponse du détecteur à basse énergie, qui a été paramétrisée avec une courbe d'efficacité en fonction de l'énergie des neutrinos. Cette paramétrisation peut être appliquée directement pour la simulation de tout flux astrophysique de neutrinos avec des énergies entre 1 et 100 MeV.

La méthode de détection utilisant les coïncidences a été optimisée pendant cette thèse et a été appliquée aux premières données de KM3NeT pour mesurer le bruit de fond. Avec ces estimations du bruit de fond et du signal attendu, la sensibilité de détection aux neutrinos de supernova avec KM3NeT a été évaluée. Les résultats obtenus indiquent que plus du 95% des supernovae galactiques pourront être détectées avec KM3NeT. Ces résultats démontrent que KM3NeT pourra contribuer à la détection de la prochaine explosion supernova galactique.

### **Premiers résultats en temps réel**

La stratégie adoptée pour l'analyse supernova a été mise en place dans le système de déclenchement appliqué directement aux données qui sont traitées en temps réel, et qui sélectionne les événements d'intérêt physique. La caractérisation et rejection du bruit de fond atteints a permis à l'expérience KM3NeT de joindre le système d'alertes SNEWS, qui reçoit les alertes individuelles de tous les détecteurs sensibles aux neutrinos de supernova, et en déclenche une si deux expériences observent un signal supernova en coïncidence.

À l'heure actuelle, KM3NeT est capable d'engendrer des alertes en combinant les données de ARCA et ORCA en temps réel, avec une latence qui est en dessous de 20 secondes. Avec six lignes qui prennent des données, ORCA peut observer des sources jusqu'à 6-9 kpc (en fonction de la masse du progéniteur) avec le seuil de significativité requis par SNEWS.

Un des objectifs de ces recherches en temps réel est de pouvoir identifier le signal dans des différents messagers (neutrinos, rayonnement électromagnétique et ondes gravitationnelles), et pouvoir déterminer quand et où a lieu l'explosion. De fait, les photons produits lors d'une supernova sont émis jusqu'à des heures après les neutrinos. De plus, les explosions de supernova sont une des sources dont on attend aussi une émission d'ondes gravitationnelles. Ainsi, une détection prompte du flux de neutrinos faciliterait une observation électromagnétique et en ondes gravitationnelles.

Pendant la dernière période de prise de données par les détecteurs d'ondes gravitationnelles, deux alertes ont été déclenchées pour des signaux qui pourraient provenir d'une supernova. À ce moment, quatre lignes d'ORCA étaient actives. Ces alertes ont été suivies avec les données d'ORCA, auxquelles l'analyse supernova a été appliquée. Il n'a pas été observé d'excès dans les données correspondant à un potentiel signal de neutrinos au MeV. Avec cette non-détection, des limites sur une potentielle explosion supernova ont été placées, avec une distance minimale de 6-12 kpc (suivant la masse du progéniteur). De plus, les limites obtenues avec cette analyse ont pu rejeter l'hypothèse d'une explosion supernova avec une énergie totale émise en neutrinos plus grande que  $3 \times 10^{53}$  erg, qui est l'énergie typique pour ces explosions. Cette analyse a permis de mettre en place un premier suivi et ainsi de vérifier le fonctionnement et validité de l'algorithme de déclenchement dans un cas réel, en prouvant une capacité de réponse rapide.

## Étude des propriétés du flux de neutrinos

Une autre partie du travail a été d'évaluer les performances de KM3NeT pour contraindre et distinguer entre les différents modèles de production des neutrinos. Pour ceci, il est crucial de déterminer quelle est la résolution temporelle, angulaire et en énergie du détecteur.

Pour mener des analyses qui impliquent des variations temporelles, il est nécessaire d'avoir une bonne résolution temporelle. En particulier, dans le cas d'un flux de neutrinos de basse énergie, l'idéal est une résolution à l'échelle de la milliseconde pour pouvoir étudier des changements rapides en temps et déterminer avec précision quand débute le signal. Pour ceci, l'instrument doit être capable de détecter une quantité de neutrinos élevée pour avoir de la statistique. Avec KM3NeT, ceci est possible seulement si on utilise toutes de coïncidences. La coupure en multiplicité permet une diminution du bruit de fond plus grande et une meilleure sensibilité de détection, mais au dépend d'une grande perte d'événements de signal.

L'analyse temporelle principale qui a été menée pendant cette thèse a été le développement d'une méthode pour combiner les courbes de lumière de neutrinos détectées par différents instruments. Le but est d'extraire avec cette combinaison le décalage temporel du signal observé par les différents détecteurs, et de déterminer l'incertitude de cette mesure expérimentale. Cette méthode permettra de mesurer ce décalage temporel de façon indépendante. Pour ceci, on a considéré dans la simulation une paramétrisation simple qui modélise l'évolution temporelle du flux de neutrinos attendu, et une caractérisation simplifiée de la réponse des détecteurs à ce flux, en utilisant des données publiques. Les incertitudes obtenues pour l'estimation de ce décalage temporel sont en dessous de 1 ms pour le meilleur des cas, et jusqu'à  $\sim 7$  ms pour la combinaison des détecteurs la moins performante. Finalement, ces résultats ont été utilisés pour estimer la position de la source par triangulation du signal dans les différents détecteurs. La précision obtenue est une boîte d'erreur de  $\sim 70$  deg<sup>2</sup> pour la localisation de la supernova. Cette analyse a été conçue pour fournir une réponse rapide. La boîte d'erreur peut être réduite ensuite en combinant des informations et analyses supplémentaires.

## Recherche de neutrinos de haute énergie issus de sources transitoires d'ondes gravitationnelles et de sursauts gamma détectés à haute énergie

Comme introduit au début de ce résumé, on s'attend à ce que l'origine des neutrinos cosmiques de haute énergie soit la même que celle des rayons cosmiques ultra énergétiques. L'émission de neutrinos pourrait aussi avoir lieu au même temps que le rayonnement gamma de haute énergie et un signal gravitationnel. Pour cette raison, une partie du travail de cette thèse est consacrée à la recherche d'une émission de neutrinos de haute énergie associée à un signal électromagnétique ou gravitationnel d'une source confirmée. Une attention particulière a été portée aux sources d'ondes gravitationnelles (collision d'objets compacts dans des systèmes binaires), et à des sursauts gamma qui ont été détectés à des énergies autour du TeV par la première fois.

Les corrélations temporelles et spatiales entre les photons détectés aident à identifier des topologies d'événements caractéristiques des interactions des particules chargées dans l'eau. Un cône de lumière qui traverse le détecteur est caractéristique du passage d'un lepton chargé ("trace"): muons atmosphériques ou muons issus de l'interaction par courant chargé d'un neutrino électronique. Un point brillant (sphère lumineuse en expansion) dans le détecteur, indique la présence d'une gerbe hadronique ou électromagnétique produite par des interactions par courant neutre ou par courant chargé dans le cas d'un neutrino électronique ("cascades"). Les corrélations causales permettent d'identifier ces topologies et de rejeter des événements de bruit de fond. Ainsi, à haute énergie, la composante de bruit de

fond qui domine sera constituée de muons et neutrinos atmosphériques.

La méthode habituelle pour rejeter la composante de bruit de fond atmosphérique est de garder les événements qui arrivent au détecteur en ayant traversé la Terre (montants), puisque seuls les neutrinos peuvent la traverser. Par ailleurs, les neutrinos atmosphériques présentent un spectre en énergie différent de celui des neutrinos cosmiques. Aussi, une sélection des neutrinos plus énergétiques permet de discriminer statistiquement les neutrinos atmosphériques traversant la Terre et les neutrinos d'origine cosmique.

Une autre possibilité est de réaliser une analyse où on cherche des coïncidences spatio-temporelles avec une détection confirmée d'une source transitoire. Une région du ciel petite et une fenêtre temporelle courte où rechercher le signal permettent de réduire le bruit de fond et augmenter le potentiel de découverte. En fait, le bruit de fond peut être diminué tellement qu'il est possible e3 chercher des sources qui sont au dessus de l'horizon d'ANTARES, vues comme événements descendants qui sont plus probablement des muons. De cette façon, la recherche peut être étendue à tout le ciel et toutes les saveurs de neutrinos (traces et cascades).

Une partie du travail présenté dans ce manuscrit a été consacrée au développement d'un critère de sélection pour des événements de type cascade qui soit applicable dans ces recherches multi-messagers. Cette sélection, comme pour les traces, se base sur une méthode qui consiste à trouver les coupures dans les paramètres de qualité de la reconstruction de sorte qu'un événement qui passe les coupures dans la fenêtre de la recherche et a une position compatible avec celle de la source, mène à une détection à  $3\sigma$  de niveau de confiance. Cette stratégie offre un bon compromis entre une bonne sensibilité (limites plus contraignantes) et un bon potentiel de découverte.

Cette analyse a été appliqué aux données d'ANTARES dans deux contextes différents: la recherche de neutrinos en coïncidence avec les signaux d'ondes gravitationnelles du catalogue O2, et la recherche de neutrinos associés avec une émission de photons gamma de très haute énergie  $O(\text{TeV})$  provenant de sursauts gamma longs. Pour la première fois, les cascades ont été incluses dans ce type d'analyse, ce qui a abouti à une amélioration de la sensibilité d'un 15-30% pour des sources dans l'horizon d'ANTARES et jusqu'un 200% pour des recherches d'événements descendants.

**Mots clés:** astroparticules, neutrinos, astrophysique, haute énergie, astronomie, multi-messagers, supernova, ondes gravitationnelles



## **Part I**

# **Neutrino astronomy**



# Chapter 1

## An introduction to neutrino astronomy

This chapter is a short introduction to the current knowledge in the field of neutrino astrophysics. The scientific motivations for a neutrino astronomy are summarised, insisting on the role that neutrinos could play in different scenarios and pointing out the interesting known and potential candidate astrophysical sources. The interaction properties of neutrinos place them as potentially unique astronomical messengers in the information they carry. A special focus is thus given to multi-messenger astronomy, which aims at exploiting the synergy between the multiple messengers emitted by these astrophysical sources, presenting their respective advantages.

### 1.1 Historical introduction

When talking about neutrino astronomy, one has to keep in mind that we are facing a relatively new-born field. It has been almost one century since a new fundamental particle called neutrino was proposed by Pauli in order to explain the missing energy observed in radioactive decays [1]. Moreover, already 60 years have passed since the initial idea and the basis of high-energy neutrino telescopes appeared. Neutrino astronomy was born in the 1960's with the first observation of neutrinos from the Sun [2]. This detection brought the discovery of neutrino oscillations and revealed the fact that neutrinos are massive particles, which was not predicted by the Standard Model (SM). The nature of neutrinos (Dirac or Majorana [3]<sup>1</sup>), their mass and the mechanism that makes them massive still remain unknown as well as many other mysteries involving these enigmatic particles. In particular, three flavours of neutrinos are observed ( $\nu_e$ ,  $\nu_\mu$  and  $\nu_\tau$ ) but additional neutrinos (so-called sterile neutrinos) are hypothesised in order to explain the different experimental data.

From 1911, Victor Hess performed a set of observations of the dischargement of an electroscope at different altitudes with balloon flights [4]. He measured an increase of this dischargement up to 4 km high, later reproduced at higher altitudes, which could only be due to a cosmic origin. This was how he was attributed the discovery of a flux of charged particles coming from outside the Earth, since then referred to as cosmic rays (CR). Their discovery had an immediate impact on particle physics, with the study of CR interactions and their products allowing for the discovery of a large number of new particles, such as positrons, muons, kaons and pions.

It was not until the 20th century that multi-wavelength astronomy appeared, with observations of the Universe using other wavelengths than visible light. This led to a set of important discoveries in astronomy such as the first observations of pulsars, gamma-ray bursts and fast radio bursts among

<sup>1</sup>A Majorana particle is a fermion which is its own anti-particle. Contrary to Dirac particles for which an antiparticle with opposite quantum numbers exists.

others. Since then, the full electromagnetic (EM) spectrum has been covered. But the connection of the EM emission with cosmic-ray acceleration and neutrino production is still to be made.

The first detection of neutrinos from outside the Solar System dates back also to the 20th century, with the explosion of the supernova SN1987A, in the Large Magellanic Cloud. Their detection made possible to confirm the basic theoretical picture of massive stars explosion at the final stage of their evolution. The energy of the detected neutrinos from that source was at the MeV scale. It is, historically, the first extra-solar multi-messenger (MM) detection, with an electromagnetic signal and astrophysical neutrinos observed. The question of the detection capability with neutrino telescopes is the subject of Part II of this manuscript.

In 2013, the first detection of cosmic neutrinos at very high energies (above tens of TeV) was reported by the IceCube Collaboration [5, 6]. The discovery of a diffuse high-energy neutrino flux has been confirmed with the growing statistics of high-energy neutrino (HEN) events detected, whose angular and energy distribution is consistent with an extra-galactic origin. These first observations constitute a revolution inside the field, but even after these observations many questions regarding their exact origin remain open.

The beginning of gravitational-wave (GW) astronomy with the first observation of a signal in 2015 by the LIGO interferometers [7] marked the next important step for the community, with new probe for observing the Universe and the confirmation of General Relativity prediction for their existence. This event represents also the first observation of the coalescence of two black holes in a binary system.

The detection of cosmic neutrinos and GW marked a major step in the development of multi-messenger astronomy. In the MM era, constraining possible scenarios of cosmic neutrino production at different sources is made possible by combining the information coming from the detection of a same astrophysical event through different cosmic messengers: cosmic rays, photons or GWs. This was shown with the detection of the first GW-EM multi-messenger observation of a binary neutron star merger (GW170817/GRB170817A) [8] and the first potential coincident detection of a high-energy neutrino and gamma rays from the blazar TXS 0506+506 [9, 10].

## 1.2 Cosmic Rays

Cosmic rays consist mainly of high-energy protons and nuclei coming from the cosmos. They are detected directly by experiments on board satellites and balloons and indirectly by observing the extensive air showers they generate in the Earth's atmosphere. The flux of cosmic rays measured on Earth is shown in Fig. 1.1, represented by a broken power law spectrum with energies that span over about 10 orders of magnitude. Two changes of the spectral index are observed in the distribution of the cosmic ray flux at "low" ( $\sim$ PeV) and "high" ( $\sim 10^3$ PeV) energies, called respectively the knee and the ankle. The knee is thought to reflect the maximum proton energy that most Galactic accelerators can reach. A second knee appears due to the fact that this maximum energy is shifted for heavier elements present in the CRs compared to protons. The ankle is believed to indicate the transition between Galactic and extra-galactic origin of the CR sources.

The very high energies these particles can reach suggest that some astrophysical objects provide acceleration sites capable of bringing these particles up to extremely high energies. However, the sources of the CRs cannot be directly identified, because their directions are deflected by their interaction with magnetic fields. One way of identifying CR sources is detecting neutrinos produced by interactions of CR in or around the source.

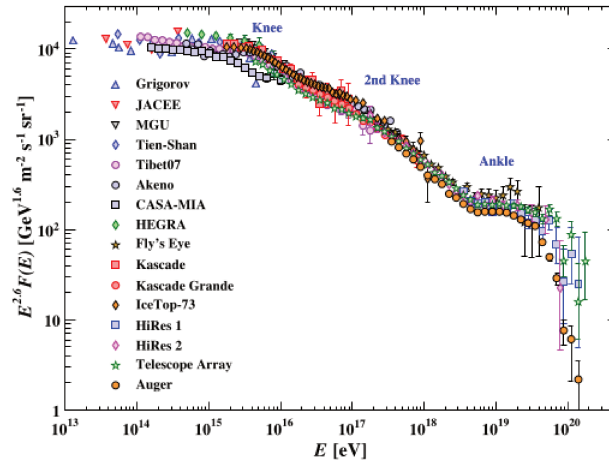


Figure 1.1: The cosmic-ray spectrum measured on Earth, with the characteristic features indicating a change of the index in the power-law spectrum, the knee and the ankle. Figure extracted from [11].

The mechanism by which CRs may be accelerated is one of the missing clues in the field and the question of the CR origin remains unknown more than a century after their discovery. Indeed, one of the main motivations for the attempts to detect cosmic neutrinos is related to the lack of knowledge on high-energy cosmic rays. Not only because neutrinos offer the possibility to identify the sources of CRs but also because the CR spectra at the source are a key ingredient for models of neutrino production, hence neutrinos carry information about the acceleration mechanisms.

The current scenario that is believed to explain the production of CRs up to the knee supports the fact that they are likely produced in Supernova Remnants (SNRs), which are Galactic sources. However, the standard SNR diffuse shock-wave model can not explain the acceleration of CRs up to energies larger than  $10^{14}$ - $10^{17}$  eV. Thus, the origin of the more energetic CRs is yet uncertain, but they are most likely produced by extra-galactic sources. Other more exotic scenarios are based on models that predict CRs originating from the decay/annihilation of particles beyond the Standard Model of Particle Physics. These exotic scenarios are less and less advocated.

In fact, a relationship can be established between the size ( $R$ ) and the intensity of the magnetic field ( $B$ ) of the acceleration region, which also depends on the charge of the cosmic-ray particle [12]. Basically, this relationship gives the maximum reachable energy ( $E_{max}$ ) for a particle with charge  $z$ , accelerated in a region of size  $R$  where one finds a magnetic field of intensity  $B$ . Such relationship is called the Hillas criterion and is shown in Fig. 1.2. This diagram provides a first hint of the viable cosmic accelerators up to extremely high energies.

As well as their origin, the composition of cosmic rays at the highest energies is not known, but it is well constrained for low-energy CRs. In 1927, Jacob Clay evidenced cosmic rays being charged particles [13], composed of electrons (1%) and nuclei (99%), with 89% of these nuclei corresponding to protons. But the current results from the Auger and Telescope Array (TA) observatories are in tension at the highest energies. Auger is finding a mixed composition with protons at energies below the ankle and heavier nuclei at higher energies, while TA finds a light mass composition. Also the cutoff on the spectrum is observed at different energies in each experiment. In fact, both data sets might be compatible but systematics have to be explored in more details in order to distinguish between the two models.

Two different scenarios emerge to explain these two datasets. In the first scenario (supported by Auger data), the acceleration mechanism at the source and the propagation of the CRs are the origin of

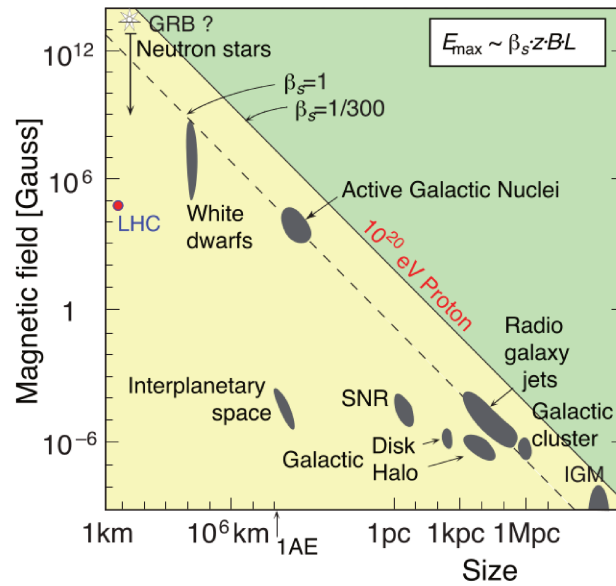


Figure 1.2: The Hillas diagram with the different cosmic-ray acceleration sources (Figure from [12]). The solid line indicates the case of  $10^{20}$  eV protons. The diagonal lines indicate the combinations of values for  $B$  and  $R$  required to accelerate a particle of a given charge with a given maximum energy.

both the ankle in the spectrum and the high-energy cut-off [14]. In the second one (supported by TA data [15]), the ankle originates from energy losses through pair production on the Cosmic Microwave Background (CMB) and the suppression at high-energies is the result of CRs interacting with the CMB photons [16]. This is the so-called GZK effect.

### 1.3 Neutrinos: a new window to the universe

High-energy neutrinos travel through the universe practically unaltered and without being deflected by magnetic fields. They thus provide a probe into the yet unexplained high-energy phenomena of the Universe, allowing to test fundamental laws as well as particle interactions in extreme conditions. Their small interaction cross-section with matter is a source of difficulty for detecting them on Earth and at the same time is also one of the main reasons for their interest as cosmic messengers.

When trying to observe the Universe with high-energy photons, above  $10^{12}$  eV, photons originating from distances beyond 100 Mpc cannot reach us because they are absorbed on their way to the Earth. This absorption is mainly due to their interaction with ambient infrared (IR) light and with the CMB as well as with matter.

In order to observe the Universe via high-energy protons (CRs), two main problems arise. On the one hand, for energies below  $10^{20}$  eV, they get deflected by magnetic fields and the information about where they originated is lost. On the other hand, above  $10^{20}$  eV, where the deflection becomes negligible, they are suppressed as explained in 1.2. This also limits the observation up to  $\sim 10$ -100 Mpc for protons with energies of  $10^{20}$  eV.

But none of these problems comes out for high-energy neutrinos, since they only interact weakly and the Universe is transparent to them, with the advantage of pointing back directly to the source. However, as already pointed out, only two sources have been identified up to now (the Sun and SN1987A) with the observation of astrophysical neutrinos at MeV energies. A third potential candidate is TXS 0506+506, for which there is evidence of neutrino emission but not significant enough to

claim a discovery.

The expected neutrino spectrum for the different known and candidate sources is shown in Fig. 1.3, spanning over more than 25 orders of magnitude in energy and about 40 in the flux intensity. The high-energy neutrino spectrum is depicted as an unbroken power law, as predicted in case CRs are accelerated within shocks according to the "diffusive shock wave acceleration model", first proposed by E. Fermi [17] and referred to as the Fermi mechanism. However, the value of the spectral index is still not well known (see section 1.3.2). The potential neutrino emitters will be discussed in section 1.5.

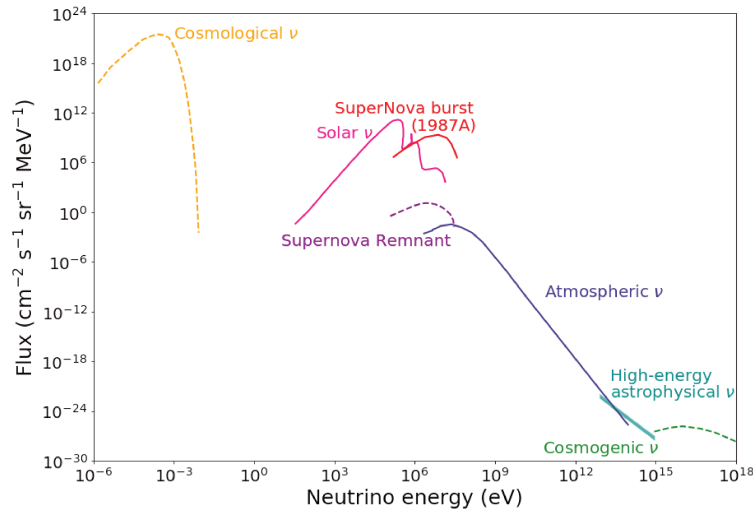


Figure 1.3: Expected fluxes of neutrinos as a function of energy.

One notices from Fig. 1.3 that the component dominating over the largest energy range is the atmospheric neutrino flux. It originates from the interaction of cosmic rays in the atmospheric, leading to the decay of hadrons producing neutrinos (see section 1.4). As will be explained in section 3.1, these atmospheric neutrinos constitute one of the main background contributions for neutrino telescopes.

Similar reasons to those predicting the existence of the CMB, also conclude that a cosmological neutrino background should have originated at the moment of the decoupling of neutrinos from matter in the Universe history. The CMB itself is an indirect proof of the existence of the cosmological neutrino background.

As already mentioned, high-energy charged particles may suffer from interactions with the CMB photons, producing secondary pions and neutrons in the same way than in sources (see section 1.4). As a result of these GZK interactions, the so-called cosmogenic neutrinos, with energies above  $10^{17}$  eV, may also be originated.

Moving to lower energies and focusing on the first astrophysical source of neutrinos observed (our Sun), a surprise arrived with the first detection of solar neutrinos by Davis and collaborators [18]: the number of observed solar neutrinos was found to be nearly a factor of three below predictions. Three hypotheses could explain this discrepancy: either the Standard Solar Model used to predict the different contributions to the solar neutrino flux was wrong, the properties of neutrinos as described by the Standard Model (SM) of particles were more complex or the discrepancy was the result of an experimental bias. The second possibility appeared to be the right one. Most of the possible solutions included unknown neutrino properties and considerations that questioned the Standard Solar Model.

Solar neutrinos therefore helped to discover a key (misunderstood) property of neutrinos: they are massive particles. More importantly, this non-zero mass allows for the oscillation of the neutrino flavour from one eigenstate to another, as will be described in section 1.3.1. Thus, neutrinos can be described as a mixing of the mass eigenstates, with the flavour eigenstate oscillating as the particle propagates.

### 1.3.1 Neutrino oscillations

According to the Standard Model of particle physics, each of the three flavours of charged leptons ( $e$ ,  $\mu$ ,  $\tau$ ) has a neutrino associated to it ( $\nu_e$ ,  $\nu_\mu$ ,  $\nu_\tau$ ). Weak interactions involving neutrinos preserve the total number of leptons of each flavour. The measurements of the width of the  $Z^0$  boson<sup>2</sup> resonance indicate that data are in agreement with the prediction of the existence of three light neutrino flavours.

It is known that the mixing between the flavour and mass eigenstates of neutrinos produces neutrino oscillations. In other words, the three flavour neutrino states interacting through the weak force are different superpositions of the three propagating neutrino states of definite mass. This means that neutrinos are produced in weak processes and detected in their flavour eigenstates but travel as mass eigenstates. The process is illustrated in Fig. 1.4.

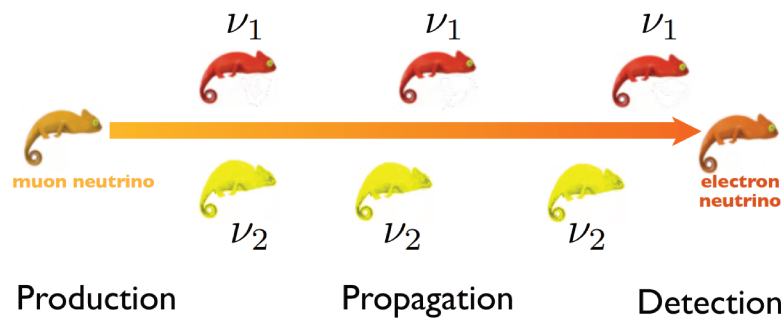


Figure 1.4: Representation of the neutrino mixing, with a neutrino flavour state oscillating into another and the two separate mass states present during the propagation.

This mixing is typically represented in the form of the so-called Pontecorvo-Maki-Nakagawa-Sakata (PMNS) matrix, noted  $U$  in the following. This matrix can be written as a function of the three mixing angles ( $\theta_{12}$ ,  $\theta_{23}$  and  $\theta_{13}$ ), that define the mass composition of each flavour eigenstate. The expression for the neutrino mixing matrix is the following:

$$U = \begin{pmatrix} 1 & 0 & 0 \\ 0 & \cos\theta_{23} & \sin\theta_{23} \\ 0 & -\sin\theta_{23} & \cos\theta_{23} \end{pmatrix} \begin{pmatrix} \cos\theta_{13} & 0 & \sin\theta_{13}e^{i\delta} \\ 0 & 1 & 0 \\ -\sin\theta_{13}e^{-i\delta} & 0 & \cos\theta_{13} \end{pmatrix} \begin{pmatrix} \cos\theta_{12} & \sin\theta_{12} & 0 \\ -\sin\theta_{12} & \cos\theta_{12} & 0 \\ 0 & 0 & 1 \end{pmatrix}$$

In addition, a complex phase ( $\delta$ ) appears in the modeling of neutrino oscillations. This phase violates the CP symmetry<sup>3</sup>, introducing a different oscillation probability for neutrinos and anti-neutrinos [19].

The probability of a neutrino of flavour  $\alpha$  to oscillate into a neutrino  $\beta$  will depend on the traveled distance ( $L$ ), the neutrino energy ( $E_\nu$ ) and the difference between the squares masses of the two mass states ( $k$  and  $j$ ) composing the neutrino flavours ( $\Delta m_{kj}^2 = m_k^2 - m_j^2$ ). They are related through the

<sup>2</sup>The  $Z^0$  and  $W^\pm$  bosons are the mediators of the weak interaction through which neutrinos interact and are produced.

<sup>3</sup>CP stands for Charge Parity, which is a quantum number characterizing a particle state. According to the physics conservation law of CP, the number of particles and antiparticles in the initial and final interaction states must be conserved.

following expression:

$$p(\nu_\alpha \rightarrow \nu_\beta) = \sum_{k,j} U_{\alpha k}^* U_{\beta k} U_{\alpha j} U_{\beta j}^* \times \exp(i \frac{\Delta m_{kj}^2 L}{2E_\nu}). \quad (1.1)$$

In case of two neutrino flavours, only once mixing angle ( $\theta$ ) and mass difference ( $\Delta m^2$ ) appear, with the equation 1.1 being simplified to the following form:

$$p(\nu_\alpha \rightarrow \nu_\beta) = \sin^2(2\theta) \sin^2(\frac{\Delta m^2 L}{4E_\nu}). \quad (1.2)$$

In the presence of matter, the oscillation patterns described above are distorted since neutrinos can be subject to interactions when propagating through matter [20]. As it will be seen in section 2.1.2, neutrinos can undergo both neutral current and charged current interactions. While the neutral current interactions have no effect on the oscillation (identical interactions for all flavours), the charged current interactions change indeed the oscillation pattern presented earlier.

In the energy range of the solar neutrinos (a few MeV), it is not possible to generate  $\mu$  and  $\tau$  leptons in the Sun. However, electrons present in the Sun (and in matter in general) will interact with the electron neutrinos produced through nuclear interactions via elastic scattering, giving rise to the so-called matter effect (see the interaction diagram in Fig. 1.5). This additional matter interaction potential has to be added to the mass matrix in the Hamiltonian describing the evolution of a neutrino state in the presence of matter. This potential can be written in the following form:

$$V_e = G_F \sqrt{2} N_e, \quad (1.3)$$

where  $G_F$  is the Fermi constant (coupling constant for the weak interaction force according to the SM and the Quantum Field Theory) and  $N_e$  the electron density in the medium generating the potential. An interesting case is when the electron density is such that it leads to a resonance, i.e. to the maximal mixing angle between the mass eigenstates. This is known as the MSW (Mikheïev-Smirnov-Wolfenstein) resonance and in fact, the solar core matches this resonant electron density.

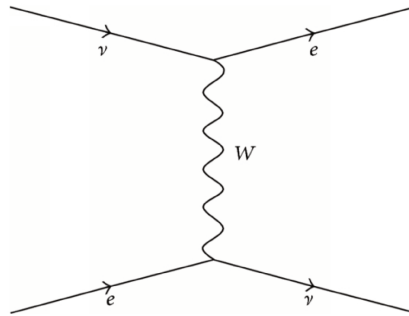


Figure 1.5: Feynman diagram illustrating the elastic scattering interaction between  $\nu_e$ 's and electrons producing the matter effect.

As a consequence of the MSW effect occurring in the Sun, the  $\nu_e$  flux is largely suppressed, which explains the deficit of solar neutrinos observed by the experiments on Earth. In fact, the ensemble of observations shows that low energy solar neutrinos are suppressed by averaged vacuum oscillations while neutrinos having more than a few MeV energy are suppressed because of the MSW effect. This will be further discussed in the case of CCSN neutrinos on section 4.3.1.

One of the unknown neutrino parameters is the sign of the mass square difference  $\Delta m_{31}^2$ , which would determine the so-called Neutrino Mass Ordering (NMO). Since  $m_2 > m_1$  is defined from solar

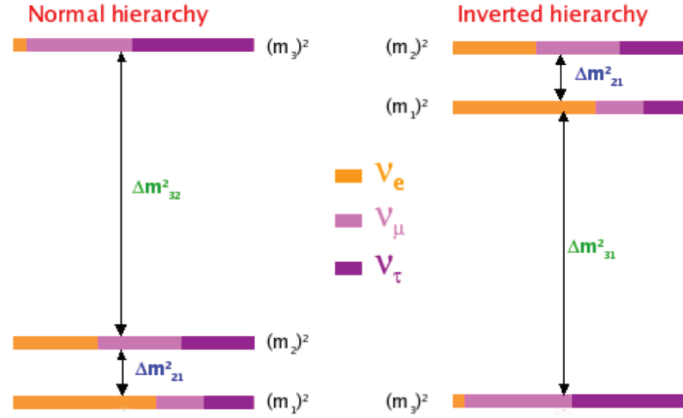


Figure 1.6: Schematic representation of two neutrino mass ordering possibilities, extracted from [21]. The colors represent the relative contribution of each neutrino flavour to each neutrino mass state.

neutrino measurements, two possibilities remain for the neutrino mass ordering: whether  $m_3 > m_1$  (Normal Ordering, NO) or  $m_3 < m_1$  (Inverted Ordering, IO). The two possibilities are illustrated in Fig. 1.6.

While vacuum oscillations are not sensitive to the sign of  $\Delta m_{31}^2$ , the existence of the  $V_e$  potential also introduces a dependence on the sign of  $\Delta m_{31}^2$ . As a consequence, the NMO can be measured by detecting this MSW resonance. In fact, exploiting this matter effect for determining the NMO is the main goal of the KM3NeT-ORCA detector, described in section 2.3. As solar neutrinos traversing the Sun, neutrinos produced in the atmosphere by the interaction of cosmic rays will suffer of this matter effects when going through the Earth. The  $\nu_e$  atmospheric flux will interact with the electrons in matter via elastic scattering producing an effective matter potential given by Eq. 1.3.

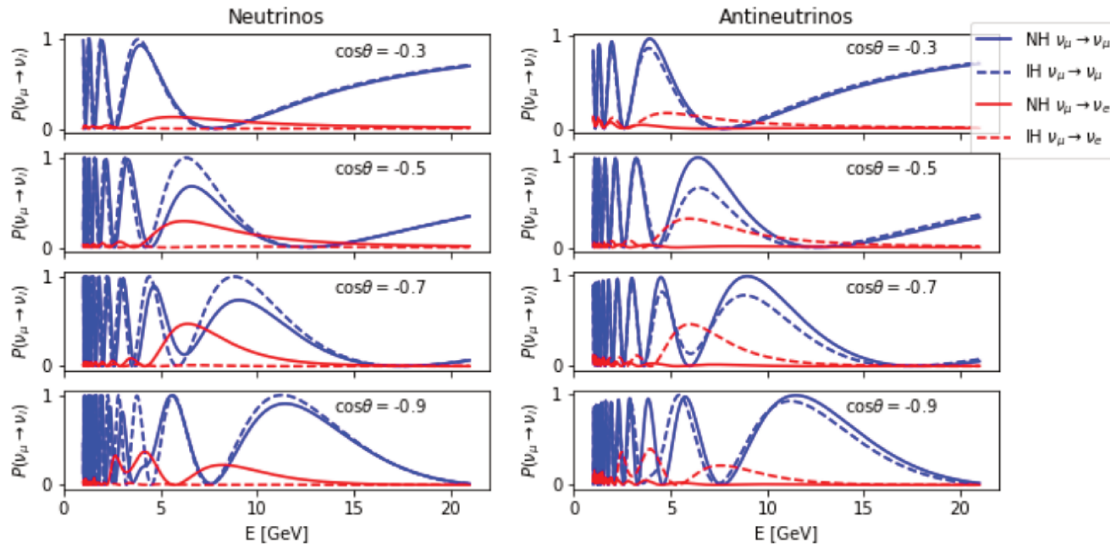


Figure 1.7: The oscillation probabilities for neutrinos passing through the Earth,  $\mathcal{P}(\nu_\mu \rightarrow \nu_e)$  and  $\mathcal{P}(\nu_\mu \rightarrow \nu_\mu)$ . They are shown as a function of the neutrino energy for the different NMO hypothesis and for four different zenith angles. Figure taken from [22].

After taking into account the perturbation effect given by this effective potential, the oscillation probabilities will change, showing a dependence on the neutrino mass ordering as can be seen in

Fig. 1.7. By detecting the atmospheric neutrino flux through the Earth, the ORCA detector will be sensitive to the neutrino mass ordering.

### 1.3.2 Recent results by the IceCube Neutrino Observatory

The first evidence for a high-energy diffuse neutrino flux of cosmic origin was reported by the IceCube (IC) Collaboration in 2013 [5, 6]. Only events with an interaction vertex inside the detector volume and an energy above  $\sim 10$  TeV were considered for this analysis. This gave name to the IceCube sample called High-Energy Starting Events (HESE). The HESE selection allows to veto atmospheric muons (which is one of the main background contributions as will be described section 3.1) and gives access to neutrino events coming from the whole sky. The drastic background reduction from these conditions allowed for the discovery.

In the first analysis, the sample had 28 signal events and the energy threshold was  $\sim 60$  TeV. Since then, the latest HESE sample analysed accounts for 82 neutrino events with energies from 20 TeV to 2 PeV. Most of these events are shower-like events (defined in section 2.1.2) with angular resolutions of 10 to 30 degrees [23, 24]. The angular resolution is the uncertainty on the estimation of the neutrino direction from the reconstruction, which will be introduced in section 3.4.4.

An astrophysical neutrino flux has also been confirmed by additional IceCube searches using other methodologies, such as the muon neutrino diffuse flux search giving name to the IC muon-track sample [25]. Despite the fact that the angular resolution is of the order of  $1^\circ$  for the muon track events, no significant evidence for a preferred sky location has been observed.

The physical information that can be extracted about this flux from IC data are the energy spectrum and the neutrino flavour ratio. For the neutrino spectrum, different hypotheses are tested : an unbroken power-law with a single spectral component, a broken power-law (single spectral power-law with a cut-off) and a double power-law, with two spectral components. The first scenario turns out to best fit the IC data both for the HESE and the muon-track sample.

The best-fit value obtained from the last HESE search (7.5 yr) is a neutrino energy spectrum following an unbroken power law with spectral index of  $\alpha=2.89$  [26]. This analysis applies to all-sky and all-flavour neutrino events. For the muon-track sample, the best fit is an unbroken power-law with a value for the spectral index of  $\alpha=2.28$ , according to the latest results (9.5 yr). This analysis is sensitive only to the northern hemisphere and the  $\nu_\mu$  flavour [27]. Therefore, it is not sensitive to Galactic sources, observed in the southern hemisphere.

A third sample has been considered: the cascade-only events. Events from the full sky are observed with this analysis, that includes both  $\nu_e$  and  $\nu_\tau$  neutrino flavours (complementary to muon-tracks) and 4 yr of data at the moment. In this case, the best-fit coming out from the measurements is a spectral index of  $\alpha=2.48$  for an unbroken power-law. The last updates of these results were presented at ICRC2019 [26, 27] and are summarised in Fig. 1.8.

The tension between the measurements from the different samples could be explained if the origin of the two fluxes is different, motivated by the two searches having been carried on different regions of the sky. In particular, the muon-track sample can be explained as an extra-galactic component with an  $E^{-2}$ - $E^{-2.2}$  spectrum. While the HESE sample may be partly originated from a closer (local) component, with a softer spectrum. In Fig 1.9 we show the best fit for each of the two analyses, which are in tension with each other. The conclusion is that the origin of this flux still remains a mystery.

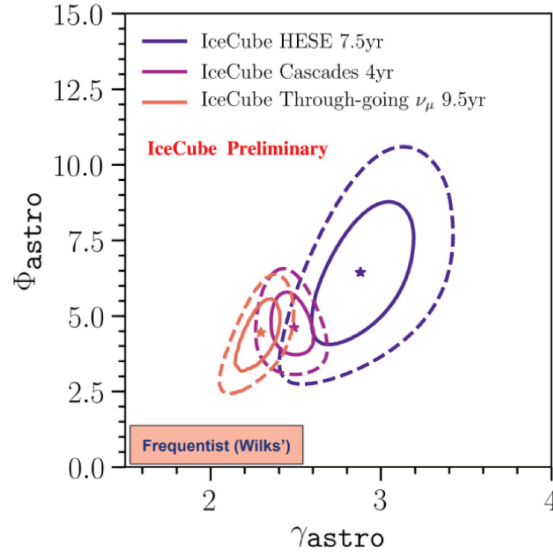


Figure 1.8: IceCube best-fit values on the flux normalization and spectral index for the observed neutrino diffuse flux for the 3 different samples: HESE (purple), cascades (magenta) and muon-tracks (salmon). Figure from [26].

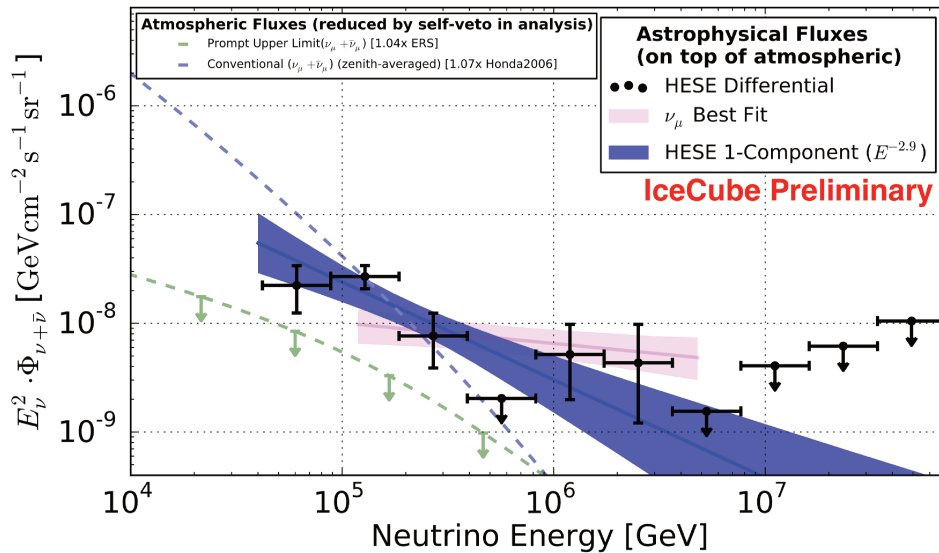


Figure 1.9: The measured differential astrophysical flux measured using all-sky contained events (black points). It is compared with the best fit obtained considering one spectral component for each analysis: pink band for the  $\nu_\mu$  track sample and blue band for the HESE sample. The atmospheric neutrino background expectation from the prompt and conventional models is also shown (dashed green and blue lines). Figure from [28].

As for the flavour composition, IceCube has detected the first two  $\nu_\tau$  neutrino events compatible with the double-bang signature (see 2.1.2), characteristic of tau neutrinos. Including this into the analysis, the latest results (presented in [29]) give as best fit for the neutrino flavour ratio:

$$\nu_e \ 0.29 : \nu_\mu \ 0.5 : \nu_\tau \ 0.21$$

It is the first time that the result gives a non-zero value for all the three flavours. Before, there was a degeneracy between  $\nu_e$  and  $\nu_\tau$  since both flavours interact via charged current producing a shower event (see section 2.1.2) and therefore both flavours were indistinguishable. Now, the two observed double-bang events provide an independent identification of a  $\nu_\tau$ . However, the uncertainties of the

measurement do not allow yet to prove or discard the predicted ratio, which would yield an equipartition between the three flavours ( $\nu_e$  0.33 :  $\nu_\mu$  0.33 :  $\nu_\tau$  33), as expected from the theory for the long traveling distances at the high energies these neutrinos are observed, and according to the production scenario presented in [30] and section 1.4.

A significant observation of this signal cannot be claimed by the ANTARES telescope, but results from a search using 11 years of ANTARES data (Fig. 1.10) lead to a "mild-excess" of  $1.8\sigma$ , with physical properties (flux normalization and spectral index fit) going into the direction of those reported by IceCube, as described in [31]. The null cosmic signal hypothesis is rejected at more than 90% confidence level (CL).

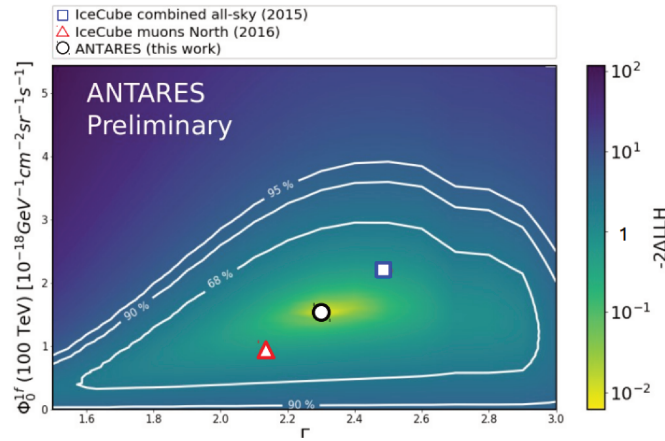


Figure 1.10: ANTARES best-fit for the diffuse neutrino flux search using 11 yr of data (from [31]). The spectral parameters of the fit are the one-flavor neutrino flux normalisation ( $\phi_0^{1f}$ ) on the y-axis, and the neutrino spectral index,  $\Gamma$ , on the x-axis. The analysis includes all-flavours and only events inside the ANTARES field of view.

## 1.4 Multi-messenger connections and neutrino production

The sites that accelerate high-energy CRs are often believed to yield high-energy photons and neutrinos. Indeed, the observational evidence that the total energy density of neutrinos is similar to that of gamma rays and cosmic rays (shown in Fig. 1.11) suggests some connection between the three messengers, which might be injected into the Universe with similar energy densities. In fact, the production of pions in the interactions of CRs with ambient matter or radiation may be the main production mechanism of gamma rays and neutrinos through their decay. The pions would be produced via a delta resonance (p- $\gamma$  interactions, Eq. 1.4) or nucleon-nucleon (p-p,p-n) interactions (Eqs. 1.5,1.6):



The charged pions will decay emitting neutrinos, whereas a neutral pion decaying will produce a pair of gamma rays. The decay chains are given in equations 1.7. According to this explanation, referred

to as the hadronic model, acceleration sites of CRs would also be regions for high energy  $\gamma$ -rays and neutrino production.

$$\begin{aligned}
 \pi^+ &\rightarrow \mu^+ + \nu_\mu \rightarrow e^+ + \nu_e + \bar{\nu}_\mu + \nu_\mu \\
 \pi^- &\rightarrow \mu^- + \bar{\nu}_\mu \rightarrow e^- + \bar{\nu}_e + \nu_\mu + \bar{\nu}_\mu \\
 \pi^0 &\rightarrow \gamma + \gamma
 \end{aligned}
 \tag{1.7}$$

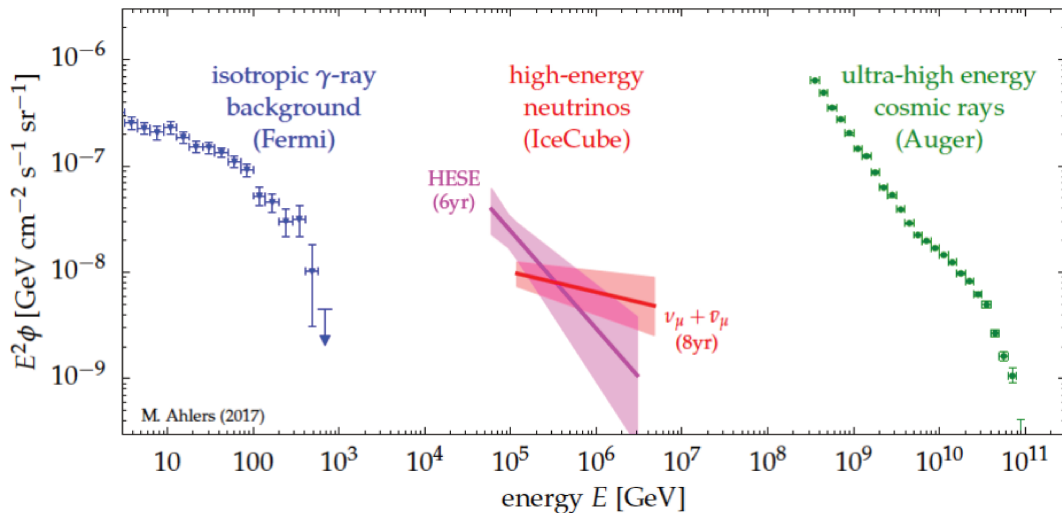


Figure 1.11: The measured diffuse energy fluxes in our Universe for the different cosmic messengers from [32]. The flux of neutrinos for the HESE and muon-track sample [24, 25] (red and magenta data) compared to the flux of unresolved extra-galactic  $\gamma$ -ray emission measured by Fermi [33] (blue data) and the ultra-high energy CR flux from Auger [34] (green data).

Fig. 1.11 can be explained by the following connection within the three messengers. As stated in the previous paragraph, cosmic-ray interactions will produce both charged and neutral pions (Eqs. 1.4,1.5,1.6) whose decay originates neutrino and gamma-ray emission (Eq. 1.7). Therefore, gamma-ray sources could also be HEN and ultra-high energy (UHE) CR emitters. The high-energy gamma rays produced in extra-galactic sources will be strongly absorbed at the highest energies and will not be observed with the current instruments. But the high-energy gamma-ray emission will originate EM cascades (through Inverse Compton) producing gamma-ray photons that will contribute to the observed fluxes below 100 GeV.

According to the hadronic scenario, sources of gamma rays are potential HEN sources. However, the sources of the observed  $\gamma$ -rays could be related to the interaction of leptons with EM fields, as suggested by the so-called leptonic model. In this case,  $\gamma$ -ray photons at low-energies are produced through non thermal processes: synchrotron radiation and Inverse Compton Scattering.

It is likely that the production mechanism within a given source cannot be explained by only one of the models. The best example is the observation of TXS 0506+506, where neither the hadronic nor the leptonic models (even not a mixture of both) can easily explain the electromagnetic emission of the blazar and the neutrino flare observed by IC from the same source, as discussed in section 1.4.1.

The current status is that leptonic models can typically explain the acceleration of electrons giving rise to gamma-ray emission up to energies of hundreds of GeV for most of the observed sources.

However, the observation of very-high energy gamma-ray emission could be a hint of hadronic acceleration. Moreover, now we have observed galactic sources in gamma rays at higher energies, since the HESS Collaboration recently announced a strong evidence of a PeV cosmic-ray emitter (PeVatron) in the Galactic Center [35]. Despite of the huge effort, new missions and more data, no clear confirmation of any other sources where hadronic processes are in play has been possible up to date.

### 1.4.1 Multi-messenger results

The beauty of the multi-messenger astronomy is that each of the messengers brings different and complementary information. Adding all this information together could allow for a complete understanding of the astrophysical phenomena and the objects in play and also give access to relevant measurements such as the time delay between the different messengers for better constraining their relation and also some physical parameters (e.g. the neutrino mass). Thus, the combination of all this information from a single source is more valuable than the sum of the information from different sources from a single messenger.

With the multi-messenger observations in 2017, MM astronomy became a reality. As the first multi-wavelength observation and the beginning of the GW astronomy, this was a breakthrough in the field of astroparticle physics. Now, it is clear that MM astronomy is the best way to proceed to learn as much as possible from the most catastrophic phenomena in the Universe and to solve the mystery of the UHE cosmic-ray sources. Closing the loop by detecting both neutrinos and EM or/and GW radiations from a same source, or even better detecting the three messengers from a unique event, is the goal of neutrino telescopes participating in MM campaigns.

It is impressive how once a transient phenomena is detected with a certain messenger, many different observatories put their efforts together to follow-up this event, searching for a counterpart both in real-time and with a refined analysis later on. In the last years, the participation and fast response of the community has significantly increased.

As seen in this section, different messengers can be emitted by the same astrophysical event very close in time. The multi-messenger astronomy tries to exploit this correlated emission to find, among other things, which are the yet unknown high-energy CR and HEN sources. The search in a restricted area and time window allows for a significant background reduction compared to diffuse and time integrated point-source searches, while the signal expectation is not lowered in case of a localised transient event. Therefore, it yields an increase of the discovery potential of an astrophysical source, notably for neutrino telescopes.

#### The binary neutron star merger: GW170817

The GW170817 gravitational-wave event occurred shortly after the advanced Virgo (aVirgo) detector joined the data taking and only a few days before the end of the run for an upgrade of the detectors [8]. However, only the advanced LIGO (aLIGO) detectors observed it, as will be explained later on in this section. This event was the first direct detection of a binary neutron star (BNS) system through the GW signal from the merger of the two compact objects. This happened almost fifty years after the first direct detection in radio of a BNS system by Hulse and Taylor [36]. Before this detection, previous GW signals were detected from Binary Black Hole (BBH) mergers, with different characteristics that will be detailed below. More than 70 observatories took part in the multi-messenger follow-up. The chronology is reported in Fig. 1.12.

The measured masses for the two merging objects were in agreement with masses of known Neutron Stars (NSs). The nature of these objects was later confirmed by the electromagnetic observations

as NSs. However, the nature of the remnant object (BH or NS) is not known. A late neutrino detection would be a proof of the presence of a long-lived neutron star, as will be discussed in Part III. The reconstructed parameters of the event are provided in [37, 38].

This event is also the most significant gravitational wave signal observed [8]. This can be surprising as a smaller amplitude of the signal is expected from the lower masses of neutron stars with respect to black holes. However, this event was also ten times closer than any previous GW signal, at a reconstructed distance of roughly 40 Mpc, with the amplitude proportional to the inverse of the distance. Thanks to the short distance of this event, it fell inside of the horizon of the three GW interferometers, including aVirgo whose horizon was at 58 Mpc during O2 for binary neutron stars.

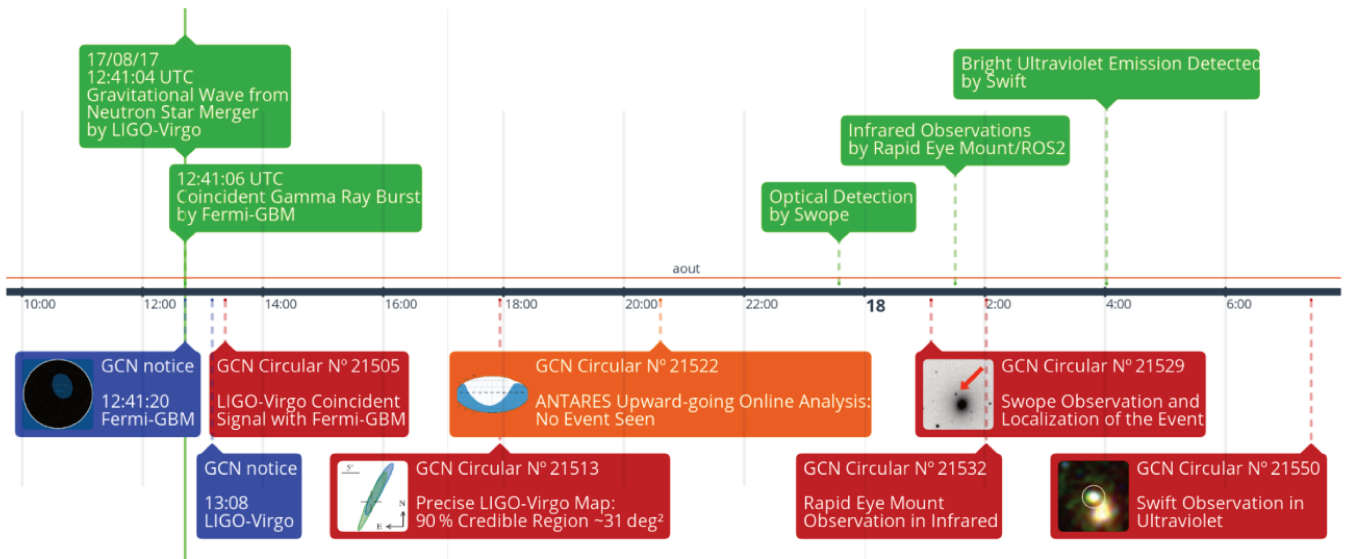


Figure 1.12: Timeline of the multi-messenger observations of the event GW170817 over the EM spectrum (green) as well as the Gamma-ray Coordinates Network (GCN) notices (blue) and circulars (red) sent subsequently in the 18 hours following the event. The ANTARES GCN circular is indicated in orange. Figure from [39].

Due to the non-detection by aVirgo, this interferometer did not contribute to the estimate of the source parameters but helps to significantly constrain the source sky position. Thanks to this, the 90% credible region of the GW signal, that using only aLIGO detectors had the size of  $190 \text{ deg}^2$ , was reduced to  $31 \text{ deg}^2$  when including aVirgo. This represents the best precision ever achieved for source localization with that kind of detectors.

Moreover, the merging time-scale of neutron star binaries being proportional to the inverse of the mass to the fifth power, makes BNS signals to be longer. This was indeed the case for GW170817, whose observed signal was  $\sim 50$  times longer than BBH signals, lasting for about 100 s compared to a few seconds. This together with the time it took to reprocess and clean the GW data before claiming a detection were the reasons why the EM counterpart was announced first and the association with the Fermi signal was reported in the form of a notice circulated within the Gamma-ray Coordinates Network (GCN), with identification number GCN #21505.

The Fermi Gamma-ray Burst Monitor (Fermi-GBM) was the first experiment to send a public alert to the community 14 s after the detection [40]. The event, whose lightcurve is shown in Fig. 1.13, was seen with a  $4.8\sigma$  significance and a rough localization of the event covering a  $3200 \text{ deg}^2$  credible region. After the aLigo-Virgo Collaborations released the GCN notice, the GW signal was linked with the GRB seen by Fermi-GBM, arriving 1.7 s after the merger. The gamma-ray signal was detected by

INTEGRAL SPI-ACS as well (GCN #21507).

This short  $\gamma$ -ray burst surprised the community by being the closest and dimmest of the short GRBs with known distance. This is probably an observation bias rather than a lucky coincidence. Among the short  $\gamma$ -ray bursts with unknown distances, some are probably similar. In fact, new faint candidates have been identified over the last year [41, 42].

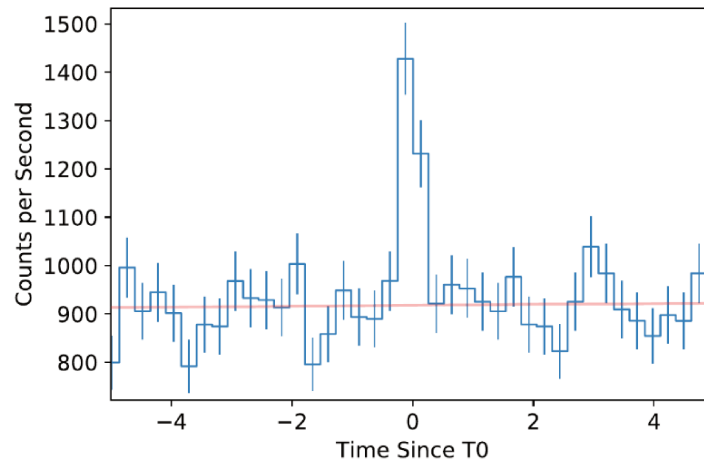


Figure 1.13: Lightcurve measured by Fermi-GBM during GRB 170817A in the 50 to 300 keV band. The red line indicates the background estimate. Figure from [43].

Only ten hours later, when it became night in Chile, the 90% credible region was in the field of view of terrestrial telescopes. The optical telescopes strategy was to target cataloged galaxies inside of the three-dimensional localization of the event accounting for their stellar mass and star formation rate. It was the 1 m Swope Telescope that first detected optical light from this source and located the event in the galaxy NGC 4993. Five other optical detections followed within an hour [44]. Once it was well localised, space telescopes also followed this event.

The optical observations of the event were followed by the near-infrared and ultraviolet signals, with continuous observations during several days after the coalescence. These signals showed an unusual rapid luminosity decline in UV-blue and brightening of the near-infrared emission. Their evolution is considered unprecedented by the community for a transient event in the nearby universe, giving name to the so-called kilonova emission. This fact made this event even more interesting and brought several physical implications of interest [45].

The nucleosynthesis of heavy elements is a key question in nuclear astrophysics. Before the kilonova detection, the preferred candidates for nucleosynthesis of heavy elements were in fact core-collapse supernova explosions [46]. However, simulations are not able to fully reproduce such phenomena at this source. The measurement of the nuclei abundances from GW170817 shows that the coalescence of a binary neutron star system is a promising candidate for the formation of heavy nuclei up to the lanthanides. Moreover, the data are perfectly matching the models tested in simulations, as seen in Fig. 1.14.

Indeed, the most important implication of GW170817 is probably the kilonova detection. A kilonova is the EM radiation observed hours to days after a compact binary system merges [47]. Such emission is the result of the radioactive decay of heavy elements produced by r-process that are heating the ejecta [48]. The r-process (r standing for rapid neutron capture) is the main mechanism of synthesis of atomic nuclei heavier than lead. Since these nuclei are not stable, the neutron capture must be faster than the decay time of the newly formed nucleus so that it does not undergo  $\beta$ -decay before another

neutron is captured. Therefore, it occurs in neutron-rich environments like matter thrown from a BNS merger. The s-process (slow neutron capture) may also take place, explaining the formation of lower mass heavy nuclei (between iron and lead for instance). The latter also takes place in core-collapse supernova.

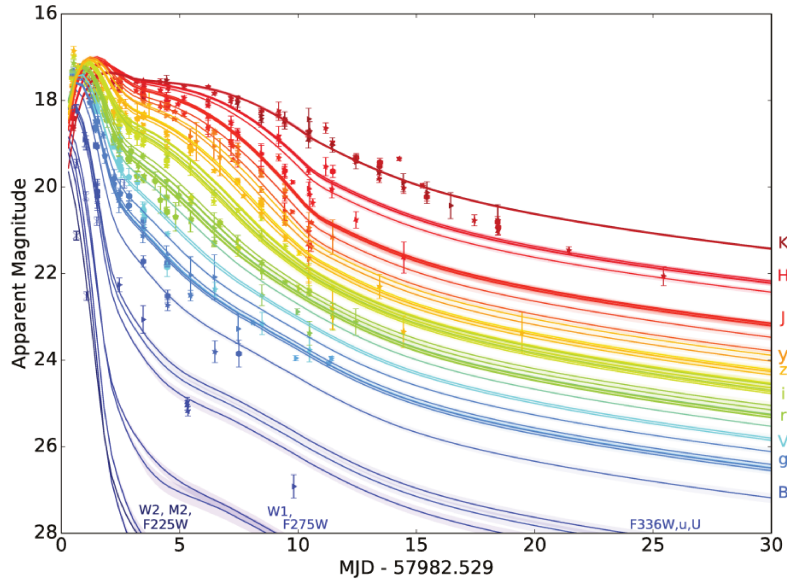


Figure 1.14: Kilonova lightcurves over the different bands of the EM spectrum for days after the merger together with the models (coloured solid lines) better matching these data (points with error bars), from [49]. The lightcurves are shown for the ultraviolet, optical and infrared observations.

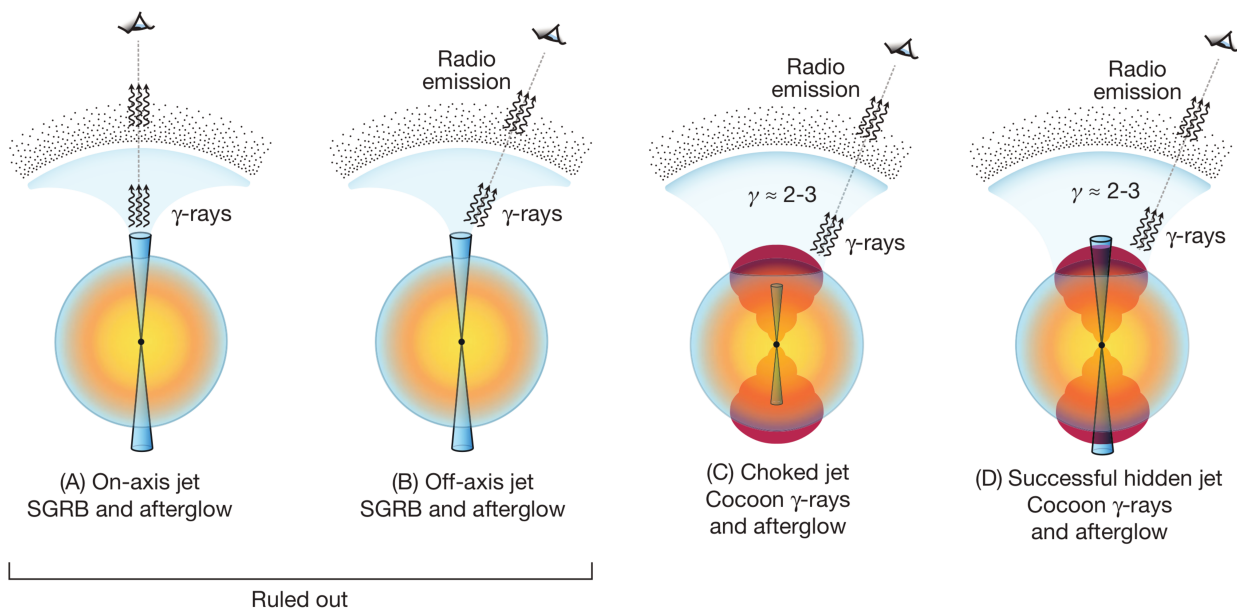


Figure 1.15: Potential scenarios for the jet and dynamical ejecta described in the text. The merger remnant is represented by the black point and the blue cones are the released jets. The spherical ejecta is represented in orange and the cocoon in red. The black dotted region represents the environment surrounding the merger, interacting with the jet. Figure from [39]

In addition to the kilonova, the Fermi-GBM detection confirmed the long-standing hypothesis that short-GRBs are originated from compact binary mergers and allowed for a more precise estimate of the neutron star merger rates for joint GW and EM detections. Moreover, both an uniform and sub-luminous jet seen on-axis is ruled out since they cannot explain the late radio observations. Thus, the simplest models which are typically used to describe short GRBs forced theoreticians to consider more complex models, summarised in Fig. 1.15.

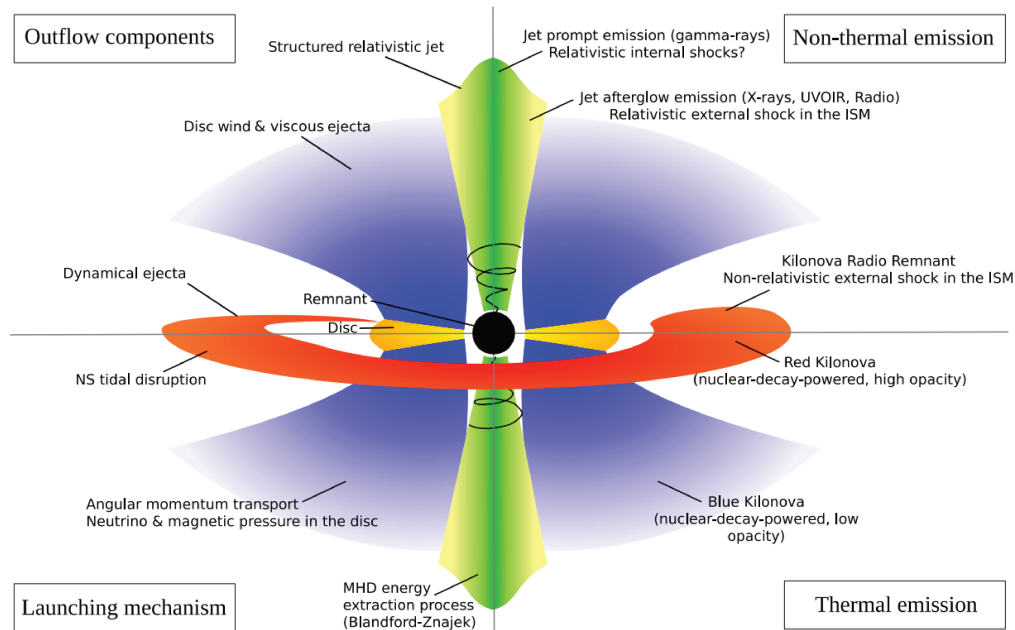


Figure 1.16: The current picture of the scenario describing GW170817 multi-messenger emission, with the different mechanisms, outflow components and emission processes as understood from data [50].

In principle, two different scenarios within this assumption could accommodate the different observations. The first is simply that the jet can be shocked if it does not escape from the ejecta. The second one suggests a successful jet which is very collimated (structured) and with a Lorentz factor decreasing with the opening angle. The afterglow (late radio) emission is explained by the interaction of the jet with the medium surrounding the merger, which would give rise to the so-called cocoon (midly relativistic region), explaining the low luminosity observed in gamma rays. Thanks to the long-term radio and X-rays observations [51], a choice could be made between the two scenarios. In fact, it is the structure-jet mechanism that is in agreement with all available data rather than the choked jet scenario. This was confirmed by the VLBI radio interferometric observations [52]. The state-of-the-art description of these phenomena, in Fig. 1.16, has been built from what was learned from this event.

Finally, some cosmological applications have been possible with GW170817 multi-messenger observations. On the one hand, the GW and EM data from this event have been used to independently determine the Hubble constant [53], allowing to help solving the tension between the measurements by Hubble (from the late Universe) and Planck (from the early Universe), which is yet not understood. On the other hand, these data have been used to perform some gravitation tests such as the measurement of the difference between the speed of light and the speed of gravity.

A neutrino follow-up was jointly carried out by the ANTARES, IceCube and Auger Collaborations. The results yielded no neutrino observed in coincidence with the GW trigger. From this null detection, constraints on the neutrino spectral fluence were derived, presented in Fig. 1.17 compared to the neutrino emission models, for two different time window searches. In part III, the neutrino flux predictions (chapter 9) and ANTARES search method (section 10.4) will be presented.

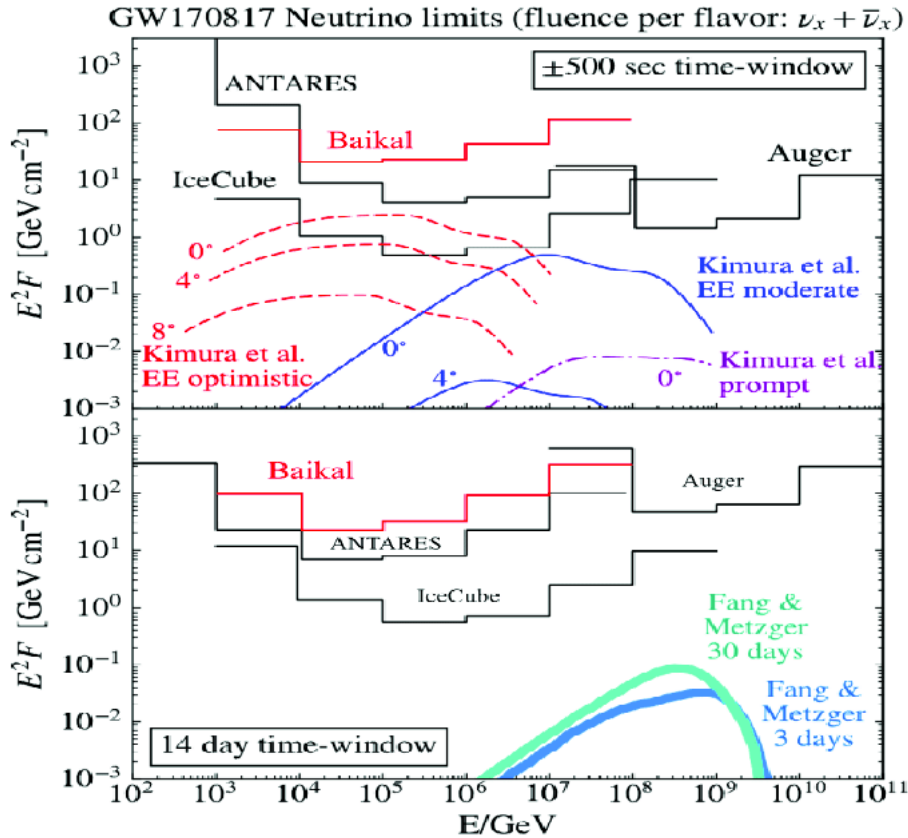


Figure 1.17: 90% confidence level (CL) upper limits on the neutrino spectral fluence obtained with ANTARES, IC and Auger data [54]. On the top, for the search of a prompt extended emission over  $\pm 500$  s with neutrino predictions from [55]. On the bottom, for the search of a long neutrino emission over 14 days with neutrino flux expectations from [56].

### The case of blazar TXS 0506+506

On September 2017, one high-energy neutrino was observed by IceCube in the direction of the blazar TXS 0506+506 in coincidence with a gamma-ray flare detected by Fermi-LAT and MAGIC [9]. The evidence of a multi-messenger connection from this source motivated a search for a point-like neutrino excess from this blazar in the archival IceCube data. Surprisingly, a neutrino flare of  $13 \pm 5$  neutrinos was found in 2014-2015 [10]. The two flares are shown correspondingly in Fig. 1.18 (2017) and Fig. 1.20 (2014-2015). Going back to the electromagnetic data, no coincident flare was observed during this earlier period. Yet today, many people are trying to interpret the experimental data in order to understand the leptonic and hadronic processes at play for the two flares.

Regarding the 2017 flare, one can state the facts that on the one hand if the emission is purely leptonic, then no neutrino is expected in coincidence. On the other hand, if the emission is hadronic, then it is constrained by the X-ray detection. Let's see the different cases in Fig. 1.19. On the left plot, one sees that the leptonic models only can fit the EM spectral distribution observed. But does not explain that neutrinos are produced. On the middle, we see that the typical  $p - \gamma$  models are not compatible with the X-ray observations. On the right, we have the case where the conventional synchrotron self-compton emission dominates and there is a sub-dominant hadronic component that could lead to the observed neutrino flux, with a consistent spectral energy distribution between the data and the model.

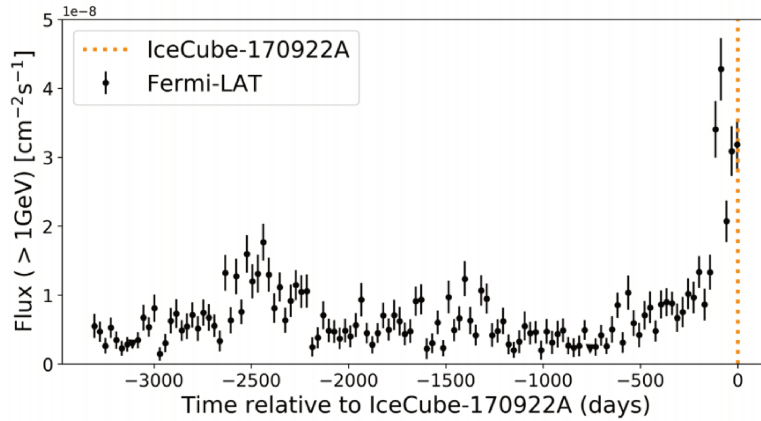


Figure 1.18: Lightcurve of blazar TXS 0506+506 observed by Fermi together with the time of the IceCube event IC190922 (orange dashed line). Figure from [9].

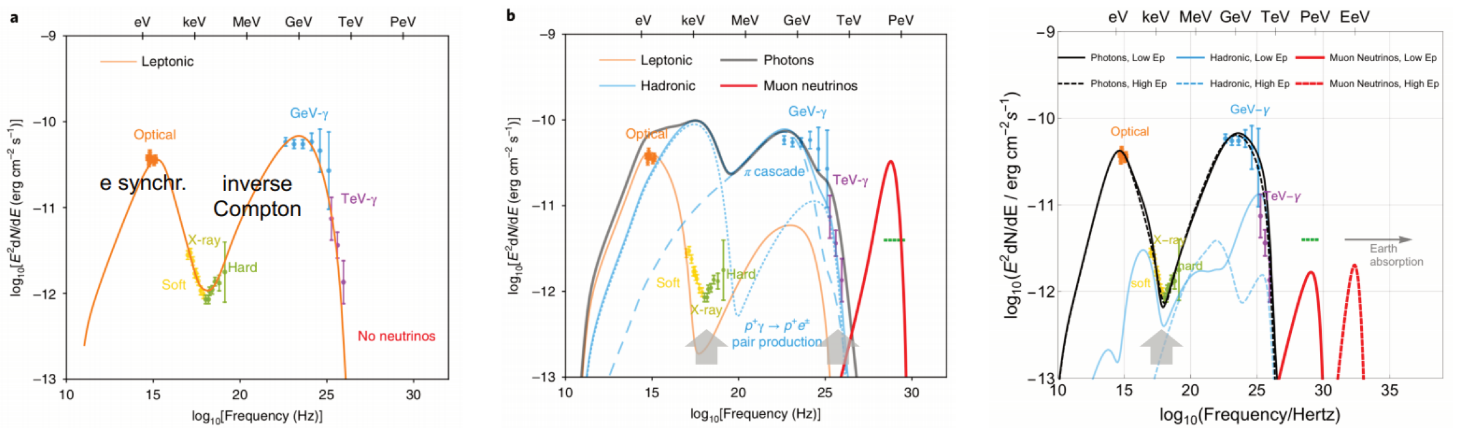


Figure 1.19: On the left, the leptonic emission one-zone model. In the middle, the hadronic (pion cascade) model. On the right, hadronic-synchrotron one-zone model. Figure from [57].

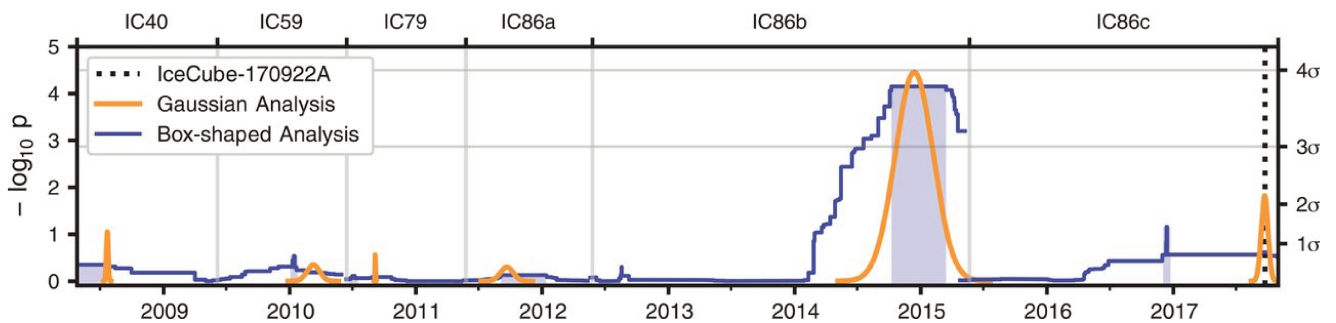


Figure 1.20: Neutrino lightcurve observed by IceCube from the direction of the blazar TXS 0506+506, including the 2014-2015 flare and the 2017 neutrino event. The results for two time profiles used for the time-dependent analysis by the IceCube Collaboration are shown in orange (gaussian) and dark blue (box-shaped). The shaded blue boxes correspond to the the most significant time window in each period. Figure from [10].

Moving to the 2014-2015 neutrino flare, the description of an excess of 13 neutrino events above the expectation from the atmospheric background with no EM counterpart requires physical conditions in which the gamma rays can be absorbed. The imprints of these conditions in the Spectral Energy

Distribution (SED) seem to be in contradiction with observations. The theoretical challenge is to explain on the one hand, where all the energy in HE photons and electron goes (since no EM flare is observed), and on the other hand the high neutrino flux, whose luminosity is about 4 times larger than the gamma-ray luminosity.

The first attempts to model this flaring emission are the so-called one-zone models. In this case, one has to accept that either the Eddington luminosity is significantly exceeded or that the observed neutrino flux is not reproduced by the model. In fact, more than two neutrino events emitted are difficult to accommodate in this model. Multi-zone models (external radiation fields or compact core models) can produce substantially larger neutrino fluxes with reasonable energetics as well as a spectral hardening in gamma rays, seeming good candidates to explain the data [58]. However, the spectral hardening observed in Fermi data is not significant and still debated. One of the most recent studies on the modeling of this source can be found in [59, 60, 61].

The ANTARES Collaboration also carried out a search for high-energy neutrinos in the direction of TXS 0506+506. Three different analyses were performed: a real-time follow-up, a time integrated point-source search and a time dependent search for a neutrino flare. They all yield no excess of neutrinos from this source [62].

After this short overview with the latest interpretations about the TXS 0506+506 observations, the conclusion is that more multi-messenger associations are needed for solid predictions as well as a multi-wavelength monitoring of the candidate neutrino sources for a better indication of an hadronic contribution.

## 1.5 Candidate neutrino sources

Natural suspects for neutrino sources are astrophysical objects which exhibit a hint for particle acceleration because if hadrons are accelerated on these sites, they could be sources of HEN. The most relevant candidate sources, galactic and extra-galactic, are discussed below.

### 1.5.1 Extra-Galactic neutrino potential emitters

- **Active Galaxy Nuclei (AGN)** are very luminous compact regions located at the center of a galaxy which probably host a Super Massive Black Hole (SMBH) actively accreting matter which emits radiations from the radio domain to the gamma-ray band. These objects are known to release an amount of energy placing them as the most luminous persistent sources. This energy is thought to be coming from the gravitational energy released by matter falling onto the SMBH, generating an accretion disk. In some cases, AGNs may also emit relativistic jets while the exact connection between accretion and relativistic ejections are still not precisely understood. Neutrino production is possible in both the accretion disk and in the jets. In the first case, the pion production is provided by thermal photons while in the latter the target can also be synchrotron photons.

It is convenient to divide AGNs according to the strength of the radio signal into radio-quiet and radio-loud AGN. In the radio-loud objects, the emission contribution from jets and lobes is prominent especially for radio emission. In the radio-quiet objects, the continuum radio emission comes from core regions since jet and jet-related emission are weak. We focus in this section on neutrino production in CR accelerators. The accelerators at these sources can be jets for radio-loud AGNs, or AGN cores for both radio-loud and radio-quiet AGNs.

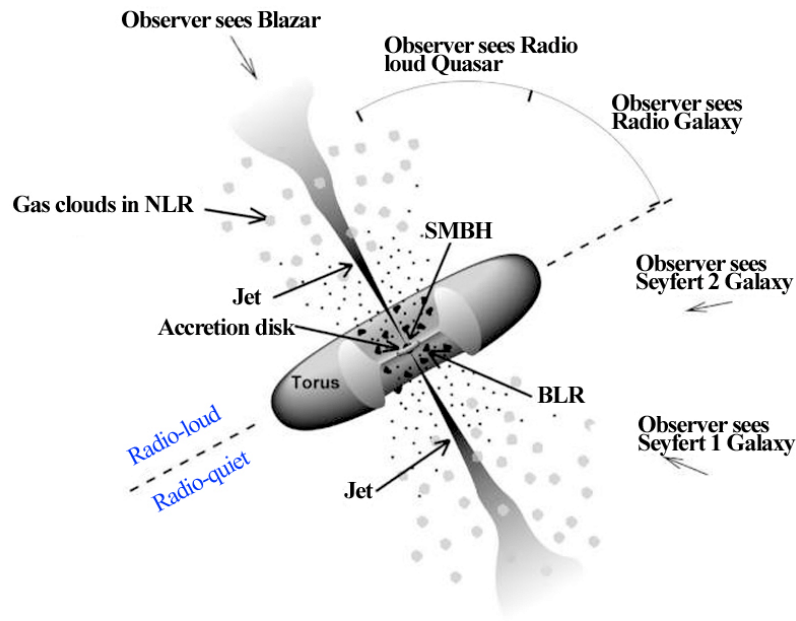


Figure 1.21: Illustration of the two different classifications of active galactic nuclei. The dashed line separates the radio-low and the radio-quiet regions. The different names of the object depending on the orientation of the jet with respect to the line of sight are shown. Figure from [63].

Different classifications exist for AGNs (Fig. 1.21) depending on the orientation of the jet with respect to the observer, which is also related to the intensity of the radio signal. In particular, if the jet axis is oriented along the line of sight, such objects are called blazars. Blazars are interesting as neutrino emitters because higher neutrino fluxes are expected when the jet is directly pointing towards the observer. The radio and X-ray fluxes detected can be explained by synchrotron and/or Inverse Compton acceleration. For higher energies, both leptonic and hadronic models have been used to fit the photon spectral energy distribution of observed blazars.

The IceCube Collaboration has performed different searches considering jetted AGNs [64] and AGN cores [65] in order to estimate their contribution to the observed diffuse neutrino flux. The observational evidence of a high-energy neutrino emission from the direction of blazar TXS 0506+506 has led to different searches aiming at proving them as cosmic neutrino sources. In particular, the IceCube Collaboration has performed searches using the Fermi blazar catalogs [66, 67] as well as dedicated time dependent searches on the archival data as it was done for the TXS 0506+506 2014 flare (see section 1.4.1).

None of these searches yields to a contribution larger than 30% of the total astrophysical neutrino flux measured by IceCube. However, this can still be due to the fact that the catalogs built from EM observations are not representative of the source population. In fact, some recent models show that unresolved blazars could power the diffuse IceCube (PeV) neutrino flux without violating the limits imposed by the lack of correlations with known sources provided some astrophysical conditions are fulfilled. The ANTARES Collaboration has also carried out similar kind of searches [68].

- **Fast Radio Bursts (FRBs)** are astrophysical phenomena showing an intense radio emission in a very short time period (a few ms). So far, they have been measured in the 400 MHz and 1.4 GHz bands by various radio telescopes [69], except for one observation at 8 GHz [70]. No counterpart (optical/x-rays/gamma-rays/VHE gamma-rays) has been identified yet despite many multi-wavelength follow-ups. Their origin is still unknown but measurements indicate that they are extra-galactic/cosmological sources [71].

There seems to be two different classes of FRBs, the repeating ones and the single cataclysmic events. However, the lack of observations does not allow yet for a clear classification. For a recent review on the possible origin of FRBs, see [72]. Indeed, models which include non-explosive events driven by a neutron star, are an example of good astrophysical candidates to explain both types of repeating and non repeating FRBs. These models include giant pulses from young and rapidly rotating neutron stars, magnetar giant flares and hyperflares from soft gamma-repeaters as potential sources; as well as the possibility that they originate from the interior of young supernovae or by a young neutron star embedded in a wind bubble. On the other hand, violent cataclysmic events could be powered by compact objects where the progenitor does not survive afterwards, where an explosion takes place, such as neutron star mergers, possibly associated to short Gamma-Ray Bursts.

A large fraction of the total energy radiated during these radio bursting events may be emitted at high energy while being still undetected. In fact, if the radio emission is likely produced by coherent emission of leptons, hadronic processes may take place in these sources. In this case, HEN can be produced by photo-hadronic interactions. These hadronic processes may occur in the energetic outflow released during a cataclysmic FRB event or in the vicinity of the FRB progenitor through the interaction of the outflow with the surrounding environment.

A single detection of a gamma-ray GRB-like counterpart in association with FRB 131104 has been achieved, but with a small significance to allow for any conclusion. The lack of an FRB counterpart to GRB170817A, also constrains their association with short GRBs. Neither the IceCube Collaboration nor the ANTARES Collaboration have found any neutrino signal in correlation [73, 74]. In fact, if FRBs do emit neutrinos and they are also the source of short GRBs, then this FRB sources can be ruled out in a very nearby environment ( $d < 1\text{kpc}$ ) by ANTARES limits [73].

Due to the lack of additional information on the broadband FRB spectra, it is very difficult to discriminate between the various proposed models. This makes of FRBs a very promising target for future space and ground missions, remaining still an intriguing mystery.

- **Gamma-Ray Bursts (GRBs)** are very luminous prompt emissions of MeV (and higher energy) photons, typically emitted in very collimated jets. They are among the most energetic processes observed in the Universe. They are believed to be produced by electrons that are accelerated in the relativistic jet by shock waves. However, if protons are also accelerated in GRBs, CRs and neutrinos may also be produced.

The so-called "fireball" models stand that the radiation pressure accelerates the fireball to relativistic speeds [75, 76]. This would generate internal shocks in which hadrons may be accelerated and subsequently interact producing neutrinos. According to these models, a large density of photons is radiated, leading to a large number of emitted neutrinos. For this reason, GRBs are one of the preferred neutrino candidate sources.

Two different types of GRBs have been identified according to their duration, short ( $\lesssim 2$  s) and long, and they are believed to have a different origin. On the one hand, long GRBs are thought to be produced in the late stage of rotating massive stars, with the evidence of the association of GRBs with Core-Collapse Supernova [77]. On the other hand, short GRBs are believed to be originated in compact binary mergers (of two neutron stars or a neutron star and a black hole). This was confirmed by the recent multi-messenger observation of a binary neutron merger through GWs (GW170817) in coincidence with a short gamma-ray burst (GRB170817A), as detailed in section 1.4.1 [43].

A combination of different components can be identified in the detected lightcurves of short and long GRBs: the prompt emission, followed by an extended emission (EE), then X-ray flares, and finally plateau emission, (the afterglow). Prompt emission from the central engine is considered responsible for X and  $\gamma$  rays.

For each of the components, different energy scales for the neutrino emission are expected, going from MeV neutrinos produced during the compact object formation (after the stellar collapse or the merging of two compact objects), passing through TeV-PeV neutrino radiation following the prompt phase and up to the PeV-EeV energies reached by neutrinos released at the afterglow. This makes GRBs prime candidates for neutrino emissions. A review of the neutrino production mechanisms will be made in chapter 9 and more details can be also found in [78].

Regarding the long GRB emission, present models rely on the induced gravitational collapse for a possible explanation [79]. In a binary system with a massive star exploding in supernova and a NS companion, the supernova ejecta of the first component would be accreted onto the compact (NS) component. According to this paradigm, electrons and positrons annihilate in the accretion flow producing neutrinos, with energies of some tens of MeV. Contrary to other well known scenarios (such as the Sun or core-collapse supernova), in this case the neutrino-self interaction becomes more relevant than the matter effects. This is due to the extremely high neutrino density near the NS surface, particular to these models. Aside from MeV neutrinos, GeV-TeV neutrinos can be produced within shocks inside the jet and PeV-EeV neutrinos may be released through the interaction of CRs with the interstellar medium.

The lack of a neutrino counterpart observed has set very stringent limits to the neutrino flux predicted by these models. The latest results by the IceCube [80, 81] and ANTARES [82] Collaborations on neutrino searches from GRBs suggest that these sources do not account for more than 1% of the total diffuse neutrino flux measured by IceCube.

In the last year, the first detections of GRBs at very high energies (TeV) were achieved by the MAGIC, GRB 190114C (GCN#23701), and H.E.S.S., GRB180720B [83] and GRB190829A (GCN#25566), Cherenkov Telescopes. The high-energy  $\gamma$ -ray emission by these sources makes them interesting candidates for neutrino production and they will be studied in details in Part III.

Among the sources described here, it is to be mentioned that both GRBs and magnetars together with supernova explosions are also expected to be sources of GW emission. The first coincidence of GW emission with a GRB has already been discussed in section 1.4.1. The different sources of GW emission and their interest as potential neutrino emitters will be discussed in chapter 9 of this manuscript.

### 1.5.2 Neutrino source candidates in our Galaxy

- **Supernova remnants (SNRs)** are the matter ejected in supernova (SN) explosions surrounding the newly formed compact object (typically a NS) after the stellar collapse. The supernova ejecta collide with the interstellar matter, forming a shock wave where particle acceleration might take place.

Indeed, cosmic rays are believed to be accelerated in supernova remnants also according to the "diffusive shock wave acceleration model". Consequently, they are believed to be a natural candidate neutrino source. In fact, SNRs are considered to explain the production of CRs with energies up to the knee ( $10^{15}$  eV) and thus they are one of the preferred candidate source of hadronic acceleration [84, 85].

Nowadays, several SNRs have been observed to emit gamma rays with energies up to the TeV. Different types of SNR exist depending on the morphology. In shell-type SNRs, light emission is dominated by the presence of an expanding outer-shell, which is formed as the shock wave from the SN explosion expands throughout the interstellar medium, heating it. In this environment, interactions of CRs with ambient matter are expected to produce neutrinos and gamma rays via the decay of charged and neutral pions, as explained in 1.4.

**Pulsar wind nebulae** are hosted by SNR and are due to the wind of the rapidly spinning neutron star created after the CCSN, also called pulsar. In this case, the non-thermal emission comes predominantly from the compact object result of the progenitor star which finished its life with the SN explosion. The remnant is formed at the center and fills the SNR with what is referred to as "pulsar wind", consisting of electrons and positrons emitting strong synchrotron radiation. Two alternative scenarios are possible for hadronic acceleration at these sites [86]. Both the shocks in the pulsar and the magnetic field configuration of the pulsar could lead to the acceleration of hadrons. The supernova remnant itself would provide a target environment for the interaction of these particles. Again, leptonic and hadronic models are considered to explain the observed fluxes.

- **X-rays binaries** are binary systems that consist of a compact object (a neutron star or a stellar mass black hole) which accretes matter from a companion star [87]. An accretion disk is formed around the compact object, which is the engine of the observed radiation. They are called X-ray binaries because most of the energy is indeed released through X-rays, but a gamma-ray component is typically also observed. While the first one may be due to the synchrotron radiation (leptonic), the latter could be related with a hadronic component.

If the system exhibits a relativistic jet, as it happens in some cases, then the system is called **microquasar**. In this case, the hadrons of the jet can reach much higher energies (up to a hundred of PeVs or more). Microquasars can be powered either by a weakly magnetised neutron star or by a black hole. Some of them are gamma-ray sources, as proved by the observation of very high-energy emission from the microquasar LS 5039 using the HESS telescope. In microquasars, the presence of relativistic hadrons in the jets can lead to neutrino production through photo-hadron or proton-proton interactions. In the latter case, the target protons are provided by the stellar wind of the companion.

However, a hadronic component from these sources is difficult to motivate using the scenario in section 1.4. The arguments are well explained in [88]. On the one hand, proton-proton processes are not favored in these binary systems since the interaction time  $p - p$  (Eq. 1.5) is very large for

these sources with a low matter density. This implies that the protons have a larger probability of escaping the source than of interacting producing accelerated hadrons. On the other hand, photo-hadronic processes (Eq. 1.4) are not favored either due to the energy threshold, which is of some PeV for protons interacting with visible or UV light. Moreover, there is no evidence for protons to be accelerated to such high-energies on these systems given their size and magnetic field (see Fig. 1.2).

The latest results from the ANTARES [89] Collaboration report no evidence of neutrino emission found so far. Some predictions for the IceCube neutrino observatory are presented in [90].

- **The Sun** is the first astrophysical source of neutrinos identified. Indeed, neutrino production is expected at the several layers of the Sun by different mechanisms.

First, the core of the Sun is known to be a source of nuclear reactions turning Hydrogen to Helium and producing a large flux of neutrinos [91]. The fusion of atoms in the Sun's core leads to neutrinos being produced through different interaction channels: the so-called pp, pep and hep chains; the  ${}^7\text{Be}$  and the  ${}^8\text{B}$  solar neutrinos are the main channels [18]. Their energies extend from hundreds of keV to tens of MeV.

Also in the solar plasma a thermal neutrino flux is expected, being the dominant component in the keV energy range [92]. In this case, neutrino pairs are produced by non relativistic electrons coupling to the Sun's electromagnetic field. Different processes contribute to the total thermal neutrino flux: atomic deexcitation, bremsstrahlung, Compton scattering and photon decays. Due to the low energy threshold, this flux has not been observed so far.

Similarly to the interactions happening in the Earth's atmosphere, one can expect neutrino production from cosmic-ray interactions with the solar atmosphere [93]. This neutrino flux accounts for the addition of the so-called prompt component (produced by charmed hadrons), the contribution from the different mesons (kaons and pions) and also from the decay of secondary muons into neutrinos. The high-energy mesons in the solar atmosphere have a larger chance to decay before being absorbed than in the Earth's atmosphere. The resulting high-energy solar atmospheric neutrino flux is therefore larger than the terrestrial one. However, these high-energy neutrinos might be lost through interactions with the solar material when traveling towards the Earth. This solar atmospheric neutrino flux has not been detected so far. Even though, predictions have evaluated the expected event rates [94] and large neutrino detectors such as IceCube or KM3NeT might be sensitive to this flux.

Finally, solar flares may also be considered as a transient neutrino source as proposed in [95]. The creation of a solar flare is due to the magnetic reconnection of the Sun's magnetic field. As a consequence, electrons and ions present on the solar atmosphere are accelerated with the solar flare emission. Once the accelerated ions reach the chromosphere, the higher density of this layer forces them to interact. Then, the threshold for pion production can be reached for protons which are energetic enough. This would give rise to neutrino production with energies from MeV up to a few GeV.

- **The Galactic Center and the Galactic Plane** are regions of interest for high-energy neutrino astronomy because of various reasons [96]. For what concerns the Galactic Center, a SMBH has been found at the location of SgrA\*, which is the only known source producing PeV photons, as mentioned in 1.4, and hence of high-energy protons. Secondly, the high density of dust and of astrophysical objects around the Galactic Center and in the Galactic Plane, that are active regions

of star formation, makes these sources good candidate sites for hadronic acceleration. Not only the Galactic Center but also the **Fermi Bubbles** present strong non-thermal gamma-ray emission and dense hadronic environment where neutrinos could be produced [97, 98, 99]. These sources being extended regions, a diffuse neutrino flux is expected to arise from them rather than a point-like emission. The neutrino signal predicted could be detected by the neutrino telescopes.

Recent combined searches by the ANTARES and IceCube Collaborations report a non-significant excess of  $1.9 \sigma$  for an extended region of  $2^\circ$  around the Galactic Center. Constraining upper limits have been derived for the neutrino flux from this source [100]. Also a combined search with ANTARES and IC for a neutrino emission from the Galactic Center has been performed and yield no significant excess [101]. This search allowed to exclude the hypothesis of a Galactic Center contribution explaining the IceCube measured flux (with Galactic and Extra-Galactic origin) described in 1.3.2. Also neutrino searches from the Fermi Bubbles search have shown no significant signal contribution from this source so far [102, 103].

- **Supernovas** are, as already mentioned, the second identified source of astrophysical neutrinos. Indeed, the prompt neutrino flux at MeV energies from the core-collapse phase of SN1987A was observed. Currently, no neutrino detector is sensitive to CCSN MeV neutrinos beyond the Small and Large Magallanic Clouds. This prompt neutrino emission and production mechanism will be discussed in detail in Part II together with the experimental performance of current and near-future detectors and the physical implications of the next observation.

As the previous described sources, CCSN can also be classified in two types according to the presence or absence of certain elements in their optical spectra: Type II in the presence of hydrogen and Type I in absence of hydrogen in their spectrum. The Type I can be divided into three sub-classes: Ia in the presence of Si, Ib in the presence of He and absence of Si and Ic in the absence of Si and He. With respect to the believed physical mechanism giving rise the Supernova explosions, one can distinguish two different kinds of events: **Core-Collapse Supernova** (CCSN) and **Thermonuclear Supernova**. The focus is given to the first type, CCSN, since the presence of hydrogen allows for nuclear reaction producing thermal neutrinos that are being released.

After the prompt emission, CCSN are believed to produce neutrinos also at higher energies. A particular situation is that high-energy (GeV-TeV) neutrinos can be emitted from the shock of jets released during the explosion [104], that could be promptly detected and allow for a fast follow-up. Also, there is evidence for dense material around the progenitor undergoing the Core-Collapse (circumstellar medium, CSM). In this case, proton-proton interaction in the CSM may lead to an efficient hadronic acceleration, with 10-1000 HEN events expected to be observed in a detector like IceCube from explosions occurring at 10 kpc [105]. In this case, the signal may be seen hours to days after the collapse.

If fact, neutrino emission is also expected from these sources at the so-called pre-supernova phase [106], mainly due to the silicium burning. This neutrino radiation will be at lower energies and it will have a considerably lower luminosity than the observed spectrum at tens of MeV energies from the collapse phase itself. This signal would help both to alert of a CCSN event happening and to probe the final stages of the star evolution. However, with current experiments the detection of such neutrinos is only possible for very nearby sources ( $\sim 0.2$  kpc).

# Chapter 2

## Neutrino telescopes

The present chapter introduces the detection principle of Cherenkov neutrino telescopes, with a focus on the main neutrino interactions at high-energies (TeV-PeV range), to which large underwater detectors are sensitive. The ANTARES and KM3NeT detectors, the latter being under construction, are described. The analyses presented in this manuscript rely on data of these experiments, but other relevant detectors for the global comprehension of the thesis context are also described. The basics of the detection technique, the detector layouts and data acquisition system are described.

### 2.1 Detection principle

Neutrinos can only be detected when they interact through the weak nuclear force with a nucleon or with electrons/positrons. Depending on the force carrier, the interaction can occur via neutral current (NC), through the exchange of a Z boson, or charged current (CC), by the exchange of a W boson.

High-energy neutrino interactions will yield relativistic charged particles subsequently inferring Cherenkov light in media such as sea water. The Cherenkov light is then detected with a three-dimensional array of photomultiplier tubes (PMTs).

#### 2.1.1 Cherenkov radiation

Emission of Cherenkov light takes place when a charged particle travels through a transparent medium with a velocity that exceeds the speed of light in the medium. This is due to the polarization of the molecules and atoms of the media by the charged particle crossing it at relativistic speed. This radiation is emitted under a characteristic angle with respect to the incoming particle, called the Cherenkov angle, which is given by the following expression:

$$\theta_c = \arccos\left(\frac{1}{\beta \cdot n}\right), \quad (2.1)$$

where  $\beta$  is the velocity of the particle ( $v$ ) expressed as a fraction of the speed of light in vacuum ( $c$ ), i.e  $\beta = \frac{v}{c}$ , and  $n$  is the index of refraction of the medium. In water, this angle turns out to be  $\theta_c=42.5^\circ$  for highly relativistic particles ( $\beta \approx 1$ ). As seen in Fig 2.1 (left), where the detection principle is illustrated, a cone of light under this Cherenkov angle is the observational signature of the passage of a relativistic charged particles. The two event topologies observed in water Cherenkov detectors are illustrated in Fig 2.1 (right) and will be detailed in section 2.1.2.

The expected number of photons emitted per unit of length  $x$ , and wavelength  $\lambda$ , can be expressed as

$$\frac{dN_\gamma^2}{dx d\lambda} = \frac{2\pi\alpha Z}{\lambda^2} \left(1 - \frac{1}{\beta^2 n^2}\right), \quad (2.2)$$

where  $\alpha$  is the fine-structure constant,  $Z$  is the charge of the particle, and  $\lambda$  is the wavelength of the Cherenkov photon. This means  $3.5 \times 10^4$  photons emitted at wavelengths between 300 and 600 nm per metre traveled by the lepton. It can be inferred from this formula that the largest intensity of the Cherenkov light is reached in the blue and UV range. Therefore, neutrino telescopes use PMTs which are sensitive to this range of wavelengths.

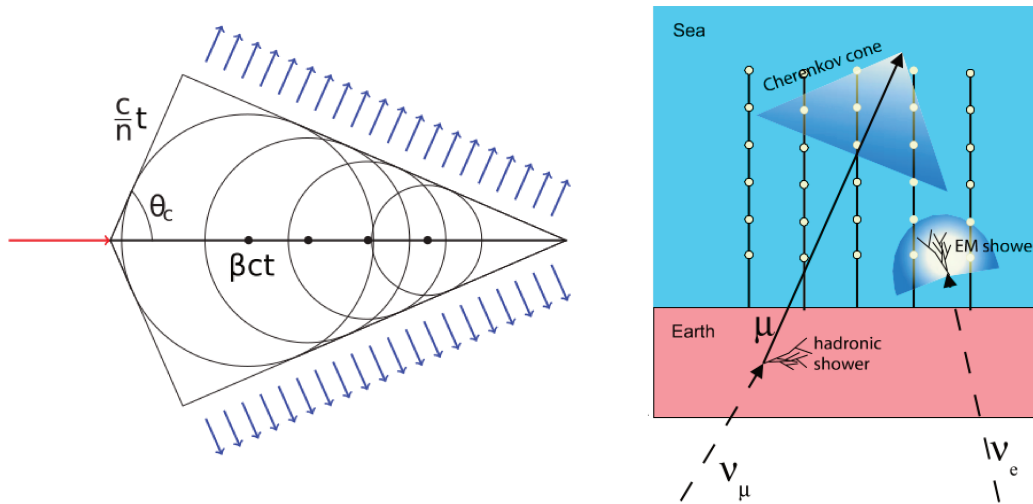


Figure 2.1: On the left, the scheme of the wavefront created through Cherenkov radiation. On the right, the detection principle of underwater Cherenkov neutrino telescopes.

### 2.1.2 Neutrino interactions and event topologies in underwater Cherenkov detectors

In general, high-energy neutrino interactions produce hadronic showers as a remnant of the break-up of the target nucleon during the interaction. However, different signatures can be distinguished in the detector depending on the interaction type (CC or NC), the neutrino flavor involved ( $e$ ,  $\mu$  or  $\tau$ ), the possible decay of an outgoing lepton and the part of the interaction which is observed in the detector. They are summarised in the following:

1. **NC neutrino interactions:** The event signature of these interactions is often referred to as shower or cascade due to the fact that only the hadronic shower can be detected in this case. In these interactions, it is not possible to measure the total energy of the incoming neutrino, since not all of the neutrino energy is deposited inside the detector. This is because most of the energy is transferred to the outgoing neutrino and only a fraction to the nucleus inducing the Cherenkov light.
2. **CC neutrino interactions:** In contrast to NC, during CC interactions not only the hadronic cascade is produced but also an outgoing charged lepton, producing additional Cherenkov light.
  - *Muon-neutrinos interacting through CC:* This interaction is characterised by the production of an outgoing muon together with the hadronic shower. The signature of the muon is often referred to as track event. This muon can travel a considerable distance (several kilometers) before being stopped or decaying, since it is moving at a relativistic speed. At high-energies (above 10 TeV), the scattering angle is very small and the incoming neutrino is almost collinear with the outgoing muon. Thus, by reconstructing the muon direction, the

direction of the neutrino can also be estimated. Contrary to shower-like detected events, which are generally contained in the detector, track-like events usually start outside the instrumented volume.

- *Electron-neutrinos interacting through CC*: In this case, instead of a muon, an electron is produced after the neutrino interaction and two types of showers are produced: the hadronic cascade and an electromagnetic shower. The latter is generated by the interaction of the outgoing electron with matter, while the first one is the result of the break-up of the nucleon. The two cascades are hardly distinguishable. As in NC interactions, a shower topology is the observed signature.
- *Tau-neutrinos interacting through CC*: As a product of this interaction, the third charged lepton type ( $\tau$ ) is produced, again together with an hadronic shower as for the previous interactions discussed. The different decays of the  $\tau$  particle can be seen as different event topologies at the decay vertex. There is a 65% chance that a  $\tau$  decays into hadrons, producing an hadronic cascade; while 35% of the times, the  $\tau$  will decay into a lepton. When the  $\tau$  decays into hadrons or into an electron, a second cascade produced by the  $\tau$  decay is observed. Even if it is almost impossible to distinguish both cascades for energies under about 2 PeV, both cascades can be (separately) observed over the energy range between 2 and 20 PeV, leading to the so called double-bang pattern. At higher energies, the length of the path traveled by the  $\tau$  is larger than cubic-kilometre sized neutrino telescopes. In these cases, a cascade and a track signature are observed, as for  $\nu_\mu$  CC interactions.

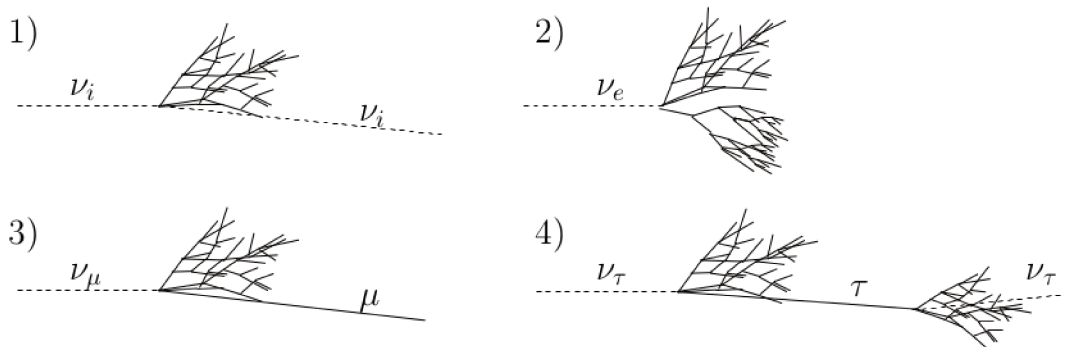


Figure 2.2: Signatures of the event topologies observed for different types of neutrino interactions. 1) NC interaction producing only a hadronic shower. 2) CC interaction of a  $\nu_e$ , initiating an EM and an hadronic shower. 3) CC interaction of a  $\nu_\mu$  producing a long muon track with an hadronic shower. 4) CC interaction of a  $\nu_\tau$ , generating a  $\tau$  that decays producing the double-bang signature.

The description of the topologies (or signatures) expected for each kind of interaction for high-energy neutrinos described in this section, and illustrated in Fig. 2.2, will be relevant for Part III of this manuscript. However, on Part II we focus on low-energy (1-100 MeV) neutrinos, and thus the kind of interactions which are important to the study carried out on this part of the thesis are described in chapter 5.

## 2.2 The ANTARES neutrino telescope

The ANTARES detector is located at (42° 48' N, 6° 10' E) about 40 km offshore Toulon (France), at a depth of 2475 m in the Mediterranean Sea. The deployment of the ANTARES detector started in 2001



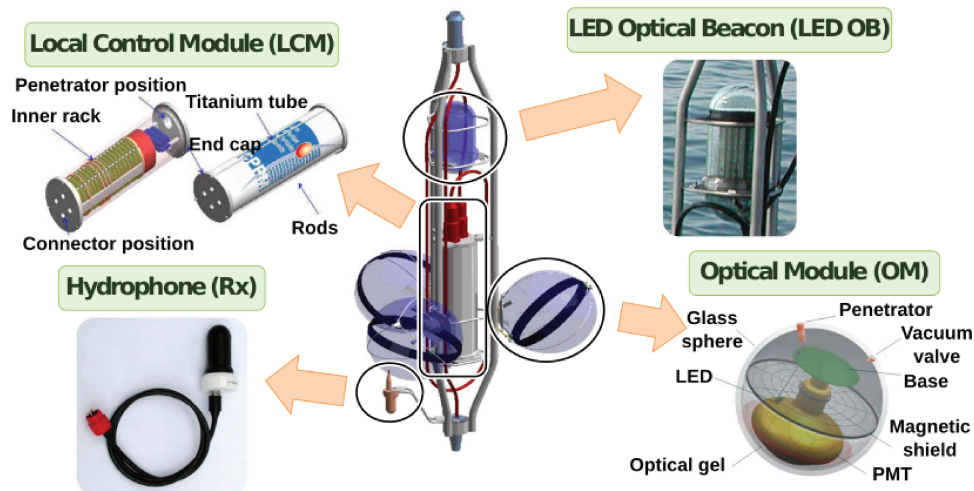


Figure 2.4: The schema of an storey with the three OM (in purple), the LCM (grey cylinder in the center) and some equipment for the calibration: the hydrophones (orange, bottom left) for the positioning and the LED Optical Beacons (blue capsule on top) for time calibration and monitoring of the water properties.

Each OM is linked to two chips called Analogue Ring Samplers (ARSs) located in the LCM, whose main function is to digitize the time and amplitude of the PMT pulses.

In each line, storeys are grouped in sectors. Each sector is controlled by a Master Local Control Module (MLCM), which holds both the LCM electronics and an Ethernet switch. The latter receives data from all the LCMs of the sector.

A String Power Module (SPM), located at the seabed where strings are anchored, provides the power needed for the whole line. The connection between the strings and the shore station is done through the Junction Box (JB), which provides the power supply to the detector. The shore station and the JB are linked via the Main Electro-Optical Cable (MEOC). The electronics for the data transfer between the string and the Junction Box are contained in the String Control Module (SCM). This transfer is done with an electro-optical interlink cable.

### 2.2.2 The Data Acquisition System

The data acquisition system of ANTARES relies on an "all-data-to-shore" implementation. The information on each photon detected by a PMT is sent to shore via an optical fiber after being digitised offshore at the LCM. The light detection by an optical module happens when a photon hitting the photocathode is converted into a photo-electron, producing a pulsed electric signal. This signal is processed only if the charge amplitude is greater than 0.3 photo-electrons (p.e.). This is the threshold to define a hit (or L0 level 0 hit).

The amplitude (charge) is measured together with the hit arrival time. A local clock is present at each storey and they are synchronised with an onshore master clock. The hit information is organised in data frames of about 105 ms before being sent to the shore by a Central Processing Unit (CPU). The data streams are finally sent to shore through the MEOC.

## 2.3 The KM3NeT neutrino detectors

The KM3NeT neutrino Cherenkov detectors ORCA and ARCA are under construction at two underwater sites in the Mediterranean Sea, each of them with a different prime physics goal and different geometries. Both share the same technology and send data to shore where the communication between the two different sites is possible at the KM3NeT computer farm. The Data AcQuisition system (DAQ) will be further described in this section.

The most basic element of the KM3NeT detectors is the digital optical module (DOM) featuring 31 photomultiplier tubes in a glass sphere. The DOMs are connected in groups of 18 to form a vertical line called detection unit (DU), while a group of 115 DUs forms a building block (BB). The different parts of the detector layout will be covered in the following subsections.

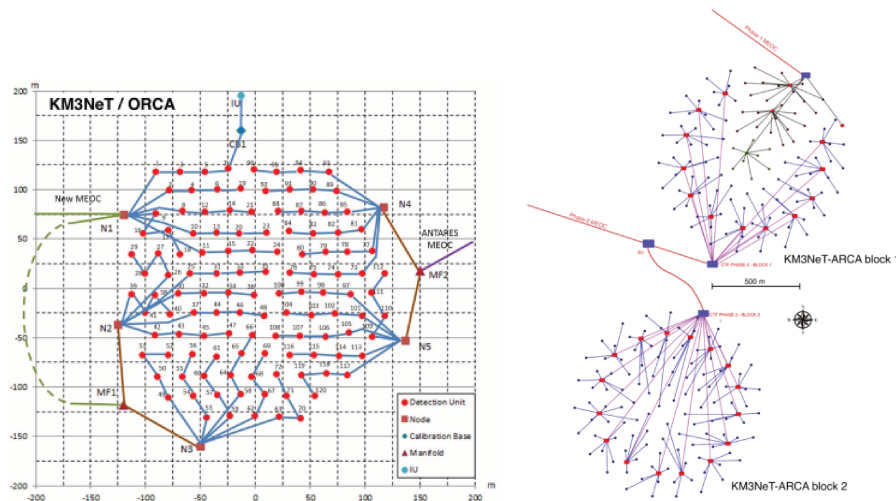


Figure 2.5: View of the distribution of the strings in ORCA (left) and ARCA (right) detectors. (Not to scale.)

ORCA (Oscillations Research with Cosmics in the Abyss) is aimed at the determination of the neutrino mass ordering and oscillation studies, exploiting a densely instrumented detector with sensitivity in the GeV scale. ORCA is located at ( $42^{\circ} 48' N$ ,  $06^{\circ} 02' E$ ), off the French coast close to La Seyne Sur Mer, at a depth of 2450 m and will be made of 1 BB. The ORCA detection strings represent an instrumented effective mass of 5.7 Mt.

ARCA (Astroparticle Research with Cosmics in the Abyss) is dedicated to the search for high-energy (TeV-PeV) astrophysical neutrino sources, using a large instrumented volume at the  $\text{km}^3$ -scale. ARCA will be located at ( $36^{\circ} 16' N$ ,  $16^{\circ} 06' E$ ), off Capo Passero (South-East Sicily, Italy), at a depth of 3500 m. The ARCA detector will consist of two instrumented buildings blocks.

In ARCA, two Main Electro-Optical Cables will connect the detector to the shore station. These two cables are split into two branches, each of them connected to a Cable Termination Frame (CTF). The CTFs are connected to secondary junction boxes: 12 for the block 1 and 16 for the block 2. Each secondary JB can power up to 7 detection strings in total.

In ORCA, also two MEOCs will connect the station with the detection block. The DUs will be powered by five JBs, located at the surroundings. Each JB has eight connectors, and each connector can power up to 4 strings that are connected in series. A view of the layout and the connections is given in Fig. 2.5.

### 2.3.1 The Digital Optical Module and the Detection Unit

The Digital Optical Module is the core element of the KM3NeT detectors. It consists of a glass sphere of 17 inches of diameter, which holds 31 directional PMTs and their corresponding readout electronics. As in ANTARES, an optical gel is placed between the PMT and the glass sphere. A KM3NeT DOM can be seen in Fig. 2.6 (left) together with the view of their assembling into a DU (right).

The PMTs used are the ETEL D792KFL and Hamamatsu R12199-02 models. Their diameter is at least 72 mm with a total length smaller than 122 mm. They present a Transit Time Spread (TTS) of 4.5 ns and a Quantum Efficiency (QE) of about 27% for a 404 nm wavelength. The PMTs are distributed on the surface of the DOM in 5 rings, each housing 6 PMTs. Within the same ring, the PMTs are equally spaced and the vertical separation between rings is of  $30^\circ$ .

The multi-PMT DOM presents important advantages compared to the traditional use of one single PMT. An ANTARES storey hosts three PMTs of 10 inches each. There are 31 PMTs of 3 inches each in a KM3NeT module. Thus, both yield similar photocathode areas. However, with a similar sensitive detection surface, the KM3NeT DOMs are more compact and have a wider angle of view. Moreover, the multi-PMT DOM allows for directional information of the detected light and digital photon counting, not feasible by the former ANTARES storeys. Additionally, with the KM3NeT DOM multiple photons arriving to the same DOM but seen by different PMTs can be identified. This feature allows for a better rejection of the optical background, as will be discussed later in section 3.1, and will be extensively exploited for the work of this thesis (Part II). Last, but not, least, this configuration reduces the number of connectors at the optical modules, which improves the robustness of the detector.



Figure 2.6: On the left, a KM3NeT DOM. On the right, a simplified view of a KM3NeT DU (note that only part of the DOMs are shown, for better visibility of the scheme).

Each DOM also contains several instrumentation items for the detector calibration. In particular, a LED is placed in the upper hemisphere of the DOM for time calibration purposes, a compass and a tiltmeter are included in each DOM in order to determine its orientation, and an acoustic sensor is also attached to the DOM for determining the exact positioning.

A string or Detection Unit consists of 18 DOMs attached to two parallel ropes. In ARCA, the total height of the string is of 700 m, with the first DOM sitting 80 m above the seafloor. The vertical distance between the DOMs is 36 m and the average horizontal spacing between DUs is 95 m. In ORCA, the total length of each line is of 200 m, with the first DOM at 40 m above the seafloor. The vertical separation between the DOMs is 9 m and the average distance between the DUs is 20 m.

The information and power are transferred to the DU with the use of an electro-optical cable, which provides the power supply, and 18 optical fibers for data transmission. As in ANTARES, though, the DU keeps itself in vertical position by design (due to the buoyancy of the DOMs), an additional buoy is placed on the top of the string to help keeping it upright in case of fast strong current.

### 2.3.2 The Data Acquisition System

As ANTARES, KM3NeT also adopts an "all-data-to-shore" DAQ design, so that all signals are sent to the shore station. Signals satisfying a threshold of 0.3 pe are considered. The Time over Threshold (ToT) is the time that PMT signal is measured to be above the threshold of 0.3 p.e.. The data streams arrive on shore and are assembled in a computer farm. They contain all hit information given by the PMTs: the arrival time, the ToT, and the PMT identification where the hit was detected.

A total of 25 GB of data are sent each second to shore per building block. This huge amount of data needs to be filtered and reduced as will be discussed in section 3.3. Apart from physics data that is permanently stored, a sampling of the rates of all PMTs is sent with a lower frequency. This sampling of the baseline rates is needed in order to know the total optical background for its implementation in the Monte Carlo simulations and event reconstruction.

On-shore, hit data are grouped in 100 ms time segments (*timeslices*) to be processed by parallel software data filters. The data acquisition of a PMT is suppressed when its rate is detected above 20 kHz over a 100 ms basis. This is called the *high-rate-veto* logic, that is applied so that DAQ does not saturate and the PMTs are not damaged when bioluminescence conditions produce a big increase of the rates.

Two types of data are available after the data filtering: *triggered events* and *timeslice data*. Timeslice data consists of all hit data for a selection of coincidences that is based on (i) a maximal time difference between the hit times defining a coincidence (ii) a minimum number of coincidences (iii) a maximal opening angle between the corresponding hit PMTs. Multiple timeslice streams can be produced with selections dedicated to different purposes.

A triggered event is built when at least one trigger algorithm has identified a cluster of causally connected coincidences matching a topology of interest (see section 3.3). The hits matched by the trigger as part of the physics signature are referred to as *triggered hits*. A triggered event stores also the information on all the hits recorded by the detector in a time window that extends over the time range spanned by the triggered hits (*snapshot*).

For the purpose of CCSN neutrino searches (that will be discussed in Part II), a dedicated data stream containing all high-level coincidences is continuously acquired for online monitoring and permanent storage. The same data stream is simultaneously analysed in real time for the purpose of alert generation. The raw data from the two sites is then combined at the computer farm to evaluate a combined trigger. A buffer for the lower multiplicity coincidence data is foreseen in order to store the maximum amount of useful raw data in case an alert is either received or self-generated.

The structure of the processing chain is outlined in Fig. 2.7. A common infrastructure is shared between the CCSN processing pipeline and the online event reconstruction for high-energy neutrino events. In this way, all the real-time alerts for the multi-messenger follow-ups are handled following the same chain and at the same infrastructure.

The DAQ system is present on shore and manages the data quality (DQ) and the data filters. It accounts for a control unit and a GPS for the online time calibration. The DAQ works according to the following chain:

1. A monitoring of the mean baseline rates PMT by PMT is done.

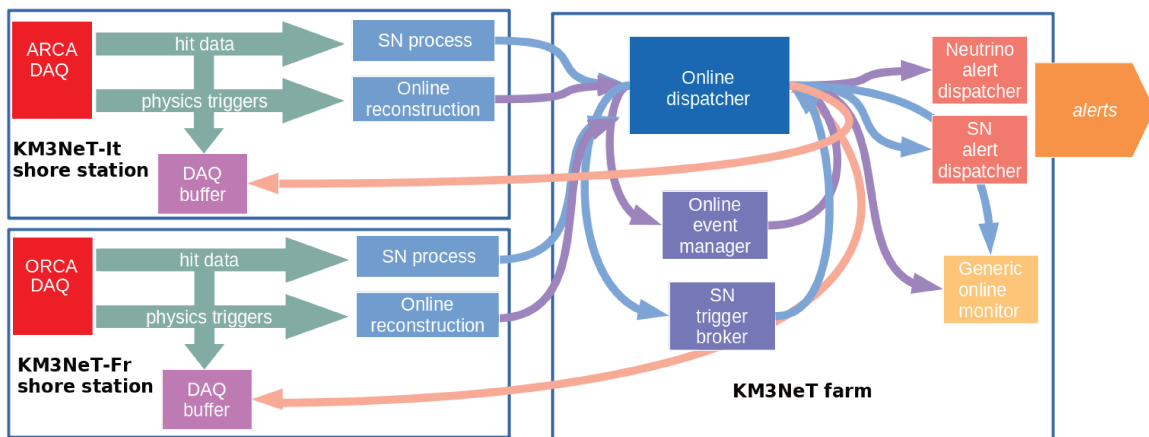


Figure 2.7: Functional diagram of the KM3NeT DAQ system and online framework outlining the information exchange between the two shore stations and the central farm dedicated to the real-time processing applications.

2. A real-time calibration of the events is performed.
3. The triggers are applied to the events.
4. If they pass the triggers, the events are reconstructed in real-time and written on disk.

### 2.3.3 The deployment

To date, the milestones in terms of ORCA and ARCA deployments have been as follows:

- April 2013: A prototype KM3NeT DOM is deployed on an ANTARES instrumentation line.
- May 2014: A prototype DU, consisting of three DOMs, is deployed at the ARCA site.
- January 2016: The first ARCA DU is deployed and begins taking data.
- June 2016: A second DU is deployed in ARCA. Two DUs taking data for one year.
- July 2017: Electrical problem in the ARCA seabed infrastructure. Data taking stops.
- September 2017: The first ORCA DU is deployed and begins taking data.
- December 2017: Failure of the main cable. Stop of data taking.
- January 2019: 2nd deployment of a first DU at the ARCA site.
- February 2019: 2nd deployment of a first DU at the ORCA site.
- May 2019: Two more DUs deployed in ORCA but the first was lost. Two lines taking data.
- June 2019: Two more DUs deployed in ORCA. Four DUs taking data.
- January 2020: Two more DUs deployed in ORCA. Six DUs taking data.

For the deployment, the DU is rolled into a spherical metal frame of  $\sim 2$  m diameter, called the Launcher of Optical Modules (LOM). The LOM is lowered down to the seabed, where the DU is connected to the seafloor using a Remotely Operating Vehicle (ROV). Once the DU is securely anchored and the functionality of all DOMs is confirmed, the LOM is released and the progressive unfurling of the DU takes place. During this last stage of the process, which is done remotely, the LOM floats up to the surface, where it can be covered and reused. A picture of a DU deployment is on Fig. 2.8.



Figure 2.8: A picture of a DU deployment, where the detection unit is furlled into the LOM.

## 2.4 Other Cherenkov neutrino detectors

### 2.4.1 The IceCube Neutrino Observatory

The IceCube neutrino observatory is located in Antarctica, at the South Pole. The South Pole offers ice, rather than water, as transparent medium for Cherenkov radiation. Ice has several advantages and disadvantages compared to seawater. The main advantage of ice is the stable, low noise rate of about 500 Hz, compared to the 200-400 kHz due to  $^{40}\text{K}$  decays and bioluminescence in KM3NeT detectors. However the optical properties depend on the quality of the ice and on the depth, which complicates the analysis of experimental data. On the one hand, the strong scattering causes a larger delay in the photon propagation, leading to a worse angular resolution in ice compared to water. On the other hand, the larger absorption length of ice results in better photon collection. Also, the ice is not homogeneous; there are layers of distinct properties, in contrast to seawater.

The IceCube neutrino telescope consists of a  $\text{km}^3$  instrumented ice volume located 1.5 km below the surface. The deployment started in 2003 and was completed in December 2010, with the final detector consisting of 86 vertical strings, each connecting 60 digital optical modules, or DOMs. This makes a detector with a total of 5160 PMTs. The strings have an averaged horizontal spacing of 125 m while the DOMs are located every 17 m along the string.

IceCube is the successor of the AMANDA detector, that will not be detailed here. It was thus built from the knowledge acquired with the first experience from AMANDA. The two detectors are compared on an schematic view in Fig 2.9, together with the two "sub-detectors" described below.

A Digital Optical Module consists of a 35 cm diameter glass sphere which contains a 10-inch PMT with its own DAQ system and readout electronics. The DOMs are required to withstand pressures up to 600 atm and temperatures down to  $-55^\circ\text{C}$ . The DOMs were designed so to have a maximum noise rate of the PMTs of  $\sim 500\text{ Hz}$  and a  $\text{TTS} \leq 2.5\text{ ns}$  for single photo-electron pulses. A set of LEDs are included in the DOM for calibration and determination of the ice optical properties.

A set of ice tanks are installed in the surface aiming at the detection of the products of the cosmic ray interactions in the upper layers of the atmosphere. They constitute a different sub-detector called IceTop, which is also used as a veto to reject the atmospheric muon background in neutrino searches, described in 1.3.2. The IceTop surface array consists of 81 pairs of ice tanks placed on the same grid as the IceCube strings. Each tank has a diameter of 1.8 m and a depth of 50 cm and contains two IceCube DOMs. The distance between the two tanks in a pair is of 10 m and each pair is placed in a triangular

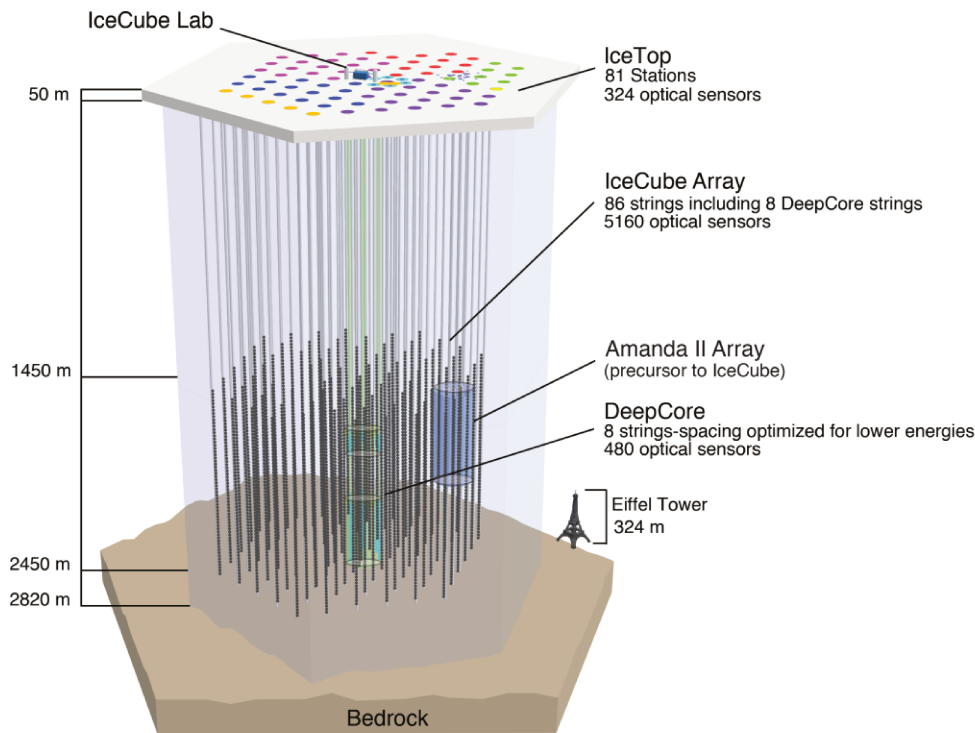


Figure 2.9: Schematic view of the IceCube Neutrino Observatory with the IceTop array and DeepCore. For comparison, the AMANDA detector is illustrated.

grid of about 125 m.

A denser sub-detector, named DeepCore, is installed at the center of the array. Characterised by smaller spacings between strings (70 m) and DOMs (7 m), DeepCore offers a lower energy threshold, opening the neutrino detection down to about 10 GeV. Actually, DeepCore is used for both neutrino oscillation studies and low-energy neutrino astrophysics.

An upgrade of the IceCube detector is planned in the next  $\sim 3$  years, that will include seven new strings inside of DeepCore in order to have a denser detector sensitive at GeV energies [107]. As already mentioned, a better performance in this energy range is necessary both for oscillation studies and low-energy astrophysics. This will be possible with the upgrade. More than that, these new detection lines will be designed making use of a new technology: different kinds of DOMs (inspired by the KM3NeT design) and additional calibration instruments that will allow for an improvement in the reconstruction techniques enhancing their results. The upgrade array configuration is illustrated in Fig. 2.10.

The IceCube upgrade is a first step in the direction of a next-generation neutrino telescope, IceCube-Gen2. The IceCube-Gen2, currently under design optimization, is a proposed project that will consist of an instrumented ice array of approximately  $8 \text{ km}^3$  with about 1,000 optical sensors. The upgrade, will be useful for testing the prototype instrumentation for the development of the large IceCube-Gen2 array. Aside from the current IceCube (and KM3NeT) goals that will be achieved with a larger detector built using new tested technology, the IceCube-Gen2 detector will also host an array of radio antennas to raise the energy threshold up to very high-energies ( $> 10 \text{ PeV}$ ) and be sensitive to cosmogenic neutrinos, among other motivations.

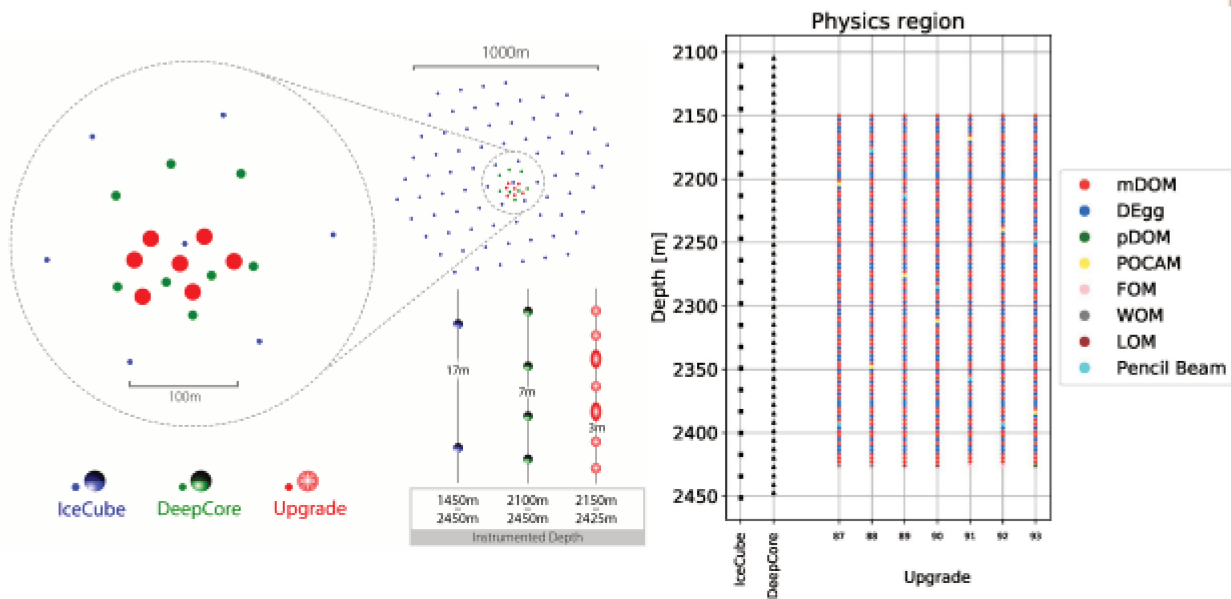


Figure 2.10: The IceCube Upgrade array geometry. Red marks on the left panel shows the layout of the 7 IceCube Upgrade strings with the IceCube high-energy array and its sub-array DeepCore. The right panel shows the depth of sensors/devices for the IceCube Upgrade array (physics region). The different colors represent different optical modules and calibration devices. The Upgrade array extends to shallower and deeper ice regions filled with veto sensors and calibration devices (special calibration regions). Figure taken from [107].

#### 2.4.2 The Baikal Neutrino Telescope and the Gigaton Volume Detector

The Baikal Neutrino Telescope is located in the southern part of the Lake Baikal. The Collaboration reported the first atmospheric neutrino detected underwater. The full configuration of the initial detector, consisting of an array of 192 optical modules, was completed in 1998 and took data until 2005, were a first upgrade of the detector took place.

Since 2015, a new upgrade of the Baikal detector is under construction. The Gigaton Volume Detector (GVD) is aimed to host more than  $10^4$  OMs for an instrumental volume larger than  $2 \text{ km}^3$ . GVD will present OMs arranged on 8 (and up to 18 in a second phase) clusters of 8 strings, each string carrying 24 optical modules. The OMs will be spaced uniformly along 350 m, starting at 900 m below the surface and with the anchor located at a depth of 1350 m. The lateral separation between clusters is of 300 m. The schematic view of the detector is shown in Fig 2.11.

The first clusters have been recently deployed. According to simulations, the energy threshold of this detector would be of about 3-10 TeV, with competitive results at the 100 TeV range and below. Actually, two clusters of the GVD detector are more or less equivalent to twice the full ANTARES instrumented volume. There are seven cluster deployed and taking data since spring 2020.

#### 2.4.3 From Kamiokande to Hyper-Kamiokande

The Kamioka mine in Japan gave name to the original Kamiokande detector, located underground inside the mine. It was a Cherenkov detector consisting in a cylindrical tank filled with 3 ktons of water. The main physics goal of the Kamiokande detector was looking for nucleon decays and constraining the measurement of the proton lifetime. It started operating in 1983 and after some upgrades observed the solar  $^8\text{B}$  and atmospheric neutrinos. Apart from this, it detected in 1987 a dozen neutrinos

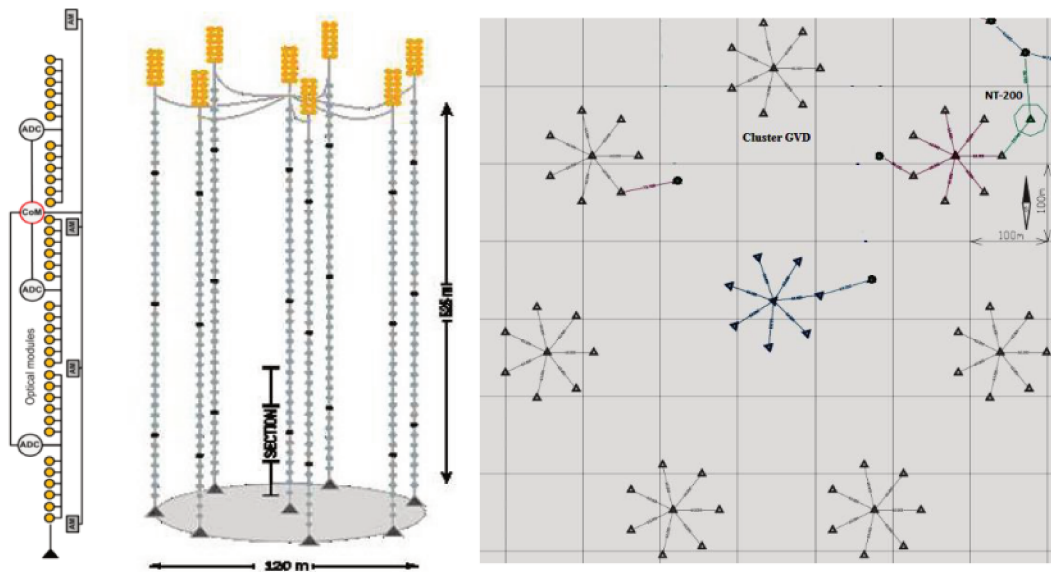


Figure 2.11: Baikal-GVD detector. The left figure shows a scheme of a GVD string. The second figure shows the configuration of a GVD cluster of 8 strings. The right figure shows a group of 8 clusters.

from SN1987A, contributing to the first multi-messenger observation. The physics results produced by Kamiokande were awarded in 2002 with the Nobel Prize for Physics, jointly attributed to Ray Davis Jr. and to the Kamiokande collaboration's leader Masatoshi Koshiba for their "pioneering contributions to astrophysics, in particular for the detection of cosmic neutrinos".

Super-Kamiokande is Kamiokande's successor, located in the Mozumi mine in Japan, below 1km of rock shielding, equivalent to 2700 m under water. The construction lasted for more than four years and it started taking data in 1996. It consists of a cylindrical tank with a diameter of 39 m and a height of 42 m, containing 50 kt of water. A view is given in Fig. 2.12. The inner region accounts for a fiducial detection volume of approximately 22.5 kt of water. The outer region acts as a veto against both incoming (background) particles and radioactivity from the surrounding rock.

Super-Kamiokande can detect multiple photons from each neutrino interaction. This produces an easily identifiable pattern of hits in the PMTs and allows an accurate event reconstruction up to low energies (above  $\sim 4.5$  MeV). A water purification system is employed to reduce scattering losses, which negatively impact the detector's energy resolution due to the delayed arrival time of the scattered photons at the PMTs.

An upgrade of the Super-Kamiokande detector took place from March 2018 to January 2019. At present, SK is running. During this operation, several actions took place: the cleaning of the walls and the detector structures, the removal of potential sources of rust, the covering of the damaged parts of the detector, the replacing of dead PMTs, etc. The most relevant change was the modification of the in-tank piping, with a new hall that was excavated for the new Gd water system.

In fact, the goal of this upgrade was to fill the tank this time not only with pure water but with water doped with Gadolinium (Gd). Indeed, Gd is a transparent material for the Cherenkov light as well as water. Adding a small concentration of Gd (0.2%) to pure water would allow to tag the neutrons product of the neutrino interaction with protons in water by Inverse Beta Decay (IBD). Being this the main interaction channel of CCSN neutrinos in water, this might help identifying the astrophysical signal. But more than that, separating the IBD from the elastic scattering interaction would allow for  $\bar{\nu}_e$  separation by tagging the neutron product of the IBD interaction that is going to be captured by

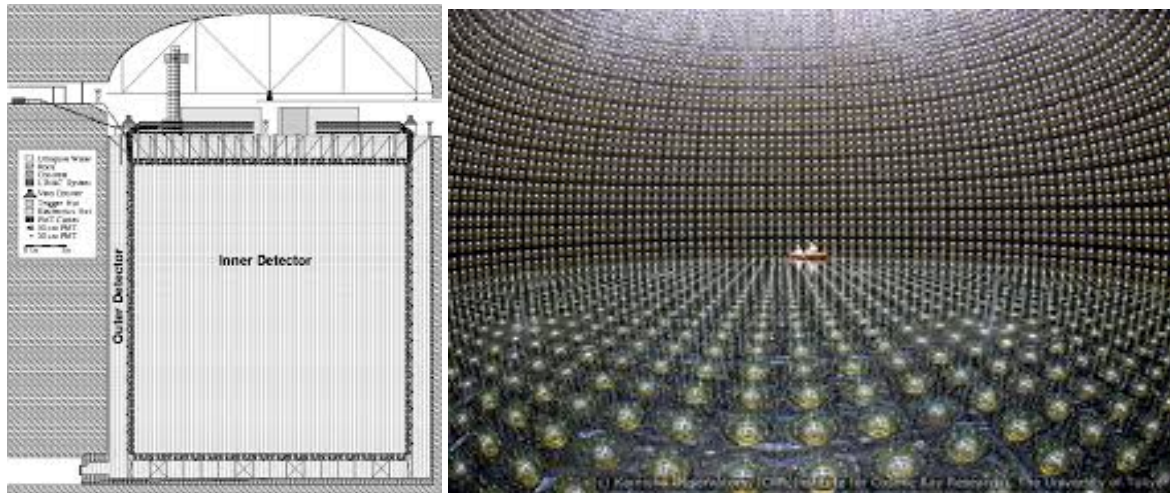


Figure 2.12: On the right, the schematic configuration of Super-Kamiokande, with the outer and inner detectors. On the left, a picture from the interior of the detector. The total detection volume is divided into an outer shell of 2.5 m width and an inner region with a diameter of 33.8 m and a height of 36.2 m. The two regions are separated by a support structure, sustaining the PMTs.

Gd. This provides promising expectations for source pointing (neutrino astronomy) and measuring the neutrino mass ordering (see section 1.3.1).

Hyper-Kamiokande is the coming successor to Super-Kamiokande, yet a proposed project. The construction is expected to start mid 2020 and the scientific data-taking is scheduled to begin in 2025. It will be located about 8 km south of Super-Kamiokande at 648 m underground, equivalent to a shielding of 1750 m of water. The detection tank will be buried 600 m deep to reduce interference from cosmic radiation. In addition to the measurement of solar, atmospheric and supernova neutrinos, Hyper-Kamiokande will use a beam of neutrino/anti-neutrino from the J-PARC accelerator for oscillation measurements.

Hyper-Kamiokande detector will be 20 times larger than Super-Kamiokande, with a tank with 1000 million liters of ultrapure water. This larger effective detection volume (560 kton) will be accompanied by a proportional growth in the number of sensors (photomultipliers). The tank of Hyper-Kamiokande will be a double cylinder, each with outer dimensions of 48 m x 54 m x 247.5 m.

# Chapter 3

## From the detected photons to the physics results: analysis tools

This chapter describes what happens from the moment a photon hits the detector up to the final results obtained with the measured data. In this way, the present chapter provides an overview of the different data treatments and analysis tools used in neutrino astrophysics. The triggering, simulation, and reconstruction techniques are covered together with the characteristics of the physical backgrounds and some statistical concepts of interest for the analyses presented in the following chapters.

### 3.1 Sources of background in the Mediterranean Sea

This section aims at describing and characterizing the different possible sources of light impacting the detector that may render difficult the neutrino signal detection.

There are essentially three relevant sources of background: bioluminescence, radioactive decays in sea water and atmospheric background. The PMT counting rates are dominated by the continuous emission of radioactive decays, and can occasionally increase due to bioluminescence activity. Due to this baseline, the ANTARES and KM3NeT telescopes are continuously detecting photons even if daylight is not visible at the depth they are deployed.

The main radioactive isotope present in the seawater salt contributing to this background is  $^{40}\text{K}$ , which  $\beta$ -decays into a relativistic electron inducing Cherenkov emission. The electrons produced by these radioactive decays have energies up to 1.33 MeV.

Bioluminescence is the background source coming from light emission by biological organisms in sea water. It has two different components, a continuous one that determines the baseline, and a discrete one which appears as localised bursts of light in the detector lasting for some seconds. Bioluminescence can exceed the background due to  $^{40}\text{K}$  decays by as much as a factor of 20. This background contribution is correlated with the sea current and shows a seasonal dependence, as more biological organisms are present in spring.

The atmospheric background is originated from the interaction of cosmic rays in the atmosphere generating muons and neutrinos, which in turn can produce muons after interacting, both producing

Cherenkov radiation in seawater. Atmospheric muons and neutrinos represent two different background types in neutrino telescopes, which cannot be identified in an event basis, but can be discriminated in an statistical basis.

While the first two optical backgrounds can hardly mimic a cosmic neutrino interaction, the atmospheric backgrounds are the main source of concern for the search for high-energy astrophysical neutrinos. The muon component can be mitigated by looking at upward-going muon track-like events, since only neutrinos can travel through the Earth. As regards atmospheric neutrinos, one can disentangle them from the astrophysical signal using the fact that a different energy spectrum is expected for atmospheric neutrinos and high-energy cosmic neutrinos, as can be seen in Fig. 1.3. Other strategies can be to look for accumulations in space or time, since the atmospheric neutrino background is homogeneous in time and space.

Contrary to high-energy searches, when one is interested in low-energy neutrinos the dominant background components are the two first optical backgrounds described in this section. Nevertheless, the KM3NeT multi-PMT technology is well suited to handle this, as will be shown in Part II.

The multi-photon Cherenkov radiation will result in coincidences at the few-nanosecond scale between the different PMTs in a DOM. The number of PMTs in a DOM detecting a photon within a time window of 10 ns is later on referred to as *multiplicity* ( $M$ ). Radioactive decays in sea water and atmospheric muons are the dominant contributions to the multiplicity spectrum in the ranges  $M \leq 5$  and  $M \geq 8$ , respectively. The contribution of coincidences from uncorrelated photons produced by bioluminescence or radioactive decays becomes negligible above  $M = 3$ . This signature can be used to discriminate between the different background sources and the signal and will be exploited to search for low-energy astrophysical neutrinos in Part II.

## 3.2 Detector calibration

In order to identify the signature of neutrino interactions in long-string underwater Cherenkov detectors, one follows the time, position and amplitude sequences of the photons observed through the different PMTs. Therefore, it is of major importance to achieve a precise timing, positioning and p.e. yield of the detector light sensors. In this sense, an accurate calibration procedure is needed for achieving the less biased results. This section briefly describes the different calibration procedures used in ANTARES and how they have been adapted to KM3NeT.

### 3.2.1 Time calibration

Two main types of time calibration are needed in ANTARES. On the one hand, the absolute timing of the events is required to correlate them with any astrophysical phenomena observed in the Universe. This is obviously of crucial importance for multi-messenger astronomy, but does not require a much better precision than  $O(ms)$ . On the other hand, a more demanding and accurate relative time calibration between the PMTs with a  $\leq 1$  ns precision is needed to achieve a good angular resolution. For the latter, two measurements are performed: the time resolution of each OM and the relative time offset between OMs.

For an absolute time calibration, an echo-based clock system is used to synchronize all the optical modules of the ANTARES detector. The absolute time is synchronised with respect to a GPS signal, which presents an accuracy at the level of  $\sim 100$  ns. The time delays from the shore station to each LCM is the main source of uncertainty for the determination of the absolute time.

Several factors affect the measurement of the time between the photon being detected in a PMT and reaching the shore station ( $T_0$ ), which changes with time. The time offsets between the different lines may also vary with time. For these reasons, the relative time calibration between OMs is regularly monitored in situ. Different methodologies are used to achieve a better time resolution: the time residuals from the reconstruction of muon tracks, coincident events coming from the radioactive decays of  $^{40}\text{K}$  nuclei in sea water and the Optical Laser Beacon system. Combining all of them, different calibrations are carried out: time differences between PMTs in an OM (for KM3NeT) or between OMs in the same storey (for ANTARES), time differences between DOMs (or storeys) in a detection line, and time difference between the different lines. The same strategies and methods are applied in KM3NeT, with the advantage of the additional information of the time delays between the 31 PMTs of a DOM, allowing for a more accurate timing.

The impact of the time calibration on time-dependent searches and final reconstruction parameter quality is not negligible. This has been evaluated in [108], where a new time calibration was incorporated.

### 3.2.2 Position calibration

Sea currents produce a movement of the detection lines, which are pulled up by buoys. Therefore the position of the OMs slowly changes with time. For this reason, a position calibration is needed to determine the position and orientation of each storey in almost real time as well as the absolute detector position. This is required to meet the targeted precision on the event reconstruction.

To this aim, triangulations of the measured acoustic signals at each storey are performed to determine their position. This is done by an acoustic sensor located at the bottom of the detection lines. In addition, several hydrophones are strategically placed at some detection storeys. The time delay between the emission and reception of the acoustic signals allows for measuring the distance between the storeys and inferring their position. In fact, by monitoring the sound velocity in seawater using oceanographic instruments, distances can be determined to infer the storey's position.

The tiltmeters and compass hosted by the storeys measure their orientation, allowing for an independent measurement of their position. Finally, the absolute detector position is obtained by the GPS of the boat used during the deployment of the lines.

The deviation of the OM position due to sea currents can reach up to several meters at the top of the line in ANTARES. The positioning system of the ANTARES detector is described in [109]. After the calibration, an accurate positioning with an uncertainty of the order of 10 cm is achieved well within specification. The positioning affects the final reconstruction parameters and analysis results significantly, specially when looking at space coincidences with signals observed by other instruments. The same strategy is used for the KM3NeT positioning calibration.

### 3.2.3 Charge calibration

Together with the time and the position, the energy reconstruction is the other required ingredient for an accurate reconstruction of the events. A charge calibration is demanded for a best energy estimate. Establishing the relation between the number of photo-electrons and the measured amplitude of the PMT signal is the main goal of the charge calibration.

Measurements before deployment have shown a linear relation between the number of photo-electrons and the digitised amplitude output [110, 111]. The calibration procedure relies on this assumption with an in situ monitoring of the positions of the pedestal (obtained with random triggers)

and the photo-electron peak. The impact of the charge calibration (resolution  $\sim 40\%$ ) on the final reconstruction is less relevant compared to the previous ones.

### 3.3 Physics triggers

As it would be impractical to store all data registered by the detector, a series of triggering and filtering algorithms are applied to the data once on shore. The goal is to select as much as possible series of hits resulting from physical events (neutrinos or muons) while rejecting the optical background. To do so, different criteria are used in ANTARES and KM3NeT, which are described in this section.

#### 3.3.1 ANTARES

In ANTARES, causally correlated hits between the OMs are searched for. Combining them in different ways, the following triggers can be defined. The original ingredients are the L0 hits, already defined before as the signals passing the 0.3 p.e. threshold.

The level 1 hits (L1 hits) are defined as two or more hits from optical modules of the same storey that occur within a 20 ns time window. Hits with a high amplitude (typically more than 3 p.e.) are also classified as L1 hits. The set of L1 hits being causally connected is considered as resulting from a physical event (as opposed to optical background).

Some higher level trigger conditions are then applied for a better selection of the physics events, further discriminating the astrophysical signal. The more relevant ones used for ANTARES data analysis are described below.

The 3N trigger is a robust criterion used to identify events likely to originate from a muon track. They are subsequently used to reconstruct the trajectory of the track. Different directions are scanned to evaluate whether the different hits can have been emitted or not by a same muon track. The final condition is to detect 5 L1 hits in at least one of the 210 predefined directions within 20 ns.

The TQ trigger works in a similar fashion to the 3N condition, but it applies an additional requirement by considering only upward-going events (now just half of the directions are scanned) with at least two L1 triggers and four additional L0 hits, within 20 ns.

The T3 trigger is built using L1 hits in coincidence on neighbor storeys of the same line within a time window of 100 ns (if adjacent storeys) or 200 ns (if next-to-adjacent). The 2T3 trigger is a more stringent version of this condition and requires at least three L1 events in one line triggered within  $2.2 \mu\text{s}$ , or four in the full detector in the same window.

#### TAToO triggers

Aside from these triggers aimed at data filtering, there exist additional criteria applied to data in order to define a TAToO trigger, which is required for sending alerts to other instruments. As described in [112], these conditions are:

- *Multiplet*: Detecting at least two track-like event candidates for a neutrino-induced muon coming from compatible directions in the sky and within a predefined time window.
- *High-energy*: Detecting a single high-energy muon-neutrino inducing the observed muon track, using pre-defined cuts on the energy estimation.

The TAToO framework will be mentioned later in Part III when describing the follow-up of real-time alerts received from another observatories with ANTARES.

### 3.3.2 KM3NeT

In KM3NeT, there are three sets of criteria used to define different kinds of hits:

- L0: pulse which exceeds the PMT threshold (0.3 p.e.), also referred to as single hits.
- L1: two or more coincident L0s within a predefined time window in different PMTs of a same DOM.
- L2: an L1 where the constituent L0s are separated by less than a predefined maximum space angle on the DOM.

The L1s are currently stored in runs of about 6 h duration with a frequency of 1 time-slice every 20 (downscaling rates by a factor of 20), mainly for calibration purposes and L0s only in short dedicated runs for evaluating the baseline rates. All events triggered by any of the following sets of requirements are stored for physics analysis.

Once the different kinds of hits are defined, three triggering algorithms are implemented in the KM3NeT DAQ to identify different physical signatures. The **3DShower** cascade trigger assumes that light is emitted isotropically from the neutrino interaction vertex and looks for causally connected L1s (3 for ORCA and 5 for ARCA) on DOMs separated by the maximum distance  $D_{max}$ .

The **3DMuon** trigger is designed to look for the track-like events. It looks for at least 4 (5) causally connected L1 hits in ORCA (ARCA) detector within a cylinder of width  $R_{max}$ . Both  $R_{max}$  and  $D_{max}$  have been optimised for each detector configuration.

Finally, the mixed (MX) trigger, **MXShower**, uses a mixture of L0s and L1s, in order to lower the trigger threshold and include events which do not feature the minimum of 3 (5) causally connected L1s required in ORCA (ARCA) by the 3D cascade trigger. The parameters used by the different triggers can be adapted in order to cope with the varying ambient conditions.

## 3.4 The simulation chain in ANTARES and KM3NeT

The software and simulation packages together with the reconstruction algorithms used within the KM3NeT and ANTARES frameworks are briefly discussed in this section. Some of the tools are common to both detectors, others will be specified for each of them. All the chain is outlined for ORCA and ARCA in Fig. 3.1 and the different steps are explained hereafter.

### 3.4.1 Event generation

*Generation* is the first step of the Monte-Carlo simulation chain, which consists in reproducing neutrino interactions in sea water inside a given generation (or interaction) volume, as well as atmospheric muon interactions. The different generation codes used are shortly described in the following:

- **gSeaGen** and **GENHEN** are the two different neutrino generators used in KM3NeT, specifically implemented for neutrino telescopes. While gSeaGen is based on GENIE [113] and is valid up to energies of about 5 TeV, GENHEN is an internal tool developed inside the ANTARES and KM3NeT Collaborations with the purpose of simulating neutrino interactions in seawater at high-energies (valid from 1 GeV to 1 EeV). gSeaGen is thus used for ORCA production and GENHEN for ANTARES and ARCA Monte-Carlo (MC) simulations.

Neutrinos are typically generated isotropically over the full sky and over large energy ranges. These neutrino interactions with nucleons are simulated using the measured parton distribution functions to calculate the deep inelastic scattering cross sections. Even if extrapolated for larger

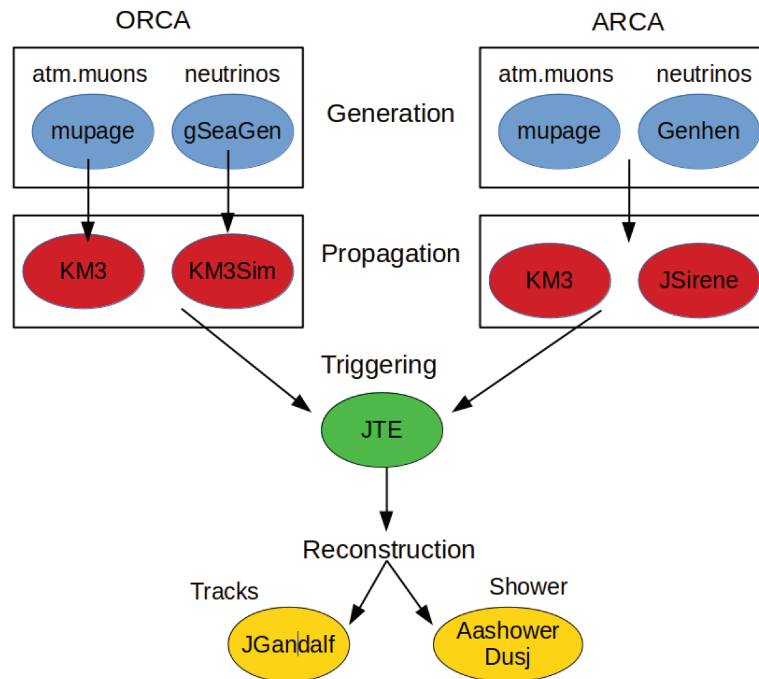


Figure 3.1: A schematic view of the software chain used in the KM3NeT detectors, going from the simulation to the physics trigger and reconstruction.

energies, they have been validated only up to energies of 10 PeV. There is ongoing work to properly extend these parton distribution functions to high energies (up to 100 PeV) and include them into GENIE so that a GENIE-based generation can be fully developed and performed over the full energy range [114]. The extension of the validity of these simulations is ongoing.

The same generated events can be used to simulate both atmospheric and cosmic neutrinos. In order to be able to do that, a weight must be associated to each event to calculate the interaction rate for any neutrino flux. For atmospheric neutrinos, the HONDA flux [115] is used while for cosmic neutrinos, different hypotheses are tested (typically, a broken or unbroken power law with different spectral indices and energy cut-offs).

- **MUPAGE** is an atmospheric muon generator, based on parametrizations obtained from a full MC simulation using the HEMAS code [116]. These parametrizations use the angular distribution and the energy spectrum of underground muon measurements [117]. The MUPAGE simulations are valid for underwater depths between 1.5 and 5.0 kilometres, and for zenith angles up to  $85^\circ$ . Data-MC comparisons over the eleven years of ANTARES data show that there is a good agreement with the atmospheric muon flux measurements [118]. Also the data from the first KM3NeT ORCA and ARCA lines deployed on the sea present a good matching with the simulation [119].

Another existing code for simulating atmospheric muons from extensive air showers is the CORSIKA [120] generator. It performs a full simulation (from the interaction of CRs in the atmosphere down to the sea surface) instead of using parametrizations and it is the framework extensively used by the IceCube Collaboration. However, it is more CPU consuming. Hence the choice of MUPAGE in the context of a run-by-run simulated approach adopted in ANTARES and KM3NeT.

- **lenugen** is a new simulation tool developed in the framework of this thesis that implements MeV neutrino interactions in seawater [121]. The aim of this generator is to estimate the interaction rate of CCSN neutrinos in the KM3NeT neutrino telescopes and will be detailed in chapter 5. It can be used not only for CCSN signals but also to simulate any astrophysical neutrino flux within the energy range from 1 MeV to 100 MeV, by accounting for the corresponding spectrum via appropriate weights. The higher energies implemented here overlap with the lower energy threshold currently simulated for ORCA.

### 3.4.2 Particle and light propagation

*Propagation* is the step where the secondary particle products of neutrino interactions in seawater are generated and propagated until they are stopped (interact/decay), inferring the Cherenkov radiation that is produced. Light is also propagated until it is absorbed or detected by the PMTs. For this purpose, a dedicated detector file with the specific geometry is used. These codes account for water properties and the various effects such as scattering or absorption.

- **KM3Sim** is a package based on GEANT4 [122]. It is a fully detailed simulation tracking every single particle interacting and Cherenkov photon produced. It has been developed inside the KM3NeT Collaboration [123]. Its computing time scales with the energy of the neutrino. This is why it is used for ORCA (GeV energies) and CCSN neutrino productions but not for higher energies (ARCA/ANTARES). It accounts for the light coming from the primary and secondary particles. Because of the large atmospheric muon statistics to be simulated, the use of KM3Sim is not appropriate for large MC productions.
- **KM3** is a light generation and propagation program which uses lookup tables rather than a full simulation as KM3Sim. All relevant physical processes such as energy losses, hadronic interactions, light emission and multiple scattering are considered in the simulation. The emission of the Cherenkov light is performed on a statistical basis, i.e. using the probability of a photon to produce a hit on a PMT. The computation of such probability is taken from tables which include the probability distributions of the number of hits and the arrival times of the hits for photons originating from different positions and with different orientations with respect to the OM. The tables used by KM3 are based on GEANT3 software. It is thus much faster and it is currently used for ANTARES and ARCA HEN simulations. It is again an internal software inside the ANTARES and KM3NeT Collaborations.

KM3 uses the multi-particle approximation, in which all particles that are not electrons or muons are simulated as equivalent electrons with the appropriate light yield. This collective approximation of the hadronic cascade makes KM3 unsuited for the simulation of low-energy neutrino events in ORCA where the individual hadronic cascade topology plays a role in event reconstruction, while the approach is well suited for ANTARES and ARCA given the larger spacing between the optical modules and the higher energy threshold.

- **JSirene** is a framework for the light propagation recently developed within the KM3NeT Collaboration. Instead of using tables, it takes analytical PDFs that give the users the probability for a photon, produced at a certain distance with a given energy and with a certain angle with respect to the light sensor, to arrive to a PMT and to be converted into a photo-electron. The distance and the angle to generate the PDFs are computed from the interaction vertex for tracks and from the maximum of electron emission in the case of a shower.

A comparison between the three light generators has been performed, and the three of them lead to compatible results with the few percent differences being understood.

In fact, aside from the development of the low-energy neutrino generator *lenugen*, during the thesis a contribution was made to the work on the comparison among the three light codes and the extension of the ORCA MC production up to higher energies (1-5 TeV) in order to have an overlap region with the ARCA detector and to be able to use ORCA on its sensitive energy range for neutrino astrophysics.

### 3.4.3 Detector response

*JTriggerEfficiency (JTE)* is the internal software used to simulate the PMT response, including electronics, accounting for the individual PMT efficiencies and the detector calibration. The program is responsible for the application of the triggers defined in section 3.3. By default, only events surviving at least one trigger are kept for the physics data analysis. JTE is the KM3NeT version while in ANTARES it is *Trigger Efficiency (TE)* that covers the same functionality.

Briefly, after the light propagation has been simulated, the time transit spread (TTS) of the PMTs is simulated. In the KM3NeT software, a gaussian smearing is applied to the hit arrival times to simulate the TTS. In ANTARES, it is simulated directly from its measured values. Coincident hits on the same PMT are also merged into a single pulse with an increased ToT.

Regarding KM3NeT, JTE allows for disabling the triggers in case all hits need to be kept. In addition to the detector response to individual hits, the background due to environmental conditions can also be directly simulated at this step, including the  $^{40}\text{K}$  contribution at each multiplicity and the total baseline rates. Note however that the program does not provide the possibility to simulate time/space correlations from bioluminescence.

### 3.4.4 Event reconstruction

*Reconstruction* is a fundamental step in the analysis chain with neutrino telescopes. The patterns of the hit time, the hit amplitude and the hit position over the detection strings are used in order to trace back the trajectory of the particle (lepton) inducing the Cherenkov light. In this way, the interaction vertex, the direction of the outgoing lepton and its energy can be inferred. Different approaches are followed according to the detector configurations and the event topology.

- **JGandalf** and **AAFit** are the main muon track reconstruction algorithms used respectively in KM3NeT and ANTARES. The main similarities and differences between the two are highlighted in the following paragraphs.

The reconstruction chain for AAFit is based on a multi-step procedure which consists on a linear pre-fit ( $\chi^2$  minimizer), an M-estimator fit (also a minimizer) and a maximum likelihood fit with a simplified PDF [124]. Based on causality criteria, a pre-selection of hits is applied to feed the reconstruction algorithm and discard pure-noise hits. After these three steps a final maximum likelihood fit, which gives the direction of the reconstructed track, is performed. The PDFs used to build the likelihood contain only the information of the hit time and the expected arrival time. This likelihood maximization is sensitive to the starting direction from the M-estimator. Because of this, the two last steps (M-estimator best fit and likelihood maximization) are repeated for eight alternative additional starting points, which are chosen from the pre-fit. The number of starting points providing a reconstructed track direction in agreement within one degree from the preferred result is kept for further quality assessment.

The approach used in JGandalf [125] is slightly different. As in the AAFit algorithm, the first step is also a linear pre-fit based similarly on a  $\chi^2$  minimization. Causally connected hits are used in this pre-fit to avoid optical backgrounds or scattered light. Different permutations of this hit selection are done from the causally connected hits, based on the minimization values. A best fit value is defined from the pre-fit, selecting the "best direction". The pre-fit procedure is repeated for different directions within one degree from the selected one. In the end, the twelve directions with a best fit value are chosen and the muon trajectory is fitted using a likelihood maximization, which is evaluated for each of these twelve directions. The PDFs used for the likelihood include information about the PMT response as a function of the minimum distance of the muon track to the PMT, the orientation of the PMT, and the time residual of the hit, which are computed semi-analytically from simulations.

- **AAshowerfit and TANTRA** are the shower reconstruction algorithms used respectively in KM3NeT-ARCA and ANTARES. While for tracks the vertex position can be reconstructed, in the case of shower events it is the position of the maximum of the shower development that is fitted. Also, since tracks can start outside the instrumented volume but showers are seen as contained events in the detector, it is easier to infer the shower energy than the track energy from the estimate of the energy deposited in the detector.

TANTRA is the main cascade reconstruction algorithm used in ANTARES [126]. It is based on a two-step procedure: first the reconstruction of the interaction vertex and second the fit of the direction of the cascade. A specific selection of the hits is applied prior to each of these two steps. The fit of the cascade direction is performed by means of a likelihood maximization. This likelihood is built by computing the probability of measuring a given charge on a given PMT. It is built using the signal and background PDFs which depend on the charge of the hit, the neutrino energy, the distance between the PMT and the interaction vertex, and two angles: the angle between the neutrino direction and the vector which connects the PMT with the interaction vertex and the angle between the direction of the PMT and the incident photon.

AAshowerfit is the main shower reconstruction framework used in KM3NeT/ARCA [125]. As TANTRA, it is based on an initial vertex position fit followed by a cascade direction fit. For the latter, no information of the previous fit is used. The hit pre-selection is performed in two steps. First, hits occurring in one PMT within a time window of 350 ns are merged into a single hit, whose arrival time is the time of the first hit. Then, among the merged hits only those that arrive in the same DOM in coincidence (within 20 ns) are used for the vertex fit, which is based on an M-estimator. The starting point of the M-Estimator is taken as the center of gravity of all the selected hits, and the starting interaction time is taken as the mean of the hit times minus 500 ns. The PDFs used in the likelihood are built by computing the number of photons which are expected to be detected from a shower-like event as a function of the distance from the interaction vertex to the center of the DOM, the direction of the cascade, the direction of the PMT and the deposited energy of the event.

Moreover, the **Dusj** reconstruction technique for cascade events has been adapted for the three detectors [127]. Slightly different versions are implemented for ORCA, ARCA and ANTARES according to the detector geometry but with the same approach, which is also a maximum likelihood fit. The Dusj reconstruction is divided into three main steps: hit selection, maximum likelihood fit and calculation of additional quality parameters. Both in ANTARES and KM3NeT, some Dusj parameters are used in an event classification via a random decision forest (RDF) algorithm. In particular, some of its variables include multivariate techniques in order to distinguish

between cascades, track-like and background events. However, due to the worst directional reconstruction performance compared to TANTRA, it is not the main algorithm used.

One key element for neutrino astronomy is the capability to infer the direction of the neutrino detected through its interaction products. For this, the angular resolution of the detector is evaluated. It is defined as the angular separation between the true direction of the simulated neutrino and the reconstructed direction. More precisely, the median value of the distribution between the true direction of the simulated neutrino and the reconstructed direction, is often reported.

The performance obtained for shower-like events in terms of median angular resolution is of  $\sim 3^\circ$  for ANTARES,  $\sim 5^\circ$  for ORCA (above 20 GeV) and below  $1^\circ$  for ARCA is achieved. Regarding the energy resolution, an uncertainty of  $\sim 10\%$  for ANTARES,  $\sim 10\%$  for ORCA and  $\sim 5\%$  for ARCA is achieved. These is shown in Fig. 3.2 (ANTARES), Fig. 3.3 (ORCA) and Fig. 3.4 (ARCA).

For track-like events, the angular resolution obtained with these algorithms is of  $\sim 0.4^\circ$  for ANTARES (above 10 TeV), smaller than  $5^\circ$  for ORCA (above 20 MeV), and  $\sim 0.1^\circ$  for ARCA. For ORCA, no difference is observed on the reconstruction performance between the two event topologies. The capabilities of ANTARES and ARCA are compared in Fig. 3.5.

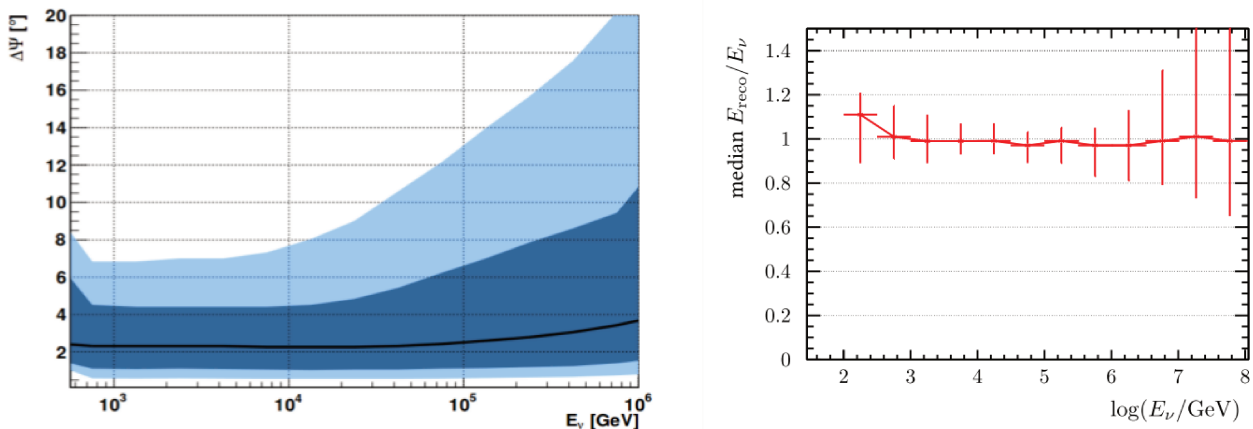


Figure 3.2: Left: Median angular resolution as a function of the neutrino energy for cascade events with ANTARES. The 68% and 98% CL contours are indicated in dark and light blue, correspondingly. Right: Median value of the ratio between the reconstructed shower energy and the true neutrino energy. The error bars indicate the 68% uncertainties for shower events with ANTARES.

### 3.4.5 Effective area and detector acceptance

The expected number of detected events from a given neutrino flux can be inferred from an effective area or detector acceptance. They both take into account the detection efficiency, the interaction probability and Earth absorption, the detector visibility in a given direction and the energy loss of muons.

The neutrino spectrum from a given source is typically described by a power law:

$$\Phi_\nu(E_\nu, \delta) = \frac{dN}{dE_\nu} = \phi_0 E^{-\gamma}. \quad (3.1)$$

The number of expected ( $N_{\text{det}}$ ) events for a given flux, in the considered detector, depends on the declination  $\delta$ . It can be computed via the following integral:

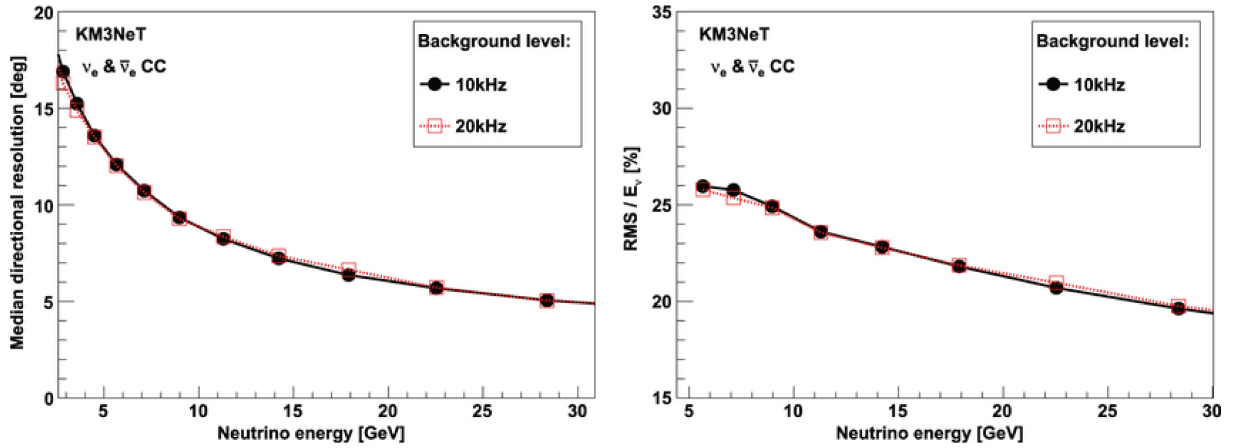


Figure 3.3: Left: Median angular resolution as a function of the neutrino energy for cascade events with the full ORCA detector. Right: Relative energy resolution for shower events with ORCA. The resolution estimates are done for two different background levels considered (black and red).

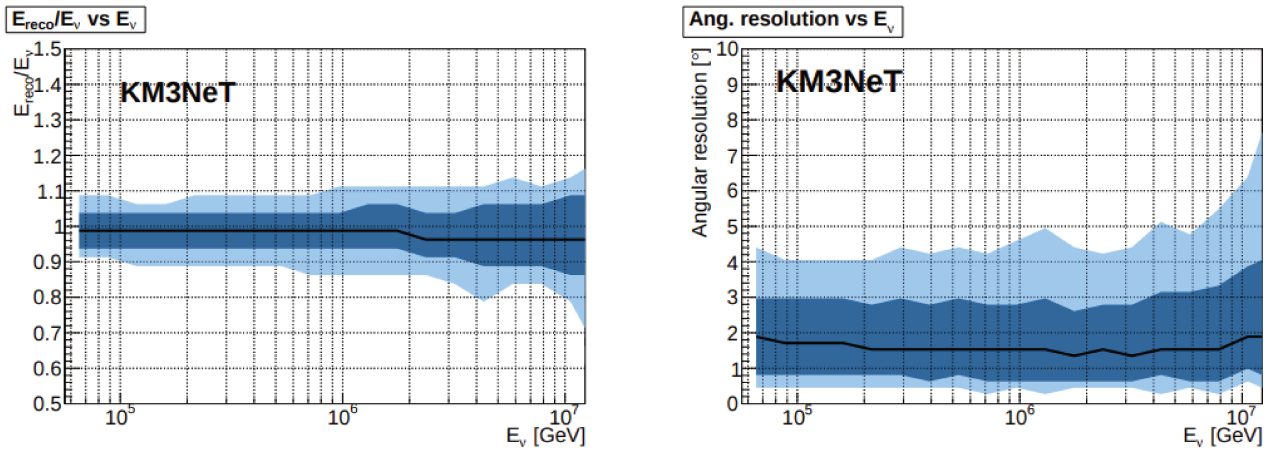


Figure 3.4: Left: Median angular resolution as a function of the neutrino energy for cascade events with the full ARCA detector. Right: Median energy resolution for shower events with ARCA. The 68% and 98% CL contours are indicated in dark and light blue, correspondingly.

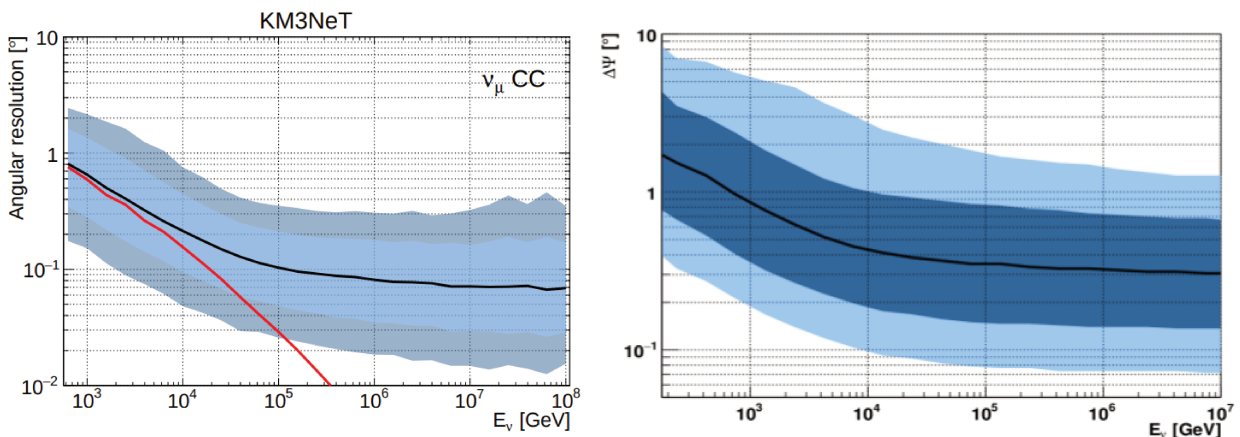


Figure 3.5: Median angular resolution for track-like events as a function of the neutrino energy for ANTARES (left) and full ARCA (right) detectors. The improvement achieved with ARCA is notable for pointing to neutrino sources.

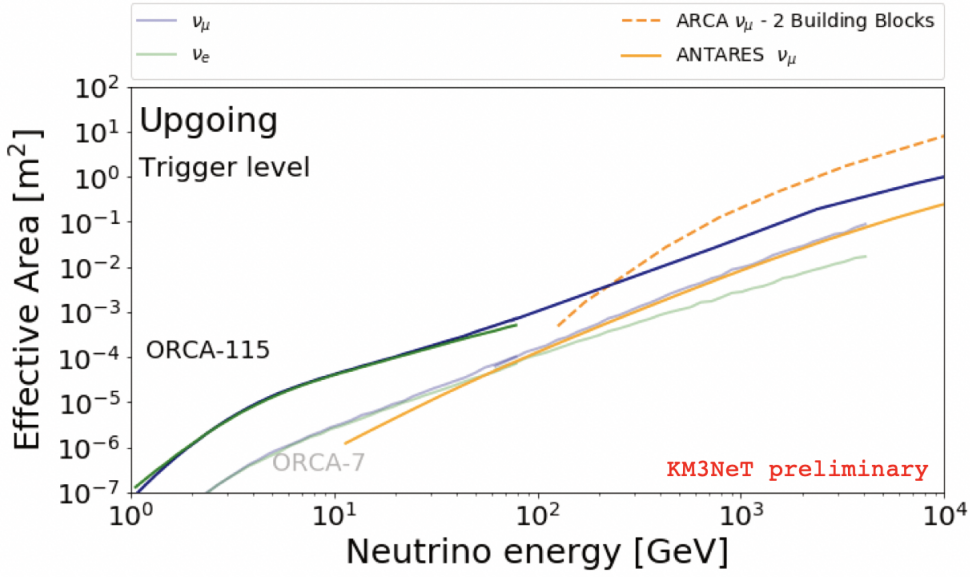


Figure 3.6: Trigger level effective area for upgoing neutrino events for the ANTARES and KM3NeT detectors. For the ORCA detector, 115 and 7 DUs configurations are considered, as well as both  $\nu_e$  and  $\nu_\mu$ . For ARCA and ANTARES, it is shown only for  $\nu_\mu$ .

$$N_{\text{det}}(\delta) = \int \int \Phi_\nu(E_\nu, \delta) A_\nu^{\text{eff}}(E_\nu, \delta) dE_\nu dt \quad (3.2)$$

where  $A_\nu^{\text{eff}}(E_\nu, \delta)$  is the effective area for a given neutrino energy and declination  $\delta$ , with  $dt$  the time interval over the number of events is calculated.

The effective area can thus be defined as the ratio between the rate of the detected events  $R_{\text{det}}(E_\nu, \delta)$ , which depends on the analysis selection, and the neutrino flux arriving to the Earth ( $\Phi_\nu(E_\nu, \delta)$ ), both depending on the neutrino energy and direction:

$$A_\nu^{\text{eff}}(E_\nu, \delta) = \frac{R_{\text{det}}(E_\nu, \delta)}{\Phi_\nu(E_\nu, \delta)} \quad (3.3)$$

The detector acceptance,  $A(\delta)$ , is defined as the ratio (or proportionality constant) between the number of signal events that are detected with an event selection ( $N_{\text{det}}$ ), and the normalisation of the signal flux ( $\phi_0$ ):

$$A(\delta) = \frac{N_{\text{det}}(\delta)}{\phi_0} \quad (3.4)$$

Putting all previous information together, the acceptance can be derived from the effective area as follows:

$$A(\delta) = \int \int dt dE_\nu A_\nu^{\text{eff}}(E_\nu, \delta) E^{-\gamma} \quad (3.5)$$

It is the quantity connecting the number of expected events with a given flux. Therefore, the effective area can be obtained from the acceptance, and vice-versa. Figure 3.6 provides a comparison of the effective area at trigger level (no analysis event selection) of the detectors: ANTARES, KM3NeT-ARCA and two configurations of KM3NeT-ORCA, the full detector and 7 instrumented lines. This plot shows the synergy between the ORCA and ARCA detectors, as well as the fact that the ANTARES detector is a direct extension at higher energies of ORCA 7 DUs.

## 3.5 Statistical concepts used in particle and astro-physics

When working on particle physics or astrophysics, we usually deal with the question: is this data containing the "signal" we are looking for or is it just background (or noise)? With signal referring to the physical measurement or characteristic we want to evidence and background or noise is any other thing producing the same observational features, sometimes very difficult to disentangle from the searched "signal".

Thus, several strategies and techniques are developed with the purpose of having the best signal and background discrimination, typically called the event selection of the analysis (or analysis cuts), that will be described for the different works presented in this thesis.

But some standard criteria and parameters must be defined in order to state in which case one can claim a discovery after the analysis is done. In other words, when the probability to observe in your data the same "signal" pattern from background is small enough to say that the data is not compatible with the background only hypothesis.

This section aims at providing a general idea and simple description of the statistical definitions and methods used in this thesis. The interested reader can find more information in [128].

### 3.5.1 Test statistic, p-value and significance

The p-value and significance are concepts typically used in particle physics and astrophysics.

The **test statistic** is the parameter defined in order to compare the background and the "signal" events. The test statistics (TS) is usually chosen to provide the best possible separation power between the signal and the background only hypotheses.

What is done in an analysis is to characterize the background and the signal. The optimised selection cuts are then applied to obtain a final data sample with, for instance, the best signal to noise ratio. After that, the value of the test statistic is computed for this data set. Then, in order to evaluate how significant is this data set, the computed test statistic is compared to the distribution of the test statistic for the background hypothesis. This allows to estimate the probability to obtain such or a greater value of the test statistics from background. This probability is what is called the **p-value**. The standard criterion is that a p-value ( $p$ ) smaller or equal than  $2.7 \times 10^{-3}$  is an evidence and a p-value  $p \leq 3 \times 10^{-7}$  leads to a discovery.

In Fig. 3.7, an illustration of the definition of the *significance* and the *power* of a hypothesis test is provided. Two hypotheses are compared: background only ( $H_0$ ) and signal + background ( $H_1$ ), with the observed value of the test-statistic ( $TS_{th}$ ). The significance gives the probability of wrongly rejecting the null hypothesis ( $H_0$ ), i.e. of observing a TS value larger than  $TS_{th}$  from the  $H_0$  hypothesis. The power is the probability of having a test statistics from the  $H_1$  hypothesis larger or equal than the observed  $TS_{th}$ , i.e. the probability of rejecting the null hypothesis  $H_0$  when the alternative hypothesis  $H_1$  is true.

The p-value can also be related to the concept of False-Alarm Rate (FAR), which is the number of times (in a pre-defined time window) this value of the test statistic would be obtained in the case where there are only background events in the data. In some sense, FAR can be also translated into a p-value, and it is usually done. But the real meaning is lost since the information on the time window is lost. Moreover, it is not directly compared to the signal expectation and its rate, so it is tricky to convert it into a detection significance as described in next paragraph.

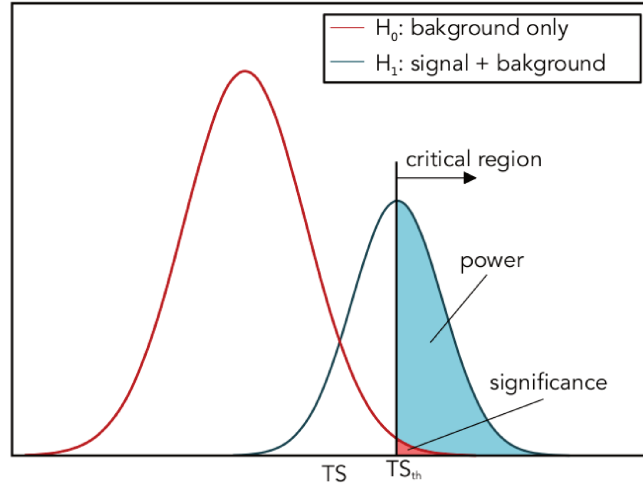


Figure 3.7: Example of a hypothesis test. The red (blue) curve corresponds to a given TS distribution for the background only,  $H_0$  (red line), and signal + background hypothesis,  $H_1$  (blue line). Given a TS threshold value obtained from data,  $TS_{th}$ , the significance is defined as the fraction of the  $H_0$  distribution for which  $TS > TS_{th}$ . The power is defined as the fraction of the  $H_1$  distribution for which  $TS > TS_{th}$ . The critical region is the range of TS values above  $TS_{th}$ .

The p-value is usually converted into a **significance** in terms of sigmas ( $\sigma$ ). In the case the distribution of the test statistic for the null hypothesis were a normal distribution, and using the two-sided convention, "evidence" is used for a significance of  $3\sigma$  and "discovery" for a  $5\sigma$  result. The significance in terms of sigmas ( $z[\sigma]$ ) is evaluated from the p-value through the error function (erf) as follows:

$$z[\sigma] = \sqrt{2} \times \text{erf}^{-1}(p) \quad (3.6)$$

When one assumes the Gaussian behavior, the definition of the significance ( $z$ , in number of  $\sigma$ ) turns out to be:

$$z[\sigma] = \frac{\text{data} - \text{background}}{\sqrt{\text{background}}} = \frac{\text{signal}}{\sqrt{\text{background}}} \quad (3.7)$$

where data is typically background plus the potential something else we are looking for (the signal if the true hypothesis is signal+background) and with the background being "known" (characterised a priori).

### Combining p-values

Sometimes, we may want to combine the results of different experiments or samples in order to increase the final significance. Something that one detector alone cannot significantly observe may be discovered by combining two different experiments.

Which is the best way of estimating the combined p-value (or significance) is a question that is ill-posed. Indeed, large amount of literature exists treating the problem and proposing different methods [129]. When methods for combining two p-values differ significantly, the difference typically comes from the way they rank the combination of two similar p-values compared to the combination of a high one and a low one. The preferred ranking depends of course on which parts of the test statistic distribution the alternative hypotheses tend to populate.

The first simple way for this combination was proposed by R. Fisher in [130], hence the name Fisher's method. It is based on the intuitive choice of the multiplication of p-value and the relation

with the  $\chi^2$  probability distribution:

$$f(p_1, \dots, p_N) = \prod_i p_i \quad (3.8)$$

$$-2 \sum_i p_i = \chi_{nof,p}^2 \quad (3.9)$$

with  $nof = 2N$  being the number of degrees of freedom and  $p$  the combined p-values given by the  $\chi^2$  probability.

One of the problems encountered using this method (coming from the way of weighting the two p-values) is that if one wants to combine two p-values with one of them being larger than 0.5, the combination leads to a worse significance result than the best p-value that is combined by its own. However, this is not what one looks for when profiting of the combination of additional data. This problem was encountered when combining ORCA and ARCA for time-dependent CCSN analyses (see chapters 6 and 7). Moreover, in the case when the number of signal and background events for the two combined experiments are quite different (e.g. by an order of magnitude), the weighted combination turns to be the best approach. This was found when applying a different selection in ARCA and ORCA for CCSN neutrino searches (chapters 6 and 7) that could lead to this condition.

A possible strategy that can be used in order to solve this issue is the linear combination of the significances, that would be done according to:

$$\sigma_{comb} = \frac{\sum_i \sigma_i W_i}{\sqrt{\sum_i W_i^2}} \quad (3.10)$$

where  $W_i$  is a weight applied to the significance of each data set  $i$ , which should be predefined and can be optimised. This weight is needed to account for the different signal contribution on each experiment/data set. Indeed, when the knowledge of the experimental data is limited to the size and precision of the samples but further details are not known, there is strong motivation to weight the two p-values differently.

The relevant message in the end is that the perfect way for the p-value (or significance) combination has not been yet found. Therefore, the best way to proceed, if possible, is combining directly the experimental data samples rather than the p-values. In fact, this is the strategy followed in the combined ANTARES and IceCube analyses (e.g. [100]).

Moreover, combining data (or what is the same, the PDFs used in the likelihood analysis that is typically carried out in these cases) would allow for the combination not only of data from different experiments but even of different samples from the same detector. For example, imagine one would like to combine the HESE and muon-track IceCube samples to enhance the significance of a given analysis performed using both separately.

### 3.5.2 The sensitivity, discovery potential and upper limit

In the previous section, we discussed how to estimate and provide information about the significance of an observation. On the current one, we want to try to answer to the following questions:

- What is the performance of the detector?
- What are the best selection cuts to optimize the analysis?
- In case of a non-significant observation, can we say something about the signal we search for and constrain the models from the non-observation?

First of all, it should be noted that the data analyses in particle and astroparticle physics are done blindly, i.e. without looking at the relevant data where the searched-for signal may be contained (see [131], where different strategies to blind the data are described). Therefore, the definition and optimization of the analysis are done using MC simulations and without looking at the data where the analysis will be applied. Different criteria can be used to optimize the analysis:

1. For the best **discovery potential**: get the greatest chance to detect a signal of a given amplitude.
2. For the best **sensitivity**: get the most stringent constraint and model discrimination power from a non-observation.

### Upper limit

We tackle the case of a non-significant observation. This means, for instance, that we have a number of observed events over the background expectation but not enough to say it that is not compatible with a background fluctuation with a high enough probability (at least above  $3\sigma$ ). In this case, an *upper limit* (usually at at 90% CL) can be derived, i.e. a constraint can be stated on the maximum number of signal events we expect from the searched source from the fact that it was not observed.

Let's take the easiest example, the case of  $n_{obs}=0$  with a poissonian behavior of the data. In that case, the Poisson probability of observing 0 events is smaller equal to 10% when 2.3 events are expected as maximum from signal plus background. So when the background is negligible, the upper limit at 90%CL is  $\mu_s^{90\%}$  2.3.

The *upper limit* is therefore defined as the maximum number of events that may be originated from signal, given the (known) background expectation and the observation  $n_{obs}$ , and cannot be detected. Thus, it sets a limit on the maximum expected signal from a source, that is used to constrain the models.

Unless no events are observed, the procedure consists in fitting  $n_s$  (typically using an unbinned likelihood method, but others exist) considering that the background is well known and characterised, and the total number of observed events,  $n_{obs}$ . From the fitted value of  $n_s$  one gets the corresponding value of  $\mu_s^{90\%}$ . In order to do this fit, a signal model must be used.

### Sensitivity

The *sensitivity* corresponds to the largest number of signal events that the detector would be able to distinguish from background (typically in 50% of the cases). Smaller signals will be indeed compatible with background. In other words, the sensitivity is the smallest signal that can be proved. Thus, this limit value quantifies the sensitivity of the experiment to a given signal. The sensitivity can also be seen as an average upper limit.

### Discovery potential

The *discovery potential* is defined as the number of signal events that need to be emitted from the source (at least) in order for your experiment to be able to claim a discovery at a given significance. In other words, it indicates how strong the signal has to be for the experiment to achieve a significant detection. As the *sensitivity*, it is computed without looking at the unblinded data and used as criteria to define and optimize the selection cuts in the analysis as mentioned before.

## **Part II**

# **Detecting Galactic core-collapse supernova neutrinos with KM3NeT**



# Chapter 4

## Core Collapse SuperNova neutrinos: What we know today.

The current chapter briefly presents the core-collapse supernova (CCSN) explosion mechanism and the neutrino production in such energetic phenomena, motivating the search carried out during this thesis. The CCSN neutrino fluxes studied are introduced, with a discussion on the potential of a multi-messenger detection of a CCSN event and a short description of the SuperNova Early Warning System (SNEWS).

### 4.1 Historical introduction to CCSN neutrinos

It was already in 1934 that the mechanism of stellar evolution was linked to the formation of a compact object at the end of the life of a massive star. At the same time, Supernovae remnants were proposed as a candidate site for the process of hadronic acceleration. This was the idea of W. Baade and F. Zwicky, published in [132, 133, 134], who first used the term *supernova* (SN).

They based their arguments on the insight that the energy released observed from the SN phenomenon originates from the gravitational binding energy of the collapsing star. This basic picture continues to be the solid foundation of our present knowledge of stellar evolution and the birth of neutron stars (NSs).

Therefore, these objects start to be investigated as sources of cosmic rays, which were first identified as of extra-terrestrial origin by V. Hess in 1911. The origin of these really high energetic particles reaching the Earth still remains a mystery (see chapter 1).

The discovery in 1968 of the Crab pulsar inside the Crab nebula, with the testimony of the Crab SN observed in 1054, confirmed the existence of neutron stars as well as their association with SN remnants. This has been firmly established also by many recent observations.

A direct confirmation of the scenario of stellar core collapse, with neutrinos as possible agents to drive the SN explosion, occurred with the detection of two dozen neutrinos from SN 1987A [135] in the underground experiments of Kamiokande II [136], Irvine-Michigan-Brookhaven [137] and Baksan [138]. This event originated in the Large Magellanic Cloud, a dwarf galaxy satellite of the Milky Way. The total luminosity released in neutrinos is measured to be around  $3 \times 10^{53}$  erg/s and events were observed over about 10 s [135]. The time profile of the detected events is shown in Fig. 4.1.

Since then, no nearby supernova has occurred. With only 1-3 events expected per century in the Galaxy, astronomers anxiously wait to the next SN in the Milky Way. Current and near-future neutrino detectors will be sensitive only to nearby supernova, and only a few of them will reach a distance horizon outside of the Galaxy, up to 50-500 kpc [139, 140, 141].

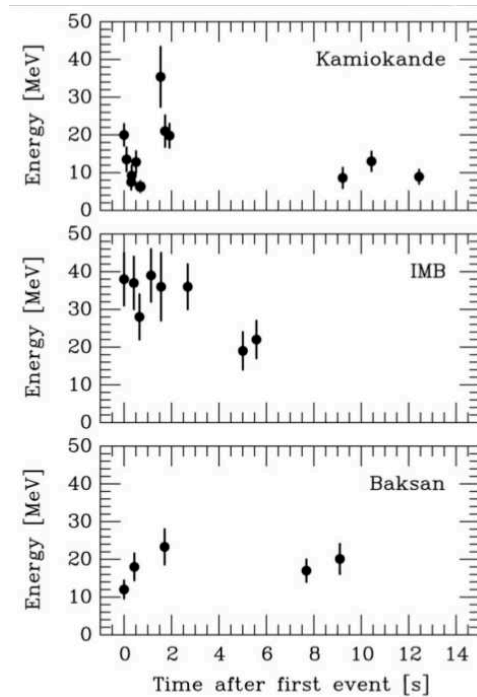


Figure 4.1: Time distributions of neutrino events observed by the three observatories from SN 1987A. Figure extracted from [135]

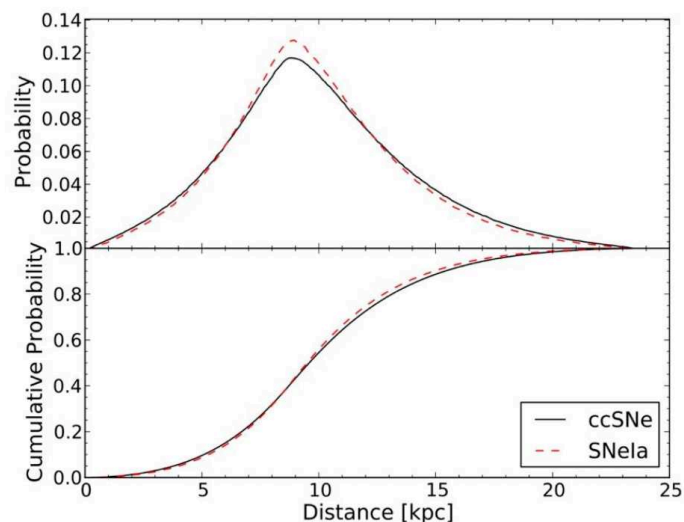


Figure 4.2: The differential (top) and cumulative (bottom) probability distribution of the distance to a supernova in the Milky Way from the model in [142].

Sampling the CCSN progenitors population in our Galaxy, the probability of a CCSN occurring as a function of the distance can be inferred (see Fig. 4.2). As expected due to the higher density of stars in the Galactic Centre, the probability peaks at that region. From this distribution, one can infer that more than 99% of Galactic CCSN will happen within  $\sim 21$  kpc from the Solar System.

## 4.2 Phases of a Core-Collapse Supernova: the explosion mechanism

The lessons learned from these unique data and more than 20 years of numerical improvements on simulating these extreme phenomena have brought to the Delayed Neutrino-heating Mechanism as the best attempt of putting together all the notions about SN physics to try to explain these astrophysical events. This mechanism was proposed in [143, 144]. Even though the basis of the neutrino-driven mechanism presented here are well understood, the most sophisticated multi-dimensional hydrodynamical simulations yet present some unresolved questions. Some examples of opened issues are the processes affecting the supernova energetics, the progenitor asymmetries, the consequences of different multidimensional instabilities and rotation, or the effects of the multi-dimensional neutrino transport; see [145] for a complete review.

Large neutrino production takes place during a CCSN, related to the process of compact object formation. During the star evolution, there is a continuous competition between the thermal pressure resulting from nuclear reactions and the gravitational force. The main sequence of the life of the star is characterised by the fusion of the hydrogen and helium, leading to the formation of heavier elements. When the conditions needed for the carbon fusion to take place are reached, a core of oxygen, neon and magnesium is formed. If the star has more than  $10 M_{\odot}$ , then oxygen and neon can undergo new nuclear fusion reactions, producing silicium, which in turn fusions and creates iron and nickel. At this stage, we have what is typically referred to as star with an onion structure (see Fig. 4.3). The fusion stops with iron nuclei, which present the highest binding energies per nucleon.

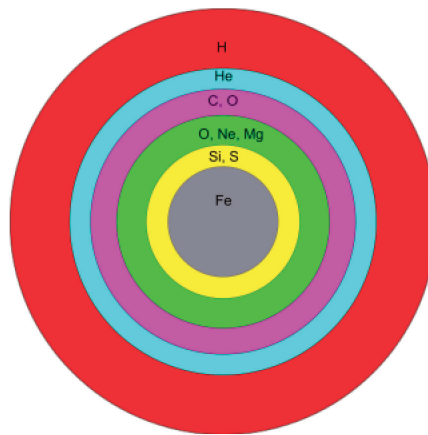


Figure 4.3: Structure in "onion" layers of a CCSN progenitor star (not to scale). Figure from [146].

After the nuclear fusion stages, the iron-nickel core and outer shells of lighter elements remain, sustained by the pressure of degenerate electrons that compensates the gravitational force of the Fe-Ni core. The iron photo-dissociation and electron capture processes in play produce a decrease of the number of electrons, so their pressure cannot prevent anymore the star from the gravitational collapse. This triggers the gravitational instability that initiates the collapse of the stellar core (Fig. 4.4 upper left), which happens when the core reaches the *Chandrasekhar mass*<sup>1</sup>. The time between the beginning of Si fusion and the collapse of the iron core is of a few days up to one week.

The gravitational collapse produces the contraction of the degenerate core, which increases the probability of having electron captures on nuclei:



<sup>1</sup>The Chandrasekhar mass is the maximum mass that an object can have when the degeneracy pressure is opposing gravity.

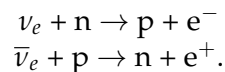
Initially, the electron neutrinos produced in these electron captures can freely escape the stellar core. But the core continues contracting under gravity, and when the so-called nuclear density is reached, neutrinos get trapped in the collapsing stellar core. The *neutrinosphere* is the name given to the border defining the limit between the confinement and the free escape of neutrinos, i.e. it is defined as the last scattering surface for neutrinos. Their radius depends on the interaction probability, thus mainly on the neutrino flavour and the number of targets. Different neutrinospheres can be identified for  $\nu_e$ ,  $\bar{\nu}_e$  and  $\nu_x = \{\nu_\mu/\bar{\nu}_\mu, \nu_\tau/\bar{\nu}_\tau\}$ . A smaller radius implies a lower scattering probability and higher mean energy of emission.

When the collapsing core reaches the nuclear density saturation point ( $\rho_0 \sim 2.6 \times 10^{14} \text{ g cm}^{-2}$ ), nuclear interactions become repulsive, which produces the bouncing of the core, creating a shock that starts propagating towards the interstellar medium. At this point, neutrinos can not freely escape anymore, as it has been mentioned above. With the shock, the outer layers of light elements are expelled (Fig. 4.4 upper right). The bouncing of the core gives birth to the proto-neutron-star (PNS), which consists on the neutron rich matter that remains close to the core and it is not expelled.

The core bounce is followed by the emission of an intense flash of  $\nu_e$  from electron captures, which takes place as the shock crosses the  $\nu_e$  neutrinosphere. This is identified as the first neutrino emission phase, called *shock-breakout neutrino burst* (Fig. 4.4 upper right), which lasts some milliseconds and produces a large peak in the  $\nu_e$  luminosity. The time evolution of the neutrino luminosity during the burst is shown in Fig. 4.5 (left).

During the propagation of the shock inside the outer core, it loses energy through the photo-dissociation of iron nuclei and electron captures. This prevents the shock from propagating for more than some milliseconds, and the shock is stalled well before the boundary of the iron core (Fig. 4.4 middle left). However, while the shock propagates, it carries matter with neutrinos towards the less dense outer regions, where the core becomes again transparent to neutrinos.

In fact, the shock expansion loses energy until it is stopped, and neutrinos can freely escape again. The  $\nu_e$  burst is then followed by an accretion phase, during which the outer matter shells are ejected. It lasts hundreds of milliseconds long. Electron neutrino flavor dominates over the accretion phase, since  $\nu_e$  and  $\bar{\nu}_e$  streaming away from the neutrinosphere are reabsorbed by free protons and neutrons:



But emission of all flavor neutrinos is possible by neutrino-antineutrino pair creation. The time profile of the neutrino luminosity predicted during the accretion phase is shown in Fig. 4.5 (middle)

The stalled shock receives energy from the neutrinos escaping from the neutrinosphere. This situation defines the phase of *neutrino heating* (Fig. 4.4 middle right). During the accretion phase the core is stirred by violent hydrodynamical instabilities. In particular, the *Standing Accretion Shock Instability* (SASI) has been shown to take place in the latest 3D simulations. Both SASI and convection are believed to play a relevant role in the shock revival by enhancing the neutrino heating. Finally, neutrinos are able to transfer enough energy to the stellar plasma and accelerate the shock, which is revived (Fig. 4.4 lower left).

The SASI mechanism is thought to favor the energetic final explosion, which is not yet fully reproduced by simulations and could explain the asymmetry of the shock as well as the neutron star kick observed. The presence of fast time variations in the neutrino luminosity due to the SASI oscillations can be observed in Fig. 4.5 (middle). An observational confirmation of the presence of such hydrodynamical instabilities during the CCSN accretion phase would significantly help to unveil the explosion

mechanism.

With the revival of the shock, the final explosion takes place (Fig. 4.4 lower right). During the cooling phase, which lasts a few tens of seconds, the luminosity and temperature gradually decrease. The corresponding luminosity time evolution along this phase is shown in Fig. 4.5 (right). This final phase is dominated by all-flavor neutrino pair productions. The so-called neutrino-driven wind is launched by neutrino-energy deposition in the NS which has just born. This wind is essentially a spherical flux of baryonic matter going out from the NS surface, and favours the nucleosynthesis of heavy elements (Fig. 4.4 lower right). An overall feature of the neutrino flux at this stage is the luminosity being roughly equal for the three neutrino flavors.

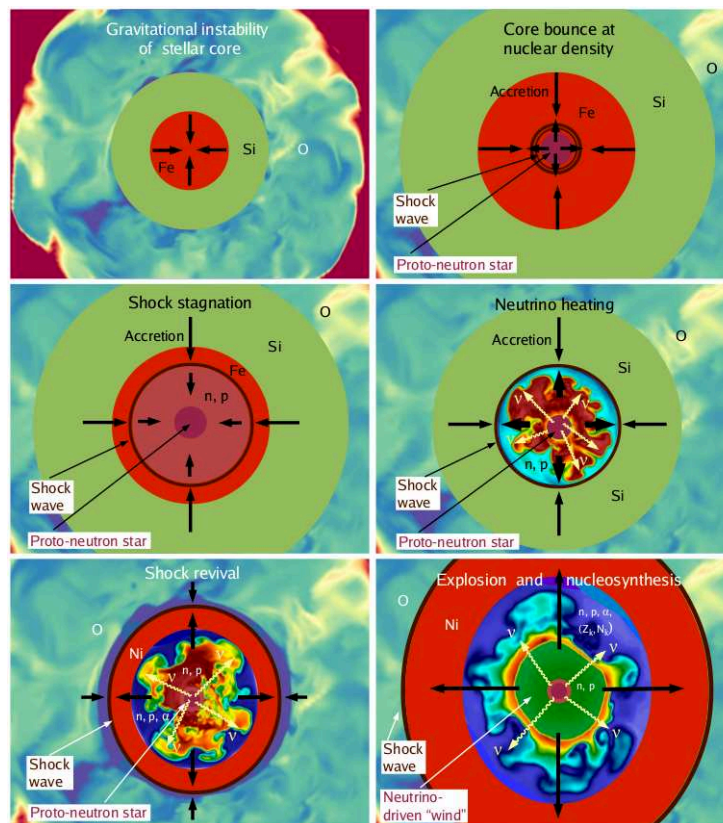


Figure 4.4: Dynamical phases of stellar core collapse and explosion by the neutrino-driven mechanism: infall, core bounce, stagnation of the bounce shock, accretion and neutrino heating, shock revival, and outward acceleration of the neutrino-powered SN shock front (from top left to bottom right). Figure taken from [147].

During a CCSN,  $\sim 99\%$  of the gravitational binding energy is released in the form of neutrinos with energies of 1 to 100 MeV over a timescale of a few seconds. For a typical total energy of  $3 \times 10^{53}$  erg, this equates to an emission in an excess of  $10^{58}$  neutrinos. This highly efficient energy loss via neutrinos occurs because neutrinos interact only via weak interaction and can easily escape, whereas photons remain trapped for a longer time. Indeed, the main phases of a core-collapse supernova explosion occur at a stage in which the star is opaque to optical photons.

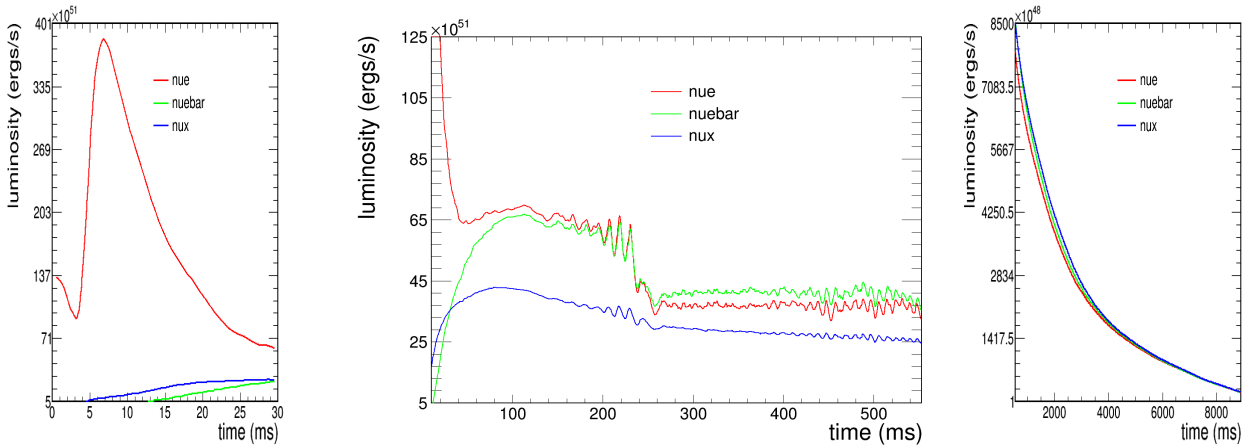


Figure 4.5: Simulations of the neutrino burst (left), the accretion phase (middle) and the cooling phase (right) of a CCSN are shown here. The notation  $\nu_x$  includes all the non-electronic neutrino flavors that in this case can be considered as one for what concerns their evolution. The middle plot comes from the 3D simulation of the  $27M_{\odot}$  progenitor in [148]. The right and left plots come from the 1D simulation of an  $8.8M_{\odot}$  in [149].

In summary, the neutrino emission occurs in three main phases. At first, the *neutronisation burst* results in a bright pulse of  $\nu_e$  as the shock breaks out crossing the  $\nu_e$  neutrinosphere. In the following *accretion phase*, an intense all-flavour emission takes place over a few hundreds of milliseconds, as the core is heated and stirred by the infalling matter. Finally the remaining energy is radiated through an all-flavor emission during the *thermal cooldown* of the core on a 10-20 s time scale.

In this mechanism, illustrated in Fig. 4.4, the shock expansion is driven by the neutrino-energy deposition to the stellar plasma. The neutrino time profile of the three phases is shown in Figure 4.5. The simulation of the accretion phase is described in [148] and the simulation of the burst and cooling phases used here can be found in [149]. More detailed information about the physics of the explosion and its implementation into numerical simulations can be found in [147, 146].

### 4.3 Prompt SN neutrino fluxes and spectra

Simulations of the SN explosions are well advanced nowadays and are compatible with the detected spectra and time distributions of the only CCSN detected through neutrinos so far: SN1987A (for a review see, for example, [150]). The neutrino flux depends on the spectral pinching shape parameter, the total neutrino luminosity and the mean neutrino energy. Different simulations using different models predict a different time dependence and different values of these 3 parameters. These differences come mainly from the different neutrino transport models used, the different simplified treatment of General Relativity considered, and some different assumptions. In this study, a state-of-the-art 3D simulation of the accretion phase of a CCSN provided by the Garching group is considered.

The simulations used for this thesis work were performed with the PROMETHEUS-VERTEX code [151], which couples the hydrodynamics solver PROMETHEUS with the neutrino transport code VERTEX. Such a numerical code is used for treating the time and energy dependent neutrino transport in hydrodynamical simulations of CCSN. The code is based on a variable Eddington factor method to deal with the solution of the Boltzmann equation. This code is well suited to solve relativistic and multi-dimensional problems accurately. This simulation has been extensively used to test IceCube and Super-Kamiokande sensitivity to CCSN neutrinos [148, 152].

As it was shown in ref. [148], the time dependent SN neutrino spectrum can be represented by a quasi-thermal distribution of the form:

$$\frac{d\Phi^\nu}{dE_\nu}(E_\nu, t) = \frac{L(t)_{SN}^\nu}{4\pi d^2} \times f(E_\nu, \langle E_\nu \rangle(t), \alpha(t)) \quad (4.2)$$

$$f(E_\nu, \langle E_\nu \rangle(t), \alpha(t)) = \frac{E_\nu^{\alpha(t)}}{\Gamma(1 + \alpha(t))} \left( \frac{1 + \alpha(t)}{\langle E_\nu \rangle(t)} \right)^{(1 + \alpha(t))} \exp\left(-\frac{E_\nu(1 + \alpha(t))}{\langle E_\nu \rangle(t)}\right) \quad (4.3)$$

where  $\langle E_\nu \rangle$  is the average neutrino energy,  $L(t)_{SN}^\nu$  is the neutrino luminosity and  $\alpha = \frac{\langle E_\nu^2 \rangle - 2(\langle E_\nu \rangle)^2}{(\langle E_\nu \rangle)^2 - \langle E_\nu \rangle^2}$  is the spectral pinching shape parameter, spanning in the range of  $2 \lesssim \alpha \lesssim 5$ .

The spectral pinching parameter indicates the shape of the quasi-thermal distribution.  $\alpha = 2$  corresponds to a Maxwell-Boltzmann distribution, while the spectrum is "pinched" for  $\alpha > 2$ . In fact, the energy dependence of the cross section results in a radial smearing of the neutrinosphere and a corresponding alteration (*pinching*) of the neutrino thermal spectrum.

Furthermore, the flavors have an expected energy hierarchy. Energies decrease with increasing order of the interaction strength:  $\nu_e$  have more interactions than  $\bar{\nu}_e$  because of the excess of neutrons in the core, so less average energy, and  $\bar{\nu}_e$  have more interactions than the other neutrino flavors (noted  $\nu_x$ ), which are restricted to neutral current interactions.

As explained in ref. [153], data are provided in files for each neutrino flavor ( $\nu_e$ ,  $\bar{\nu}_e$  and  $\nu_x$ ) containing the current post-bounce time in the first column and the luminosity, the average neutrino energy and the second energy moment of the neutrino for three different observer directions in the following three columns.

The time and energy evolution of these three parameters is given by the simulation. The time dependence of the three parameters is shown in Fig. 4.7 for the  $27 M_\odot$  progenitor. How these parameters behave in time from the core bounce at the collapse stage is one of the open questions and different prediction come out from the different models.

The evolution of the neutrino flux is shown in Figure 4.8 as a function of the energy. It can be seen that, during the first  $\sim 30$  ms of the explosion, the  $\nu_e$  flux from the neutrino burst are dominating. The fluxes evolve towards equipartition among the three flavors at the end of the accretion phase ( $>400$  ms after  $T_0$ ). The neutrino fluence (time-integrated spectrum) at a reference distance of 10 kpc is shown in Figure 4.9 for the three considered progenitor models.

In the following, KM3NeT sensitivity will be tested using the neutrino flux simulated for:

1. Four progenitor star simulations of masses:  $40 M_\odot$  [154],  $27 M_\odot$  [148],  $20 M_\odot$  [148] and  $11 M_\odot$  [148]. The first is an example of failed CCSN, in which case a BH is formed at the end of the explosion, with a sharp cut-off on the neutrino luminosity and no electromagnetic counterpart is expected. The second and latter will be compared as extreme cases for the CCSN sensitivity in chapter 6. The second and third are compared in section 7.3 as pessimistic and optimistic models of fast time variations in the neutrino light-curves in case of a normal CCSN. The duration of the simulated emission is of 543 ms for the  $27 M_\odot$  simulation, 340 ms for the  $20 M_\odot$  and  $11 M_\odot$  progenitors, and 572 ms for the failed CCSN ( $40 M_\odot$ ).

2. An observer looking in the direction of the SASI sloshing, along which the variations of neutrino flux due to SASI oscillations are the largest. This privileged direction is indicated by the white arrows in Figure 4.6 showing the evolution of the shock instability.

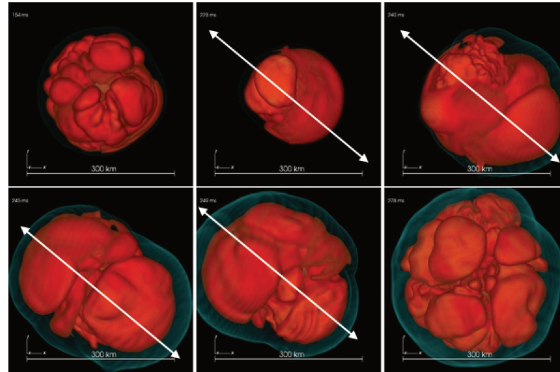


Figure 4.6: Evolution of the shock during the SASI instability observed in the 3D simulations. The white arrows point to the direction in which SASI oscillations take place, where the modulations of the neutrino flux are strongest. Figure taken from [155].

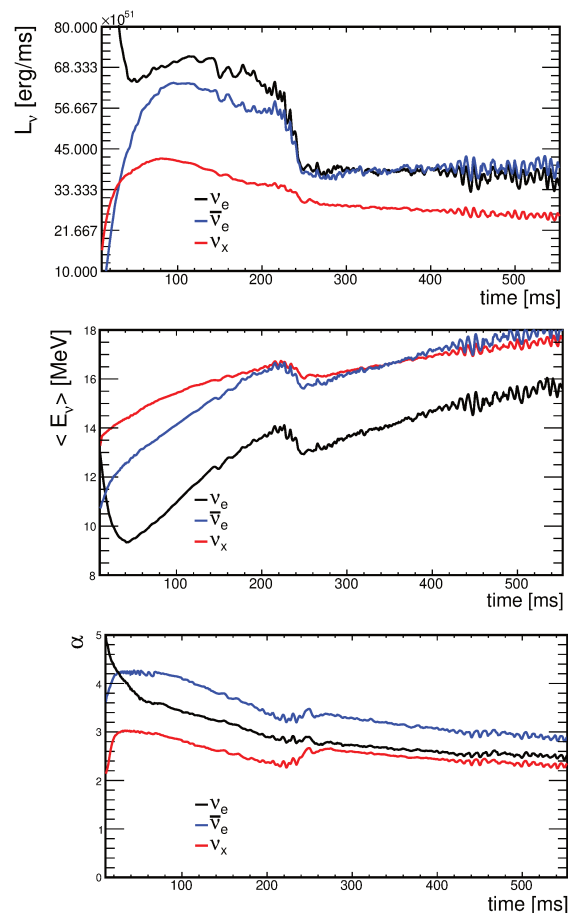


Figure 4.7: Time evolution of the neutrino luminosity (top), the mean neutrino energy (middle) and the spectral pinching shape parameter (bottom), for each of the neutrino flavors, illustrated for the  $27 M_{\odot}$  progenitor. Figure done using data from [148].

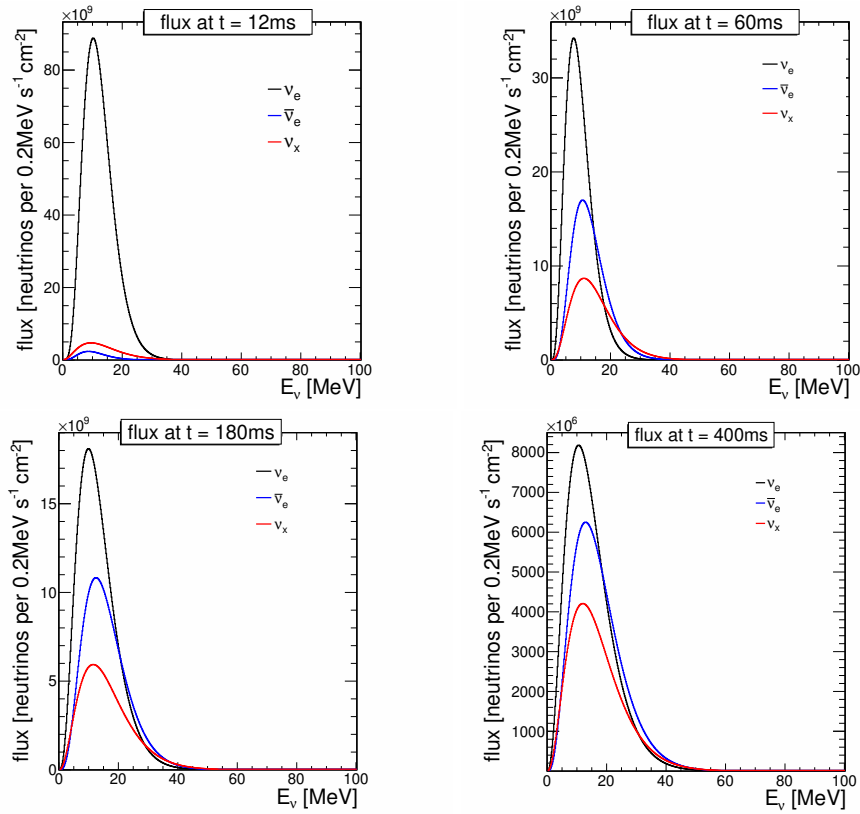


Figure 4.8: Neutrino flux as a function of the energy at different times of the core collapse, for the  $27 M_{\odot}$  progenitor simulation. Figure built with data from [148].

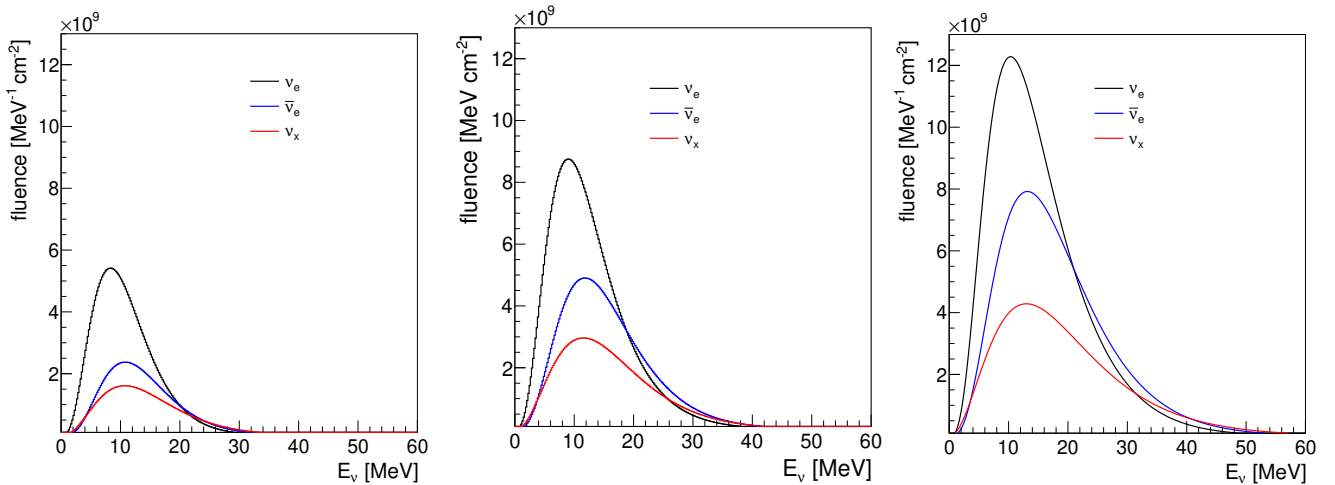


Figure 4.9: Neutrino fluence for the accretion phase of a core-collapse supernova at 10 kpc for the Garching 3D simulation models of  $40 M_{\odot}$  (right),  $27 M_{\odot}$  (middle) and  $11 M_{\odot}$  (left) over a time of 543 ms and 340 ms, respectively.

### 4.3.1 Neutrino flavor conversion models in CCSN

The traditional picture of neutrino flavor conversion occurring in CCSN is that adiabatic flavor conversion (MSW effect, see section 1.3.1 or [20]) takes place inside the star. An analogy with solar neutrinos is used here. The occurrence of the MSW effect for the high energy solar neutrinos shows that these particles change flavor in vacuum in a very different way than in matter. This also applies to MeV CCSN neutrinos. A nice overview of neutrino flavor conversion in CCSN is given in [156].

In the inner high density regions of the star, the neutrino flavor and matter eigenstates coincide. While propagating towards the edge of the star, they can suffer resonance effects that lead to neutrino flavor conversion. It is believed that the MSW resonance condition is fulfilled for CCSN neutrinos as for solar neutrinos, leading to flavor conversion [157].

The MSW effect in supernovae is well established. Actually, since the star is very dense, the MSW resonance condition can be fulfilled three times for typical supernova density profiles [158]. The sign of the neutrino mass-squared differences determines if neutrinos or anti-neutrinos undergo a resonant conversion. The MSW effect in CCSN is illustrated in Fig. 4.10, for the two neutrino mass ordering hypothesis. In case of Normal Ordering (NO),  $\nu_e$  flux will be affected by the MSW effect. If the true ordering is the Inverted Ordering (IO), then the  $\bar{\nu}_e$  flux is suppressed through the resonance. In fact, the recent measurement of the third mixing angle  $\theta_{13}$  being fairly large suggests that the entire three-flavor conversion process would be adiabatic. In this picture, all  $\bar{\nu}_e$  will undergo the MSW resonance and leave the star as  $\bar{\nu}_x$  in case of inverted mass ordering. In the normal ordering hypothesis, a 70%  $\bar{\nu}_e$  survival probability is expected.

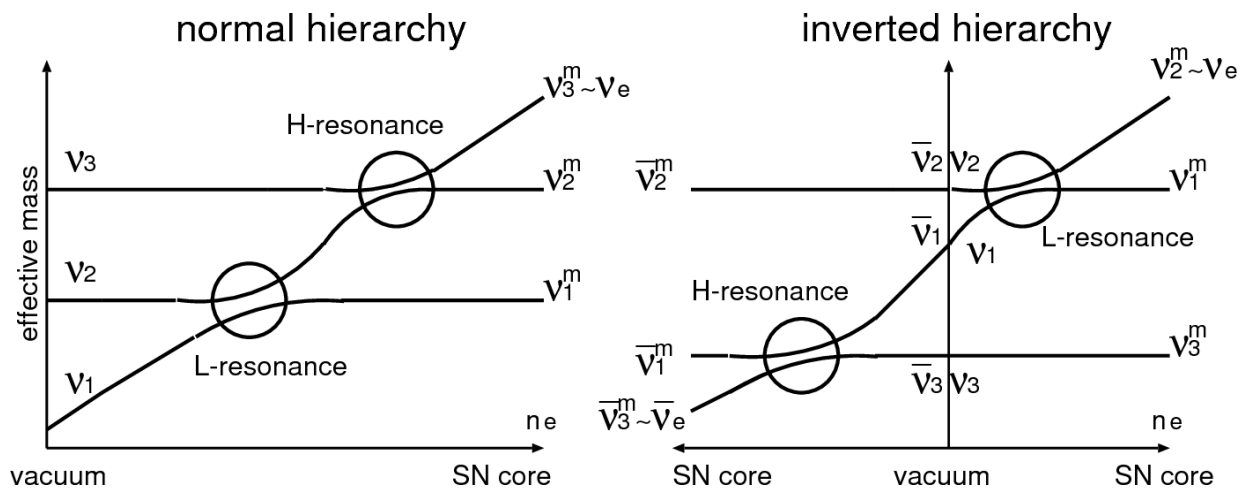


Figure 4.10: Schematic level crossing diagram in CCSN, for normal (left) and inverted (right) mass hierarchies. The circles show the resonance points. Figure from [159].

The adiabatic evolution implies that the mass eigenstates mix according to neutrino oscillations in matter (see 1.3.1) is suppressed at the resonance, i.e. the strong matter effect in the extremely dense CCSN media “de-mixes” neutrinos. In this case, electron neutrinos can efficiently convert into muon and tau neutrinos, which can be considered as a same flavor state from what their evolution concerns in this context. In the following, the non-electron neutrinos will be noted  $\nu_x$ . The problem can be therefore simplified to two mass eigenstates.

Even though the adiabatic flavor conversion is a good approximation, recent calculations have shown the emergence of new phenomena that could make the neutrino evolution become completely non-adiabatic when the shock passes through the MSW region. The effect of neutrino-neutrino interactions, the presence of shock waves and turbulences, as well as steep changes of the stellar density profile, are examples of physical processes that affect the flavor conversion in CCSN, leading to a complicated non-adiabatic case. This is an additional uncertainty in the predicted flux.

The  $\bar{\nu}_e$  flux arriving at the detector will be some superposition of the original  $\bar{\nu}_e$  and  $\bar{\nu}_x$  flux spectra. The two extreme possibilities will provide the maximum variation in the number of expected neutrinos. The first is the hypothetical scenario where no flavor conversion (NFS) takes place, which corresponds to the original  $\bar{\nu}_e$  spectrum as emitted at the source. The second is the opposite case, given by the scenario where all  $\bar{\nu}_e$  will oscillate into  $\bar{\nu}_x$  (Full Flavor Swap, FFS). Fluxes in this case correspond to the expected detected SN neutrino flux at Earth if the true hypothesis for the neutrino mass ordering is the inverted ordering. For the purpose of the analysis developed in this chapter, no flavor conversion will be considered.

#### 4.4 Towards a multi-messenger detection of the next Core-Collapse Supernova: the SNEWS network

If an astrophysical process is driven by non-spherical mass-energy dynamics including quadrupole or higher order contributions, Gravitational Waves (GWs) are emitted together with neutrinos and photons. Such asymmetric magnetohydrodynamic processes are expected to take place in CCSNe, in particular, during the stalled-shock phase previous to the explosion. In fact, these GW emission may be crucial to fully understand the CCSN mechanism.

The latest advances in 3D CCSN simulations have led to a number of gravitational wave signal predictions from these sources [160, 161, 162, 163]. However, there is a large uncertainty on the models leading to different predictions of the GW signal. Despite the lack of knowledge of the exact GW signal, some common features happening in CCSNe have been identified to enhance the GW emission. In some models, a GW signal peak is predicted at the core bounce time for rapidly rotating CCSNe. Simulations also show that the SASI instability might give rise to low frequency gravitational wave emission. Additionally, high-frequency gravitational-wave emission related to the oscillations of the surface of the proto-neutron star (PNS), called g-modes, is also present in simulations.

The current sensitivity of GW detectors is not high enough to detect extragalactic CCSN by themselves due to the small amplitude of the expected signal [164]. Therefore, identifying the core-bounce time or the SASI oscillations with a resolved neutrino light-curve can be helpful to identify a GW counterpart to a CCSN. The detection of GWs from a CCSN could allow to constrain the explosion mechanism, as well as the presence of hydrodynamical instabilities predicting specific features (SASI and g-modes) in the observed signal.

These simulations provide the prediction of the expected GW signal shape in the time-frequency domain. An example is shown in Fig. 4.11, which illustrates the interest of timing the CCSN signal via a prompt neutrino detection in order to achieve a GW detection. Knowing the frequency range in which the signal shows up, as well as having possible hints on the time window where to look at, is specially relevant for GW detectors to reduce their noise. The evolution of the frequency in time also helps to discriminate between the patterns corresponding to different signal sources, and discriminate the GW signal from noise.

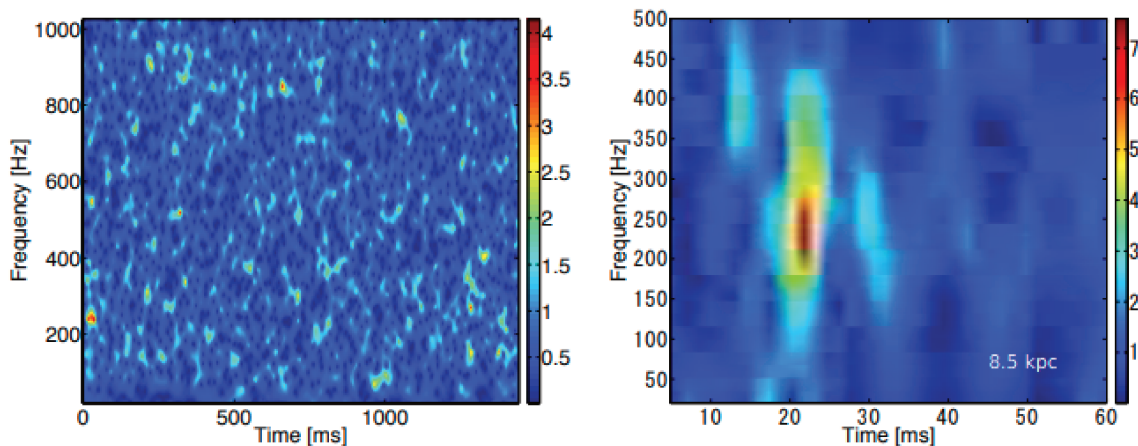


Figure 4.11: Expected observed signal as a function of frequency and time, for a CCSN exploding at 8.5 kpc. The color code corresponds to the signal-to-noise ratio. Left: GW data analysis over window longer than 1 s without a neutrino trigger. Right: GW search over the smaller time-frequency window constrained with the neutrino signal information. Figure from [165].

The time profile of the multi-messenger signals (EM, GW and neutrinos) from a CCSN is illustrated in Fig. 4.12. The aid for a successful multi-messenger observation of a CCSN event is the main goal of the SuperNova Early Warning System. SNEWS is a network of neutrino detectors sensitive to a CCSN signal, that aims at combining the information on the triggers sent by the different experiments that are part of the Collaboration. The requirement for SNEWS to send an alert to the astronomer community is at least two experiments detecting a signal in coincidence (within 10 seconds). Additionally, it requires to each detector that the fake trigger rate is below one fake in eight days in order for the trigger to be processed by SNEWS. This strategy allows to lower the sensitivity threshold for CCSN neutrino searches in each individual detector. Moreover, each experiment can send their own measurement of the arrival time of the signal and/or the source location. This information is shared to the EM and GW observatories, which may help to point to the right place and to achieve a fast response, facilitating the follow-up. KM3NeT has joined SNEWS following the results and developments achieved inside the Collaboration as a part of this thesis work. A schema of the different experiments that collaborate in the SNEWS infrastructure is shown in Fig. 4.13. SNEWS is evolving towards an upgrade (SNEWS2.0), with more detectors joining the network in the near future (DUNE, JUNO, Hyper-Kamiokande, Darkside, NovA, etc.)

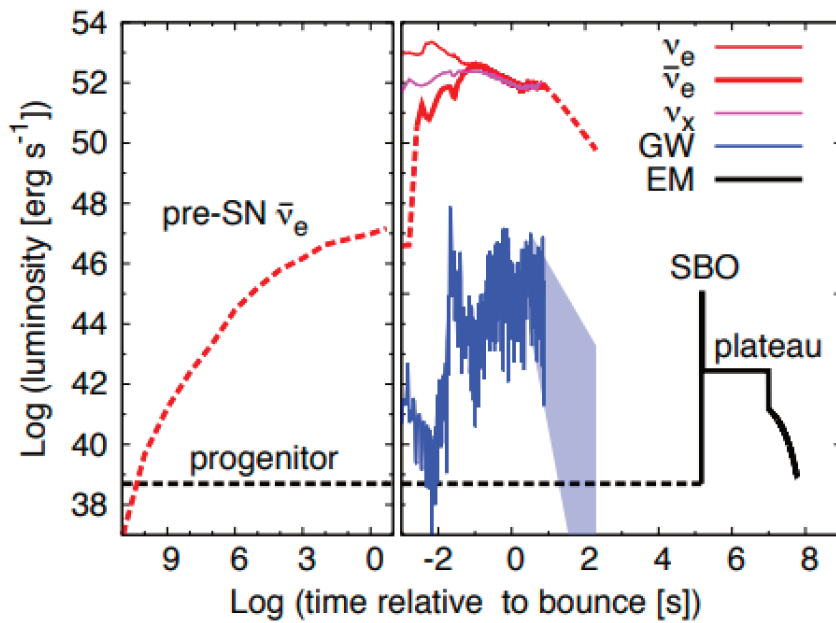


Figure 4.12: CCSN neutrino luminosity, GW luminosity, and electromagnetic luminosity (optical for the progenitor and the plateau, UV X-rays for the shock breakout, SBO) based on a core-collapse two-dimensional simulation of a non-rotating  $17 M_{\odot}$  progenitor. The x-axis shows time relative to the core bounce. The considered CCSN numerical simulation provides the neutrino and GW luminosities up to 7 s after the core bounce. The first is extrapolated up to 200 s based on the GW energy released, estimated using [166, 167]. The physical parameters of the simulation are used to estimate the EM light-curve. The pre-SN emission is taken from [168]. The total energy output emitted after bounce in the form of anti-electron neutrino, photons, and GW is  $\sim 6 \times 10^{52}$  erg,  $\sim 4 \times 10^{49}$  erg, and  $\sim 7 \times 10^{46}$  erg, respectively. See reference [165] for details.

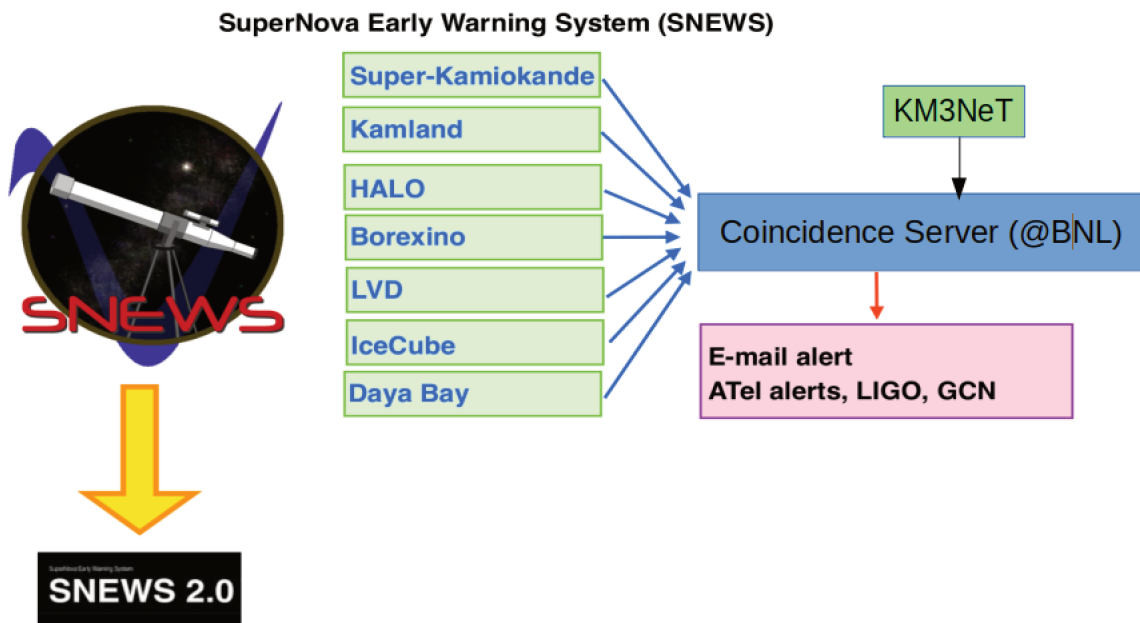


Figure 4.13: Schema of the experiments that are part of the SNEWS Collaboration with the diagram of their interaction with the SNEWS network for alert sending.



# Chapter 5

## CCSN neutrino simulation in KM3NeT

This chapter is devoted to describe the context of CCSN neutrino detection with the KM3NeT neutrino telescopes and explain the detailed simulation of the detector response to CCSN neutrino fluxes that has been developed during this thesis. Moreover, the SNOwGLOBES public software for a fast simulation of the CCSN detection rates is presented.

### 5.1 General context

Although KM3NeT detectors are mainly designed for high-energy neutrino detection, the 10 MeV-scale neutrino signal from a CCSN can be identified as a simultaneous increase of the counting rate in the PMTs of the detector.

The main interaction modes of these MeV neutrinos (see [169]) in water are:

- The interaction with free protons (Inverse Beta Decay, IBD):  $\bar{\nu}_e + p \rightarrow e^+ + n$
- The interaction with free electrons (Elastic Scattering, ES):  $e^- + \nu \rightarrow e^- + \nu$
- The interaction with oxygen nuclei:  $\nu_e + {}^{16}\text{O} \rightarrow e^- + {}^{16}\text{F}$ ,  $\bar{\nu}_e + {}^{16}\text{O} \rightarrow e^+ + {}^{16}\text{N}$

The outgoing electron/positron produced through these interactions radiates Cherenkov light that can be detected by the PMTs. The length of the Cherenkov track released is some centimetres. In particular, IBD interactions lead to charged particle tracks of about  $0.5 \text{ cm} \times \frac{E_\nu}{\text{MeV}}$  length [170].

Event reconstruction is not possible due to the short track length of low energy positrons/electrons produced in MeV neutrino interaction compared to the large distance between the DOMs. However, a supernova neutrino burst should produce a collective increase of PMT rates in the whole detector.

Using the simulation described in this chapter, the goal of chapter 6 will be to evaluate the discrimination power between this MeV neutrino signal and main background sources, which have been described in section 3.1. The optical background due to  ${}^{40}\text{K}$  decays in sea water and bioluminescence can be significantly reduced by using nanosecond coincidences between the nearby placed PMTs (as explained in section 3.1). This technique has been tested with the ANTARES telescope [171], consisting of storeys with three 10-inch PMTs (see section 2.2), and has been optimised for the KM3NeT telescope where the directional DOMs containing 31 3-inch PMTs provide better background rejection power. Atmospheric muons represent also a source of background for this measurement.

The Cherenkov photons from CCSN neutrinos can be detected by the KM3NeT DOMs as hits on single PMTs or coincidences between multiple PMTs on the same DOM. A coincidence is defined as a sequence of hits on the same DOM within a predefined time window. The number of PMTs in a DOM detecting a hit within 10 ns is called *multiplicity* ( $M$ ). As a generalisation, coincidences and single hits are from now on referred as *events* with multiplicity  $M = 1$  for single hits and  $M \geq 2$  for coincidences.

## 5.2 MeV neutrino interactions in sea water

In this section, we go into the details of the Monte Carlo simulation framework for low-energy neutrino generation developed during this thesis work (called *lenugen*, see section 3.4). The aim is to estimate the number of CCSN neutrino events that will interact in our detector as a function of the neutrino energy and time and to build the interaction rates. For this, two ingredients are needed: the fluxes as a function of energy and time (as predicted by the 3D CCSN Garching models, given in section 4.3), and the interaction cross section of each interaction channel.

### 5.2.1 Computing the interaction rates

As stated in section 5.1, MeV CCSN neutrinos can undergo three different interactions: Inverse Beta Decay (IBD), Elastic Scattering (ES) and neutrino interactions with oxygen nuclei. They account for about 97%, 3% and less than 1% of the interactions, respectively. Therefore, KM3NeT will be sensitive mainly to the  $\bar{\nu}_e$  signal detected indirectly via IBD interactions.

Indeed, the elastic scattering interaction cross section is well lower than the one of IBD. Moreover, the outgoing electrons producing the Cherenkov light have a lower energy (about 1 MeV) compared to the IBD positrons, making it difficult to get a detected photon from this interaction. As regards the interaction with oxygen nuclei, its energy threshold is higher due to the higher mass of oxygen compared to protons and electron. Therefore, the probability of this interaction occurring at the typical CCSN energies over the accretion phase (1-30 MeV) is significantly lower than the one of IBD, as inferred from Fig. 5.1.

Because the KM3NeT detector is mainly sensitive to IBD interactions, whose emission takes place predominantly during the accretion phase, and three-dimensional simulations only include this time window (see section 4.3), which lasts about half a second, the focus will be placed for the subsequent study on this time window. The burst contribution only accounts for  $\sim 1$  per mille of the total detected signal in KM3NeT, while the cooling can bring up to about 20% of the detected events. Therefore, increasing the time window would only degrade the sensitivity to these MeV neutrinos.

Only charged particles will produce light observed in water Cherenkov detectors. Due to the low energy and short length of the tracks released by CCSN neutrino interactions, no secondary particles will lead to additional leptons inducing detectable light. Therefore, only the primary lepton is simulated in the framework discussed.

In the current simulations, cross sections are computed from the latest models available for this energy range for the IBD and ES interactions [172, 173]. For the neutrino interactions with oxygen, we use cross sections from the tables used by SNOwGLoBES [174].

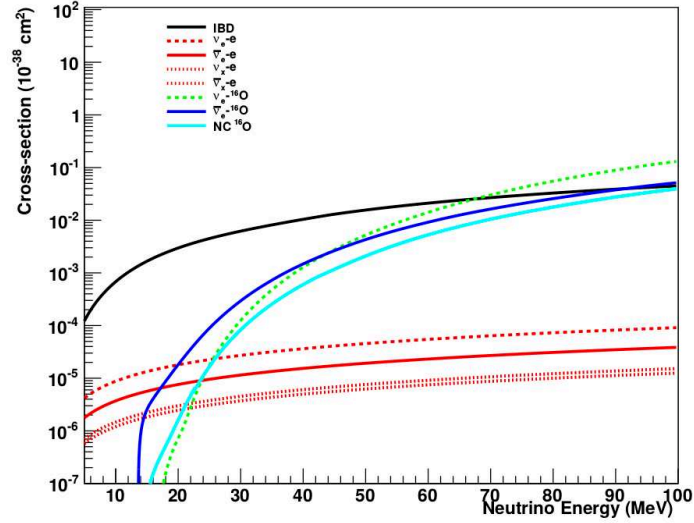


Figure 5.1: Cross sections of neutrinos in water for the different interaction modes.

For the simulation of the outgoing particles, we use the angular differential cross sections, shown in Figure 5.2, to account for the directionality dependence of their energy. In practice, the angular dependent lepton spectrum is used for getting the information of each interaction (energy, direction and interaction mode). The positron energy in the IBD processes is calculated as indicated in [172]:

$$E_e = \frac{(E_\nu - \Delta m)\left(1 + \frac{E_\nu}{m_p}\right) + \frac{E_\nu}{m_p} \cos\theta \sqrt{(E_\nu - \Delta m)^2 - \frac{m_e^2}{\kappa}}}{\kappa}, \quad (5.1)$$

where,  $m_e$  is the mass of the electron,  $m_p$  the mass of the proton,  $E_\nu$  the energy of the incoming neutrino,  $\theta$  the scattering angle, i.e. the angle between the incoming  $\nu$  and the outgoing lepton,  $\Delta m = \frac{m_n^2 - m_p^2 - m_e^2}{2m_p}$  and  $\kappa = \left(1 + \frac{E_\nu}{m_p}\right)^2 - \left(\frac{E_\nu}{m_p} \cos\theta\right)^2$ . The ES electron energy is given by the following expression, derived in [173]:

$$E_e = \frac{m_e \left(1 + \frac{E_\nu}{m_e}\right)^2 + \frac{E_\nu^2 \cos^2\theta}{m_e}}{\left(1 + \frac{E_\nu}{m_e}\right)^2 - \left(\frac{E_\nu}{m_e} \cos\theta\right)^2}. \quad (5.2)$$

Figure 5.3 shows the cross section as a function of the neutrino energy integrated over all scattering angles, for the IBD (left) and ES (right) interactions, respectively.

The total cross section is obtained by integrating the differential cross section in energy and over the possible scattering angles. Finally, the interaction rates, shown in Figure 5.4, are computed for the accretion phase using the above-mentioned flux and the integrated cross sections with the following relation:

$$R_{int}(\text{MeV}^{-1}\text{s}^{-1}) = \sigma(\text{cm}^2) \times \text{flux}(\text{cm}^{-2}\text{MeV}^{-1}\text{s}^{-1}) \times N_{\text{target}} \quad (5.3)$$

where  $N_{\text{target}}$  is the number of protons, electrons or oxygen nuclei (depending on the considered interaction channel) in a reference water detection volume, which is arbitrary taken as equal to 100 kton.

For the neutrino interactions with oxygen, the angular dependence is taken into account using the kinematics of the interaction. The 2D distributions obtained for  $\nu_e + {}^{16}\text{O}$  and  $\bar{\nu}_e + {}^{16}\text{O}$  interaction rates are shown in Figure 5.5 for a 100 kton water detector.

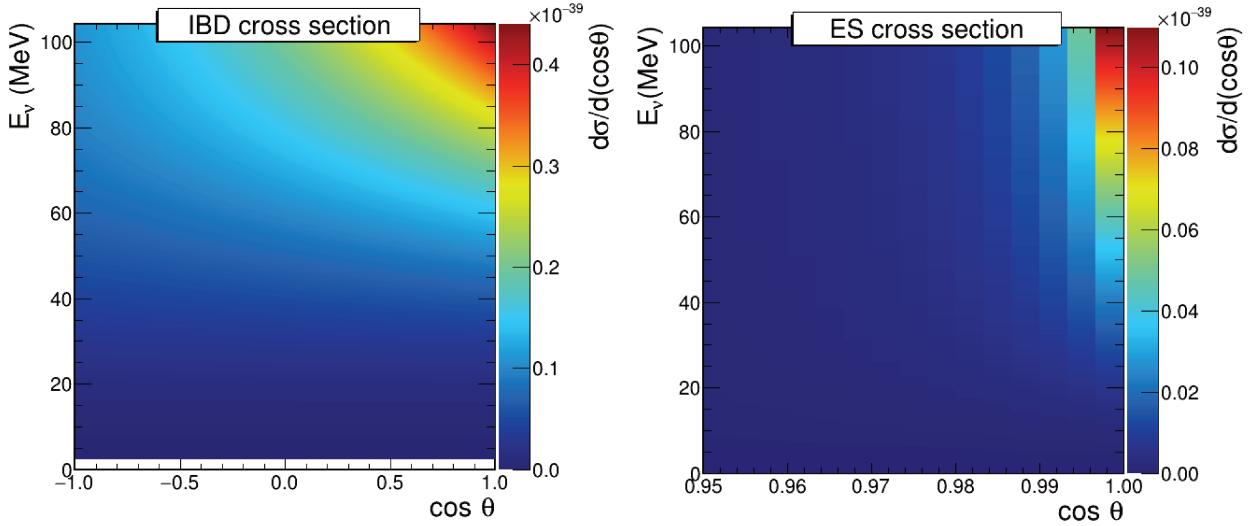


Figure 5.2: IBD (left) and ES (right) cross sections as a function of the neutrino energy ( $E_\nu$ ) and the scattering angle ( $\theta$ ).

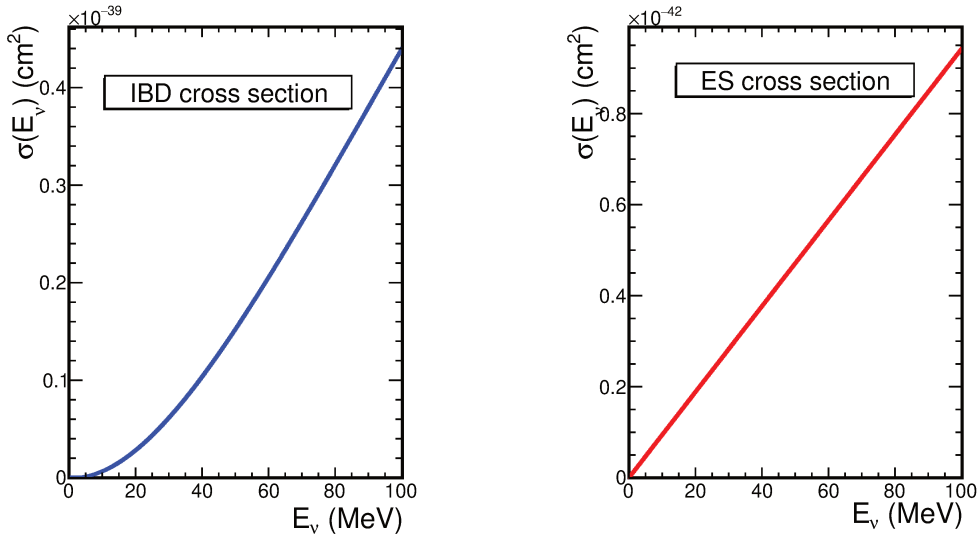


Figure 5.3: IBD (left) and ES (right) cross sections as a function of the neutrino energy ( $E_\nu$ ) integrated over all possible scattering angles.

## 5.2.2 Simulation of the neutrino interactions in the KM3NeT detector

SN neutrino interactions are then simulated following these interaction rates uniformly inside a chosen volume where interactions are generated, called the generation volume ( $V_{gen}$ ). This generation volume has to be optimised so that no signal efficiency is lost in the simulation if the volume is chosen too small, as we will see in section 5.2.3.

In order to optimize the computing time, interactions are simulated around one DOM instead of over the full detector. Then, a simple scaling for the total number of active DOMs is applied for estimations at the full-detector scale. This can be done due to the low energy of these neutrinos that will only produce detectable light locally, if they interact close to a DOM. Because of the geometry of the DOM,  $V_{gen}$  was considered as a spherical volume for the simulation of one KM3NeT DOM.

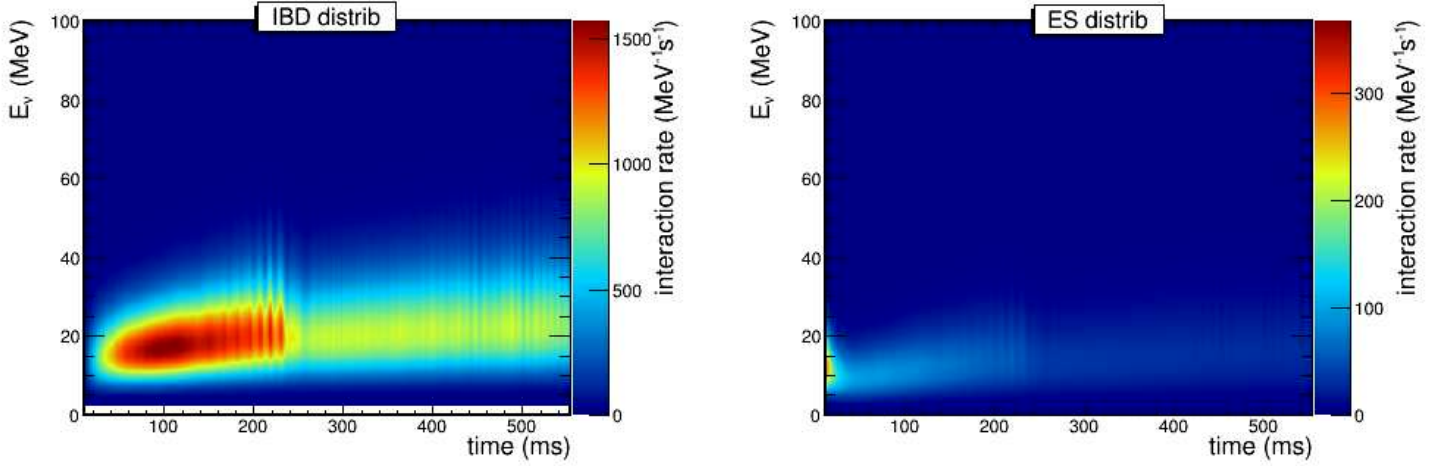


Figure 5.4: IBD (left) and  $\nu_e$  ES (right) interaction rates in a 100 kton water detector.

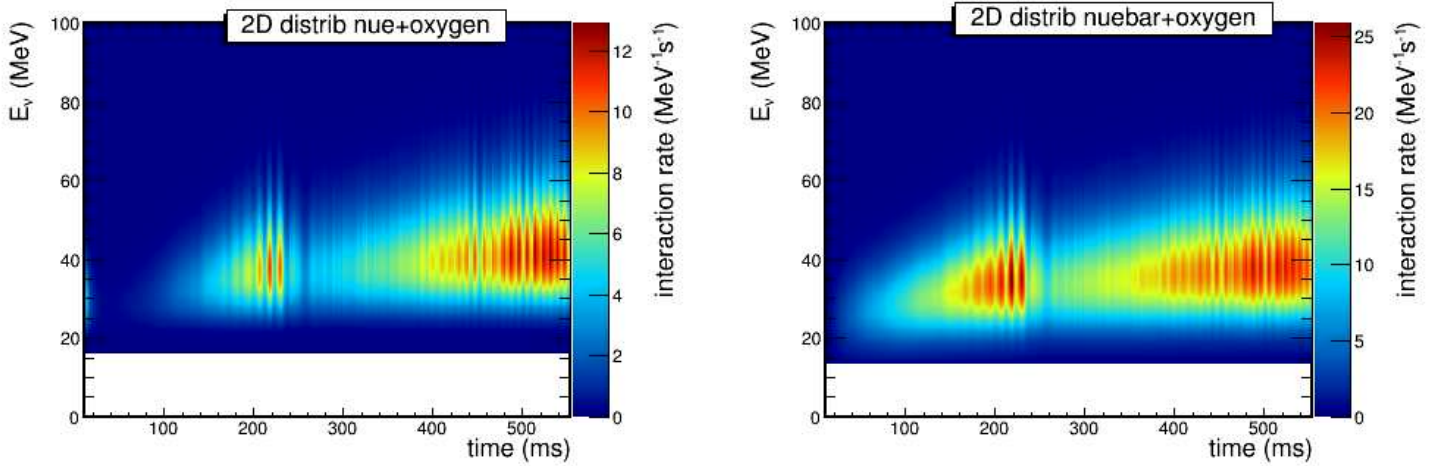


Figure 5.5: Interaction rates in a 100 kton water detector. Distribution for  $\nu_e + {}^{16}\text{O}$ , (left) and  $\bar{\nu}_e + {}^{16}\text{O}$  (right) interactions.

The output of the simulation contains the information about the incoming neutrino and the outgoing particles for each generated interaction. Following this step, the Geant4 event-by-event simulation KM3sim (see section 3.4 or ref. [123]) is used to propagate these particles inside the detector, and simulate the Cherenkov light production and detection. The DOM model in KM3Sim defines each PMT as a flat disc, and includes the full PMT description through a detailed parametrisation of the angular PMT acceptance and the PMT quantum efficiency (QE). The photon detection efficiency is calculated by detailed simulations for each incident angle and wavelength.

The output light files are processed through different steps with the KM3NeT software, called Jpp [175] for the complete simulation of the detector response. First, *JAANeTPreProcessor* removes all the interactions for which there is no hit PMT and converts the KM3Sim files into root format. Then, *JEventTimesliceWriter* (JETW) simulates the PMT response, generating the "real hits" (i.e., observed p.e.) from the MC photons, and providing the time-over-threshold (ToT) information. Here, photons impinging in coincidence on the same PMT are merged. The output MC data format is converted at this stage into the same as the sea data format used by the DAQ. The data are structured in *Timeslices*, which are time segments of 100 ms duration (see section 2.3.2). In fact, JETW is equivalent to *JTriggerEfficiency*, described in section 3.4.3, but without applying the triggers, and with the possibility of keeping the MC time ordering information of the simulated events. Finally, *JMonitorMultiplicity* is used to build time coincidences between the different PMTs in a DOM.

In this framework, all simulated neutrinos are forced to interact, since significant MC statistics is needed, and the input interaction rates are provided for a reference detection volume. Therefore, a scaling factor must be applied to the output MC hits in order to reproduce the total number of events that will be observed in the KM3NeT detector from a CCSN event emitting a given neutrino flux, noted  $N_{det}$  and given by Eq. 5.4:

$$N_{det} = N_{MC} \cdot \frac{N_{SN}}{N_{gen}} \cdot \frac{(\rho_{water} \cdot V_{gen})}{10^8 \text{ kg}} \cdot N_{DOM}, \quad (5.4)$$

where  $N_{MC}$  is the number of events in the output of the Monte Carlo simulation (observed hits),  $N_{gen}$  the total number of generated neutrinos,  $N_{SN}$  the total number of CCSN neutrinos interacting in a reference water mass of 100 kton (volume of  $10^5 \text{ m}^3$ ) from a source distance of 10 kpc,  $\rho_{water} \cdot V_{gen}$  the mass of the chosen generation volume and  $N_{DOM}$  the number of DOMs of the detector. The first factor accounts for the simulated statistics compared to the number of neutrinos expected to interact from a CCSN at a given simulated distance. The second factor is for the correction of the simulation reference volume (100 kton) to the KM3NeT effective detection volume.

The values obtained are  $N_{SN} = 3964$  for the  $11 M_{\odot}$ ,  $N_{SN} = 12930$  for the  $27 M_{\odot}$ , and  $N_{SN} = 32562$  for the  $40 M_{\odot}$ . For the neutrino generation, the contribution of the salinity to the seawater density is neglected and  $\rho_{water}$  is assumed as equal to the pure water density,  $\rho_{water} = 10^3 \text{ kg} \cdot \text{m}^{-3}$ . The effect of the salinity is taken into account at the light propagation stage and simulated by KM3Sim.

For the estimate of the sensitivity in chapter 6, a fixed time window of 500 ms will be used for all progenitors. Therefore, the numbers provided in the previous paragraph have to be rescaled to evaluate signal expectation in this window. For the  $11 M_{\odot}$  progenitor, this is done by artificially extending the tail of the signal, assuming a constant interaction rate between 340 and 500 ms. For the 27 and  $40 M_{\odot}$  progenitors, the number of signal events within 500 ms is computed from the integral of the total interaction rate in the first 500 ms of the simulation. The numbers become then:  $N_{SN} = 5657$  for the  $11 M_{\odot}$ ,  $N_{SN} = 12216$  for the  $27 M_{\odot}$ , and  $N_{SN} = 30852$  for the  $40 M_{\odot}$ .

### 5.2.3 Optimisation of the generation volume $V_{gen}$

The generation volume has been optimised in order to maximise the expected CCSN neutrino rates inside it. The optimization is performed using the double coincidence selection: events that give at least 2 hits within 10 ns in two different PMTs of the same DOM. This choice is made because if  $V_{gen}$  is optimised for double coincidences, no signal efficiency will be lost either for higher multiplicities, and single simulation can be used to explore all possible selections.

CCSN neutrino rates have been computed for different radii of the sphere from the complete Monte Carlo simulation. The results are shown in Figure 5.6. A saturation is reached at  $r = 20 \text{ m}$  for events producing at least two hits, hereafter referred to as double coincidences. The choice of a 20 m radius is conservative when events with higher number of hits are considered, as the optimal radius decreases with the coincident number of hits generated by one single neutrino event. Coincidences between different events are not probable to happen due to the distance between the CCSN interactions being larger than  $\mu\text{s}$ .

Note that the optimal generation volume obtained is larger than the distance between optical modules in KM3NeT/ORCA. This means that some photons will be detected and shadowed by another DOM, closer to the interaction vertex, which effect is not taken into account in the simulation. In fact,

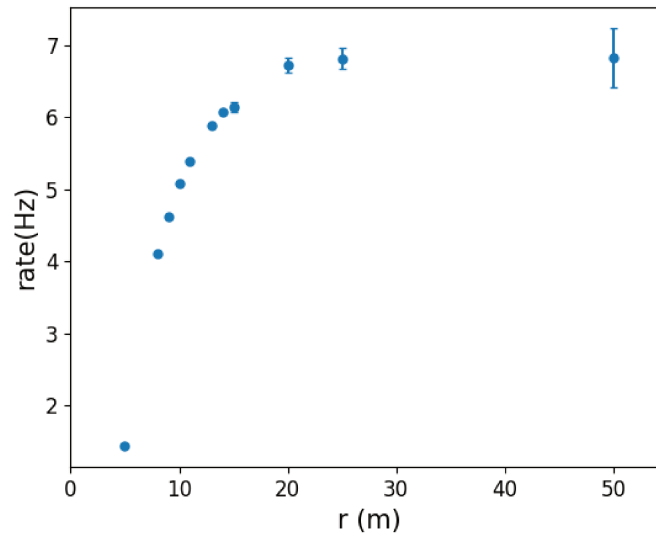


Figure 5.6: SN detection rates for events producing at least two hits (double coincidences) as a function of the radius of the generation sphere.

each DOM shadows an area of  $\sim 0.15 \text{ m}^2$  on a spherical surface of  $\sim 10^3 \text{ m}^2$  (at 9 m radius), which accounts for a negligible ( $\sim 0.3$  per mille) percentage of the solid angle, which shown that the shadowing effect is negligible.

### 5.3 Lightcurve simulations of background and CCSN neutrinos

The time profile of CCSN neutrinos can provide important information and help to reveal the unknowns on the explosion mechanism and the properties of both neutrinos and the astrophysical object (e.g., the neutron star and progenitor mass and radius), as well as on the arrival time information, among others. Therefore, the neutrino lightcurve is an important key for constraining the models in the scenario of a multi-messenger observation of a CCSN. To reach this aim and have a good resolution of the neutrino time profile, high event statistics are needed.

In this section, the approach to build the signal lightcurve and the treatment of the background on the millisecond time scale are described. The lightcurve simulation can be performed, both for signal and background, for different multiplicity and coincidence time window selection. For illustration, all coincidences with at least two hits within 5 ns are considered in the following.

#### 5.3.1 Run-by-run MC simulation of background single rates from raw data

The raw data available for 1-2 DUs detector configurations, for ORCA and ARCA, are used to emulate the background of an arbitrarily-sized detector. In this view, single DU data already provide information on the vertical space correlation, i.e. background events contributing to the double coincidence rate of several DOMs in a line are taken into account in the simulation. Horizontal space correlations are instead emulated using the correlation of contiguous time intervals. In other words, the effect of a background event illuminating some lines more than others and changing the total double coincidence rate of the full detector, is expected to be seen by another set of DOMs shifted in time. Therefore, it is taken into account by considering consecutive time intervals with background conditions moving in time, similarly to as it will evolve across lines in the detector.

In practice, the background for a time bin in a detector of  $N$  DUs is simulated integrating over  $N/n$  time bins of the measured background with  $n = 1, 2$  DUs. By default, the  $N/n$  time bins are chosen as a continuous sequence of the original data, but additional randomisation can be added to reduce the amount of correlations in the output. An example of the measured lightcurve applying a coincidence selection with 5 ns window is shown in Fig. 5.7, for ORCA (right) and ARCA (left).

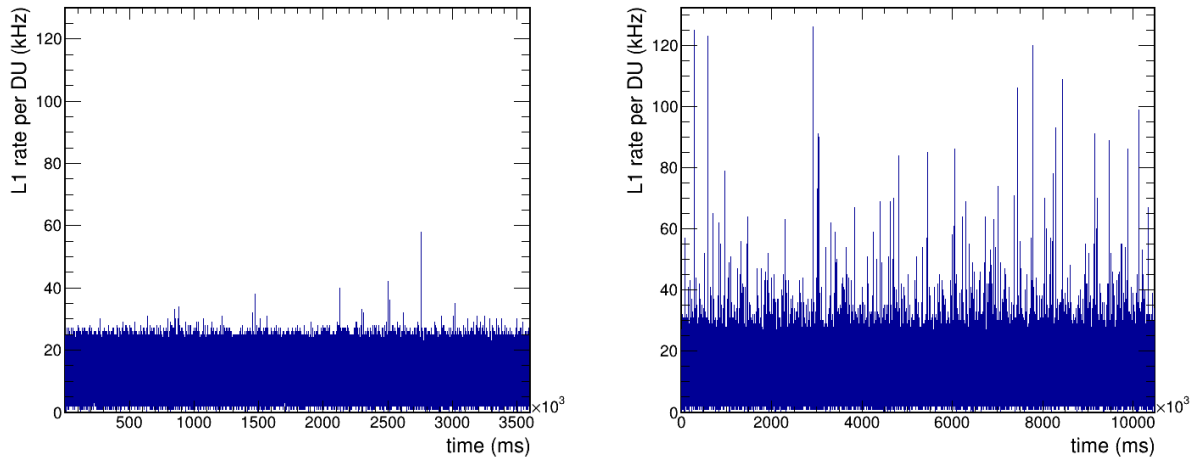


Figure 5.7: Example of background lightcurves measured from raw data, sampled with a 1 ms binning. On the left for ARCA, on the right for ORCA. They are generated with a selection of 5 ns L1 coincidences. The spikes observed in ORCA data (not observed in ARCA due its deeper location and the larger distance between the DOMs, which prevent to detect such coincidences) are correlated at sub-ms scale and thus may be induced by correlated muon coincidences.

### 5.3.2 CCSN neutrino lightcurve using L1 data

The simulation of the different stellar progenitors are used to compute the CCSN neutrino lightcurve, with masses:  $40 M_{\odot}$ ,  $27 M_{\odot}$  and a  $20 M_{\odot}$ . From the output of the *lenugen* simulation, the number of detected events for each time bin  $i$ ,  $N_{det}[i]$  is estimated in analogy with equation 5.4:

$$N_{det}[i] = \frac{N_{MC}[i]}{N_{gen}} \cdot \frac{N_{SN}}{10^8 \text{ kg}} \cdot (\rho_{\text{water}} \cdot V_{gen} \cdot N_{DOM}) \quad (5.5)$$

where  $N_{MC}[i]$  is the number of events in the simulation output for the time bin  $i$  (events per bin) and  $\rho_{\text{water}}$  the water density.  $N_{MC}[i]$  follows the time distribution of the generated neutrino spectrum.

## 5.4 Parametrisation of the detector response and SNOwGLoBES

SNOwGLoBES stands for Supernova Neutrino Observatory with GLoBES, and it is a public software available under the GitHub repository: <https://github.com/SNOwGLoBES/snowglobes>. It allows to compute the detection rates for different experiment configurations using a smearing matrix to simulate the detector response for a given CCSN neutrino flux model [174].

The work done to implement the KM3NeT detector into SNOwGLoBES is presented here. This work has been performed to provide an easy and fast way of estimating the expected number of CCSN neutrinos detected by the different neutrino detectors involved in the SNEWS collaboration. The MC framework presented before is a proprietary code belonging to KM3NeT and is not dedicated to be used outside the Collaboration.

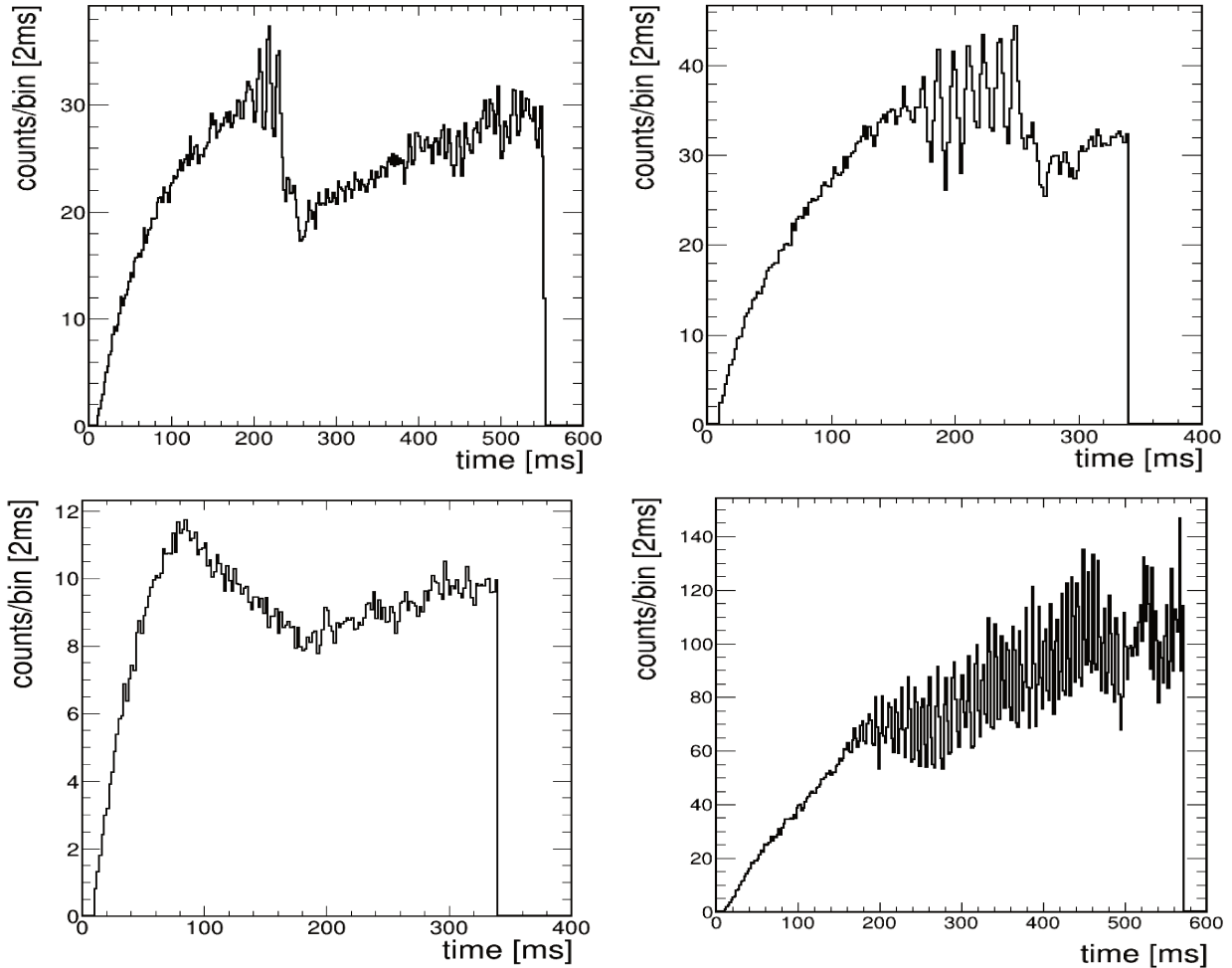


Figure 5.8: The detected neutrino lightcurve in 1 KM3NeT block for a CCSN signal at 10 kpc. Four different progenitor masses are considered:  $27 M_{\odot}$  (top left),  $20 M_{\odot}$  (top right),  $11 M_{\odot}$  (bottom left) and  $40 M_{\odot}$  (bottom right).

The parametrization of the KM3NeT experimental response using the knowledge from the detailed simulation in section 5.2 allows to evaluate the expected detected signal in an immediate way without the need of going through the full and computationally expensive simulation each time one wants to consider a different model.

To include KM3NeT into SNOwGLoBES, we provided the efficiency as a function of the lepton energy, as well as the generation volume. The generation volume is a sphere of 20 m radius around each DOM, corresponding to a detector mass of 69 Gt per instrumented KM3NeT block.

In order to parametrise the detector response of KM3NeT, the dedicated simulation presented in section 5.2 is used. The procedure is the following:

1. Evaluate the number of generated events interacting in the detector as a function of the lepton or the neutrino energy.
2. Evaluate the number of events producing at least two hit PMTs in the simulated KM3NeT DOM, for the optimised generation volume ( $V_{gen}$ ).
3. Determine the efficiency as function of the neutrino (or lepton) energy. The efficiency being defined as the ratio of detected to interacting events.

4. Evaluate the PMT response through JPP using JEventTimesliceWriter and JMonitorMultiplicity. This effect is not dependent on the energy.
5. The ratio of events after to before JPP processing is applied as a correction to the efficiency since there is no energy information event by event in JPP for non-triggered events. This efficiency correction ( $\text{Eff}_{\text{corr}}$ ) is given in Table 5.1 as a function of the multiplicity.

Table 5.1: Efficiency correction that accounts for the PMT response (and QE) after JPP processing as a function of the multiplicity. These values are computed with a x1.5 light factor used for km3sim.

Multiplicity	2	3	4	5	6	7
$\text{Eff}_{\text{corr}}$	0.539	0.512	0.490	0.465	0.434	0.402

Figure 5.9 shows the KM3NeT efficiency as a function of the lepton energy above multiplicity 2.

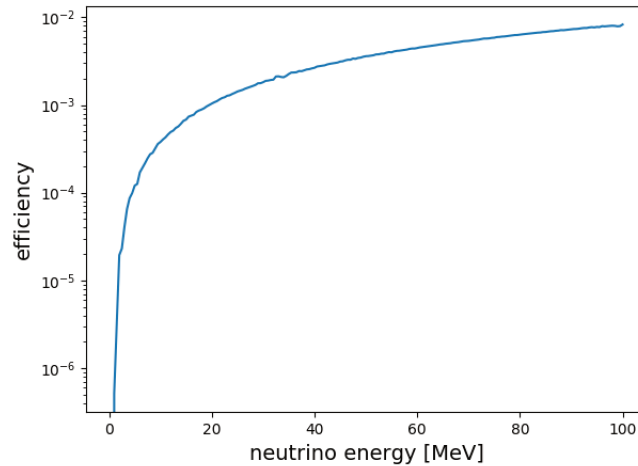


Figure 5.9: KM3NeT efficiency as a function of the lepton energy for events above  $M=2$ .

Then, the smearing matrices have been calculated with the scripts provided in the SNOwGLOBES package. The smearing matrices are computed as a pure kinematic mapping between the lepton and the neutrino energy for the different channels (IBD and ES). Interactions with oxygen nuclei are not considered since their contribution is negligible and the smearing matrix to be used for KM3NeT in order to include them was not available in SNOwGLOBES.

Applying the efficiency  $\frac{N_{\text{det}}}{N_{\text{gen}}}$  as a function of neutrino energy, and its corresponding correction ( $\text{eff}_{\text{correction}}$ ) for each multiplicity, the detector effective mass can be evaluated for each  $M$  selection:

$$M_{\text{eff}} = \frac{N_{\text{det}}}{N_{\text{gen}}} \times \text{eff}_{\text{correction}} \times V_{\text{gen}} \times \rho_{\text{water}} \quad (5.6)$$

In this way, by convolving the effective mass as a function of the neutrino energy with the neutrino interaction rates (also as a function of energy) in section 5.2, one gets directly the KM3NeT detection rates including the detector response effects evaluated with the dedicated simulation in section 5.2. The total number of detected events expected for a considered model is given by the total integral (in energy and time) of the detection rates.

The total effective mass is computed as an average over energy, and changes with the progenitor/model spectrum. The effective mass as a function of the multiplicity is provided for three different progenitors of  $11 M_{\odot}$ ,  $27 M_{\odot}$ , and  $40 M_{\odot}$ , with different average energy. As shown in Table 5.2, the KM3NeT efficiency also depends on the multiplicity selection applied. The effective mass of a KM3NeT 115-lines instrumented block is 40-70 kton for all coincidences and 1-3 kton for coincidences with six or more hit PMTs.

Table 5.2: Effective mass for a KM3NeT detection block as a function of the multiplicity for the  $11 M_{\odot}$  ( $\langle E_{\nu} \rangle = 13.7$  MeV),  $27 M_{\odot}$  ( $\langle E_{\nu} \rangle = 15.7$  MeV) and  $40 M_{\odot}$  ( $\langle E_{\nu} \rangle = 18.2$  MeV) progenitors.

<b>Multiplicity</b>	<b>2</b>	<b>3</b>	<b>4</b>	<b>5</b>	<b>6</b>	<b>7</b>
$11 M_{\odot}$	$40 \pm 4$	$12 \pm 3$	$5 \pm 1$	$2.5 \pm 0.6$	$1.3 \pm 0.4$	$0.6 \pm 0.2$
$27 M_{\odot}$	$53 \pm 5$	$16 \pm 3$	$7 \pm 1$	$4.0 \pm 0.9$	$2.0 \pm 0.6$	$1.0 \pm 0.4$
$40 M_{\odot}$	$67 \pm 7$	$21 \pm 4$	$9 \pm 2$	$5 \pm 1$	$2.7 \pm 0.8$	$1.5 \pm 0.5$



# Chapter 6

## Detecting CCSN neutrinos with KM3NeT

This chapter is dedicated to the detection method and performance of the KM3NeT detectors to MeV CCSN neutrinos. The signal and background characterization, the noise rejection strategies and the systematic uncertainties on the analysis will be provided. Both the real-time (online) capabilities and the performances from a refined dedicated search (offline) for the detection of the CCSN neutrino signal in KM3NeT will be described.

### 6.1 Signal and background

Recapitulating from sections 5.1 and 3.1, the MeV neutrino signal from a CCSN will be identified as an overall increase of the detection rate. The multiplicity distribution of signal events can be compared with those of the background sources, which are bioluminescence, radioactive decays in sea water (and in the DOM glass) and atmospheric muons. This is used to identify the different contributions and reject what does not look like CCSN neutrinos.

On this analysis, the signal is estimated from 3D CCSN simulations (described in section 4.3) while the background is measured from data. The CCSN simulations provided by the Garching group have a limited duration, covering only the accretion phase. Table 6.1 reports the expected number of detected events from a CCSN neutrino flux as a function of the multiplicity for three considered stellar progenitors, with masses of  $40 M_{\odot}$ ,  $27 M_{\odot}$  and  $11 M_{\odot}$ , at a reference distance of 10 kpc.

Table 6.1: Expected number of signal events as a function of the multiplicity for one building block. Statistical uncertainties from the Monte Carlo simulation are reported in parentheses.

Multiplicity	2	3	4	5	6	7	8	9	10	11
$N_{ev} 11M_{\odot}$ (340 ms)	1119(3)	258(1)	100.4(8)	48.9(5)	25.8(4)	13.3(3)	7.2(2)	3.4(1)	1.29(8)	0.50(5)
$N_{ev} 27M_{\odot}$ (543 ms)	4806(9)	1120(5)	442(3)	218(2)	116.0(15)	64(1)	35.2(8)	19.4(6)	8.0(4)	1.9(2)
$N_{ev} 40M_{\odot}$ (572 ms)	15240(30)	3650(10)	1449(8)	723(6)	399(4)	226(3)	127(2)	69.5(18)	36.6(13)	15.0(8)

As already mentioned, the background of single hits (L0s in section 3.3) is dominated by radioactive decays, accounting for typical rates of 200 – 250 kHz per DOM. The rates are also subject to significant diffused or local increases due to bioluminescence activity. These features make very difficult to exploit this channel for the CCSN detection. Coincidences are in general given by different types of Cherenkov light emissions. Radioactive decays (mostly  $^{40}\text{K}$ ) dominate at low multiplicities, with a rate that roughly follows the empirical expression that has been derived in the Collaboration from the first

data analysed:

$$R_{40K} = (\sim 500) \cdot 10^{2-M} \text{ Hz.} \quad (6.1)$$

Atmospheric muons typically produce tracks that can cross the entire volume of the detector, being detectable as coincidences on multiple DOMs.

The available data from the lines deployed in the sea comes from a 2 DU configuration for ARCA (ARCA2) and 4 DU configuration for ORCA (ORCA4). The measured multiplicity rates in these configurations are given in Fig. 6.1, where the two different background components can be identified. In Fig. 6.2 the measured rates as a function of the multiplicity are shown and compared to the simulated signal rates.

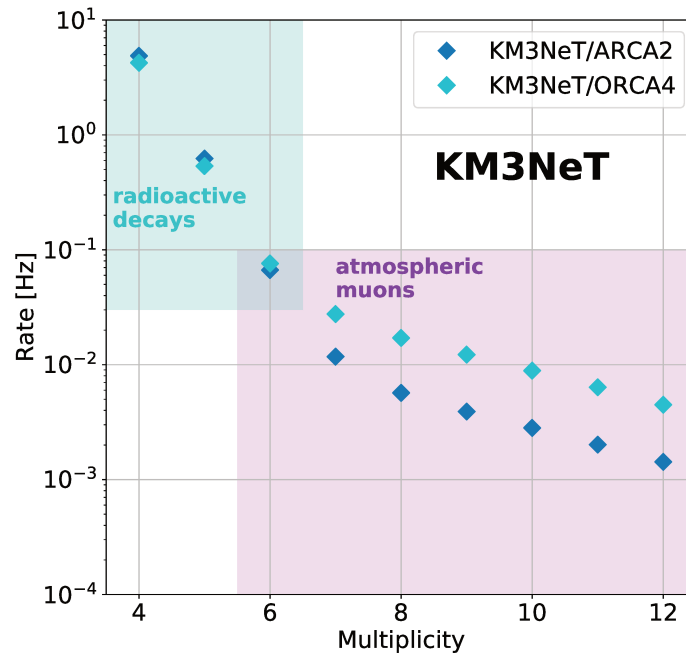


Figure 6.1: Average DOM rates as a function of the multiplicity measured with the KM3NeT ARCA2 and ORCA4 detectors. Statistical errors are included, but are smaller than the markers. The multiplicity range shown covers the most relevant region for CCSN neutrino detection.

Figure 6.2 shows the comparison of the simulated signal expectation and measured background rates. The best signal-to-background ratio is achieved above  $M=6$ , and will be optimised in section 6.6.3. In this region, the contribution from atmospheric muons starts to overtake the one from radioactive decays, and some muon rejection algorithms can be adopted to further reject this atmospheric background component. In the following, signal and background will be characterised and the optimised selection for the CCSN neutrino sensitivity of KM3NeT is presented leading to a final evaluation of the KM3NeT detection performance.

## 6.2 Background rejection

The correlation of coincidences between different DOMs on a  $\mu\text{s}$  time scale can be used to reduce the muon background, as shown in subsection 6.2.1. PMT afterpulses can also produce spurious coincidences that result in multiple counting of the same event. They can be easily suppressed due to their correlation on a  $\mu\text{s}$  timescale with the genuine event.

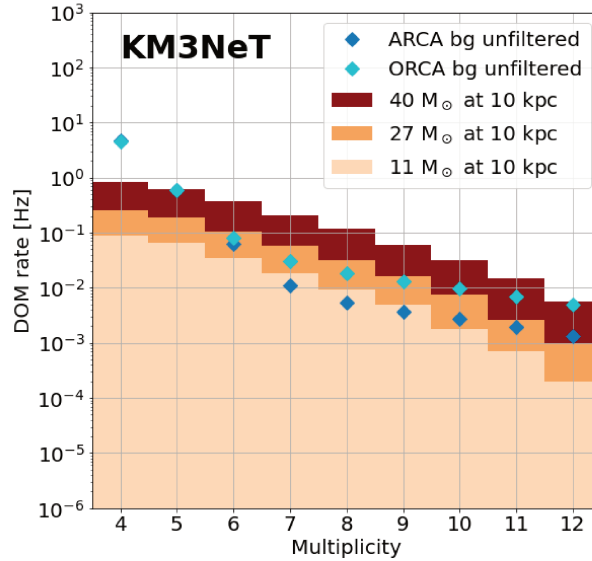


Figure 6.2: DOM event rates as a function of the multiplicity for ORCA (light blue dots) and ARCA (dark blue dots) backgrounds from measurements. Superimposed, the CCSN signal at 10 kpc for the  $40 M_{\odot}$  (dark red filled), the  $27 M_{\odot}$  (orange filled) and the  $11 M_{\odot}$  (beige filled) progenitors, obtained from simulations. The signal values correspond to the average rate over the accretion phase.

The dedicated trigger algorithms in KM3NeT (see section 3.3) are designed to identify a minimum number of causally connected hits within extended cylindrical sections (*track-like*) or localised spherical sections (*shower-like*) of the instrumented volume [21]. Therefore, triggered events, dedicated to select physical events at higher energies, can be used as a background filter in the search for MeV neutrinos, as explained in subsection 6.2.2.

### 6.2.1 Muon rejection: coincidence correlation

The great majority of CCSN neutrino interactions are detected on a single DOM. The signal contribution over multiple DOMs is found to be negligible ( $< 0.01\%$ ) for events at  $M \geq 6$ .

On the contrary, Cherenkov tracks induced by atmospheric muons are likely to produce coincidences over multiple DOMs in a time interval determined by the time of flight of the muon across the detector volume. This interval ( $\tau_{veto}$ ) is estimated to be around  $1 \mu s$  for ORCA and  $3 \mu s$  for ARCA.

These features are exploited in a muon rejection algorithm operating as follows:

1. coincidences with  $M < 4$  are discarded;
2. clusters are defined with the group of remaining coincidences in the veto window,  $\tau_{veto}$ ;
3. clusters containing coincidences on more than one DOM are discarded.

Each of the remaining clusters consists of one or multiple coincidences on the same DOM. The latter can be the product of spurious coincidences due to afterpulses. In this case, the cluster is counted as a single event with multiplicity equal to the highest multiplicity observed in the cluster. In case of multiple coincidences with the same highest multiplicity, the event time is taken from the first.

Event rates for multiplicities  $\geq 4$  are obtained for ORCA4 and ARCA2 detectors. The rejection efficiency, given by the ratio of the number of background events before and after the filter, is given in

Table 6.2 for each multiplicity. The ORCA background rate for  $M \geq 6$  is only slightly higher than the residual radioactivity contribution (0.05 Hz), confirming an excellent performance.

Table 6.2: Rejection efficiency of the coincidence correlation filter in ARCA2 and ORCA4.

Multiplicity	4	5	6	7	8	9	10	11	12
ARCA2	0.4%	2%	9%	21%	24%	24%	24%	24%	25%
ORCA4	4%	21%	67%	90%	95%	95%	96%	96%	96%

A signal event from a CCSN neutrino interaction will be vetoed if occurring within  $\pm\tau_{veto}$  from the time of any background coincidence with multiplicity  $\geq 4$ . The coincidence rate per DOM with  $M \geq 4$  being equal to 5 Hz, the corresponding dead time fraction is  $2 \cdot \tau_{veto} \cdot R_{M \geq 4} \cdot N_{DOMs}$  totalling 2% for a full ORCA-like building block and 6% for a full ARCA-like building block. Simulations show that veto fraction due to two coincident signal events is less than 1 per mille of the detected CCSN interactions.

The rejection efficiency in ARCA is limited by the relation between maximum multiplicity and distance of closest approach of the muon to the DOM, which is illustrated in Fig. 6.3. About 40% of muons producing a maximum multiplicity of 6 have the closest approach to the DOM in the 5-8 m range, while about half of the muons producing a maximum multiplicity of 4 have the closest approach between 7 and 15 m. Therefore, a spacing between adjacent DOMs below 23 m is required in order to reject at least 40% of the muons. This condition is not satisfied by the ARCA geometry.

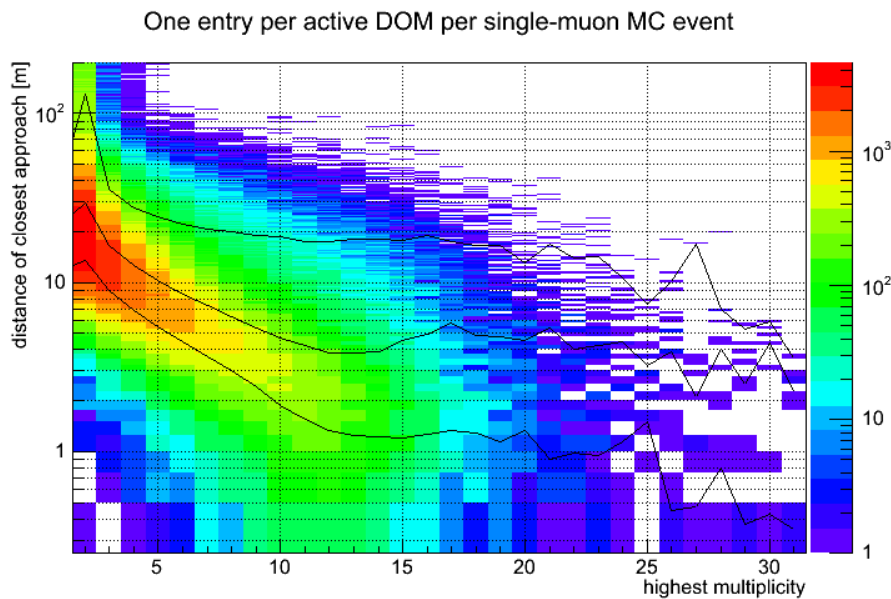


Figure 6.3: Highest multiplicity coincidence of single-muon events versus the distance of closest approach, determined from atmospheric muon Monte Carlo. The black lines show the 10%, 50% and 90% quantiles.

## 6.2.2 Muon rejection: triggered events veto

In order to improve the performance of the muon filter and reduce the dead time, an alternative approach has been implemented exploiting the KM3NeT physics triggers, generally used to identify track-like and shower-like events at higher energies (detailed in section 3.3), as a veto mechanism.

KM3NeT triggers are designed to look for clusters of hits correlated in space and time across multiple DOMs, in order to identify track-like or shower-like events. The main information content of a triggered event is a collection of *triggered hits*, namely the set of causally-connected hits recognised by the algorithm as part of a physics event, usually atmospheric muons.

For each triggered event, a *veto window* is defined by a set of DOMs and a time interval that covers all the triggered hits. In parallel, coincidences are filtered and clustered as described in steps 1 and 2 of subsection 6.2.1. For each cluster, the (first) coincidence having the highest multiplicity is considered. The coincidence is discarded if it occurs on a DOM and at a time covered by the veto window. The surviving coincidences are counted as potential signal events in the final distribution.

To test the approach, data of ARCA2 and ORCA4 have been analysed. Each run is processed using timeslice and triggered event data. All available triggers (described in section 3.3) are considered. The typical parameters for each trigger are the following:

- **3DMuon**: minimum 3 L1 hits on 3 different DOMs within a cylinder of 43 m diameter for ORCA; min 4 L1 hits on 4 DOMs, within a cylinder of 120 m for ARCA.
- **3DShower**: 3 L1 hits on 3 different DOMs with  $D_{max}$  of 52 m for ORCA and 250 m for ARCA.
- **MXShower**: one L1 + at least 7 L0 hits on 3 different DOMs with  $D_{max}$  47 m for ORCA and within 110 m for ARCA.

In this analysis, for each triggered event produced by the data filter, a *veto* is applied on the set of DOMs detecting at least one triggered hit in the time interval defined by the range of the triggered hit times. Typical values for this interval are  $\sim 1 - 3 \mu\text{s}$ . The remaining coincidences are analysed on a DOM-by-DOM basis. If one or more coincidences occur in a DOM within  $1 \mu\text{s}$ , only the coincidence with the highest multiplicity is kept. This filtering strategy results in an effective reduction of the background rates and in the suppression of spurious coincidences. This is verified on data from the ARCA2 and ORCA4 detectors. The rejection efficiency evaluated on the operating detectors is given in Table 6.3. Comparing with Table 6.2, the trigger veto is shown to be more efficient for the atmospheric muon rejection than the coincidence veto.

Table 6.3: Rejection efficiency as a function of the multiplicity for the triggered events based filter in ARCA2 and ORCA4

Multiplicity	4	5	6	7	8	9	10	11	12
ARCA2	0.4%	2%	10%	22%	26%	27%	28%	29%	31%
ORCA4	4%	22%	70%	94%	98%	99%	99%	99%	99%

The *efficiency* of the background rejection is also evaluated for a full KM3NeT ARCA and ORCA building block by means of a Monte Carlo simulation. The simulation chain is based on the atmospheric muon event generator MUPAGE [117] and the Cherenkov light simulator JSirene which is part of the custom KM3NeT software suite Jpp [175]. The generation of the simulated hit data follows the procedure outlined in [119]. The fraction of coincidences rejected by the trigger as a function of the multiplicity is shown in Figure 6.4 (left) for the ARCA and ORCA building block simulations. The denser geometry of the ORCA detector allows to identify and suppress more than 95% of the background starting at multiplicity eight or above. For comparison, ARCA reaches 65% rejection efficiency at multiplicity eight. Figure 6.4 (right) shows the comparison of the background and expected signal rates after the filter, in contrast to Fig. 6.2 which is shown before the rejection.

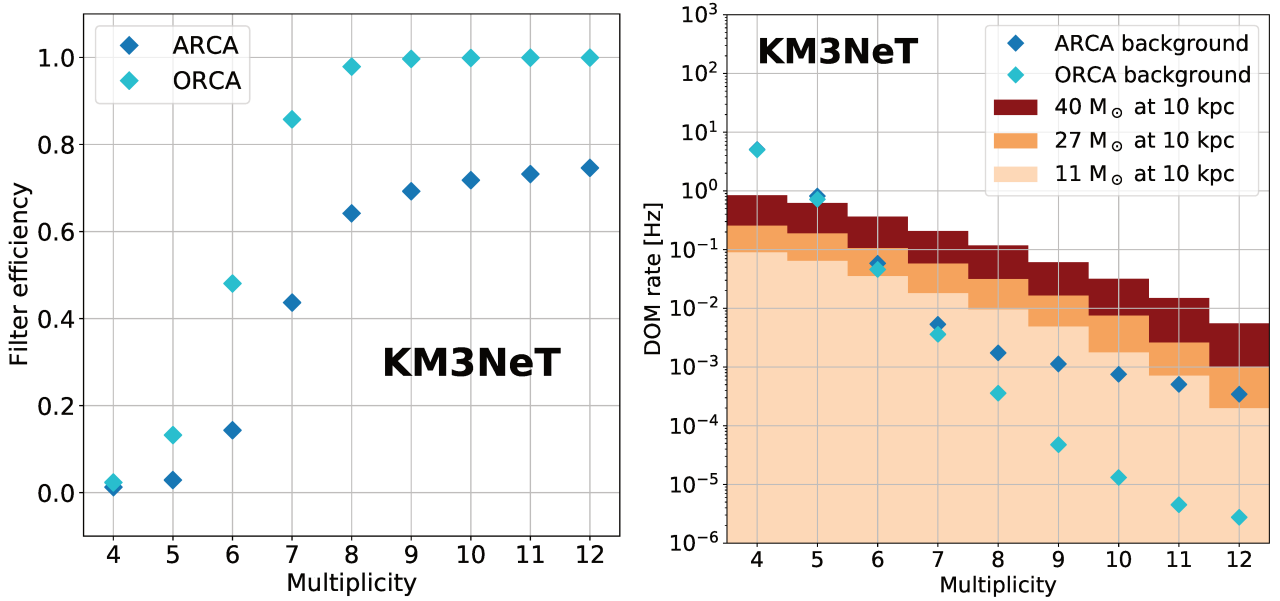


Figure 6.4: Left: Fraction of coincidences rejected by the background filter estimated with a simulation of KM3NeT ARCA and ORCA building blocks. Right: DOM event rates as a function of the multiplicity for ORCA (light blue dots) and ARCA (dark blue dots) backgrounds from measurements, after applying the muon veto defined in section 6.2.2. Superimposed, the CCSN signal at 10 kpc for the 40  $M_{\odot}$  (dark red filled), the 27  $M_{\odot}$  (orange filled) and the 11  $M_{\odot}$  (beige filled) progenitors, obtained from simulations. The signal values correspond to the average rate over the accretion phase.

### 6.3 Optical background characterisation: Bioluminescence impact on detector efficiency

Atmospheric muons and seawater radioactivity are mostly stable in time. However, the time variations in bioluminescence activity affect the number of active PMTs, which is not constant in time and can change over short timescales. For a correct evaluation of the sensitivity, the expectation value for the number of background events needs to be known for any fraction of active PMTs that is considered as eligible for the search live time. The expected number of background events in a 100 ms timeslice has been evaluated as a function of the number of active PMTs in the data of the ORCA4 detector.

The off-shore *high-rate-veto* shuts the data acquisition for PMTs exceeding a 20 kHz counting rate on a 100 ms basis. The distribution of the vetoed channels across the detector can follow a multitude of spatial patterns with effects that can be both localised and diffused. At the same time, multiplicity rates have a non-linear dependence on the number of active PMTs on a DOM. The average fraction of PMTs in high-rate-veto is of a few per mil in ARCA and a few per cent in ORCA.

Data from the ORCA4 detector have been analysed to extract a parameterisation of the detection efficiency  $\epsilon$  as a function of the fraction of active channels  $f_A$  for a CCSN event. The estimation of the efficiency relies on two approximations:

1.  $\epsilon$  is the same for signal and background events;
2. on average,  $\epsilon$  depends only on the number of active PMTs and not on their spatial distribution.

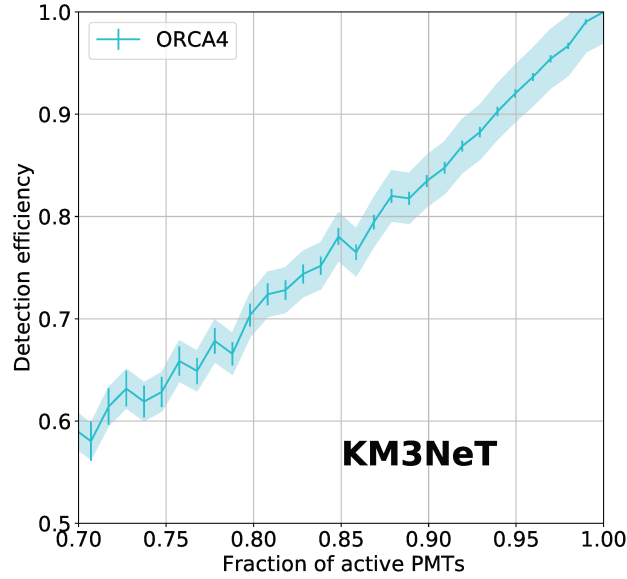


Figure 6.5: Background detection efficiency as a function of the fraction of active PMTs in the ORCA4 detector. The efficiency is calculated by dividing the expectation value of the number of background events as a function of the fraction of active PMTs by its maximum obtained for an active PMT fraction above 99%. Statistical errors are shown as error bars. Monthly variability is covered by the shaded area.

These two approximations will be verified by means of a run-by-run Monte-Carlo simulation of the data taking conditions when it will be available in the near future, but no significant impact is expected.

Following (1) and (2), the expectation value of the background as a function of the fraction of active PMTs  $\mu_B(f_A)$  is estimated from the ORCA4 data in the period up to January 2020. The efficiency as a function of  $f_A$  is defined with respect to the maximal number of active channels,  $f_A = 1$ :

$$\epsilon = \frac{\mu_B(f_A)}{\mu_B(1)}$$

and is shown in Fig. 6.5. An interpolation of the curve is used to predict the detection efficiency of the CCSN supernova selection, both for signal and background, and their expectation value at any point in time.

Comparing the monthly averages of ORCA4 data from October 2019 to January 2020, the background expectation values as a function of  $f_A$  are within  $\pm 3\%$ . This range will be assumed as a systematic uncertainty on the detection efficiency.

## 6.4 Background stability

In order for the sensitivity estimation to be reliable, it has to be verified that the expected number of background events on the time scale of the CCSN search is compatible with the Poisson distribution. To this aim, the *number of background events* after the muon filter is evaluated in the 7 – 11 multiplicity selection (optimised in section 6.6.3) for every 100 ms timeslice across the whole considered data taking periods for ARCA2 and ORCA4. Figure 6.6 shows the distribution of the number of background events detected in a timeslice. Timeslices with a fraction of active PMTs (i.e. non in *high-rate-veto*) above 95% are considered. Here, the total number of samples is given by the livetime of the data, divided by

the timeslice duration (100 ms). The Poisson distribution with expectation value equal to the mean of the data sample is compared to the data, which are found to be perfectly compatible with the Poisson statistics.

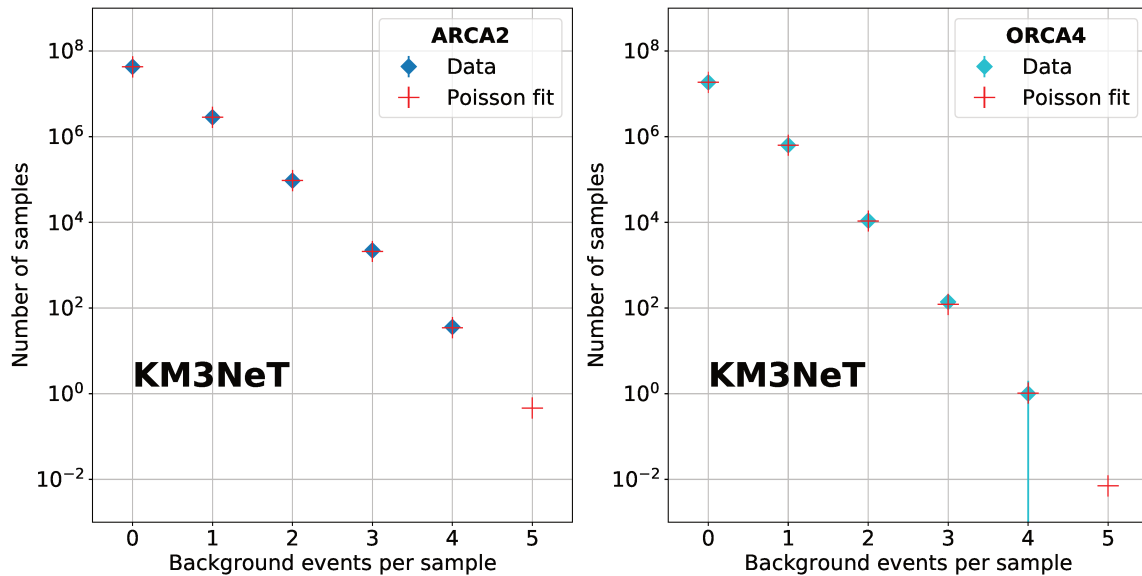


Figure 6.6: Number of 100 ms samples as a function of the number of the background events in the sample for the considered ARCA2 (left) and ORCA4 (right) data taking periods. Statistical errors are included. A Poisson distribution with expectation value equal to the mean value of the data is overlaid.

The selected data taking periods are from December 23, 2016 to March 2, 2017 for ARCA2 and from September 30, 2019 to November 4, 2019 for ORCA4. In these periods, the detectors show stable average photon detection efficiencies.

## 6.5 Study of the systematic uncertainties

The systematic uncertainties can be divided into two groups: the uncertainties related to the detector response to a given flux of CCSN neutrinos, and the uncertainties on the flux model itself.

### Detector response

The uncertainties on the detector response come from: the uncertainty on the PMT efficiencies, the uncertainty on the number of active PMTs, the water absorption length, the uncertainty on the generation volume and the uncertainty on the filter efficiency.

The first uncertainty of relevant comes from the uncertainty on the PMT efficiency, and the dependence of the signal rate on it. Here, QE PMT efficiencies are referred to as relative values, which are calibrated comparing the data to the PMT simulation model. In this way,  $QE = 1$  would be a perfect agreement between data and MC (and all PMTs behaving on average the same way), while values above and below one indicate the relative difference of the QE of active PMTs with respect to the simulated PMT model. As shown in Fig.6.7, the dependence of the signal rate with respect to the PMT efficiency is found to be linear in the multiplicity selection range [7,11]. For the both considered models, the variation of the rate is shown to be of a  $\pm \sim 20\%$  for a  $\pm 10\%$  change of the PMT efficiency. From calibration studies, the uncertainty on the absolute PMT efficiency is 5%. The corresponding

uncertainty on the DOM expected CCSN detection rate is assigned a value of 10%. For the final sensitivity, the calibrated QE values for the DUs taking data is used.

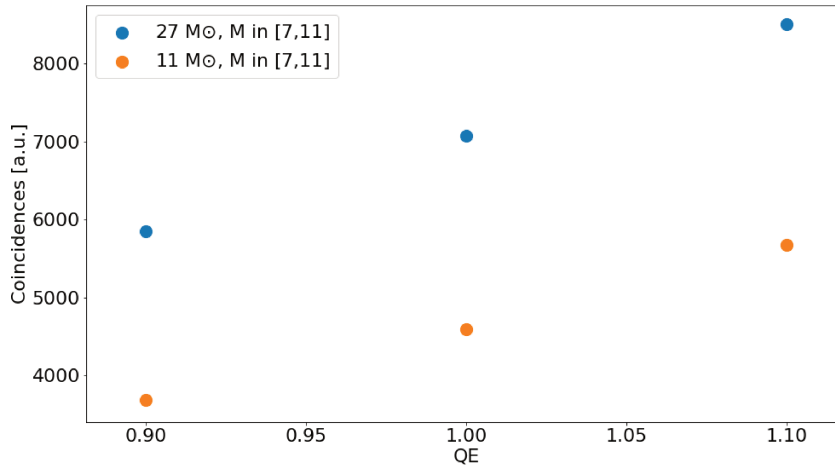


Figure 6.7: Variation of the number of detected signal events in the multiplicity range [7,11] as a function of the PMT efficiency, for the two models considered.

The background rates vary with the number of active PMTs as a function of time. This variation is translated into a reduction of the overall efficiency as illustrated in section 6.3. Such reduction can be evaluated from the knowledge of the number of active PMTs with an uncertainty of  $\pm 3\%$  on the expected number of background events in any considered time interval. The same uncertainty is applied to the signal.

While the first two relevant uncertainties are estimated directly from data and impact both the background and signal estimates, on the following we focus on the related detector uncertainties that may play a role in the signal simulation, already listed at the beginning of this subsection. Therefore, simulations are performed to study the effect of varying the different inputs, evaluated as a systematic uncertainty.

The uncertainties on the water density and absorption length have been evaluated by changing these parameters in the simulation, resulting in an effect smaller than 1% in the range  $M[6,10]$ , and 3% when all coincidences ( $M \geq 2$ ) are considered. Finally, the IBD and ES cross sections are precisely measured, and thus known with an uncertainty below 1% [172, 173].

The efficiency of the background filter is evaluated through a Monte Carlo simulation of KM3NeT ORCA and ARCA building blocks (see section 6.2.2). From the data – Monte Carlo comparison based on ARCA2 data, a 15% uncertainty is assumed on the filter efficiency for the determination of the background rate, with an overestimate of the MC over data.

A summary of the results for the different systematic uncertainties studied is shown in Table 6.4. When (S) is indicated, it means that the systematic error only affects the signal estimate, while (S,B) stands for the case where the systematic uncertainty affects both signal and background.

Table 6.4: Systematic uncertainties in terms or relative deviation in the number of neutrinos in the selection multiplicity range.

Variable	Uncertainty	Syst. err.
PMT efficiency	$\pm 5\%$	(S) $\pm 10\%$
Active PMTs	$\pm 3\%$	(S, B) $\pm 3\%$
Generation radius	$\pm 5$ m	(S) $< 1\%$
Absorption length	$\pm 10\%$	(S) $\pm 1\%$
Water density as function of depth	$\pm 10\%$	(S) $< 1\%$
IBD/ES cross sections	$< 1\%$	(S) $< 1\%$
Filter efficiency	data – MC	(B) $+15\%$

### Flux model

The second type of systematic uncertainties is related to the total observed rate of each neutrino flavor, including changes in the neutrino-flavor dependent luminosity and energy. These uncertainties are given by the variations observed within the different hydrodynamical simulation codes, coming from the neutrino transport mechanism or the relativistic approach used, among others. The oscillation effects in the star and in the Earth as well as opacity effects due to neutrino-self interaction will also produce a change in the total amount of  $\bar{\nu}_e$  emitted and detected. However, for what concerns this study, only detector-related uncertainties will be taken into account.

Due to the large uncertainties in the final neutrino flux, the NFS hypothesis is assumed for the oscillation scenario as a reference to evaluate the detector performance in this analysis, for the different progenitors considered (see section 4.3). In fact, the impact of this assumption compared to the opposite extreme case (FFS) depends on the energy neutrino spectrum predicted for each progenitor. As an example, in case of FFS, the variations are respectively a 15% loss for the  $27 M_{\odot}$  progenitor and a 26% gain for the  $11 M_{\odot}$  model. This will correspond to use the most optimistic expectation for the  $27 M_{\odot}$  while the most pessimistic scenario for the  $11 M_{\odot}$ , which are the two extreme cases for which the sensitivity will be shown.

## 6.6 Sensitivity of KM3NeT detectors to a CCSN neutrino signal

In summary, the analysis steps to evaluate the sensitivity as explained in this section are following:

- The coincidence rates as a function of the multiplicity are measured from ARCA2 and ORCA4 data for the background estimate, and evaluated from simulations for the signal expectation.
- Two approaches are used to filter and reduce the atmospheric muon background.
- The efficiency of the filter for the full detector at each multiplicity is evaluated from the simulation of a full building block, for the ORCA and ARCA geometries.
- The background rate after the filter is given by the coincidence rates measured in the sea multiplied by the rejection efficiency expected for the full detector.
- The multiplicity selection providing the best sensitivity is identified.
- The robustness of the muon filter with respect to the optimised multiplicity selection is tested on ARCA2 and ORCA4 data.

- The detection sensitivity is estimated from the expected number of signal and background events in a 500 ms search window, within the optimal multiplicity range of the selection. This is done for the complete ARCA and ORCA detectors (230 and 115 DUs respectively).

### 6.6.1 Sensitivity definition

The sensitivity of an experiment to a given signal hypothesis can be characterised by its expected median significance. Here, it is of interest to evaluate the KM3NeT sensitivity to a CCSN neutrino signal by reporting the expected median significance. Hereafter, sensitivity and median significance will be referred to independently with this same definition.

The expectation values of signal and background,  $\mu_s$  and  $\mu_b$ , are used here for the evaluation of the median significance. In general, in a Poisson counting experiment with known background, the expected significance is derived from the Poisson p-value, evaluating the probability of observing  $n \geq \mu_b + \mu_s$  when expecting  $\mu_b$ . A good approximation of the full numerical calculation for the sensitivity is given by the formula in Eq. 6.2, whose derivation can be found in [176]:

$$z = \sqrt{2 \cdot \left( (\mu_s + \mu_b) \cdot \ln \left( 1 + \frac{\mu_s}{\mu_b} \right) - \mu_s \right)} \quad (6.2)$$

where  $z$  is the sensitivity, calculated directly from the number of expected background ( $\mu_b$ ) and signal events ( $\mu_s$ ). In this analysis,  $\mu_s$  and  $\mu_b$  are evaluated for a 500 ms time window from the onset time of the event, assumed to be known from an independent observation. The median significance  $z$  derived from Eq 6.2 is defined as the equivalent Gaussian significance with the one-sided convention, and is given in "number of sigmas".

Notice that the approximation of the significance in Eq. 3.7 is usually considered as valid for a sufficiently large number of data events, signal ( $n_s$ ) + background ( $n_b$ ), but it is strictly correct only if  $n_s \ll n_b$ , as shown in [176]. In the statistical regime for CCSN neutrino searches, Eq. 6.2 should be used to evaluate the significance in an accurate way.

The significance does not linearly depend on the signal-to-noise ratio, but on their absolute scale. Therefore, a signal selection that increases the signal-to-noise but reduces the total amount of events is not guaranteed to provide a better result.

### 6.6.2 Combined sensitivity

In order to compute the combined sensitivity for both KM3NeT detectors, ARCA and ORCA, different approaches can be followed to combine the p-values or median significances. A nice overview of the different combination methods can be found in [129].

One of the most common approaches is combining p-values using the Fisher's method. The significance (given by Eq. 6.2) can be converted into a p-value according to the following relation:

$$p_i = \text{Erfc} \left( \frac{z}{\sqrt{2}} \right) \quad (6.3)$$

Then, the p-values are combined in a  $\chi^2$  test statistic as follows:

$$\chi_{2k}^2 = -2 \sum_{i=1}^k \ln(p_i) \quad (6.4)$$

The  $\chi^2$  probability with number of degrees of freedom equal to twice the number of combined p-values ( $2k$ ) gives the resulting p-value, and therefore the median combined significance.

It can happen that the optimal selection is different for each detector, as well as different orders of magnitude in the number of background events can be expected for the detectors that are going to be combined, resulting in different sensitivities. In this case, the Fisher method is not optimal and will penalize the most performing detector sensitivity when combining it with a worse one.

The weighted combination of significances, also called Stouffer's combination, is a better option in this case. This approach is used by the NovA Collaboration <sup>1</sup> and the combined significance can be written as follows:

$$z_{comb} = \frac{z_{ARCA} \cdot z_{ARCA}^{ref} + z_{ORCA} \cdot z_{ORCA}^{ref}}{\sqrt{(z_{ARCA}^{ref})^2 + (z_{ORCA}^{ref})^2}} \quad (6.5)$$

where  $z_{ORCA}^{ref}$  and  $z_{ARCA}^{ref}$  are the reference sensitivities for ORCA and ARCA at 10 kpc.

### 6.6.3 Multiplicity selection

The comparison between expected rates in subsection 6.1 suggests the range above multiplicity 5 as the most favourable in terms of signal-to-noise ratio. After the muon filter is applied, the optimisation of the multiplicity selection is performed by maximizing the sensitivity in the two detectors for the signal expected considering each progenitor model.

Considering the background rates after the muon rejection approaches described in subsection 6.2.2, the sensitivity as a function of the *number* of expected background and signal events is estimated for the two progenitors and the two detectors, for a reference distance of 10 kpc. The results are summarised in Fig. 6.8. Here, the background data is extracted from ORCA4 and ARCA2 and scaled up to the full detector size. Because of the large variability of the ORCA detection efficiency with the number of active PMTs discussed in section 6.3, only timeslices with more than 99% of active PMTs are considered for the ORCA background estimate.

To account for the difference between the real detector (used to measure the background) and the nominal detector (used to simulate the signal), the background level is scaled to the nominal efficiency for each detector. This determines the average QE of each detector that is used to estimate the background expectation in a nominal detector. For ORCA4, the average efficiency of the DOMs is 0.96 for the selected data period, with variations below 1% over time. For ARCA2, an average efficiency of 1.025 is measured for the selected runs. The scaling applied to the background follows the relationship established in Fig. 6.7 for the signal.

The conclusion extracted from Fig. 6.8 is that not in all cases there is an optimal multiplicity selection. Therefore, the best multiplicity selection is chosen so that to maximise the  $5\sigma$  discovery distance for the lower progenitor mass. The multiplicity range [7,11] is found to be the optimal for both ARCA and ORCA, specially considering that for  $M=12$  the signal expectation for the  $11 M_{\odot}$  progenitor is close to zero.

<sup>1</sup>[https://indico.cern.ch/event/800827/contributions/3429831/attachments/1863050/3062552/NovaSN\\_SNEWS2\\_0\\_slides.pdf](https://indico.cern.ch/event/800827/contributions/3429831/attachments/1863050/3062552/NovaSN_SNEWS2_0_slides.pdf)

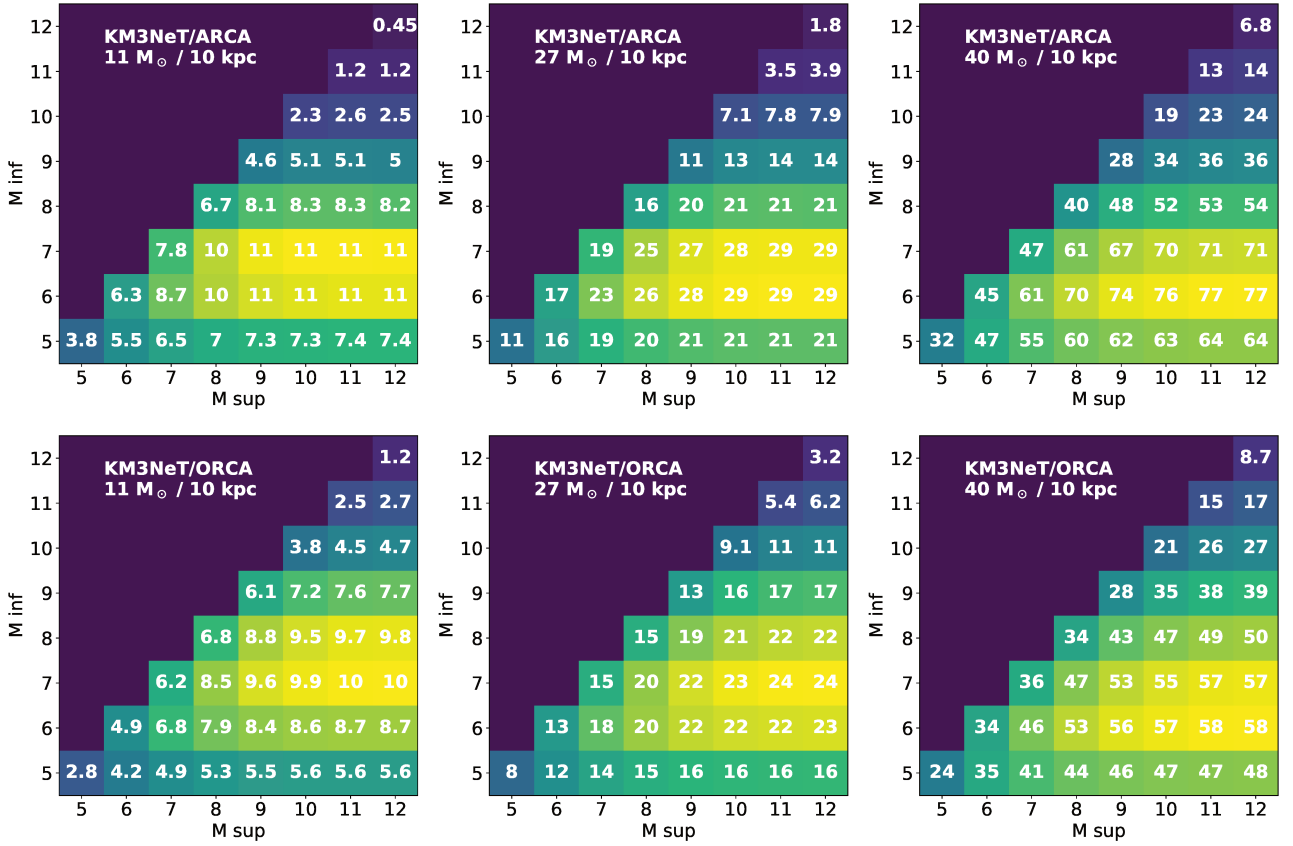


Figure 6.8: Sensitivity (number of sigmas, in white) estimated at 10 kpc for the 11 M<sub>⊙</sub> (left), 27 M<sub>⊙</sub> (middle) and 40 M<sub>⊙</sub> (right) CCSN progenitors as a function of the minimum and maximum multiplicity. Top panels refer to the ORCA detector, and bottom panels to ARCA. The muon filter described in section 6.2.2 is used.

#### 6.6.4 Sensitivity results

The sensitivity for each considered CCSN progenitor as a function of distance is estimated according to Eq. 6.2. The sensitivity results are provided in Fig. 6.9 after applying the CCSN selection: the muon filter and the optimal multiplicity cut. They are presented as a function of the distance for different progenitor masses and for the two KM3NeT detectors: ORCA and ARCA.

To evaluate the performance of each of the combination methods, the significance has been evaluated for a set of pseudo-experiments in the H0 (background only) and H1 (signal plus background) hypotheses, with the optimised multiplicity selection in the range [7,11]. The signal hypothesis is chosen so that the expected number of signal events provides an individual median significance in ORCA and ARCA of about  $3\sigma$ , i.e. a flux equivalent to the 27 M<sub>⊙</sub> CCSN progenitor at 37 kpc. Both the number of signal and background events are simulated following a Poisson distribution with mean the expectation value. Figure 6.10 shows the comparison between the Fisher's (right) and Stouffer's (left) combinations explained in subsection 6.6.2. The two methods are shown to be fairly equivalent in performance in case the detectors that are combined have similar individual significance, which is the case with the CCSN selection applied in ORCA and ARCA.

The two combination methods explained in subsection 6.6.2 are compared in Fig. 6.11 for the case where the same or a different multiplicity selection is used for ORCA and ARCA<sup>2</sup>. It shows that the sum of p-values leads to a combined result where the most sensitive detector is penalised when considering it with a less performing experiment. When the two detectors have similar performance (with same selection), both approaches lead to comparable results.

Assuming the multiplicity selection  $7 \leq M \leq 11$ , the number of signal ( $n_s$ ) and background ( $n_b$ ) events in the 500 ms window search after applying the muon rejection strategy in section 6.2.2, proven to be the optimal one in subsection 6.6.3, are given in Table 6.5 for the two CCSN stellar progenitors and the two detectors, at a reference distance of 10 kpc. The number of signal events as a function of the distance is naturally:

$$n_s(D) = n_s^{10\text{kpc}} \cdot \left(\frac{10\text{kpc}}{D}\right)^2$$

Table 6.5: Expectation values for the number of background and signal events after the background rejection in the 7-11 multiplicity selection, for ARCA and ORCA. Signal and sensitivities are given for a CCSN at 10 kpc, for each detector and CCSN progenitor.

Progenitor mass	ARCA			ORCA		
	$\mu_b$	$\mu_s$	$\sigma_{10\text{kpc}}$	$\mu_b$	$\mu_s$	$\sigma_{10\text{kpc}}$
11 $M_\odot$	22.1	72.2	11	4.9	36.1	10
27 $M_\odot$	22.1	240	29	4.9	120	24
40 $M_\odot$	22.1	895	71	4.9	447	57

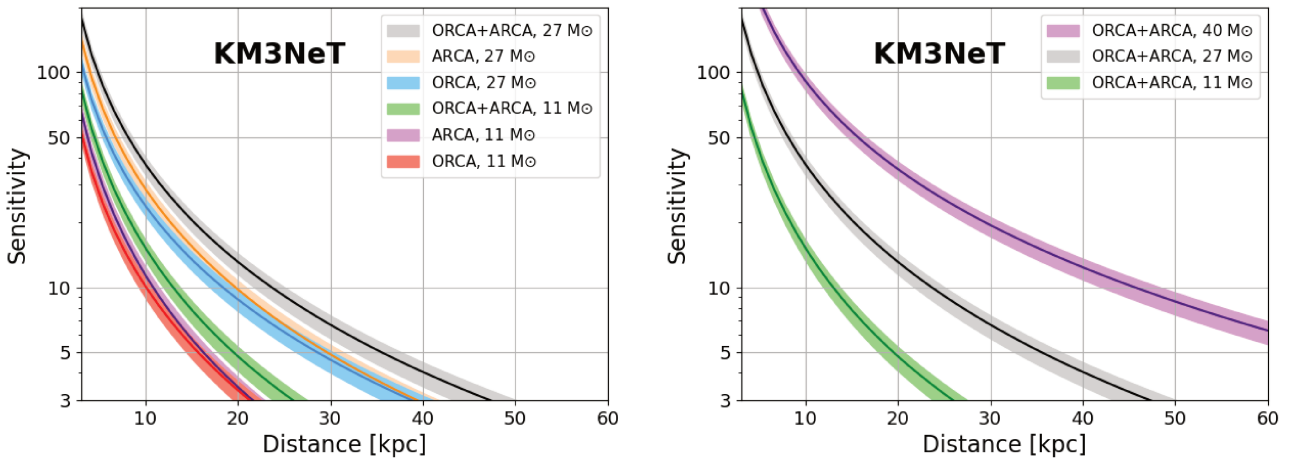


Figure 6.9: Detection sensitivity after filter over the multiplicity cuts optimised in section 6.6.3 as a function of the distance. On the left, for ORCA, ARCA and the combination of both detectors, for the two extreme mass CCSN. On the right, the KM3NeT combined results for the three progenitors considered: 11  $M_\odot$  (green), 27  $M_\odot$  (black) and 40  $M_\odot$  (purple). The error bars include the systematic uncertainties evaluated in section 6.5.

<sup>2</sup>Even though the optimisation leads to the same selection used in both detectors, this consideration is made because the background estimates in different detector configurations may lead to this scenario, since the significance depends on the absolute rates.

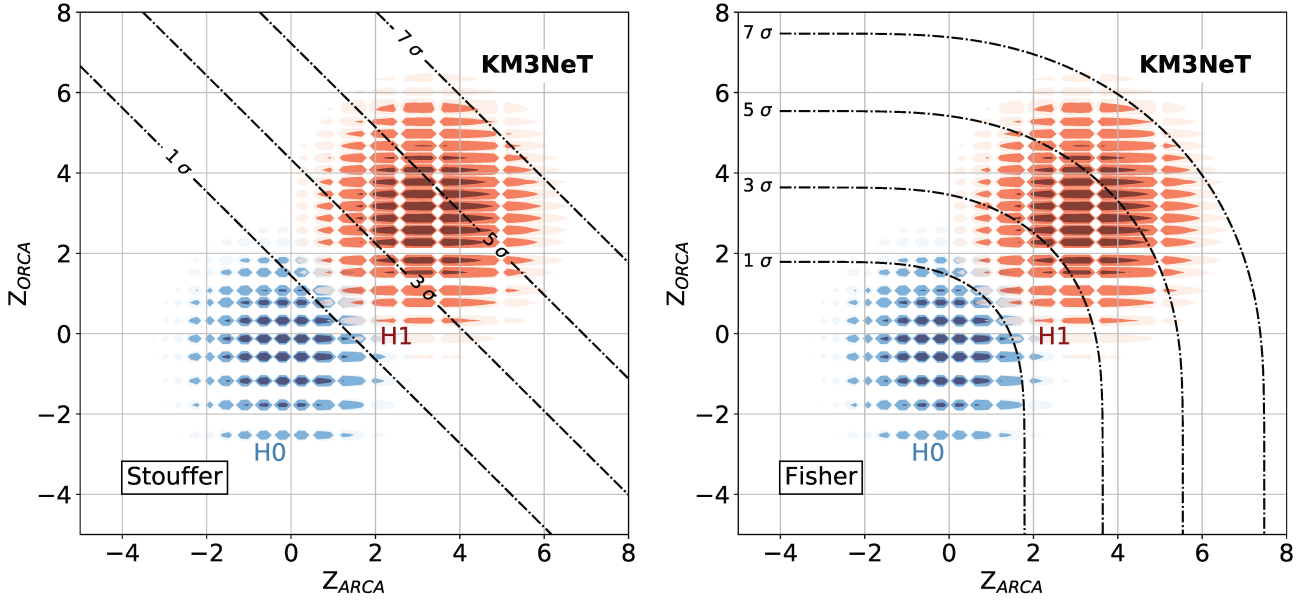


Figure 6.10: Distribution of significances for the null (H0, blue) and alternative (H1, red) hypotheses. The combined sensitivity (black lines) for the  $27 M_{\odot}$  progenitor at 37 kpc with ORCA and ARCA is drawn as function of the individual significances, using the two different methods described in subsection 6.6.2: the Fisher's method (right) and the Stouffer's method (left). The effect of the discrete domain from the Poisson statistics can be seen in this Figure, and explains that some significance values  $(z_{ORCA}, z_{ARCA})$  are not filled.

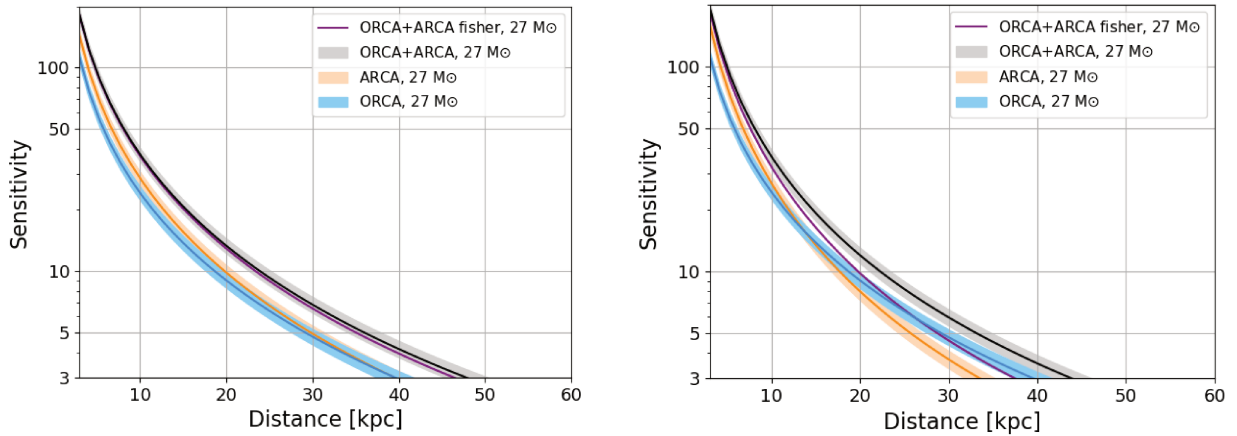


Figure 6.11: Comparison of the combined sensitivity for the  $27 M_{\odot}$  progenitor with ORCA and ARCA using the two different approaches described in subsection 6.6.2: the Fisher method (purple) and the Stouffer's combination (black). Left: if the same multiplicity selection [7,11] is applied in both detectors. Right: if the multiplicity selection for ARCA is [6,10] and ORCA [7,11].

Figure 6.9 shows the performance of the KM3NeT for detecting a CCSN neutrino flux. Combining this information with the distance probability in Fig. 4.2, one concludes that above 95% of the Galactic CCSN will be detected with a  $5\sigma$  significance by KM3NeT. In addition, for a failed CCSN the  $5\sigma$  discovery is reached at the Large and Small Magallanic clouds.

## 6.7 Online supernova trigger in KM3NeT

An approach for the real-time search of a CCSN neutrino burst applicable already in the construction stage of KM3NeT has been developed and is operational since summer 2019. The data from the first deployed ARCA and ORCA DU have been extensively analysed by sampling the background on a  $\tau = 100$  ms time scale in order to characterise the background distribution.

The signal search is based on the definition of a *trigger level* ( $x$ ) as the number of events in the chosen multiplicity selection (after the muon filter) over a time window of duration  $n\tau$ . The search is performed updating the (sliding) time window at a frequency  $\tau^{-1}$ . In practice for  $n = 5$ , every 100 ms the number of background event is evaluated over the previous 500 ms of data to produce the trigger level  $x$ . With the notation used in subsection 6.6.4,  $\mu_b = N\rho n\tau$ , where  $N$  is the number of DOMs in the detector and  $\rho$  is the (average) background rate per DOM in the designated multiplicity range.

In the case of a single detector, as a Poisson counting experiment, the false alarm rate (FAR) for an observation above or equal to a trigger level  $x_d$  is:

$$FAR(x_d) = \frac{1}{\tau} \cdot \sum_{x=x_d}^{+\infty} \mathcal{P}(x, \mu_b) \quad (6.6)$$

where  $\mathcal{P}$  indicates the Poisson probability function. In analogy with the *trial factor* usually considered in different domains, the sampling frequency  $\tau^{-1}$  can be seen as a *trial rate* for the online supernova search.

Under these conditions,  $x_d$  can be set to the expectation value of signal plus background:

$$x_d = N \cdot \left( (\rho \cdot n\tau) + x_{10\text{kpc}}^{n\tau} \cdot \left( \frac{10\text{kpc}}{d} \right)^2 \right) \quad (6.7)$$

where  $x_{10\text{kpc}}^{n\tau}$  is the expected number of selected signal events on a time window of duration  $n\tau$  for a reference distance of 10 kpc ( $\mu_s = n_s^{10\text{kpc}}$  using the convention of subsection 6.6.4).

The time window is fixed a priori to  $n\tau = 500$  ms for the real-time search. The signal and background expectation values are calculated accordingly. Combining the two equations, the maximal distance producing a signal observation above the allowed FAR can be determined. In fact, the false alarm rate can therefore be expressed as an observation frequency for a trigger level greater or equal to the expectation from a CCSN neutrino burst as a function of the distance.

To understand the shape of this relation, in Fig. 6.12 the number of signal events as a function of the distance is shown on the left. On the right, the FAR (computed from Eq. 6.6) for a background observation  $n_b$  greater or equal to an arbitrary  $x$  is shown as a function of  $x$  for ARCA and ORCA, considering the expectation value of the background in each detector,  $\mu_b$ .

For the KM3NeT combined search, the procedure is the following. First, one infers the combined significance distribution as a function of the number of signal and background events from Eq. 6.5, as a function of the distance. Then, one converts the combined significance  $z$  into a probability distribution  $\mathcal{P}(z)$  following Eq. 6.3. Finally, the false alert rate can be expressed as the product of the trial rate and the p-value, integrated above the expected combined significance,  $z_{comb}$ , for the signal plus background hypothesis at a distance  $d$ :

$$FAR(X_d) = \frac{1}{\tau} \cdot \int_{z_{comb}}^{+\infty} \mathcal{P}(z) dz, \quad (6.8)$$

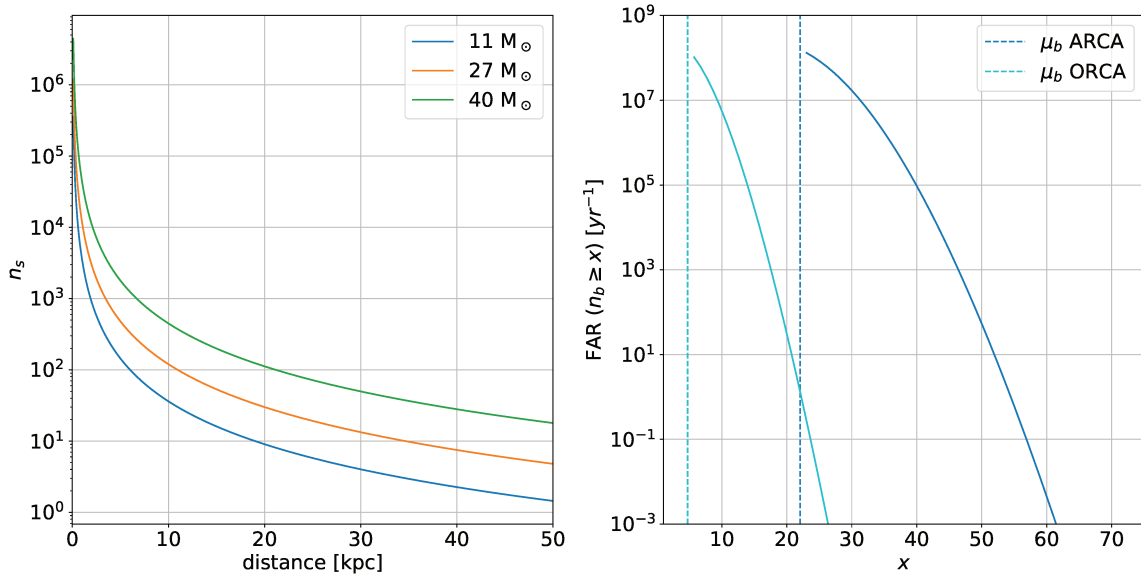


Figure 6.12: Left: number of signal events as a function of the CCSN distance. Right: false alarm rate for a background observation  $n_b$  above the trigger level  $x$  as a function of  $x$ , with respect to the background expectation value  $\mu_b$  for ORCA and ARCA detectors.

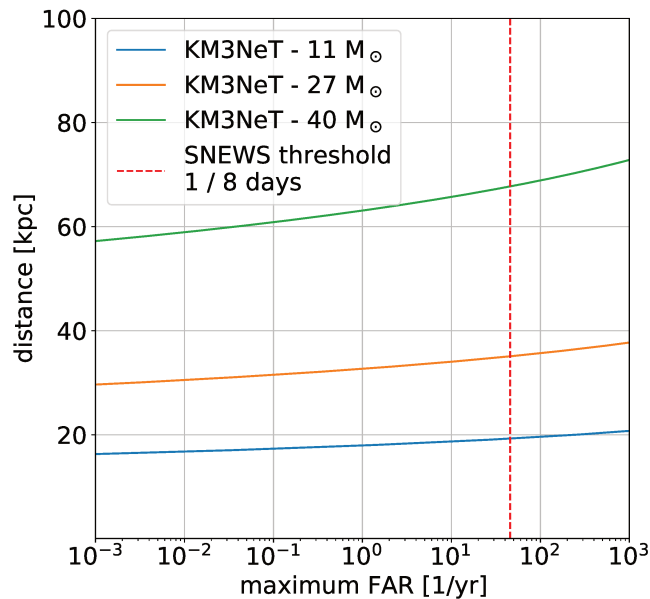


Figure 6.13: Triggering distance as a function of the maximum false alarm rate, which corresponds to the probability of an observed background level greater or equal to the expectation value of signal plus background, multiplied by the number of trials per year considering the 10 Hz trial rate (trigger level evaluated every 100 ms). The red dashed line indicates the threshold required by SNEWS of *one fake trigger in eight days*.

The farther distance at which a CCSN would be triggered as a function of the maximum FAR is shown in Fig. 6.13 for ORCA, ARCA and the combination of the two KM3NeT detectors. Here, the maximum FAR is referred to as the FAR threshold chosen to trigger an alert, which determines the trigger horizon. The requirement to participate in the global SNEWS alert network, here assumed as one false alarm in eight days, is highlighted. The combination of the two detectors allows a good triggering capability beyond the Galactic Centre considering the  $11 M_{\odot}$  progenitor.

## 6.8 Inter-DOM coincidences from a CCSN signal.

In this section, the possibility of using inter-DOM coincidences for CCSN detection is tested. The motivation is that it could potentially give a better background rejection and also give sensitivity to the neutrino energy spectrum. For this purpose, the simulation has been performed for 3 neighbor DOMs, assuming a  $27 M_{\odot}$  progenitor flux. In this case, the generated volume is taken to be a cylinder of 20m radius and 38 m height, with the ORCA inter-DOM separation of 9 metres.

Two types of inter-DOM coincidences are considered, noted (2+1) and (1+1) coincidences. A (2+1) inter-DOM coincidence is defined as an event giving at least 2 hit PMTs in a DOM and a hit in a neighbor DOM within a 50 ns time window. The time window is taken by a simple computation of the travel time between the two DOMs. The (1+1) inter-DOM coincidence does not require a second hit in one of the 2 DOMs.

From a CCSN of  $27 M_{\odot}$  at 10 kpc, the following formulæ give the expected number of inter-DOM coincidences that would be seen by the full ORCA detector, composed of 115x11 cylinders as the one simulation:

$$N_{1+1} = \frac{N_{MC} \times N_{SN} \times V_{gen}}{10^5 N_{gen}} (115 \times 11) = \frac{6.4 \times 10^7 \times 0.2 \times 0.001 \times \pi \times 400 \times 38 \times 27055}{10^5 \times 10^8} = 2091$$

$$N_{2+1} = \frac{N_{MC} \times N_{SN} \times V_{gen}}{10^5 N_{gen}} (115 \times 11) = \frac{6.4 \times 10^7 \times 0.2 \times 0.001 \times \pi \times 400 \times 38 \times 5946}{10^5 \times 10^8} = 455$$

where  $N_{MC}$  are the number of detected hits with the defined coincidence condition, (1+1) or (2+1),  $N_{SN}$  the total number of CCSN interacting in a reference volume of  $10^5 \text{ m}^3$  of water, and  $N_{gen}$  the number of simulated neutrinos. This expressions are equivalent to Eq 5.4 in chapter 5.

From  $^{40}\text{K}$  background, the expected L0 rate in each DOM is:  $R_1 = R_2 = 200 \text{ kHz}$  (per DOM). For (1+1) inter-DOM coincidence from  $^{40}\text{K}$  background withing  $\delta t = 50 \text{ ns}$ , one gets:

$$R(1+1)_{bckg} = 2 \times \delta t \times R_1 R_2 = 2 \times 50 \times 10^{-9} \times 4 \times 1e10 = 4000 \text{ Hz.}$$

During the simulated window for the considered  $27 M_{\odot}$  progenitor,  $\Delta T = 0.543 \text{ s}$ , it is obtained:  $N(1+1)_{bckg} = 2172$  inter-DOM events in a three DOM cylinder from background. Thus, in the full ORCA detector, we expect over the search time window:

$$N(1+1)_{bckg} = 2172 \times 115 \times 11 = 2.25 \times 10^6 \text{ inter-DOM background events.}$$

The simulation estimate for a CCSN at 7.5 kpc is:  $N(1+1)_{signal} = 3822$  inter-DOM events for the full ORCA detector. Provided that when looking at inter-DOM coincidences the statistics remain in the Gaussian regime, the significance can be computed as:

$$significance(\sigma) = \frac{N_{signal}}{\sqrt{N_{bckg}}} = \frac{3822}{\sqrt{2.25 \times 10^6}} = 2.5\sigma.$$

The same calculation is done for the (2+1) inter-DOM coincidences. The  $M \geq 2$   $^{40}\text{K}$  measured rate that is:  $R_3 = 1 \text{ kHz}$  (per DOM), so we have:

$$R(2+1)_{bckg} = 2 \times \delta t \times R_1 R_3 = 2 \times 50 \times 10^{-9} \times 2^8 = 20 \text{ Hz between 2 DOMs.}$$

In the full ORCA detector, the background expectation becomes:

$$N(2+1)_{bckg} = R(2+1)_{bckg} \times \Delta T \times N_{3DOMs} = 20 \times 0.543 \times 115 \times 11 = 11.240 \text{ background events.}$$

This is compared with the signal expectation from the simulation results:  $N(2+1)_{signal} = 819$  inter-DOM events in the full ORCA detector from a SN at 7.5 kpc. The significance reached is of:

$$\text{significance}(\sigma) = \frac{N_{\text{signal}}}{\sqrt{N_{\text{bckg}}}} = \frac{819}{\sqrt{11240}} = 7.7\sigma$$

In Figure 6.14, the variation of the significance as the L0 rates change for a SN at 7.5 kpc is shown. This is just a preliminary inter-DOM background estimation that must be carefully evaluated with real data, but it gives a lower sensitivity than the CCSN multiplicity selection described above. For comparison,  $\sim 30\sigma$  are reached at  $\sim 7.5$  kpc with ORCA considering the same progenitor.

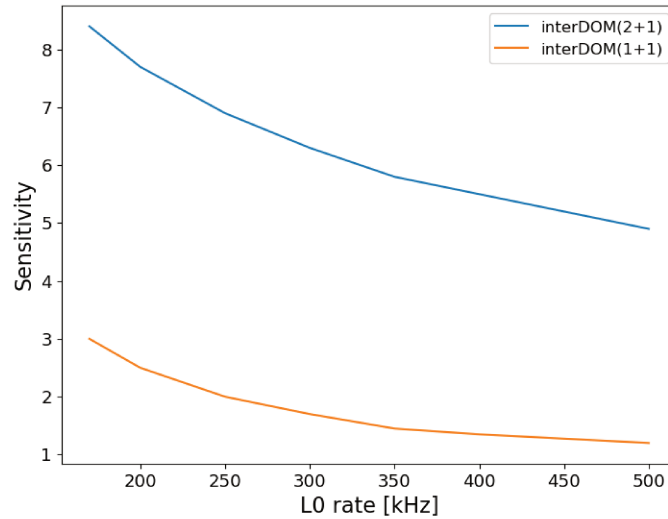


Figure 6.14: InterDOM coincidence sensitivity (median significance, in number of sigmas) as a function of L0 rate in Hz, (2+1) in blue and (1+1) in orange.



# Chapter 7

## Constraining the CCSN mechanism with KM3NeT

The current chapter addresses the KM3NeT potential to extract information about the CCSN physics and constrain the CCSN neutrino emission models. The chapter is organised as follows. First, the astrophysical constraints from the first real-time follow-up of unmodelled GW bursts are described. Second, the constraints on the CCSN energy spectrum and the determination of the mean neutrino energy are discussed. Finally, the constraints on the presence of fast-time variations on the neutrino lightcurve due to hydrodynamical instabilities are presented.

### 7.1 First multi-messenger results with KM3NeT data and the CCSN trigger

This section presents the first KM3NeT follow-up of unmodelled GW alerts, and aims at providing the p-value and setting the upper limits on potential CCSN neutrino emission in correlation. In particular, a lower limit on the CCSN distance and an upper limit (UL) on the total energy emitted through neutrinos, at 90% confidence level (CL) are obtained from a non detection of an MeV neutrino burst in coincidence with the unmodelled bursts GW signal alerts. A real-time search for an MeV neutrino emission is done applying the CCSN analysis on data from the ORCA4 lines. The search is performed within 400 ms after the GW trigger time.

#### 7.1.1 Procedure of the follow-up

The evolution with time of the detector efficiency due to the time dependence of the background rates varying with the sea current and data taking conditions must be taken into account to evaluate the expected background from the measured data.

The trigger level is defined as the event count in the CCSN selection integrated over the previous 400 ms (see Chapter 6). The search is done over 400 ms from the time of the GW alert<sup>1</sup>. From data, the observed trigger level and its background expectation are estimated, providing the corresponding pvalue. If no significant excess is observed, a 90% confidence level upper limit on the number of signal events is derived using the Feldman and Cousins method [177, 178].

The signal expectation is evaluated from simulations after applying the CCSN trigger (muon veto and multiplicity selection described in sections 6.2.2 and 6.6.3) in the search window. It is corrected

<sup>1</sup>This window was used as a compromise between the simulation durations of the 11  $M_{\odot}$  and 27  $M_{\odot}$ . After discussion, these window has been set to 500 ms, which is motivated in case of failed CCSN and covers the window with more than 80% of the expected emission. Larger windows might result in a worsening of the result.

accounting for the number of missing DOMs and the CCSN trigger detection efficiency at the time of the alert, which depends on the effective number of active channels and varies with time in correlation with the data-taking conditions.

Finally, if there is no significant observation, the upper limit on the number of signal events is compared with the signal expectation from different models, to derive physical constraints:

- A lower limit on the distance to the CCSN using the two Garching progenitor models considered for the sensitivity estimate, with masses of  $27 M_{\odot}$  and  $11.2 M_{\odot}$ .
- An upper limit on the total neutrinos emitted from the CCSN assuming a quasi-thermal distribution as in Eqs. 4.2,4.3 with the following parameters:
  - A total neutrino energy of  $E_{\nu}^0 = 3 \times 10^{53}$  erg.
  - A fixed pinching shape parameter with value  $\alpha = 3$ .
  - A fixed average neutrino energy of  $\langle E_{\nu} \rangle = 15$  MeV.
  - $f_0 = 25\%$  of the neutrino signal emitted in  $\tau_0 = 100$  ms from the onset of the event.
  - $f = 70\%$  of the neutrino signal emitted over  $\tau = 400$  ms from the start of the signal.

### 7.1.2 Gravitational wave trigger S191110af: results

On November 10th 2019, the LIGO-Virgo detectors triggered an unmodelled GW signal burst (see Chapter 10 for the description of the gravitational wave detectors and search methods), released in the circular GCN #26222<sup>2</sup>. These kind of signals are of interest as potential CCSN sources. However, this alert was retracted as the probability of this event being of terrestrial (background) origin was rather high (see GCN #26250).

Figure 7.1 shows the time evolution of the event count and detector efficiency  $\epsilon$  around the time of the event. The event count corresponds to the number of coincidences between 6 and 10 hit PMTs after muon rejection on a timeslice of 100 ms basis.

#### Lower limit on the Core Collapse Supernova distance

The trigger level is shown as a function of the timeslice in the top plot of Fig. 7.2 around the time of the alert. Remind from Chapter 6 that the trigger is the number of observed events within the multiplicity selection, not passing the muon filter. At the time of the analysis, the multiplicity cut was set in  $[6,10]$ . The detector efficiency is shown on the bottom plot as a function of time within the same window. For ORCA4, the trigger level is zero on a 400 ms window centered around the GW S191110af alert time ( $T_0$ ). For ARCA1, the trigger level is 2 at 400 ms after the  $T_0$ . For ORCA4 efficiency is assumed conservatively at 0.55 (for an observed value between 0.57 and 0.6). ARCA1 efficiency is of  $\sim 100\%$ .

The outcome of the KM3NeT simulations of the response to the Garching flux models is used to evaluate the signal expectation over the search window. For a CCSN at 10 kpc and four instrumented DUs, the number of expected signal events obtained,  $S_0$ , are:

- for the  $27 M_{\odot}$  progenitor:  $S_0 = 4$  with  $\epsilon = 100\%$  and  $S_0 = 2.2$  with  $\epsilon = 55\%$ ;
- for the  $11 M_{\odot}$  progenitor:  $S_0 = 1$  with  $\epsilon = 100\%$  and  $S_0 = 0.55$  with  $\epsilon = 55\%$ .

In case of the combination of ORCA4 and ARCA1 detectors, accounting for the missing DOMS and detector efficiency, the values obtained are:

<sup>2</sup><https://gracedb.ligo.org/superevents/S191110af/view/>

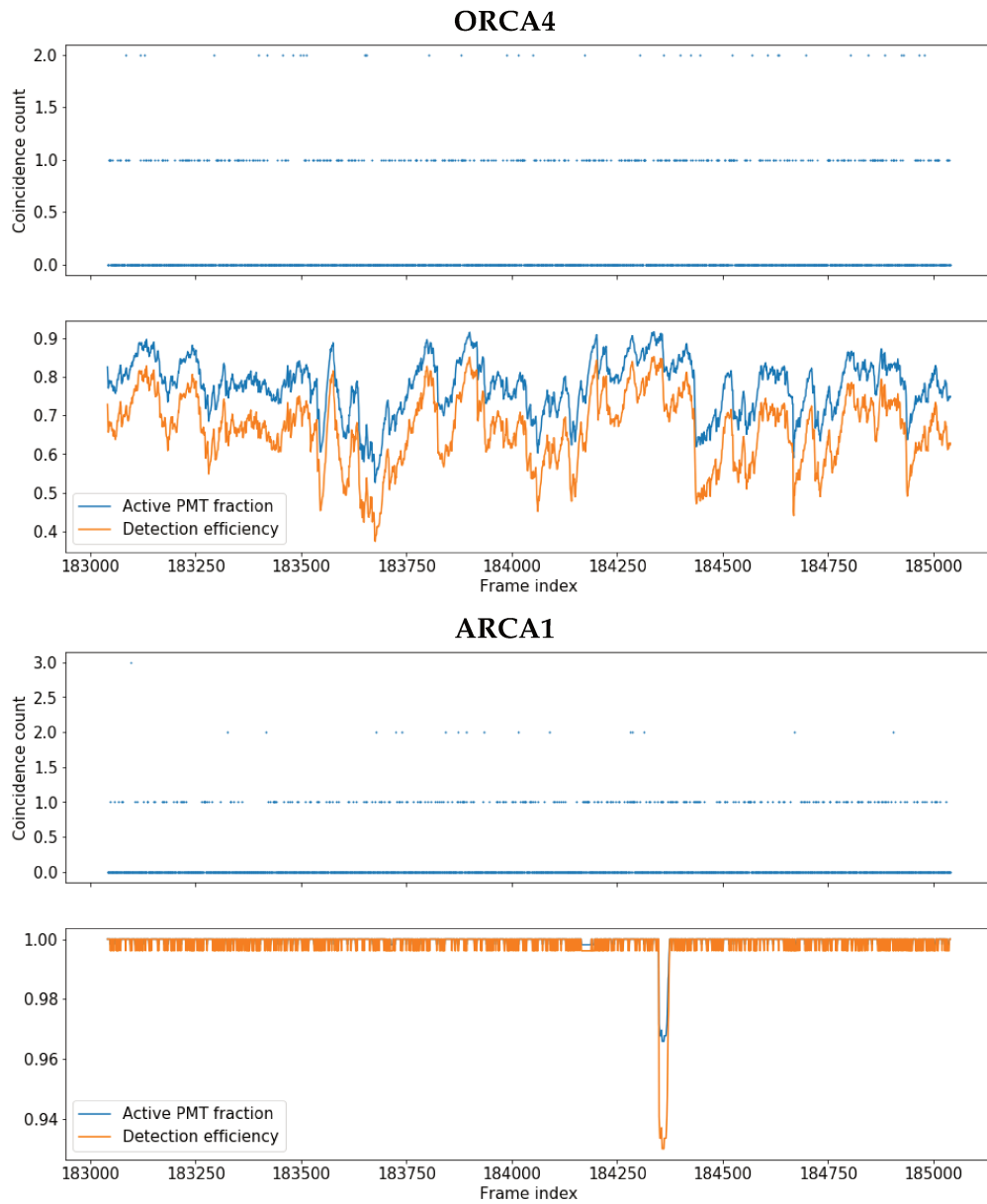


Figure 7.1: For each of the detectors, ORCA4 and ARCA1, two plots are presented. Top: evolution of the event count as a function of time. Bottom: evolution of the fraction of active PMTs (blue) and detector efficiency (orange) as a function of time. Abscissa axis is divided in 100 ms time frames. Start time of the frame 184041 corresponds to 83 ms before the GW S191110af alert time ( $T_0$ ).

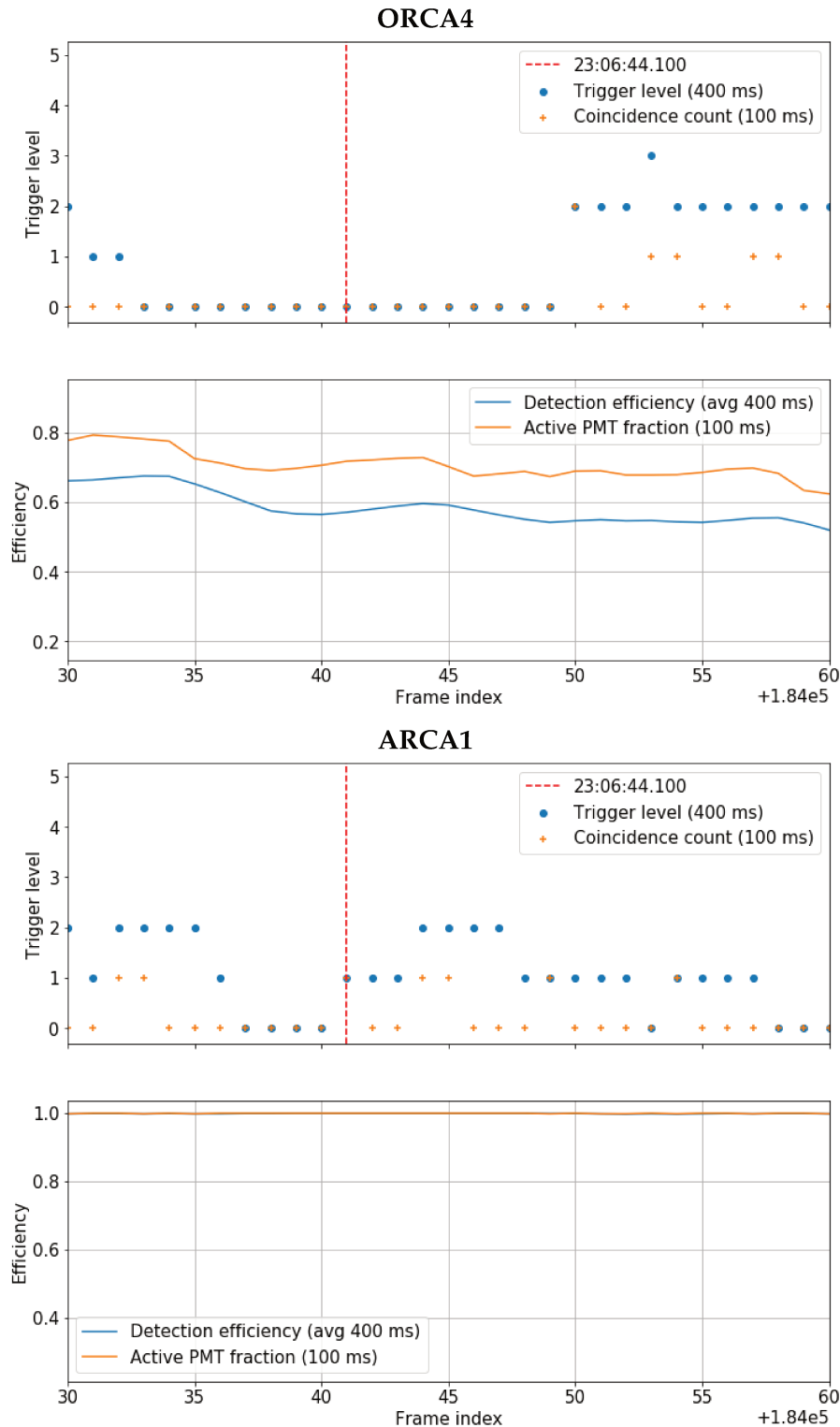


Figure 7.2: Top: event count (orange) and trigger level (blue) as a function of the timeslice. The red vertical line marks the timeslice beginning at 23:06:44.100Z, covering the T0 of the event (23:06:44.183Z). Bottom: instantaneous fraction of active PMTs and average detection efficiency over the last 400 ms as a function of the timeslice.

- for the 27  $M_{\odot}$  progenitor:  $S_0 = 4 \times 0.55 \times 0.96 + 1 \times 0.945 = 3.1$ ;
- for the 11  $M_{\odot}$  progenitor:  $S_0 = 1 \times 0.55 \times 0.96 + 0.25 \times 0.945 = 0.8$

Using the *gammapy* statistics toolkit<sup>3</sup>, the 90% CL upper limit on the expectation value for the signal is estimated using the Feldman and Cousins method as  $S_{ORCA}^{90\%} = 1.72$  for an observed trigger level of  $X_{data} = 0$  events, and a background expectation value of  $\mu_b = 0.8$  in the ORCA4 detector. In ARCA1, the observed trigger level is in this case  $X_{data} = 2$ , with a background expectation of  $\mu_b = 0.6$ . The combined upper limit is obtained using the total number of observed and expected events, resulting in  $S^{90\%} = 5.11$ .

The upper limit on the number of signal events ( $S^{90\%}$ ) is converted into a lower limit on the CCSN distance by using the relation:

$$D^{90\%} = (10\text{kpc}) \times \sqrt{\frac{S_0}{S_{90\%}}} \quad (7.1)$$

This gives the following lower limits on the distance using ORCA4 only:

- for 27  $M_{\odot}$ :  $D^{90\%} = 11.3$  kpc;
- for 11  $M_{\odot}$ :  $D^{90\%} = 5.7$  kpc.

This gives the following lower limits on the distance using ORCA4+ARCA1:

- for 27  $M_{\odot}$ :  $D^{90\%} = 7.8$  kpc;
- for 11  $M_{\odot}$ :  $D^{90\%} = 3.9$  kpc.

Note that in that case, the combination worsens the results because a higher background is observed in ARCA compared to ORCA, resulting in a higher upper limit ( $S^{90\%}$ ). Moreover, combining with one additional ARCA line, only increases the signal of 20% compared to four ORCA lines. The same will be seen in the results on the next subsection.

### Upper limit on the total energy emitted in neutrinos

The background is directly estimated from data as detailed in the previous subsections. The average background measured over 400 ms when the detector is working at maximum efficiency and the efficiency at the time of the GW alert are used for a blind background estimate. The values are the following:

- Background expectation: ORCA4,  $\mu_b = 0.8$  and ARCA1,  $\mu_b = 0.6$
- Observed trigger level: ORCA4,  $X_{data} = 0$  and ARCA1,  $X_{data} = 2$
- Detector efficiency:  $\epsilon = 55\%$  in ORCA4 and  $\epsilon = 100\%$  in ARCA1

The number of expected signal events within 100 ms window, for which the simulations is performed assuming 25% of the emission taking place in this window, is  $S_0 = 1.22$ . The number of events in the 400 ms window can be thus derived as:  $S_{\epsilon=1} = S_0 \times \frac{f}{f_0} = 1.22 \times \frac{0.7}{0.25} \approx 3.42$  events for  $\epsilon = 1$ , and it becomes  $S = 3.42 \times 0.55 = 1.88$  for  $\epsilon = 0.55$ . Finally, the observed UL on the total energy becomes, for ORCA4:

$$E_v^{90\%} = \frac{S^{90\%}}{S} \times E_v^0 = \frac{1.72}{1.88} \times 3 \cdot 10^{53} = 2.75 \cdot 10^{53} [\text{erg}] \quad (7.2)$$

<sup>3</sup>[https://docs.gammapy.org/dev/stats/feldman\\_cousins.html](https://docs.gammapy.org/dev/stats/feldman_cousins.html)

Considering the combination of ORCA4 and ARCA1, and accounting for the 4 missing DOMs in ORCA and the efficiency, the number of signal events is in this case:  $S = (3.42/4) \times 0.96 + 3.42 \times 0.945 \times 0.55 = 2.6$ , assuming 70% of the energy being emitted in 400 ms in the same way as before. Finally, the observed UL on the total energy becomes, for ORCA4+ARCA1:

$$E_{\nu}^{90\%} = \frac{S^{90\%}}{S} \times E_{\nu}^0 = \frac{5.11}{2.6} \times 3 \cdot 10^{53} = 5.9 \cdot 10^{53} [\text{erg}] \quad (7.3)$$

### 7.1.3 Gravitational wave trigger S200114f: results

About two months after the first unmodelled trigger was sent, a second alert of this type was received, see GCN #26734 <sup>4</sup>. Contrary to S191110af, this second alert was not retracted, and the event was relatively well localised within the Galactic Plane, and with a position compatible with Betelgeuse coordinates. This made of this candidate of interest for the astrophysics community. At that time, ARCA was not taking data due to ongoing operations at the shore station, and the analysis was carried out with the four ORCA lines active.

The same approach as the one discussed for S1901114af was used for the follow up of this event. The number of coincidences in the multiplicity selection 6-10 and the trigger level over 400 ms as measured in ORCA are shown in Fig. 7.3 (top) as a function of time. During the search window, the detection efficiency was 98.5% (Fig. 7.3 bottom), with a large fraction of active PMTs. In this case, two events were observed during the search window, i.e. coincidence level 2 at  $(T_0-39) + 400$  ms, while 1.4 were expected from background. This yields a p-value of 40%, which is not a significant observation, and the corresponding 90% upper limit is  $S^{90\%} = 4.448$  signal events, obtained with Feldman and Cousins.

From these results, constraints on the source distance and the total energy emitted in neutrinos were set, as indicated in the previous subsections. Since no electromagnetic counterpart was observed, the failed CCSN model of  $40 M_{\odot}$  used in the sensitivity studies (see Chapter 5) was also incorporated to the analysis this time. The lower limits on the CCSN distance are summarised in Table 7.1. The Galactic coverage provided in the Table 7.1 is evaluated from model in Fig. 4.2, giving the probability of a CCSN occurring below a certain distance. The upper limit on the total energy emitted in neutrinos, assuming a fixed distance of 10 kpc and a mean neutrino energy of 15 MeV, is evaluated as of  $E_{\nu}^{90\%} = 2.9 \times 10^{53}$  erg, at the level of the typical energies expected for CCSN events.

Table 7.1: Lower limits at 90% confidence level on the CCSN distance, for three different progenitors. The Galactic coverage is underlined in the last column.

Progenitor	$d_{90\%}$ [kpc] (lower limit)	Galactic coverage
11 $M_{\odot}$	6.1	10-15%
27 $M_{\odot}$	11.5	~65%
40 $M_{\odot}$	21	~98%

<sup>4</sup><https://gracedb.ligo.org/superevents/S200114f/view/>

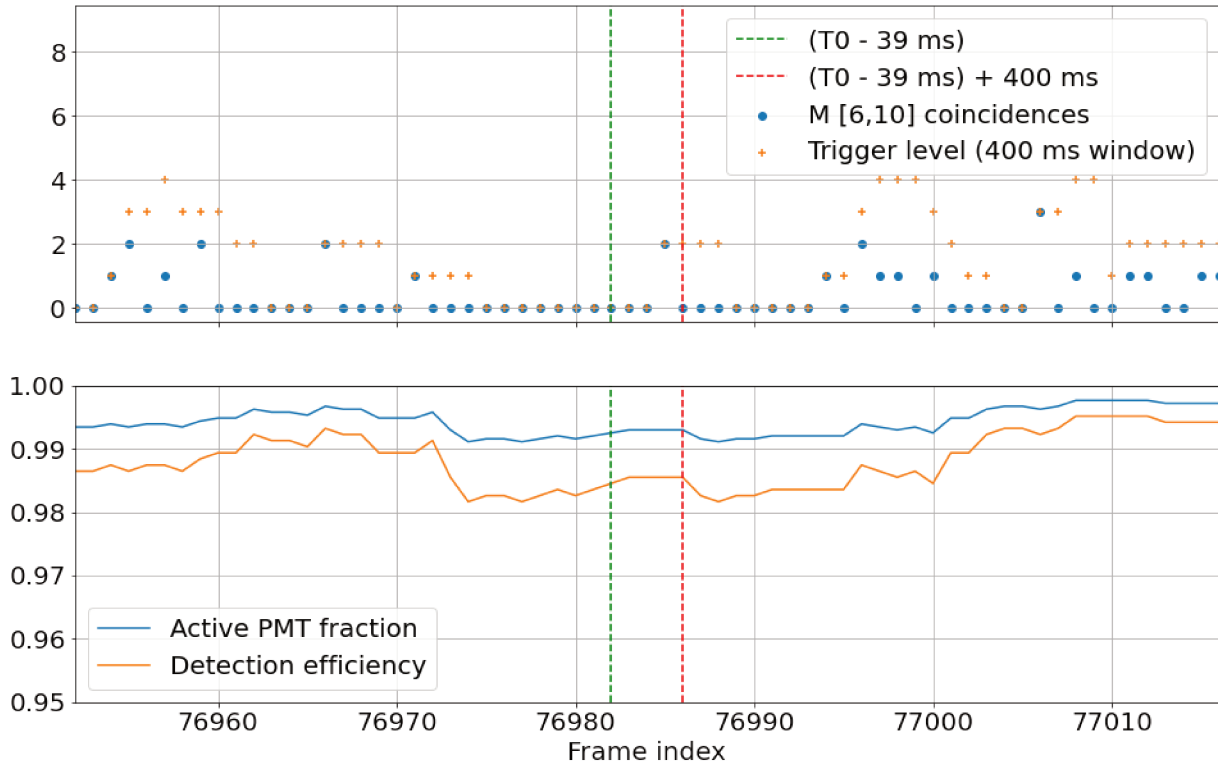


Figure 7.3: Top: Number of events observed in data with M between 6 and 10 (blue points), and the corresponding trigger level (orange cross), which is accumulated over the last 400 ms, as a function of time. Bottom: Time evolution of number of active PMTs (blue line), i.e. not in high-rate veto, and the associated detection efficiency of the CCSN trigger (orange line). The green and red dashed lines indicate the start and stop of the search window.

## 7.2 Determining the mean neutrino energy of CCSN neutrinos

In this section, we aim at constraining the CCSN neutrino energy spectrum. Considering only the  $\bar{\nu}_e$  contribution from IBD interactions, the CCSN neutrino energy spectrum depends on three parameters: the total energy emitted in neutrinos, the spectral pinching shape parameter and the mean neutrino energy. The focus is set here on the determination of the mean neutrino energy and the correlation with the  $\alpha$  parameter and the total amount of emitted signal reaching the detector.

Since the KM3NeT detectors are not able to reconstruct MeV neutrinos on an event-by-event basis, the total energy emitted in neutrinos cannot be directly measured. However, from a non-observation of triggered events, the total energy released through neutrinos can be constrained as explained in section 7.1, with an example of results reported in GCN #26249. Although the total neutrino luminosity may be estimated by other neutrino detectors, e.g. JUNO will have a good sensitivity in the case of  $\bar{\nu}_e$  spectrum [179], a signal scale accounting for the total energy and the distance, defined in Eq. 7.5, will be used as a parameter to be determined in this analysis.

A simplified CCSN spectrum model has been adopted here, assuming that the 80% of the total  $\bar{\nu}_e$  luminosity is emitted in the first 500 ms, and the total energy to be emitted in equal amount among the 3 flavors. This flux was previously used in the ANTARES-KM3NeT Collaboration for the CCSN sensitivity study [180, 121]. The expression of the time integrated flux (fluence) as a function of the neutrino energy, for a source at a distance  $d$ , is the following (Equations 4.2 and 4.3):

$$F_{\nu}^{SN}(E_{\nu}) = \frac{0.8}{4\pi d^2 \text{kpc}^2} \cdot \frac{L_{\nu}}{6 \cdot \langle E_{\nu} \rangle} \cdot E_{\nu}^{\alpha} \cdot \frac{\exp(-(1 + \alpha) \frac{E_{\nu}}{\langle E_{\nu} \rangle})}{\text{Norm}} \quad (7.4)$$

This signal scale is defined as a normalisation factor with respect to the benchmark values  $L_{\nu}^0 = 3 \times 10^{53}$  erg and  $d_0 = 10$  kpc, as in Eq. 7.5. This is used to account for the fact that fitting to a model with a different signal scale may lead to a different fitted mean energy and  $\alpha$ .

$$\text{signal scale} = \frac{L_{\nu}(\text{erg})}{L_{\nu}^0} \times \frac{d_0^2}{d(\text{kpc})^2} \quad (7.5)$$

In order to have an estimate of the energy resolution of the detector, we profit of the fact that neutrinos with a higher average energy will produce more events at high multiplicities. Thus, the number of events seen as a function of the multiplicity will depend on the average neutrino energy. This is illustrated in Fig. 7.4, where the multiplicity distribution for different mean neutrino energies are shown.

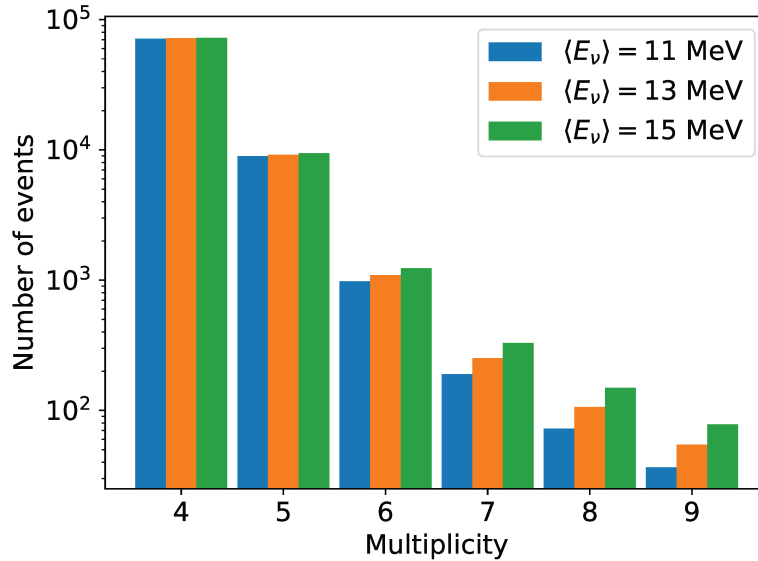


Figure 7.4: Number of events expected in ORCA+ARCA, from signal plus background, as a function of the multiplicity for different mean neutrino energies (different colors indicated in the legend). Signal is assumed to have the benchmark values ( $L_{\nu}^0$  and  $d_0$ ) and  $\alpha=3$ .

Simulations for different sets of the signal scale, the mean neutrino energy ( $\langle E_{\nu} \rangle$ ) and the spectral pinching shape parameter,  $\alpha$ , have been performed. The corresponding number of events is compared with the background expectation value over 500 ms.

A Poisson  $\chi^2$  is used to perform a fit of the signal scale, the mean neutrino energy and  $\alpha$ . This  $\chi^2$  is computed summing over bins in multiplicity (M), from M=5 to M=9, as in Eq.7.6:

$$\chi^2(\text{signal scale}, \langle E_\nu \rangle, \alpha) = 2 \sum_{M=5}^{M=9} (\mu_M - n_M + n_M \times \ln(\frac{n_M}{\mu_M})) \quad (7.6)$$

where  $\mu_M$  is computed as the signal plus background expectation. The number of observed events ( $n_M$ ) with a given signal scale,  $\alpha$  and  $\langle E_\nu \rangle$  is simulated at each multiplicity from the sampling of the Poisson distribution:

$$n_M = \text{Poisson}(\mu_M^{bg} + \mu_M^{sg}) \quad (7.7)$$

This  $\chi^2$  is scanned over all possible hypotheses and minimised to find the best estimate of the fitted parameters. For the combined results, the number of signal and background events in ORCA and ARCA are summed up for each multiplicity in the  $\chi^2$  evaluation.

The multiplicity range used here has been chosen as no change in the results is observed by adding lower multiplicities, while high M are dominated by statistical fluctuations due to the low number of events. Background is verified to have Poissonian behavior within the multiplicity range used from data distributions. The true values of the mean neutrino energy and the pinching-shape parameter are set to  $\langle E_\nu \rangle = 13$  MeV and  $\alpha=3$ , respectively. Two different values for the true signal scale are tested, 1 and 4.

The approach followed in [181] is used to evaluate the confidence level from the chi-square difference for each hypothesis ( $\chi_i^2$ ) with respect to the minimum ( $\chi_{\min}^2$ ) value. Since the three fitted parameters are not independent, the number of effective degrees of freedom of the  $\chi_i^2 - \chi_{\min}^2$  distribution needs to be evaluated. For this, the distribution of the minimum  $\chi^2$  value over realisations is drawn. This distribution is compared in Fig. 7.5 to the theoretical  $\chi^2$  function for 4 (orange) and 5 (blue) degrees of freedom ( $q$ ). One infers that the effective number of degrees of freedom is equal to one, which is given by the difference between the number of data points (5) and the value of  $q$  obtained from the distribution ( $q=4$  provides the best match). This means that the three fitted parameters are correlated and result in an only effective degree of freedom. From this result, one can concludes that it will be quite difficult to set strong constraints on these parameters unless a prior information on two of the parameters exists.

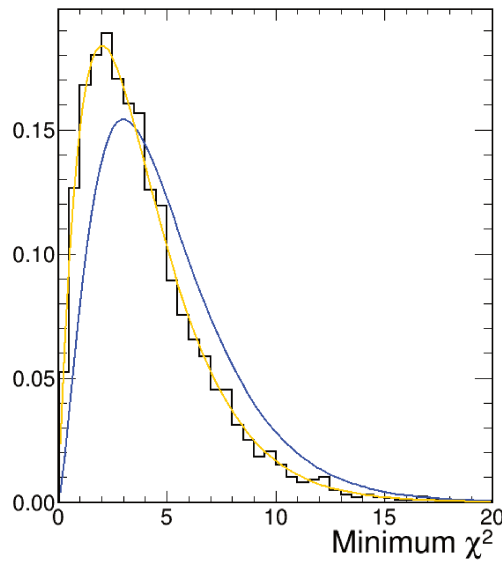


Figure 7.5: Distribution of the minimum  $\chi^2$  values over pseudo-experiments (black histogram). This is compared to the theoretical  $\chi^2$  function for different degrees of freedom:  $q=4$  (orange) and  $q=5$  (blue).

The confidence level contours obtained are shown in Figures. 7.6 and 7.7. The first one shows

the limits obtained in the 2D space (signal scale -  $\langle E_\nu \rangle$ ) with fixed  $\alpha$ , with  $\alpha$  measured with a 10% uncertainty, and with  $\alpha$  free in the fit. The second one provides the limit in the 2D space ( $\alpha - \langle E_\nu \rangle$ ) for a fixed signal scale, which is considered known. As expected, there is degeneracy between  $\langle E_\nu \rangle$  and the pinching shape parameter  $\alpha$ , as well as between the signal scale and the mean neutrino energy.

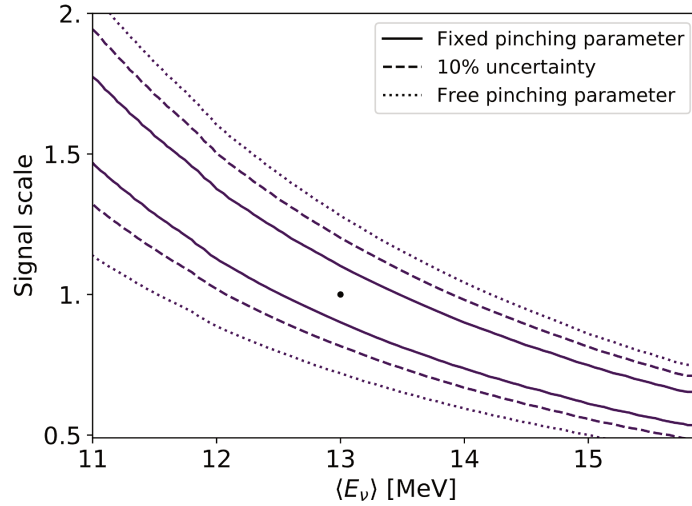


Figure 7.6: Confidence level contours at 90% CL as a function of the signal scale and the mean neutrino energy,  $\langle E_\nu \rangle$ . Three options are studied for the spectral pinching shape parameter:  $\alpha$  free in the fit,  $\alpha$  known with 10% uncertainty, and  $\alpha$  fixed. The red dot indicates the true value.

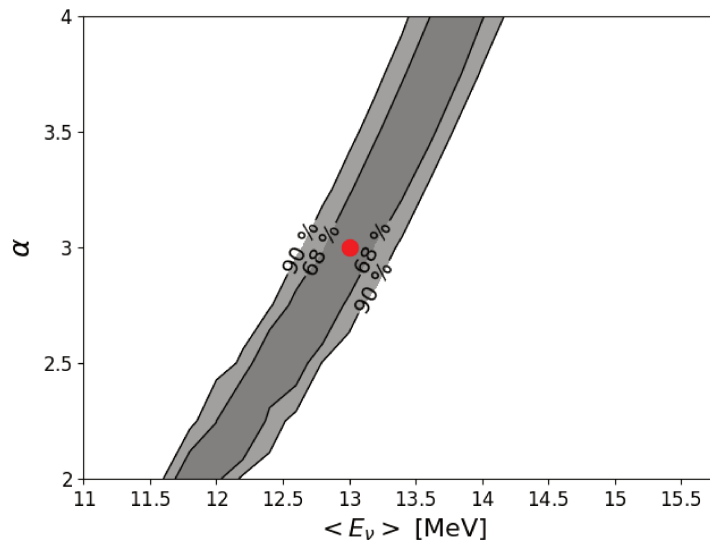


Figure 7.7: Confidence level contours at 68 and 90% as a function of 2 fitted parameters of the model: the mean neutrino energy ( $\langle E_\nu \rangle$ ) and the pinching shape parameter ( $\alpha$ ). The true value is indicated by the red dot, with the signal scale fixed to 1.

Figure 7.8 shows the distribution of the fitted energies over simulated realisations for three different cases: if the signal scale and the pinching parameters  $\alpha$  are known, and if they are known with uncertainties of 10% and 20%. The spread of the distribution gives an energy uncertainty below 0.5 MeV assuming the signal scale and the pinching shape parameters are known a priori with an uncertainty of 10%. For larger uncertainties (20% distribution), the fit starts to prefer the values at the edges in the allowed range, so part of the fits are failed and the distribution differs from a Gaussian, making the

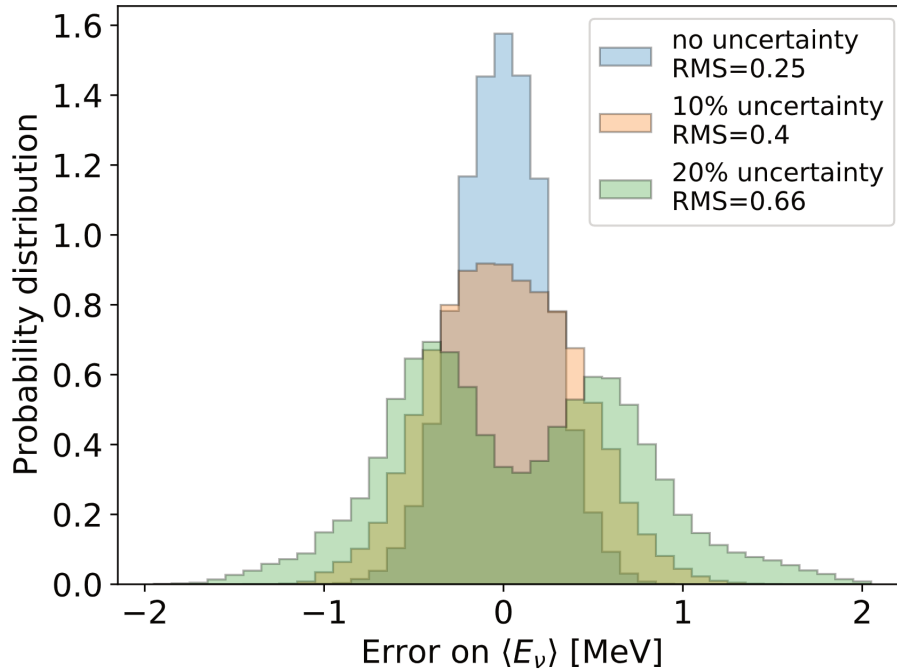


Figure 7.8: Probability distribution of the difference between the fitted and the true energies over realisations (energy error): with signal scale and  $\alpha$  known (blue), and with this two parameters estimated with 10% (red) and 20% (green) uncertainties. The corresponding error on the mean energy is given by the RMS. This is evaluated with the combination of ORCA and ARCA for a CCSN flux similar to the one predicted for the  $11 M_\odot$  progenitor at 10 kpc.

energy estimation not reliable.

Super-K and Hyper-K detectors might be able to have an estimate of the pinching parameter, the mean neutrino energy and the total energy released in neutrinos (see [182]). In particular, the future Hyper-K detector will measure the value of  $\alpha$  with an uncertainty of  $\sim 7\%$  ( $\sim 11\%$  for Super-K). Using an event-by-event energy reconstruction, they are able to estimate the mean neutrino energy with an uncertainty of  $\sim 2\%$  (Hyper-K) and  $\sim 6\%$  (Super-K). Other experiments, such as JUNO [183] or HALO [184], will accurately measure the neutrino spectrum.

Using coincidences between different optical modules, IceCube achieves an energy resolution of  $\sim 30\%$  with the actual configuration, assuming the other degenerated parameters are known [185]. Using coincidences between PMTs in the same DOM (multiplicity), and considering a CCSN explosion at 10 kpc with a flux radiated in neutrinos equivalent to that of the  $11 M_\odot$  progenitor, observed by ARCA and ORCA, KM3NeT can reach an energy resolution of  $\sim 3\%$  if the signal scale in neutrinos and  $\alpha$  are measured with a  $\sim 10\%$  uncertainty. This is estimated with the width of the energy distribution over the fitted realisations in Fig. 7.8.

Aside from the measurement of the mean neutrino energy and pinching shape parameters averaged over the full emission, the different models predict a different time evolution of  $\langle E_\nu \rangle$  and  $\alpha$ . This can be seen in Fig. 4.7 as example. According to this model  $\langle E_\nu \rangle$  increases with time, since  $\nu_x$  interactions at higher energies are produced at later times, and  $\alpha$  decreases with time. This could be confirmed by fitting the two parameters in the two different time windows, at the beginning and end of the detected flux. This could not be done during the thesis but is something that can be implemented from

the developed framework in a future step.

### 7.3 Sensitivity to fast time variations in the neutrino lightcurve.

Anisotropic hydrodynamical instabilities taking place during the CCSN accretion phase have been predicted by state-of-the-art 3D simulations, and could play an important role in the explosion mechanism. In particular, the Standing Accretion Shock Instability (SASI) is believed to enhance the neutrino heating, favoring the energetic explosion, and could explain the neutron star kick effect that has been observed. The SASI instability produces fast time variations in the neutrino lightcurve with a characteristic oscillation frequency over a specific observer direction. The aim of this section is thus to study the sensitivity of KM3NeT to the SASI features in the neutrino lightcurve.

#### 7.3.1 Event selection

Supernova lightcurve studies (and in general low-energy analyses) rely on the analysis of the aggregate detector hit rate on a time scale of 1 to 3 ms for a duration of a few hundreds milliseconds.

The use of single rates (L0) is disfavored by strong spatially and temporally correlated effects induced by bioluminescence, preventing any approximation of the background as a stationary poissonian or gaussian noise process. The following analysis is therefore limited to all coincidence events.

The 10 ns coincidence window used in the multiplicity definition and coincidence-based analyses is optimised for events with many time-correlated photons reaching the DOM, that can exhibit higher time dispersion among the hits. This optimisation is done by maximizing the efficiency, i.e. reducing as much background as possible losing the smaller fraction of signal. Moreover, the selection is done only with coincidence windows which are large enough not to be dominated by short afterpluses ( $>3$  ns) and the electronic response, but short enough to reject the maximum of random coincidences without significantly impacting the expected signal ( $<10$  ns).

For double coincidence data, reducing the time window to 5 ns allows to reduce by a factor two the background of random coincidences, which are the origin of time correlations in the background. Considering the standard deviation of the hit time difference equal to the PMT transit time spread of 2.1 ns, this selection preserves  $\geq 95\%$  of the signal. In Fig. 7.9, the signal loss from considering all coincidences from a same neutrino interaction in different PMTs of a DOM compared to applying 5 ns coincidences is shown to be smaller than 5%.

The detected neutrino lightcurve has been simulated for a  $27 M_{\odot}$  and a  $20 M_{\odot}$  stellar progenitors, and a failed CCSN model of  $40 M_{\odot}$  (see Section 5.3). The width of the time bin has been optimised to maximize the sensitivity for the model independent method (defined above in subsection 7.3.3) while keeping resolution to short time structures ( $<10$  ms features), by comparing the results for different time bins between 1 ms and 6 ms. The optimal bin size is found to be 2 ms. The method will be discussed for ARCA, which represents a higher instrumented volume and thus will allow for a better result in terms of time resolution due to higher events statistics per time bin.

The signal rates are Poisson random outcomes of the expectation values given by the models in each time bin. Muon and optical backgrounds have been included using the background simulation based on data that has been introduced in section 5.3.1. Background and signal values in each bin are summed to compute the total number of events per time bin,  $R_i$ :

$$R_i = \text{Poisson}(\mu_{s,i} + n_{b,i}) \quad (7.8)$$

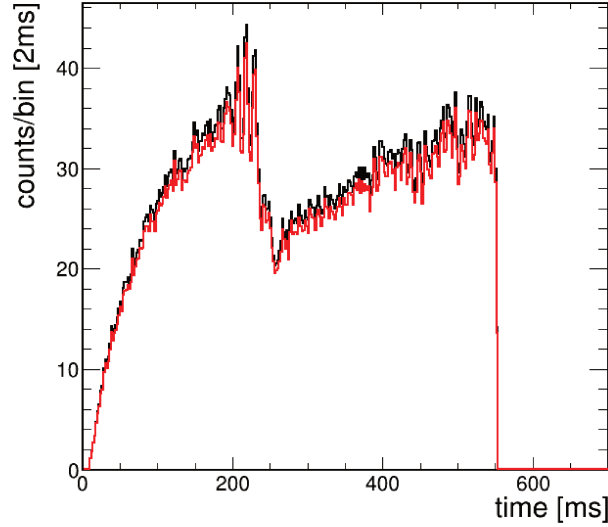


Figure 7.9: The detected neutrino lightcurve in 1 KM3NeT building block for a CCSN signal at 10 kpc, a the  $27 M_{\odot}$  progenitor. In black, all coincidences from the same CCSN neutrino interaction. In red, using a 5 ns coincidence time window.

Results are shown in Fig. 7.10 for the detected lightcurve in ARCA at 5 kpc with signal plus background. On top on the left for the  $27 M_{\odot}$  progenitor, on the right top for the  $20 M_{\odot}$  model. On the bottom, for the  $15 M_{\odot}$  progenitor (left) and the  $40 M_{\odot}$  (right) progenitors.

### 7.3.2 Analysis method

The Fourier Transform (FT) has been performed to see if it is possible to recover the frequency of the SASI oscillations. We follow here the same approach as the one given by [186].

We focus on the time interval of duration  $\tau = 200$  ms around the lightcurve peak, indicated in Fig. 7.10 by the red dashed lines. As observed in Fig. 5.8, this interval contains the strongest SASI oscillations.

To suppress effects in the FT coming from the short time window where it is applied, the event rate in this time interval is multiplied by the Hann window function:

$$w(t) = 1 - \cos\left(\frac{2\pi t}{\tau}\right)$$

The Fourier transform of  $R_H(t) = R(t) \cdot w(t)$  is in the discrete case is given by:

$$h(f_k) = \Delta \sum_{j=0}^{N_{bins}-1} R_H(t_j) e^{-2i\pi t_j f_k}$$

The time interval defined for the analysis is split into  $N_{bins} = 200$  bins, each of which has a width of  $\Delta = 1$  ms. The Fourier transform of the binned data gives values for the discrete frequencies  $f_k = k \times \delta f$  with the frequency spacing  $\delta f = \frac{1}{\tau} = 5$  Hz, from  $f = 0$  to  $f_{max} = \frac{1}{2\Delta} = 500$  Hz.

The spectral power is finally defined as:

$$P(f_k) = 2 \frac{|h(f_k)|^2}{N_{bins}^2}$$

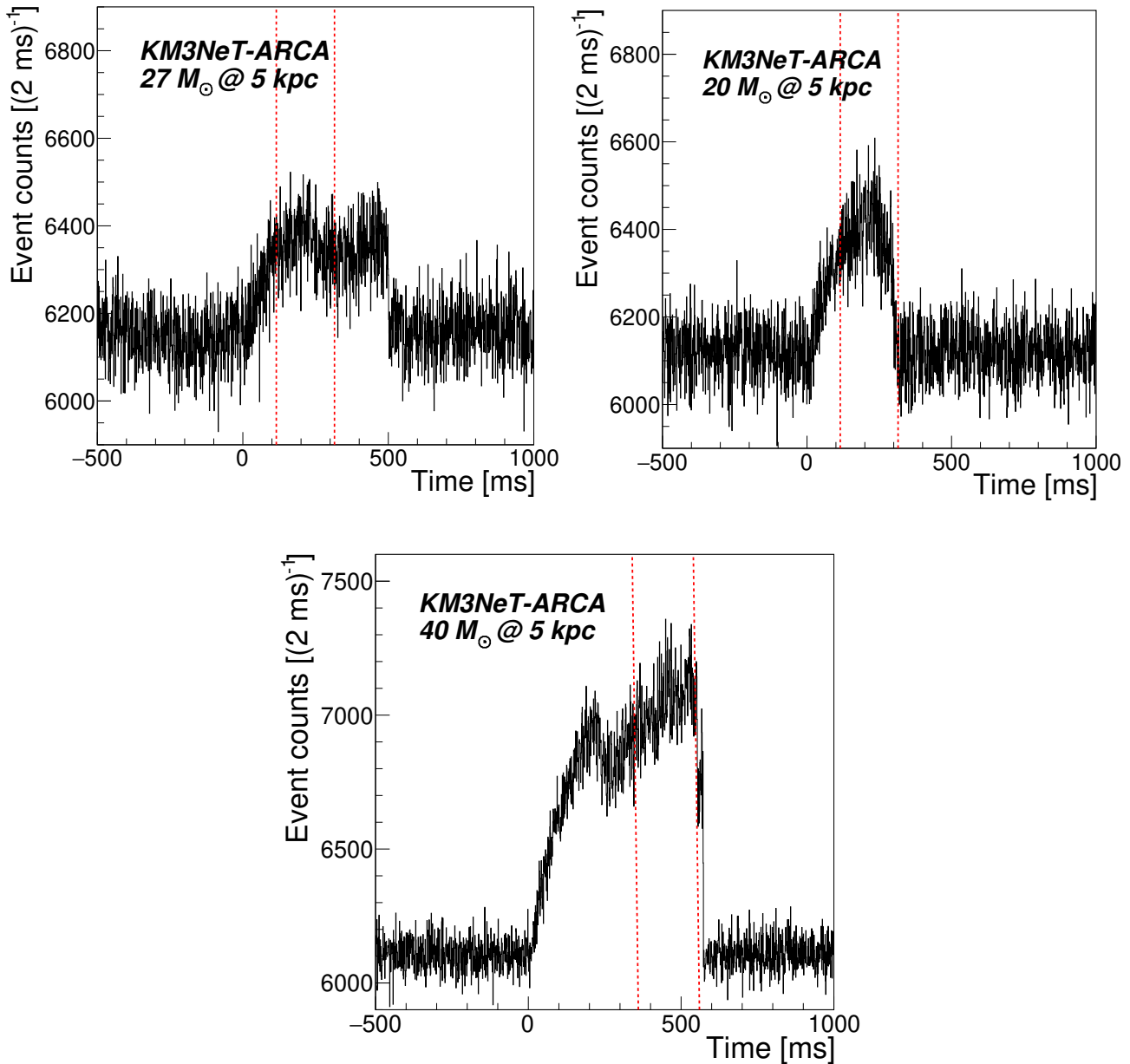


Figure 7.10: The detected lightcurve in ARCA including signal and background. For two different CCSN progenitor masses considered:  $27 M_{\odot}$  (top left) and  $20 M_{\odot}$  (top right). The failed CCSN of  $40 M_{\odot}$  is shown on the bottom plot. The source is considered at 5 kpc.

From now on, the method will be illustrated using the ARCA detector and the  $20 M_{\odot}$  stellar progenitor. Fig. 7.11 shows the Power Spectral Density (PSD) after applying the Fourier Transform (FT) to the ARCA lightcurve for three simulated realisations of a CCSN progenitor of  $20 M_{\odot}$  (right) explosion at 5 kpc. It is possible to identify the SASI frequency,  $f_{\text{SASI}} = 80$  Hz.

To estimate the sensitivity to the SASI oscillations peak in the power spectrum, MC pseudo-experiments (PEs) are used. Two different methods will be presented in the following subsections, a model-independent approach and a model-dependent approach. For illustration, the methods will be applied to the full ARCA detectors and the different considered progenitors. Then, a summary of the combined results will be provided for all the progenitors with presence of SASI emission.

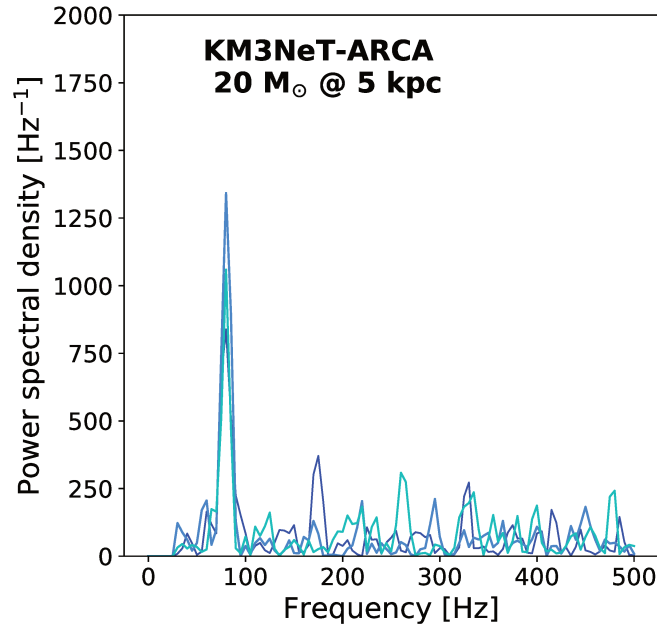


Figure 7.11: Expected observed power spectral density (PSD) in the ARCA detector for three simulated observations (different lines) of the  $20 M_{\odot}$  progenitor CCSN signal at 5 kpc, showing SASI emission on top of the background.

### 7.3.3 Sensitivity to fast time variation: frequency (model) independent approach

Within this approach, we look for a significant peak in the power spectrum, at any frequency, which is not likely to be produced from background. For this, we look at the distribution of maximum power as a function of the frequency over the PE.

The distribution of the maximum of the peak ( $PSD_{max}$ ) of the power spectrum (PS) as a function of its frequency is computed, for both background only and signal plus background cases. These distribution are shown in Fig. 7.12 for the ARCA detector: for background only (left) and for signal ( $20 M_{\odot}$  progenitor at 5 kpc) plus background (right). The background power spectrum is shown to be flat in frequency. An excess of events around the SASI peak can be observed when signal is added.

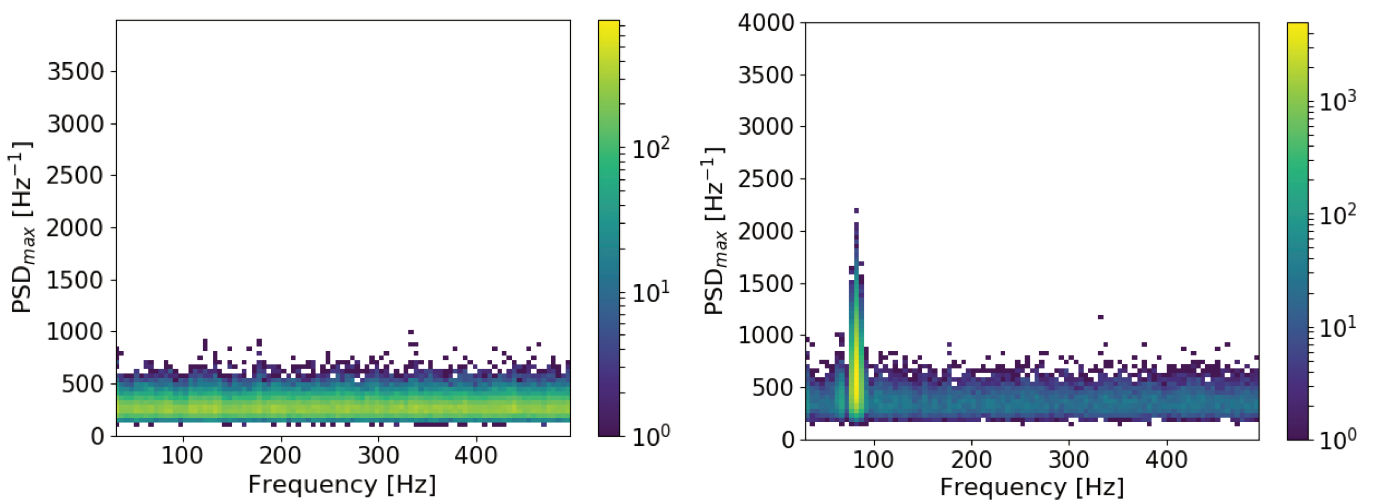


Figure 7.12: Distribution of maximum the power spectrum ( $PSD_{max}$ ) in ARCA as a function of frequency, among the background PE, for ORCA (left) and ARCA (right).

The background cumulative distribution function (CDF) is computed by integrating the 2D distribution in frequency, normalizing it to 1, and then doing the cumulative. The final background probability distribution, given by the complementary (1-CDF), is shown in Figure 7.13 for ARCA (left) and ORCA (right), for the  $40 M_{\odot}$ ,  $27 M_{\odot}$  (left) and the  $20 M_{\odot}$ . Finally, the background PDF is compared to the signal expectation, given by the mean over pseudo-experiments, to evaluate the probability of observing it from background and thus, the sensitivity to this SASI peak.

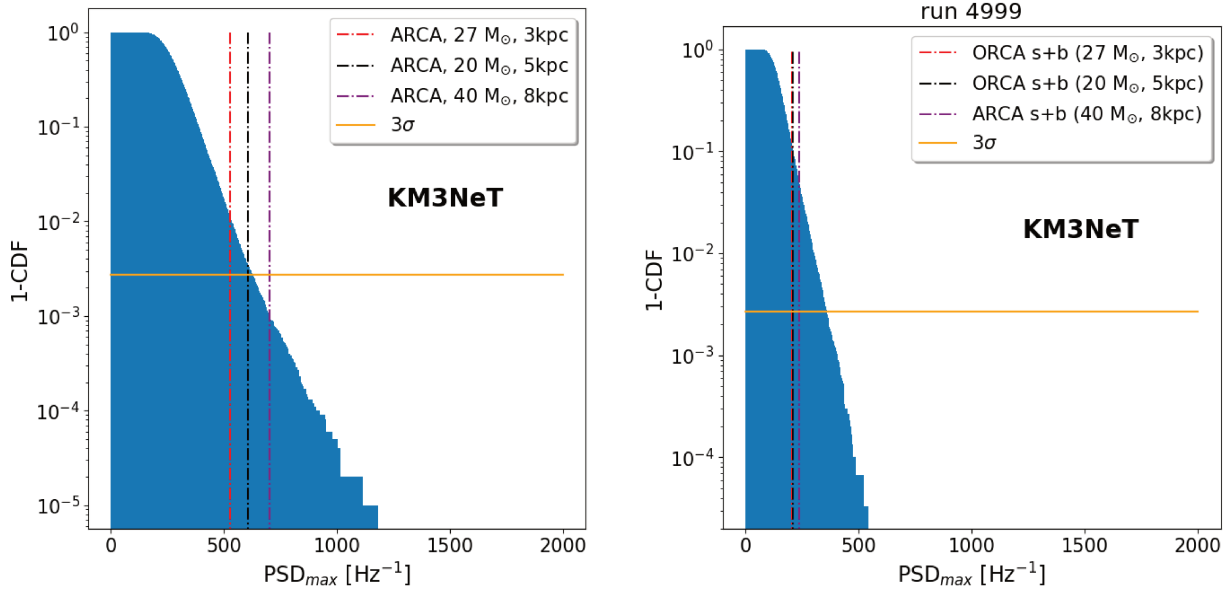


Figure 7.13: Complementary background CDF built from ARCA (left) and ORCA (right) data (blue distributions) as a function of the maximum power (model independent approach). The horizontal line (orange) indicates the  $3\sigma$  value. The vertical dashed lines (red, black and purple) correspond to the  $PSD_{max}$  expectation for the signal plus background case, assuming respectively the  $27 M_{\odot}$ ,  $20 M_{\odot}$  and  $40 M_{\odot}$  progenitor at 10kpc.

### 7.3.4 Sensitivity to fast time variation: frequency (model) dependent approach

Within this approach, we try to benefit from the fact that we know in advance, from the output of numerical simulations, the frequency of the SASI oscillations to increase increase the sensitivity and look for an increase of the spectral power around the frequency of interest.

An optimised symmetric frequency window is chosen for this analysis, centred in the expected value and covering the expected spread in frequency that will be observed,  $f \in [60, 100]$  Hz for the  $20 M_{\odot}$  and  $27 M_{\odot}$  progenitors, and  $f \in [120, 160]$  Hz for the failed CCSN progenitor of  $40 M_{\odot}$ . The distribution of the deposited energy in this frequency range is computed both for the background-only hypothesis and for the hypothesis of signal plus background. The distributions for the two hypotheses are shown in Fig. 7.14 for ARCA, assuming the  $20 M_{\odot}$  progenitor at 5 kpc.

From these distributions, the complementary background CDF is built and compared to the expected values for the signal hypothesis, defined from the mean power integral over PEs to get the sensitivity to the SASI peak. The results are shown in Fig 7.15 the different signal hypotheses (CCSN progenitors and distances).

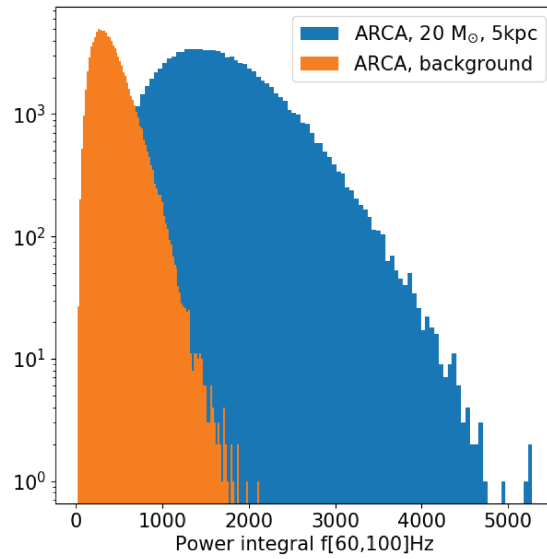


Figure 7.14: Distribution of the total power expected in the ARCA detector within the frequency range of the search. The background only hypothesis is drawn in orange, and the signal plus background in light blue. The considered signal corresponds to the  $20M_{\odot}$  progenitor at 5 kpc.

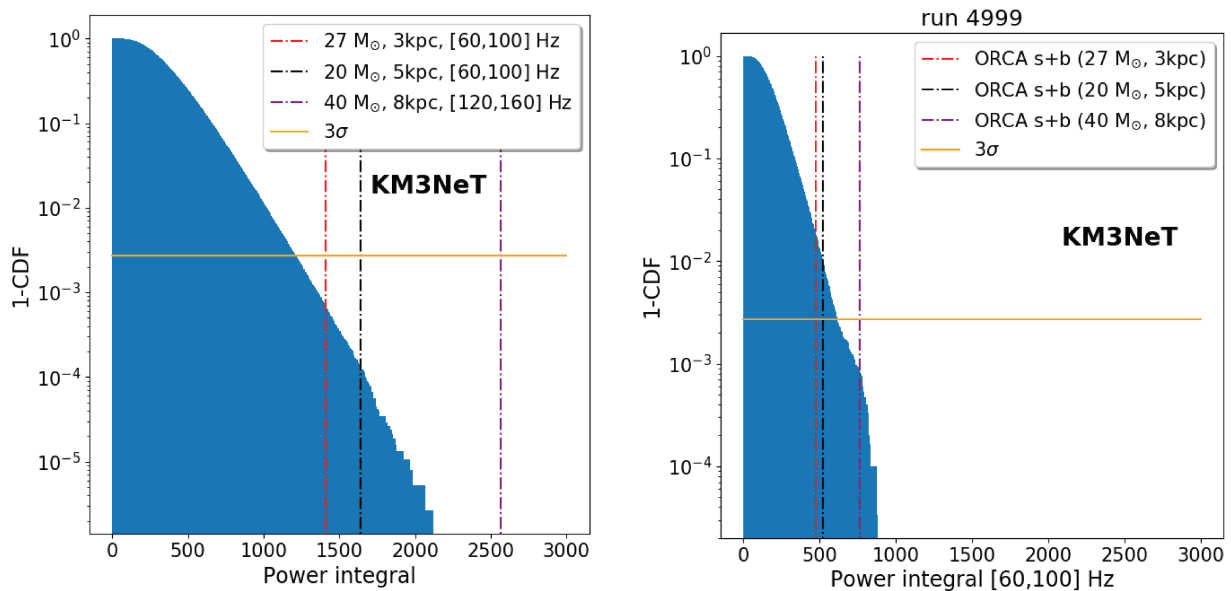


Figure 7.15: Complementary background CDF built from ARCA (left) and ORCA (right) data (blue distributions) as a function of the power integral around the SASI frequency predicted by the model. The frequency interval considered is indicated in the legend. The horizontal line (orange) indicates the  $3\sigma$  value. The vertical lines (dashed red, black and purple) correspond to the expectation for the signal+background case, assuming respectively the  $27 M_{\odot}$ ,  $20 M_{\odot}$  and  $40 M_{\odot}$  progenitor at 10kpc.

### 7.3.5 Summary of the results

Note that the sensitivity is reported here as the expected significance. Once the sensitivity is evaluated for the ORCA and ARCA detectors as illustrated in subsections 7.3.3 and 7.3.4, one can combine the results with the weighted approach explained in 6.6.2. Due to the intrinsic physical delay between the ORCA and ARCA detectors, the synchronised combination of the data is under investigation.

Results are given in Table 7.2, for the KM3NeT distance sensitivity horizon to SASI oscillations. The horizon is taken as the distance up to which a expected significance of about  $3\sigma$  is achieved with the model independent search for the two CCSN progenitors. For the failed CCSN, a more conservative horizon is taken, reaching almost  $4\sigma$  and above  $5\sigma$  in the model independent and model dependent search, respectively. The Galactic CCSN coverage is computed as the fraction of Galactic progenitors expected below the horizon distance, inferred from Fig. 4.2, and reported in Table 7.2.

The systematic effects related to the uncertainties on the PMT QE (10%), the absorption length (3%) and the bioluminescence conditions producing changes in the number of active PMTs ( $<0.1\sigma$  in ARCA,  $0.2-0.4\sigma$  in ORCA) have been evaluated and translated into an error in the SASI sensitivity, provided in the Table.

Table 7.2: Sensitivity results with the combination of ORCA and ARCA, for the three different stellar progenitors considered. The distance horizon and the corresponding coverage are also provided.

Progenitor	d [kpc]	Method 1: Search for peak in spectrum	Method 2: Search for power excess around $f_{\text{SASI}}$	Coverage of Galactic CCSN
27 $M_{\odot}$	3	$2.8 \pm 0.7\sigma$	$4.1 \pm 0.9\sigma$	3%
20 $M_{\odot}$	5	$3.2 \pm 0.7\sigma$	$4.5 \pm 0.9\sigma$	10%
40 $M_{\odot}$	8	$3.8 \pm 0.7\sigma$	$>5\sigma$	35%

# Chapter 8

## Timing and pointing the CCSN neutrino signal

The current chapter explores the possibility of reconstructing the CCSN direction by triangulation combining experimental data of the different neutrino detectors is discussed as well as using the directional information of the KM3NeT multi-PM optical modules. In addition, the capability of inferring the arrival time of CCSN neutrinos is presented.

### 8.1 Combining experimental lightcurves for timing the CCSN neutrino signal

One of the key points in neutrino astronomy is the angular resolution, i.e. being able to point to the neutrino source. The recent multi-wavelength observations of explosive phenomena in the Universe, and in particular the multi-messenger detection of the binary neutron star merger GW170817 [54], have shown the crucial importance of combining the different information brought by the neutrino, gravitational wave and electromagnetic signal to unveil the mechanisms riding these astrophysical events. For that reason, fast and precise direction reconstruction of the neutrino emission, as well as of the arrival time of the signal, are important for an efficient multi-messenger follow-up.

This section reports on the possible strategy to be used for estimating the time delay between the arrival of the neutrino signal observed by the different experiments, and its uncertainty. By exploiting these two measurements, one can use a triangulation method to infer the source localisation on the sky. The possibility of using the triangulation technique has been addressed in several works [187, 188, 189, 190, 191, 192]. In fact, using triangulation between CCSN neutrino experiments was first proposed in 1992 [187]. That work proposed to infer the uncertainty on the arrival time delay between a pair of detectors from the number of the detected neutrinos in the bulk of the emission and its duration. A Kolmogorov test for direct lightcurve comparison between detectors was later mentioned in [188], where a Rao-Kramer evaluation of the time uncertainty is carried out, with the conclusion that low event statistics detectors available at that time were not useful for triangulation. In [189], the triangulation method is revisited and a rough estimate of the arrival time uncertainty for each detector is computed assuming a generic neutrino lightcurve with an exponential rise. In [190], a more detailed lightcurve template is used. The use of the time delay estimate between the first detected events in each experiment was proposed in [191]. For the latter method, an almost background-free experiment is required in order to reach a good timing accuracy. This implies that the use of large volume Cherenkov neutrino telescopes, as IceCube and KM3NeT, is less effective. Timing with the first

events with an exponential fit was also proposed in [192].

The new idea investigated during my thesis is making use of the fit to the full spectrum, as proposed in previous works, but in a model independent way that relies on matching experimental detection rate curves. For this, current and near future detectors with large supernova detection rate statistics and sensitive to the same interaction channel,  $\bar{\nu}_e$  interacting with free protons through Inverse Beta Decay (IBD), are taken in consideration to test the method performance. Using detectors sensitive to different neutrino flavor and interaction channels may introduce a bias in the results. Such approach requires data sharing between the detectors, or having an independent and automatized common analysis platform, which can be realized within the SNEWS global network [193].

For this work, the following experiments are considered: the underground detectors, Super-Kamiokande [194] and Hyper-Kamiokande [195], and the high-energy neutrino telescopes, IceCube [196] and KM3NeT [21]. The main interaction channel in water Cherenkov detectors is inverse beta decay (IBD) of electron anti-neutrinos ( $\bar{\nu}_e$ ) on proton targets. The positrons angular distribution is slightly forward-peaked and high energy events can be selected in order to exploit this directionality [172]. A good pointing for CCSN is hardly achievable in the water Cherenkov detectors with such technique. The JUNO scintillator detector is sensitive to both IBD and elastic scattering (ES) [197]. It is to be mentioned that JUNO can additionally use the IBD events to identify positrons and neutrons and reconstruct their positions. The direction along the line connecting the positions of both products can be used to infer the neutrino direction [198]. Detectors sensitive to ES interactions can provide information on the CCSN localisation. Nowadays, Super-Kamiokande is the only running detector with enough sensitivity to the ES channel to be able to point by itself to the source [199].

The results presented in this section have been published in Ref. [263], as well as the codes have been made public in [200].

### 8.1.1 Simulation

The CCSN neutrino detection rates are estimated through simulations for the different experiments. The proposed simulation, described in this section, relies on a simplified detector response characterisation and a simple parametric function for the evolution of the neutrino luminosity as a function of time. In particular, the detectors are described with two parameters: their effective mass and background.

Additionally, some approximations are made to simplify and speed up the simulations, that allow to easily reproduce the detected neutrino lightcurves. The main assumptions are the following: a fixed detector efficiency, considered time and energy independent, and a steady neutrino energy evolution. These approximations are physically motivated in the context of this work, and required for testing and optimising the method without access to the real detector's information and knowledge of the CCSN neutrino model.

### 8.1.2 Supernova neutrino fluxes

The all-flavour neutrino total luminosity is set to  $L_\nu^0 = 3 \times 10^{53}$  erg, as in [197]. It is equally divided among all neutrino flavours and between neutrinos and anti-neutrinos. This is consistent with the more accurate estimate of the  $\bar{\nu}_e$  fraction of about 0.14 that includes oscillations in the supernova mantle [172].

The time evolution of the neutrino luminosity is taken from [201] and it is described for  $\bar{\nu}_e$  as:

$$L_\nu(t) = \frac{L_\nu^0}{6} \frac{1}{\mathcal{N}} \frac{e^{-(t_a/t)^{n_a}}}{[1 + (t/t_c)^{n_p}]^{n_c/n_p}}, \quad (8.1)$$

where  $\mathcal{N}$  is used to normalise the function as follows:

$$\mathcal{N} = \int_0^\infty \frac{e^{-(t_a/t)^{n_a}}}{[1 + (t/t_c)^{n_p}]^{n_c/n_p}} dt. \quad (8.2)$$

For these studies the chosen parameters are:  $t_a = 0.035$  ms,  $t_c = 0.2$  ms,  $n_a = 2$ ,  $n_p = 20$  and  $n_c = 1.5$ . The lightcurve simulated using these parameters approximately follows the predicted accretion phase  $\bar{\nu}_e$  luminosity in [202]. The chosen value of  $n_c = 1.5$  guarantees the convergence of the luminosity integral. The luminosity curve with the assumed parameters is shown in Figure 8.1.

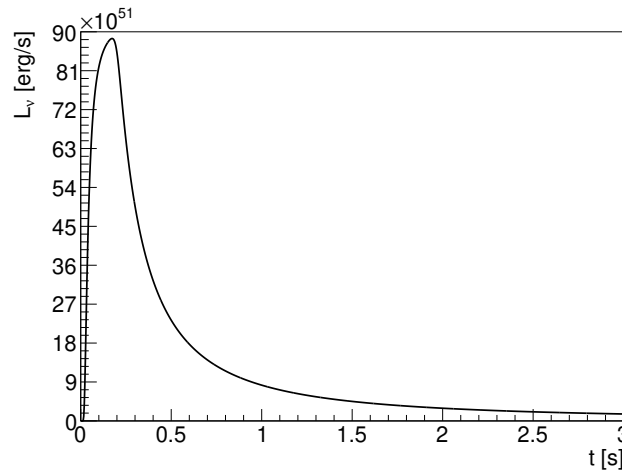


Figure 8.1: Time evolution of the neutrino luminosity in the considered simplified model.

The energy distribution can be described by a quasi-thermal distribution [202]:

$$f_E(E_\nu) = \frac{1}{\Gamma(1 + \alpha)} \left( \frac{1 + \alpha}{\langle E_\nu \rangle} \right)^{1 + \alpha} E_\nu^\alpha \exp \left( - \frac{(\alpha + 1)E_\nu}{\langle E_\nu \rangle} \right), \quad (8.3)$$

which depends on the average neutrino energy,  $\langle E_\nu \rangle$ , and the spectral pinching shape parameter,  $\alpha$ . Both parameters are generally varying with time. The typical range of the pinching shape parameter is  $2 \lesssim \alpha \lesssim 5$  [202].

Only the variation in time of the detection rates is relevant for this study. Therefore, the simulation follows the luminosity time evolution with a steady energy neutrino spectrum with  $\langle E_\nu \rangle = 14$  MeV and  $\alpha=3$ . The neutrino luminosity can be converted into a flux dividing it by the average neutrino energy. Assuming an isotropic neutrino emission from a source at a distance  $d$ , the differential neutrino flux is:

$$\frac{d\Phi}{dE_\nu}(E_\nu, t) = \frac{1}{4\pi d^2} \frac{L_\nu(t)}{\langle E_\nu \rangle} f_E(E_\nu). \quad (8.4)$$

### CCSN neutrino detection rates

As it is the main channel for the considered water detectors, only the inverse beta decay interaction channel is simulated.

Table 8.1: Simplified detector characteristics used as input for the simulation: effective mass in water equivalent units and total background rate.

	IceCube	ORCA	ARCA	Super-Kamiokande	Hyper-Kamiokande	JUNO
$M_{\text{eff}}$ [kton]	3500	90	180	22.5	560	22.5
$R_{\text{bg}}$ [Hz]	$\sim 3\text{e}6$	$\sim 1\text{e}6$	$\sim 2\text{e}6$	0	0	0
Reference	[170]	[203, 119]	[203, 119]	[186, 204, 205]	[186, 206]	[197]

The instantaneous event rate in the detector is estimated as the product of the differential neutrino flux,  $\frac{d\Phi}{dE_\nu}$ , the IBD cross section,  $\sigma_{\text{IBD}}$  [172], the number of targets per unit volume,  $2\frac{\rho N_A}{\mu_{\text{H}_2\text{O}}}$ , the detection efficiency,  $\epsilon_{\text{det}}$ , and the detector volume  $V_{\text{det}}$ :

$$R_{\text{sig}}(t) = \int_0^\infty \frac{d\Phi}{dE_\nu}(E_\nu, t) \sigma_{\text{IBD}}(E_\nu) \times 2\frac{\rho N_A}{\mu_{\text{H}_2\text{O}}} \epsilon_{\text{det}}(E_\nu) V_{\text{det}} dE_\nu. \quad (8.5)$$

The factor 2 comes from the two hydrogen atoms in a water molecule,  $\mu = 18 \text{ g/mol}$  is the molar mass of water,  $\rho$  is the density of water and  $N_A$  is the Avogadro number.

The detector properties are converted into the detector effective mass,  $M_{\text{eff}}$ , in the following way:

$$M_{\text{eff}}(E_\nu) = \rho \epsilon_{\text{det}}(E_\nu) V_{\text{det}}. \quad (8.6)$$

The detection efficiency depends on the neutrino energy, or more precisely, on the energy of the detectable interaction products. A constant efficiency is assumed above an energy threshold,  $E_\nu^{\text{min}}$ . Since this value is around the Cherenkov threshold, and below the energy range where supernova neutrinos are expected,  $E_\nu^{\text{min}} = 0$  is set for simplicity. This assumption removes the energy dependence of the  $M_{\text{eff}}$ . The detection rate is calculated as:

$$R_{\text{sig}}(t) = M_{\text{eff}} \frac{L_\nu(t)}{\langle E_\nu \rangle} \frac{1}{4\pi d^2} \times \int_{E_\nu^{\text{min}}}^\infty f_E(E_\nu) \sigma_{\text{IBD}}(E_\nu) 2\frac{N_A}{\mu_{\text{H}_2\text{O}}} dE_\nu = M_{\text{eff}} L_\nu(t) I, \quad (8.7)$$

where the simplified conversion parameter,  $I$ , is the same for all the detectors. For a CCSN at 10 kpc, this factor becomes:  $I \approx 4.3 \text{ erg}^{-1} \text{ kton}^{-1}$ .

The rates for future scintillator or other non-water detectors can be calculated using Equation 8.7, where  $M_{\text{eff}}$  is estimated in water equivalent units and  $N_{\text{target}}$  is the total number of targets in the detector:

$$M_{\text{eff}}^{\text{w.e.}} = \epsilon_{\text{det}} N_{\text{target}} \left( \frac{2N_A}{\mu_{\text{H}_2\text{O}}} \right)^{-1}. \quad (8.8)$$

### Simplified detector model

The detector model is described by two parameters: the supernova detection effective mass,  $M_{\text{eff}}$ , and the background rate,  $R_{\text{bg}}$ . The signal rates are estimated for each detector from Equation 8.7. Both the signal and the background rates are translated into an expected number of events per time bin. In order to simulate experimental fluctuations in the detected neutrino lightcurve, the number of events in each time bin is sampled assuming a Poisson distribution.

For the Super-Kamiokande and Hyper-Kamiokande detectors, the effective masses are taken from [186, 204, 206]. For JUNO, the expected number of proton targets is  $N_{\text{target}} = 1.5 \times 10^{33}$  [197], similar to Super-Kamiokande. The same effective mass in water equivalent units,  $M_{\text{eff}} = 22.5 \text{ kton}$ , is used

for both detectors. In this study, the background rates are negligible for Super-Kamiokande, Hyper-Kamiokande [205] and JUNO [197].

The assumed IceCube detector effective volume is 3.5 Mton [170]. The detector consists of 5160 optical modules, each containing one 10-inch photomultiplier. The background rate per optical module is about 300 Hz, taking an average value between standard and high efficiency optical modules.

The optical module of KM3NeT consists of 31 3-inch photomultipliers. Using nanosecond scale coincidences between the photomultipliers on the same optical module, the variable background from the bioluminescence can be suppressed [203]. The remaining background contribution is mostly coming from  $^{40}\text{K}$  decays in sea water and it amounts to a total rate of  $R_{OM}^{K40} \sim 500$  Hz per optical module [119]. The effective mass of the KM3NeT detectors is estimated as  $M_{\text{eff}} \approx 180$  kton for KM3NeT/ARCA and 90 kton for KM3NeT/ORCA from [203, Fig. 4, left]. The ARCA and ORCA detectors consist of 4140 and 2070 optical modules, respectively. The coincidence selection translates into a lower effective CCSN detection volume for KM3NeT/ARCA compared to IceCube, even if both have an instrumented volume of  $\sim 1$  km<sup>3</sup>.

The effective mass and the background rate for the different detectors used in this work are summarised in Table 8.1. The examples of the simulated experimental lightcurves are provided in Figure 8.2.

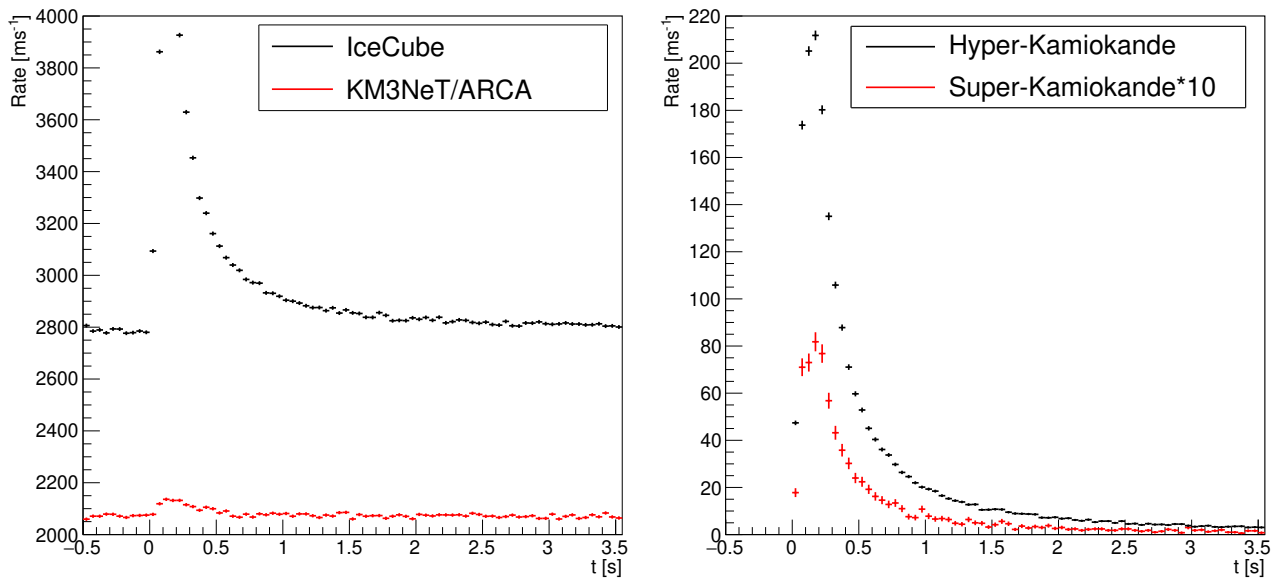


Figure 8.2: Expected neutrino lightcurves obtained with the described simulation, showing the number of event in 50 ms bins. On the left for IceCube (black) and ARCA (red), on the right for Hyper-Kamiokande (black) and Super-Kamiokande, zoomed vertically 10 times for visual purposes (red). The error bars for each bin correspond to the original statistical (Poisson) uncertainty on the number of events, scaled accordingly to the bin size.

### 8.1.3 Method

Two methods to estimate the time difference of the neutrino arrival times between two detectors have been investigated: the chi-square (section 8.1.3) and the cross-correlation (section 8.1.3). The triangulation method for the source localisation is reviewed in sections 8.1.3 and 8.1.3.

## Chi-square method

A method based on  $\chi^2$  minimisation has been developed and tested to infer the delay between two lightcurves. This technique is one of the traditional ways to verify the compatibility of two distributions and for parameter estimation. In this case, the estimated parameter is the time delay between the two detected neutrino lightcurves.

Several technical details on the  $\chi^2$  method are addressed in the current section: the construction of the chi-square function, the lightcurve normalisation, which takes into account the different background rates and detector efficiencies, the time window and the step size used to calculate the  $\chi^2$ .

### 1. Chi-square function

The  $\chi^2$  method was recently proposed in [190] for a similar purpose: defining the supernova emission time delay with respect to some model and estimating the uncertainty. The underlying distribution for the experimental lightcurve is a Poisson for each time bin, which assumes that the number of events in each time bin follows a Poisson distribution with a mean value equal to the average expected number of events computed from a CCSN neutrino emission model. This Poisson  $\chi^2$  expression cannot be used to compare two experimental lightcurves since it requires a known expectation value. Therefore, the approach is changed in this work from assuming a Poisson distribution for the content of each bin to a Gaussian. Given that the number of detected events follows a Poisson distribution, the bin size should be optimized in our method to make the Gaussian approximation valid.

Assuming a normal distribution of the number of events in each time bin, the  $\chi^2$  expression for the comparison of two experimental time-binned data sets is defined as follows:

$$\chi^2(\tau) = \sum_{t_i=t_{\min}}^{t_{\max}} \frac{((n_{t_i-\tau} - m_{t_i}) - E(n_{t_i-\tau} - m_{t_i}))^2}{V(n_{t_i-\tau} - m_{t_i})}, \quad (8.9)$$

where  $\tau$  is the time shift between the detected neutrino lightcurves,  $n_{t_i-\tau}$  is the number of observed events by the first detector in the time bin  $t_i - \tau$ ,  $m_{t_i}$  is the number of observed events by the second detector in the time bin  $t_i$ ,  $E(n_{t_i-\tau} - m_{t_i})$  and  $V(n_{t_i-\tau} - m_{t_i})$  are the expectation value and the variance of the difference in the number of events, respectively. For two normal distributions, the variance of the difference between the number of events corresponds to the sum of their squared standard deviations:

$$V(n_{t_i-\tau} - m_{t_i}) = V(n_{t_i-\tau}) + V(m_{t_i}) = (\sigma_{n_{t_i-\tau}})^2 + (\sigma_{m_{t_i}})^2. \quad (8.10)$$

The value of  $\tau = T_0^{\text{match}}$  obtained at the  $\chi^2$  minimum provides the best estimate of the true time delay between the two detectors,  $T_0$ .

### 2. Normalisation of the detected lightcurve

The expectation values still appear in the  $\chi^2$  expression in 8.10. Ideally, for the model independent approach that we are trying to build, one wants to get rid of this term. In fact, the lightcurves are normalised in a way so that signal and background expectations are almost the same for both detectors, then the expectation value  $E(n_{t_i-\tau} - m_{t_i})$  can be considered null for any  $t_i$  when  $\tau$  corresponds to the true shift. Such normalisation can be achieved in two steps. First, the mean detector background is subtracted from the lightcurve so that all combined detectors have a common baseline centered at 0. Second, a normalisation to the detector effective mass is applied in

order to account for the different detector efficiencies to the CCSN neutrino signal. Alternatively, this effect can be taken into account by normalising each lightcurve after background subtraction to have unit integral, i.e. scaling to the total amount of signal to which is detector is sensitive. The background expectation value can be taken from a time window in the detected neutrino lightcurve where CCSN signal is not present (off-signal zone) or it can be provided by each experiment based on a longer detector monitoring. In this study, an off-signal zone of 1 s duration is chosen for the background estimate.

Note that such lightcurve normalisation assumes a constant and fixed expectation value of the background rates and detector efficiencies. Even if this is in perfect agreement with the simplified simulations proposed earlier, this is generally not true in the real case. For instance, the neutrino energy spectrum may vary in time and an energy and time dependent detector efficiency may impact the results. Moreover, this approach assumes that the same neutrino flux is arriving to each site. But the observed lightcurve may change between experiments if they show different efficiency evolution or present different contributions from additional interaction channels. Therefore, the described normalisation can be improved to account for these effects by using a more detailed description of the detector response. But this requires an agreement for data sharing between detectors. However, introducing the time and energy dependent detector efficiency will only improve the simulation description if it is taken into account together with a realistic neutrino emission spectrum varying in time. The neutrino emission spectrum from detailed simulations differs across different models. This may bring a bias to a such sophisticated correction.

### 3. Chi-square calculation window

The signal arrival time is not known *a priori* in this model independent analysis. Therefore, a reference time is evaluated to define the window for the  $\chi^2$  calculation. The time window of  $[-300, 300]$  ms centred at the maximum of the detected lightcurve from one of the detectors is chosen for this analysis. The interval covers the transition between the background and the CCSN neutrino signal as well as the accretion phase, for which most of the neutrino emission is expected [202]. Using a time window too long may lead to a degradation of the performance since the optimisation will be more sensitive to background fluctuations. The  $\chi^2$  calculation window is fixed with respect to the less performing detector to preserve its background statistics during  $\tau$  scan. The choice of the fixed detector and the detector for the reference time definition is done to minimize the estimated time delay uncertainty. The procedure for the uncertainty estimation is given in section 8.1.3.

The detected lightcurves are provided as histograms with a fixed bin size. A bin width of 0.1 ms is chosen, and the same value is used for the time shift step  $\tau$ , in order to reach the  $\mathcal{O}(\text{ms})$  required resolution. The numbers of events,  $n_{t_i-\tau}$  and  $m_{t_i}$ , are calculated by summing the events of contiguous bins. The resulting effective bin size is optimised for each detector pair to reach the minimum of arrival time delay uncertainty,  $\delta t$ . Steps of  $t_{i+1} - t_i$  can be optimised in order to increase the calculation speed.

### Normalised cross-correlation

The cross-correlation can be used for matching two sets of time series [207] or for matching a time series with a template model [208]. The discrete cross-correlation is defined as:

$$\mathcal{C}(\tau) = (n \star m) = \frac{1}{N} \sum_{t_i=t_{\min}}^{t_{\max}} n_{t_i} m_{t_i-\tau}, \quad (8.11)$$

where  $n_{t_i}$  and  $m_{t_i-\tau}$  are the number of observed events by the first and the second detector in time bins  $t_i$  and  $t_i - \tau$ , respectively.  $N$  is the number of bins in the search window  $[t_{\min}, t_{\max}]$ , and  $\tau$  is the time delay between the two lightcurves. The function will present a maximum at  $\tau = T_0^{\text{match}}$ , allowing to estimate the time delay between the two detectors,  $T_0$ .

In order to account for the different effective masses and background rates of each detector, the zero-normalised cross-correlation is used. Each curve is normalised by subtracting its mean value and scaled by its standard deviation [207], which can be computed in the search window:

$$\tilde{n} = \frac{\sum_{t_i=t_{\min}}^{t_{\max}} n_{t_i}}{N}, \tilde{m} = \frac{\sum_{t_i=t_{\min}}^{t_{\max}} m_{t_i}}{N}, \quad (8.12)$$

$$\sigma_n = \sqrt{\frac{\sum_{t_i=t_{\min}}^{t_{\max}} (n_{t_i} - \tilde{n})^2}{N - 1}}, \quad (8.13)$$

$$\sigma_m = \sqrt{\frac{\sum_{t_i=t_{\min}}^{t_{\max}} (m_{t_i} - \tilde{m})^2}{N - 1}}. \quad (8.14)$$

One of the advantages of this method is that fast Fourier transformations can be used to speed up the calculations and the improvement of the response time can be significant for a large number of bins compared to the chi-square method.

### Estimating the performance of the lightcurve matching

Simulations of the different detected neutrino lightcurves are performed following the model described in section 8.1.1. An artificial delay of the neutrino signal observed between two sites,  $T_0$ , is applied to the first lightcurve. This  $T_0$  is drawn from a random uniform distribution between -30 and 30 ms. These values are chosen from the typical time delays expected for pairs of neutrino detectors,  $\Delta t_{ij} \approx 30$  ms, given that the Earth diameter corresponds to a time delay of  $\sim 40$  ms.

The result is also not expected to change when exchanging the two detectors. The best estimate  $T_0^{\text{match}}$  is inferred with the proposed methods described in this section. Finally,  $T_0^{\text{match}}$ , is compared to the true  $T_0$  value.

The distribution of  $T_0^{\text{match}} - T_0$  is built from a large number of realisations of the simulated lightcurves. To confirm the absence of systematic effects, the distribution of  $T_0^{\text{match}} - T_0$  should be compatible with a normal distribution with mean zero and standard deviation independent of  $T_0$ . The width of the distribution provides an estimate of the uncertainty on the  $T_0$  measurement,  $\delta t$ . Fig. 8.3 shows an example of the  $T_0^{\text{match}} - T_0$  distribution from pseudo-experiments of the  $\chi^2$  fit between IceCube and Hyper-K.

### Tuning the parameters using a bootstrapping

The proposed methods present some parameters that can be slightly tuned for different CCSN models, distances to the source and detectors. In most cases, it was verified that the degradation of the time precision is not significant and a common set of parameters can be identified for future combined analysis.

In order to reach the best performance once the supernova is detected, the following bootstrapping procedure can be set up. The detected neutrino lightcurve from the best performing detector is used as the model. With this model, the detected neutrino lightcurves for all the detectors can be simulated

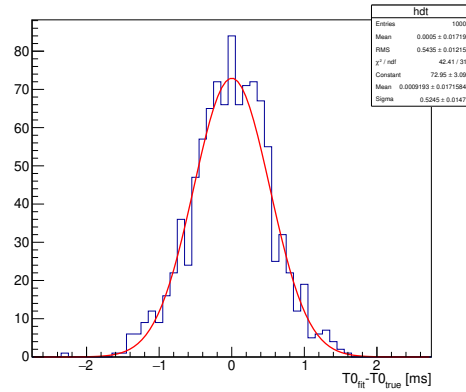


Figure 8.3: Distribution of the difference  $T_0^{\text{match}} - T_0$  obtained applying the  $\chi^2$  fit between IceCube and Hyper-K to a set of realisations of the real (observed)  $T_0$ .

and the procedure to estimate the performance described in section 8.1.3 can be repeated in order to tune the parameters.

### The triangulation method

The time difference between the CCSN neutrino signal arrival at two detectors located at  $\vec{r}_i$  and  $\vec{r}_j$  can be expressed as:

$$t_{ij} = (\vec{r}_i - \vec{r}_j) \cdot \vec{n} / c, \quad (8.15)$$

where  $\vec{n}$  is the unit vector that indicates the emission direction. This vector is calculated in the geographic horizontal coordinate system from the CCSN right ascension,  $\alpha$ , declination,  $\delta$ , and the Greenwich mean sidereal time expressed as angle,  $\gamma$ :

$$\vec{n} = (-\cos(\alpha - \gamma) \cos \delta, -\sin(\alpha - \gamma) \cos \delta, -\sin \delta). \quad (8.16)$$

On March 21 2000 at noon the J2000.0 equatorial coordinate system matches with the geographic one since  $\gamma = 0^\circ$ . For this time Equation 8.16 is simplified to the same expression used in [190]. The position of the detector  $k$  can be inferred from its latitude ( $\phi_k$ ) and longitude ( $\lambda_k$ ) angles, and the Earth radius ( $R_{\text{Earth}}$ ):

$$\vec{r}_k = R_{\text{Earth}} (\cos \lambda_k \cos \phi_k, \sin \lambda_k \cos \phi_k, \sin \phi_k) \quad (8.17)$$

The centers of the HEALPix pixels [209] with 256 pixels per side (about  $0.05 \text{ deg}^2$  per pixel) are used in this work to define the scan grid. The probability that the scanned angles ( $\alpha, \delta$ ) coincide with the equatorial coordinates of the CCSN is given by the following  $\chi^2$  function:

$$\chi_{ij}^2(\alpha, \delta) = \left( \frac{t_{ij}(\alpha, \delta) - T_{0,ij}^{\text{match}}}{\delta t_{ij}} \right)^2, \quad (8.18)$$

assuming that there is no systematic shift in the  $T_{0,ij}^{\text{match}}$  determination. The minimum of the function gives the best estimate for the angles ( $\alpha, \delta$ ) of the searched CCSN location in the sky. From Equation 8.18, one can note that the performance depends on the uncertainty of the measured time delay  $\delta t_{ij}$  of each detector pair.

Different detector pairs can be combined into a total  $\chi^2$  by summing each contribution:

$$\chi^2(\alpha, \delta) = \sum_{i,j}^{i < j} \chi_{ij}^2(\alpha, \delta). \quad (8.19)$$

The  $\chi^2(\alpha, \delta)$  function is converted into a probability as follows:

$$p(\alpha, \delta) = p(\chi_q^2 \leq \chi^2(\alpha, \delta) - \chi_{\min}^2). \quad (8.20)$$

Eq. 8.20 is the cumulative distribution function of the chi-square with  $q$  degrees of freedom,  $\chi_q^2$ , evaluated at the value of chi-square difference between the tested point,  $\chi^2(\alpha, \delta)$ , and the minimum chi-square value,  $\chi_{\min}^2$ , obtained scanning all possible directions. The number of degrees of freedom is given in that case by the number of fitted parameters ( $\alpha$  and  $\delta$ ), provided that they are independent, so  $q=2$ . The 90% confidence level (C.L.) error region on the source direction is determined by the collection of all the points in the sky for which this probability is  $p(\alpha, \delta) < 0.9$  [181].

### Procedure for the triangulation performance estimation

Two procedures are compared to evaluate the size of the confidence area and determine the uncertainty on the source localisation through the Wilk's theorem: using the true values (Asimov dataset), and the fitted parameters distribution.

For the first one, the confidence areas are built by assigning to each fitted value the true expected delay from a particular CCSN location on the sky at a given event time,  $T_{0,ij}^{\text{match}} = t_{ij}(\alpha_0, \delta_0)$ , where  $t_{ij}$  is taken from Eq. 8.15. The procedure described in section 8.1.3 provides the confidence area skymaps which are centred around the true CCSN location with such assumption.

In the second, the fitted value ( $T_{0,ij}^{\text{match}}$ ) is sampled through a normal distribution with the mean being the true value ( $t_{ij}(\alpha_0, \delta_0)$ ) and the standard deviation the experimental uncertainty  $\delta t_{ij}$ . The error box is computed at 68 and 90% C.L for each simulated set of the delays,  $T_{0,ij}^{\text{match}}$ . The average values and standard deviations of the error box areas are estimated, repeating the sampling of  $T_{0,ij}^{\text{match}}$  sets. The coverage is verified by computing the fraction of the realisations in which the fitted CCSN position lies inside the estimated confidence area. Additionally, the 68 and 90% C.L. central areas are calculated from the density of the fitted positions among the pseudo-experiments.

### 8.1.4 Results

In this section, the estimated resolution of the arrival time delay for different detector pairs is shown. Different combinations of three and four detectors are then used to estimate the resulting CCSN localisation uncertainty area.

#### Time uncertainty results

The results of the chi-square method are given for two different lightcurve normalisations in Tables 8.2 and 8.3. For the first normalisation, the true background value is assumed for the baseline subtraction and the scaling is done according the true effective mass. This corresponds to the ideal case in which the detector efficiency and the background estimations are known *a priori*. For the second one, the background expectation value is computed as the average rate in a 1 s off-signal region. The integral of the lightcurve in the analysis time window of  $[-300, 300]$  ms around the lightcurve maximum is normalised to one. By comparing Table 8.2 and Table 8.3 results, the realistic experimental curve normalisation gives similar performances compared to the ideal case. This justifies the proposed window for background estimation and the window used for lightcurve normalisation. It is verified that the mean of the  $T_0^{\text{match}} - T_0$  distribution is compatible with zero within the statistical uncertainties. The  $\delta t$  obtained from the simulations with a fixed and random delay times are compatible. This confirms that for the assumed model and detector response the chi-square method provides an unbiased estimation

of the time delay between the signal arrival at the two detector sites.

Table 8.2: Uncertainty  $\delta t$  in milliseconds obtained with the chi-square method using ideal normalization of the detector neutrino lightcurves. The detector pairs are listed in row and column names. The arrow points to the detector name that is used for the lightcurve peak definition, which is also shifted during the  $\chi^2$  scan.

	<b>KM3NeT-ARCA</b>	<b>Super-Kamiokande</b>	<b>Hyper-Kamiokande</b>	<b>JUNO</b>
<b>IceCube</b>	$\leftarrow 6.4 \pm 0.2$	$\leftarrow 1.95 \pm 0.04$	$\uparrow 0.53 \pm 0.01$	$\leftarrow 1.95 \pm 0.04$
<b>KM3NeT/ARCA</b>	-	$\uparrow 7.3 \pm 0.2$	$\uparrow 6.5 \pm 0.2$	$\uparrow 7.3 \pm 0.2$
<b>Super-Kamiokande</b>	-	-	-	$\leftarrow 2.73 \pm 0.06$
<b>Hyper-Kamiokande</b>	-	-	-	$\leftarrow 2.02 \pm 0.05$

Table 8.3: Uncertainty  $\delta t$  in milliseconds obtained with the chi-square method using average background subtraction and unity normalization of the detector neutrino lightcurves. The detector pairs are listed in row and column names. The arrows point to the detector name that is used for the lightcurve peak definition, which is also shifted during the  $\chi^2$  scan.

	<b>KM3NeT/ARCA</b>	<b>Super-Kamiokande</b>	<b>Hyper-Kamiokande</b>	<b>JUNO</b>
<b>IceCube</b>	$\leftarrow 6.65 \pm 0.15$	$\leftarrow 1.95 \pm 0.04$	$\uparrow 0.55 \pm 0.01$	$\leftarrow 1.95 \pm 0.04$
<b>KM3NeT/ARCA</b>	-	$\uparrow 7.4 \pm 0.2$	$\uparrow 6.70 \pm 0.15$	$\uparrow 7.4 \pm 0.2$
<b>Super-Kamiokande</b>	-	-	-	$\leftarrow 2.75 \pm 0.06$
<b>Hyper-Kamiokande</b>	-	-	-	$\leftarrow 1.99 \pm 0.04$

Table 8.4: Uncertainty  $\delta t$  in milliseconds obtained with the cross-correlation method using the zero-normalisation. The detector pairs are listed in row and column names. The arrows point to the detector name that is used for the lightcurve peak definition.

	<b>KM3NeT/ARCA</b>	<b>Super-Kamiokande</b>	<b>Hyper-Kamiokande</b>	<b>JUNO</b>
<b>IceCube</b>	$\leftarrow 6.2 \pm 0.1$	$\leftarrow 2.19 \pm 0.05$	$\uparrow 0.64 \pm 0.02$	$\leftarrow 2.19 \pm 0.05$
<b>KM3NeT/ARCA</b>	-	$\uparrow 9.0 \pm 0.2$	$\uparrow 6.2 \pm 0.1$	$\uparrow 9.0 \pm 0.2$
<b>Super-Kamiokande</b>	-	-	-	$\leftarrow 5.1 \pm 0.1$
<b>Hyper-Kamiokande</b>	-	-	-	$\leftarrow 2.59 \pm 0.06$

For KM3NeT, the effective mass corresponding to the ARCA detector is used for the performance estimation. The maximum signal time delay between the ARCA and ORCA sites, ( $\sim 3$  ms), is on the same order as the estimated uncertainties for any of the combinations involving the ARCA detector. This prevents a simple merging of the two KM3NeT lightcurves.

The results of the chi-square method shown in Tables 8.2 and 8.3 are computed using the optimized step and effective bin sizes of 50 ms. Using 10 ms for the step and the bin size for ARCA/IceCube and ARCA/Hyper-Kamiokande combinations provides slightly better results, reaching the value of  $6.20 \pm 0.15$  and  $6.30 \pm 0.15$  ms, respectively. Adding up to 3 Hz of background rates does not decrease the performance for Super-Kamiokande and JUNO detectors.

The performance of the cross-correlation method using the same search time window as for the chi-square method is shown in Table 8.4. The optimal effective bin size is found to be 10 ms for all combinations. The results are compatible with the chi-square method, so cross-correlation represents a viable alternative.

### Results of the triangulation: localisation skymaps

Using the uncertainties estimated for each detector combination, the triangulation algorithm is applied to reconstruct the CCSN location on the sky. To estimate the performance of different detector combinations, a CCSN on vernal equinox at noon is assumed for simplicity. The source direction of the Galactic Centre with equatorial coordinates  $(\alpha_0, \delta_0) = (-94.4^\circ, -28.9^\circ)$  as a benchmark for illustration of the results.

The size of each confidence area is obtained through numerous pseudo-experiments of  $T_{0,ij}^{\text{match}}$  sets. The error box sizes at 68 and 90% C.L. obtained using the true and the fitted values for  $T_{0,ij}^{\text{match}}$  are provided in Table 8.5 for different detector combinations, compared to average areas. These results are obtained using the uncertainties from the chi-square method given in Table 8.3. The confidence area skymaps shown in Figures 8.4 and 8.5 are drawn assuming the fitted delays as true positions. Additionally, the fitted CCSN location distributions for the same realisations are shown in Figures 8.4, 8.5.

The real coverage is verified and the values are provided with statistical uncertainties. Table 8.5 indicates that the real coverage of the estimated error boxes with numerous realisations is higher or at the same level as the set confidence level. Therefore, the frequentist statistical coverage is satisfied. In some cases, the obtained average confidence areas using the fitted delays are slightly larger compared to the confidence areas obtained assuming the true delays. However, they are compatible with each other, and also with average error box size, within the statistical errors.

Table 8.5: Uncertainty areas of the CCSN localisation (error box) in  $\text{deg}^2$  at 90% and 68% confidence level for each considered detector combination, computed in three different ways: a) assuming the true delays; b) with a set of randomised time delay realisations; c) from the surface covering 90% and 68% of the fitted position distribution. The real coverage is also provided in the last row, and it is calculated as a fraction of the realisations for which the true CCSN position lies inside the estimated confidence area for each realisation. The CCSN is considered to occur at the vernal equinox time in the direction towards the Galactic Centre, at a distance of 10 kpc.

	IceCube	✓	✓	✓		✓
	Hyper-Kamiokande	✓	✓		✓	✓
	JUNO	✓		✓	✓	✓
	KM3NeT/ARCA		✓	✓	✓	✓
90% CL	area with true delays	350	340	2060	4680	140
	average area	$340 \pm 70$	$360 \pm 40$	$2150 \pm 370$	$4680 \pm 660$	$140 \pm 20$
	fitted positions area	230	320	1440	2420	130
	real coverage (%)	$93.3 \pm 0.3$	$90.0 \pm 0.3$	$89.8 \pm 0.3$	$89.9 \pm 0.3$	$90.0 \pm 0.3$
68% CL	area with true delays	200	160	920	2100	70
	average area	$190 \pm 50$	$170 \pm 20$	$1050 \pm 230$	$2300 \pm 460$	$70 \pm 10$
	fitted positions area	70	160	720	1270	70
	real coverage (%)	$77.3 \pm 0.3$	$67.8 \pm 0.3$	$68.0 \pm 0.3$	$68.2 \pm 0.3$	$68.2 \pm 0.3$

The results in Table 8.5 indicate that the favourable position of a detector with respect to the source location, and in relation to the other detectors used in the combination, may compensate for a worse time resolution. For example, when replacing KM3NeT/ARCA with JUNO in the combination of three detectors, the area is reduced even though KM3NeT/ARCA presents a large uncertainty in the time delay measurement. Note, however, that for the considered CCSN location and time, the three detector combinations involving KM3NeT/ARCA provide confidence areas with two disjoint regions.

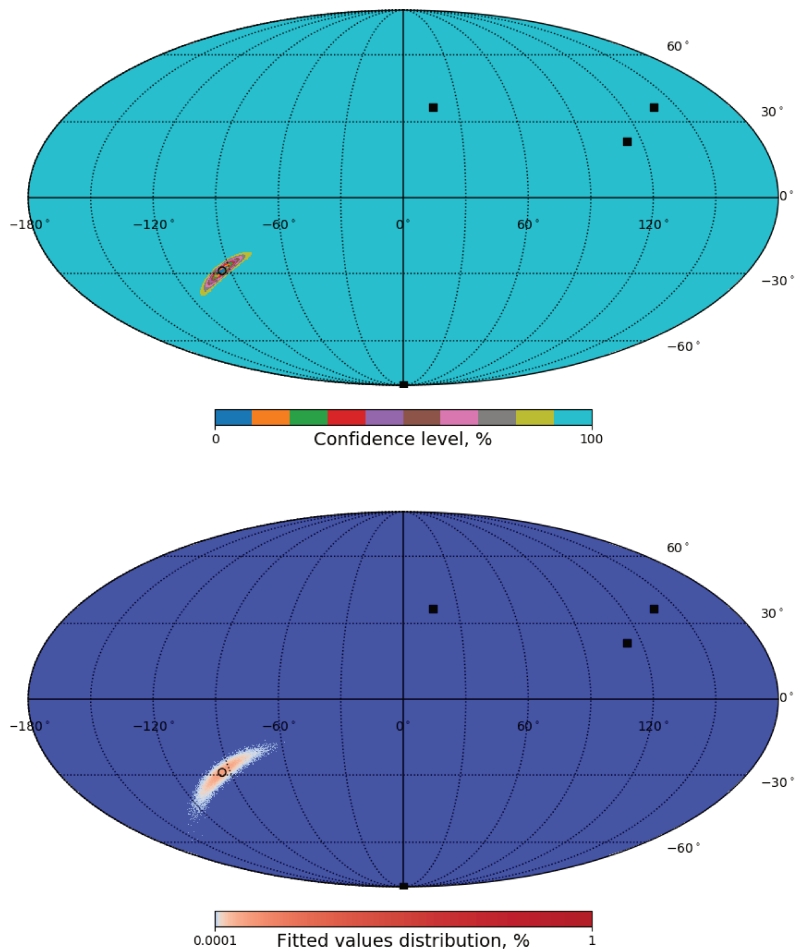


Figure 8.4: Confidence area in equatorial coordinates (mollweide projection) for a CCSN at the Galactic Centre (black circle) computed using triangulation between four detectors (black squares): IceCube, KM3NeT/ARCA, Hyper-Kamiokande and JUNO. Top: confidence area assuming true delays, bottom: distribution of the fitted source position obtained with the simulated observations.

Moreover, the confidence areas may be further reduced considering their intersection with the Galactic Plane.

The dependence of the triangulation results on the position of the CCSN on the sky has been investigated by considering two alternative directions: the one from Betelgeuse,  $(\alpha_0, \delta_0) = (88.8^\circ, 7.4^\circ)$ , as the currently most promising progenitor, and another compatible with the Cygnus constellation,  $(\alpha_0, \delta_0) = (-45.0^\circ, 40.0^\circ)$ , located on the opposite hemisphere with respect to the Galactic Centre. For these two additional directions the areas of the error region at  $1\sigma$  C.L. are  $53 \pm 5 \text{ deg}^2$  and  $50 \pm 10 \text{ deg}^2$ , respectively, which is on same order of magnitude as for the direction towards the Galactic Centre ( $70 \pm 10 \text{ deg}^2$ ). This shows that there can be an effect on the position of  $\sim 20\text{-}25\%$  when the source is located in the same hemisphere than most the considered detectors. The corresponding skymaps are shown in Fig. 8.6. The expected time delay for each detector pair is given in Table. 8.6 for the three considered sources, together with the uncertainty on its estimation obtained using the chi-square method.

The results of our work can be compared to the latest triangulation studies. In [190], the estimate of the 68% C.L. area is  $\sim 66 \text{ deg}^2$ . This result is similar to the one obtained in tis work ( $70 \pm 10 \text{ deg}^2$ ),

Table 8.6: Time delay for each detector pair, assuming the signal emission coming from the three different sources. The time delay uncertainty for each detector pair from Table 8.3 is given in the last column.

	Galactic Centre	Betelgeuse	Cygnus	$\delta t$
IceCube – KM3NeT/ARCA	-21.7 ms	9.4 ms	28.2 ms	$6.65 \pm 0.15$ ms
IceCube – Hyper-Kamiokande	-27.4 ms	17.4 ms	8.6 ms	$0.55 \pm 0.01$ ms
Hyper-Kamiokande – KM3NeT/ARCA	5.7 ms	-8.0 ms	19.6 ms	$6.70 \pm 0.15$ ms
IceCube – JUNO	-29.6 ms	21.0 ms	4.9 ms	$1.95 \pm 0.04$ ms
JUNO – KM3NeT/ARCA	8.0 ms	-12.3 ms	23.3 ms	$7.4 \pm 0.2$ ms
Hyper-Kamiokande – JUNO	-2.3 ms	4.3 ms	-3.7 ms	$1.99 \pm 0.04$ ms

although more than four detectors were combined using IBD and ES channels and the uncertainty estimate relies on the matching with a lightcurve template known *a priori*. In contrast, the result of our work represents a model independent data analysis proposal. In [192], the timing with the first IBD events has the best performance comparing to the exponential rise fit. In the latest results with the first events observation method [191], the time delay uncertainty for Super-Kamiokande and JUNO combination is 5.7 ms. This is larger than 2.8 ms estimated in our work, however, a more pessimistic model was used in the former work. This method requires an evaluation and correction for several biases due to background rates and the steepness of the luminosity curve rise. Biases and the performance degradation in the method proposed here may appear due to the detector efficiency varying with the neutrino energy and in time, or with respect to the event rates. A proper estimation of such effects is possible considering simulations with a detailed emission model and precise detector parameters. This new method relies on the agreement among the different collaborations for making their full lightcurve available to SNEWS while the method in [191] only requires sending the time information of the first events.

The results of this work can also be compared with the expected performance of Super-Kamiokande using the directionality information from the elastic scattering channel. The 68% C.L. area for the combination of four detectors in this work is smaller than the area expected with the actual Super-Kamiokande configuration ( $\sim 69$  deg<sup>2</sup> [199]). With gadolinium doping, this area might be reduced down to  $\sim 13$  deg<sup>2</sup> [199]. The expected CCSN 68% C.L. area for the JUNO IBD events reconstruction analysis will be better than 254 deg<sup>2</sup> [197]. The triangulation method presented in this chapter can be proposed as a low latency analysis. The confidence areas from Super-Kamiokande, JUNO and this triangulation analysis are independent and can be combined in order to obtain a joint refined measurement.

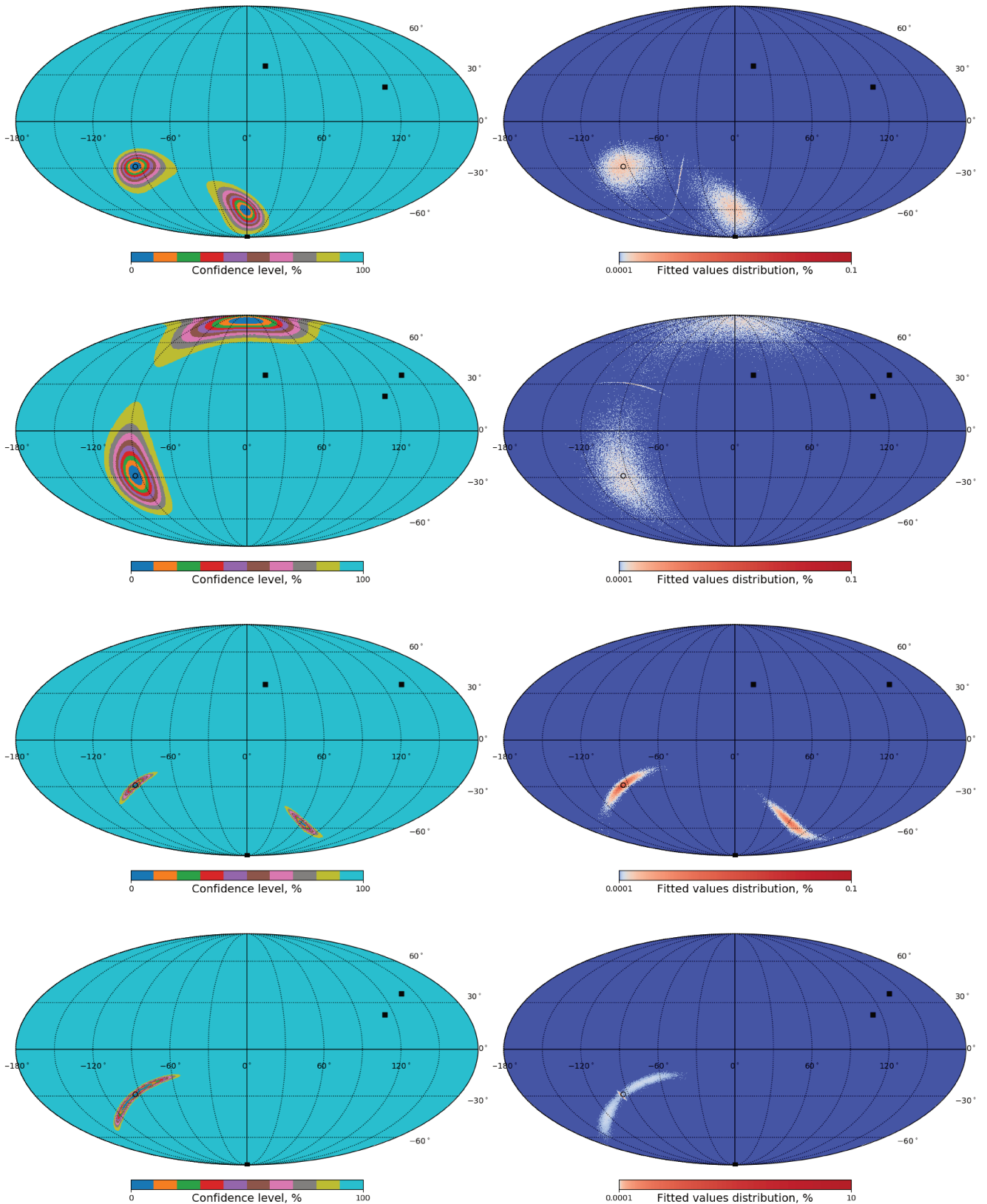


Figure 8.5: Mollweide projection of the confidence areas considering the true delays (left), and the fitted position distributions over a large set of realisations (right) in equatorial coordinates for a CCSN at the Galactic Centre (black dot) computed using triangulation between different combinations of three detector, with location indicated by the black squares. From top to bottom: IceCube, KM3NeT/ARCA and JUNO; Hyper-Kamiokande, KM3NeT/ARCA and JUNO; IceCube, Hyper-Kamiokande and KM3NeT/ARCA; IceCube, Hyper-Kamiokande and JUNO.

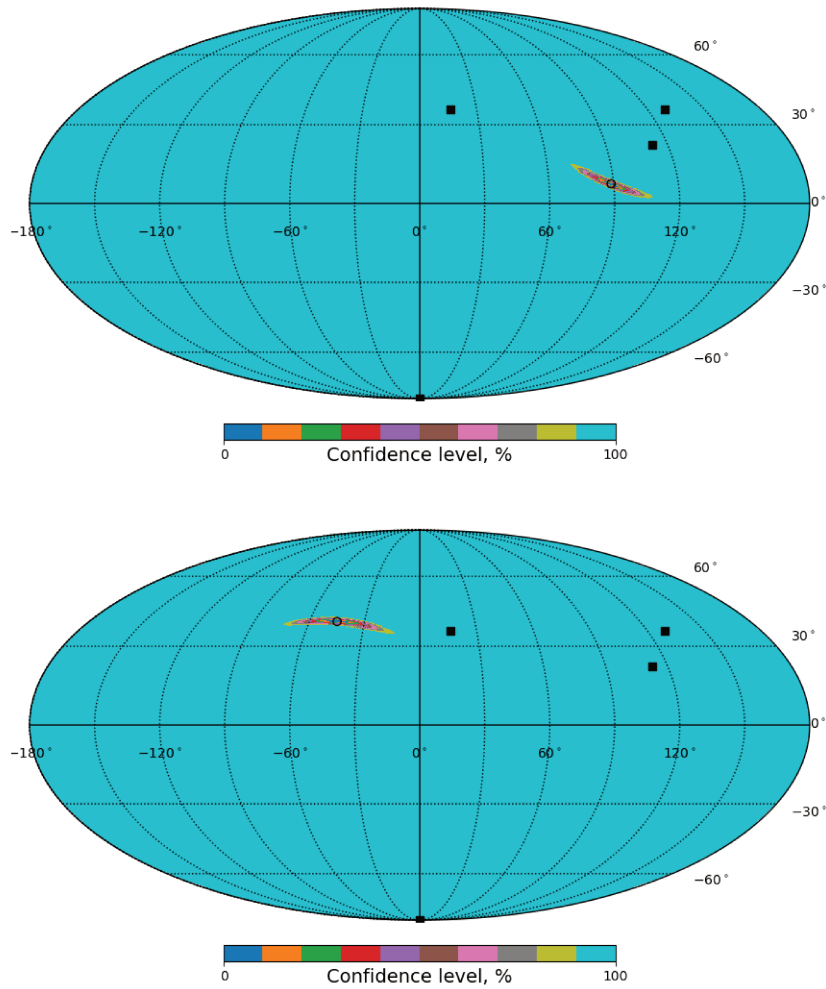


Figure 8.6: Confidence area in equatorial coordinates computed using triangulation between four detectors: IceCube, KM3NeT/ARCA, Hyper-Kamiokande and JUNO. For a CCSN at the position of Betelgeuse (top) and for a source at the location of the Cygnus constellation (bottom). The "true" position (best fit) is indicated with a black dot.

## 8.2 Preliminary study of the sensitivity to the direction of the source using the multi-PMT DOM design of KM3NeT

During the neutrino burst phase of a CCSN,  $\nu_e$  interact with electrons by ES. The outgoing electrons produced are predominantly scattered forward, in the same direction of the incoming neutrino, which also keeps the direction of the source where it was emitted. The first 70 ms of the 1D CCSN simulation of an  $8.8M_{\odot}$  progenitor star including the burst are used for this study [210]. This simulation was chosen because the 3D simulations used in chapters 6 and 7 only focused on the accretion phase, and the  $\nu_e$  emission, providing directional information, is dominant during the burst phase. The total signal predicted by this simulation including only 70 ms with the burst is  $\sim 50$  times lower than the one from the 3D accretion phase simulation (500 ms duration) of a  $27 M_{\odot}$  progenitor used before. This difference is explained by the sum of different things: the shortest window, the lower cross section of the ES compared to IBD together with the small amount of  $\bar{\nu}_e$  produced in this 70 ms window, and the lower progenitor mass (see chapter 5 for more details).

To have an estimation of the sensitivity to the direction of the source, the hit pattern of the 31 directional PMTs of KM3NeT DOMs can be used. The aim is to look for different PMTs receiving more/less photons when changing the direction of the incoming neutrinos. Here, 6 different incoming neutrino directions were simulated:

- Dir 1:  $\theta_{\nu} = -\frac{\pi}{2}, \phi_{\nu} = -\frac{\pi}{2}$
- Dir 2:  $\theta_{\nu} = -\frac{\pi}{2}, \phi_{\nu} = +\frac{\pi}{2}$
- Dir 3:  $\theta_{\nu} = -\frac{\pi}{3}, \phi_{\nu} = -\frac{\pi}{3}$
- Dir 4:  $\theta_{\nu} = -\frac{2\pi}{3}, \phi_{\nu} = -\frac{\pi}{3}$
- Dir 5:  $\theta_{\nu} = -\frac{\pi}{4}, \phi_{\nu} = \frac{\pi}{4}$
- Dir 6:  $\theta_{\nu} = -\frac{3\pi}{2}, \phi_{\nu} = \frac{\pi}{4}$

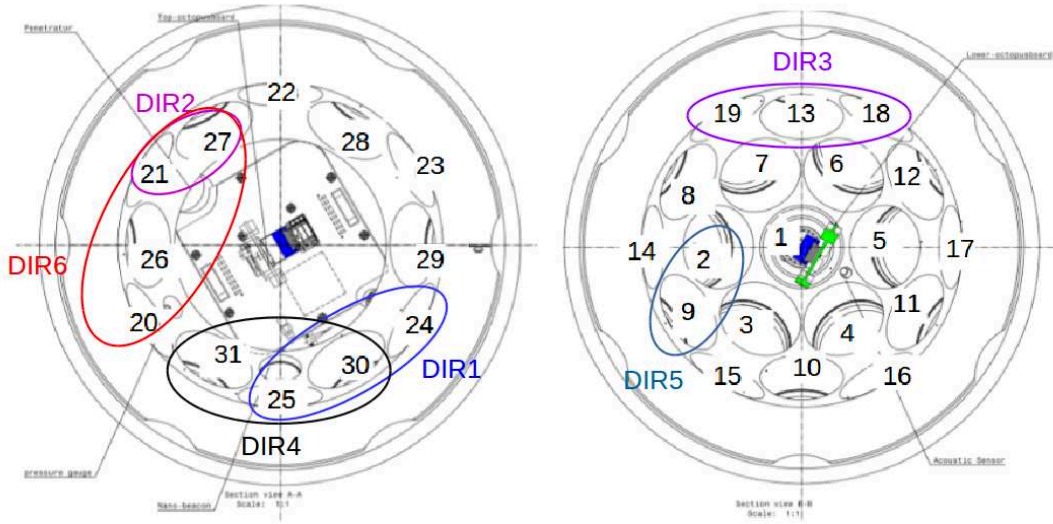


Figure 8.7: Schema of the DOM geometry. The left/right Figures indicate the upper and lower hemispheres of the DOM. The 6 simulated directions are pointed with colored circles, showing the PMTs closest to the interaction vertex in each case.

The angles  $\theta_\nu$  and  $\phi_\nu$  define the incoming neutrino direction,  $\vec{p}$ , which is given by:

$$\vec{p} = (\sin\theta_\nu\cos\phi_\nu, \sin\theta_\nu\sin\phi_\nu, \cos\theta_\nu) \quad (8.21)$$

The direction of the source (i.e. in the DOM coordinate frame) is opposite to the incoming neutrino direction,  $-\vec{p}$ . We define the PMT pointing angles  $(\theta, \phi)$  so that the  $\theta$  angle is rising from 0 at the north pole of the DOM (positive  $z$ ) to 180 degrees at the south pole (negative  $z$ ), and the  $\phi$  angle (zero along the positive  $x$ -axis) is positively increasing when rotating from the  $x$ -axis to the  $y$ -axis. To go from the incoming neutrino frame to the DOM frame, a rotation of  $\pi$  is applied ( $\theta_\nu = \theta - \pi$  and  $\phi_\nu = \phi - \pi$ ). The position  $(x, y, z)$  and direction  $(dx, dy, dz)$  vectors of the PMTs can be therefore defined, using the DOM radius ( $r = 2$  cm), as:

$$\begin{aligned} x &= r\sin\theta\cos\phi; & dx &= \sin\theta\cos\phi; \\ y &= r\sin\theta\sin\phi; & dy &= \sin\theta\sin\phi; \\ z &= r\cos\theta; & dz &= \cos\theta; \end{aligned}$$

The first 2 directions correspond to the equator between the northern and southern hemispheres of the DOMs and opposite sides. Directions 4 and 6 correspond to neutrinos arriving in the northern hemisphere of the DOM, and directions 3 and 5 to neutrinos arriving in the southern hemisphere. The six directions are illustrated with circles in Figure 8.7, where the geometry of the DOM is shown.

Also, single hits are used here since with higher multiplicity selections, the hit pattern is dominated by the fact that some PMTs have more neighbor PMTs than others and the density of PMTs is higher on the south hemisphere of the DOM. Indeed, it is more probable that low-energy neutrinos produce multiple photons that are detected in different PMTs if there are more neighbor PMTs. With less PMTs further away from each other, the number of coincidences is reduced, whatever is the neutrino direction. This effect has been observed and will be higher than any directionality effect that could be observed, suppressing it.

The 1D and 2D patterns can be seen in figures 8.8, 8.9 for the 6 different simulated directions. The 2D pattern shows the 31 PMT positions as a function of the angles theta and phi. The  $z$  axis is the number of hits in each PMT expected to be detected during 70 ms for a SN at 10 kpc. This simulation does not include background.

The closest PMTs to each incoming neutrino direction have been identified and are circled in the 2D patterns of each figure. One can infer from those 2D plots that closest PMTs to each neutrino direction, expected to be the ones with more detected photons, are indeed the ones that receive more hits in the simulation, giving a directionality pattern. The problem is the huge L0 background rate of around 7kHz per PMT, giving 490 events per PMT in 70 ms. This means background is  $10^4$  times larger than signal.

To get an estimate of the angular resolution, the simulation is repeated many times, including the signal plus background expectation. Each time, the 3-4 more lighted PMTs are taken. From their coordinates, the baricenter is computed to get the most probable direction of the source. The angular distance between the most probable direction and the true direction is computed for each pseudo-experiment. This is put into an histogram, showing the distribution of the angular distance. The mean and width of the distribution finally gives you the angular resolution. Results are shown in Figure 8.10 and the error obtained is one third of the sky (120 degrees).

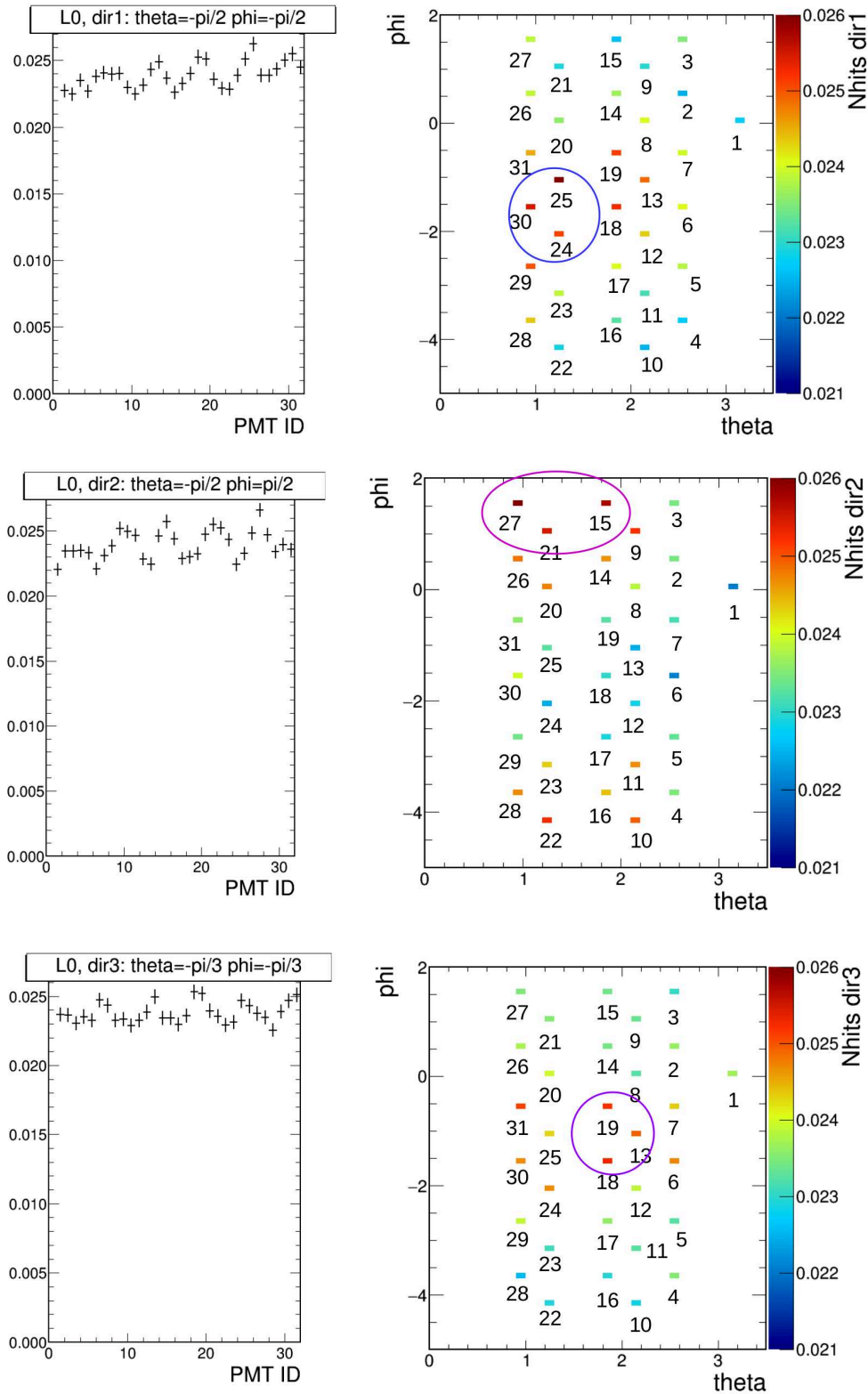


Figure 8.8: On the left, the 1D PMT pattern for dir1 on the top, dir2 on the middle and dir3 on the bottom. On the right, the 2D pattern for the same directions. The z-axis is the number of expected detected events per PMT from a CCSN signal at 10 kpc, without background. The circled PMTs in the 2D patterns correspond to the closest PMTs to the incoming neutrino direction, matching well with the PMTs receiving more hits.

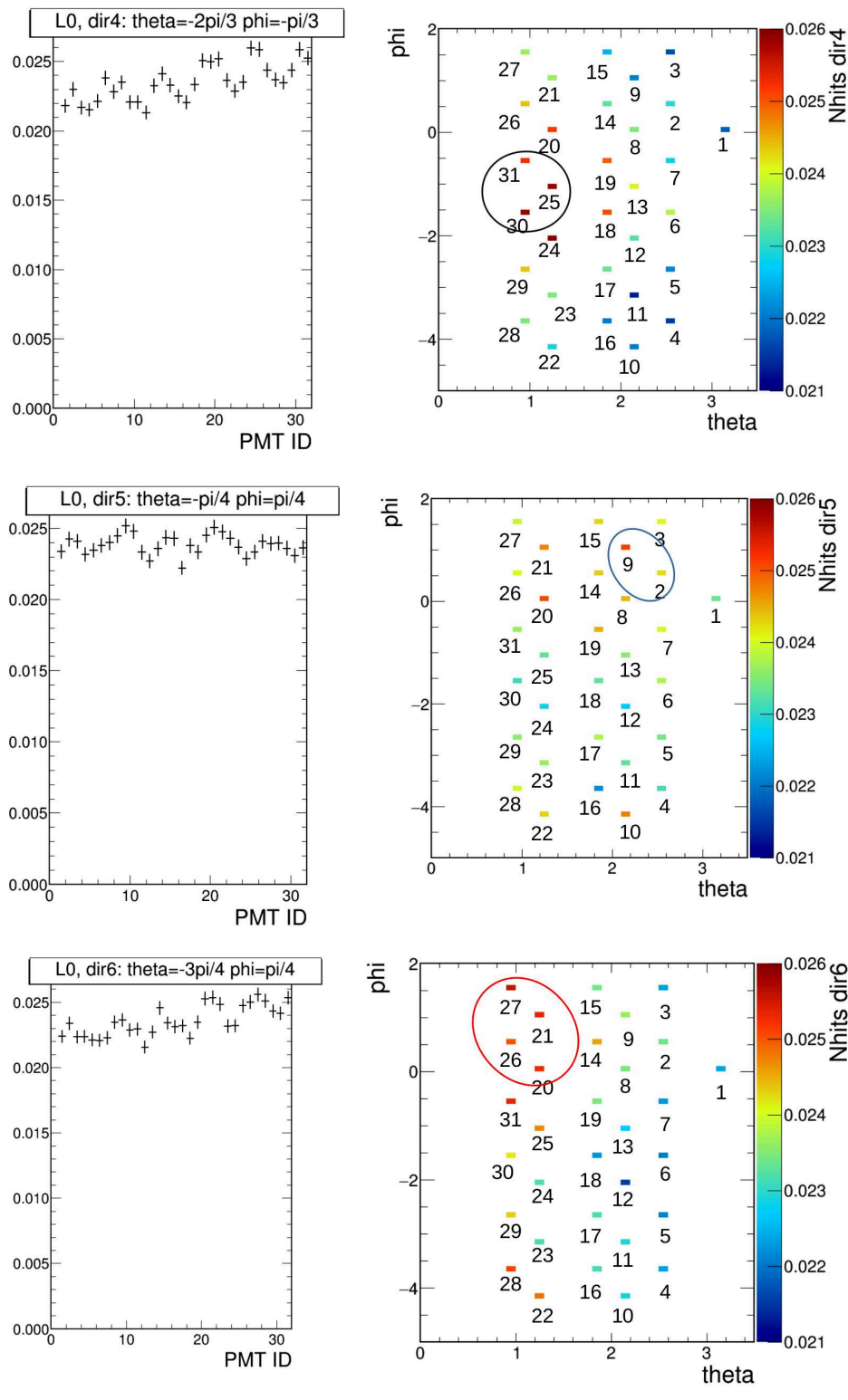


Figure 8.9: On the left, the 1D PMT pattern for dir4 on the top, dir5 on the middle and dir6 on the bottom. On the right, the 2D pattern for the same directions. The z-axis is the number of expected detected events per PMT from a CCSN at 10 kpc. The simulation does not include background. The circled PMTs in the 2D patterns correspond to the closest PMTs to the incoming neutrino direction, matching well with the PMTs receiving more hits.

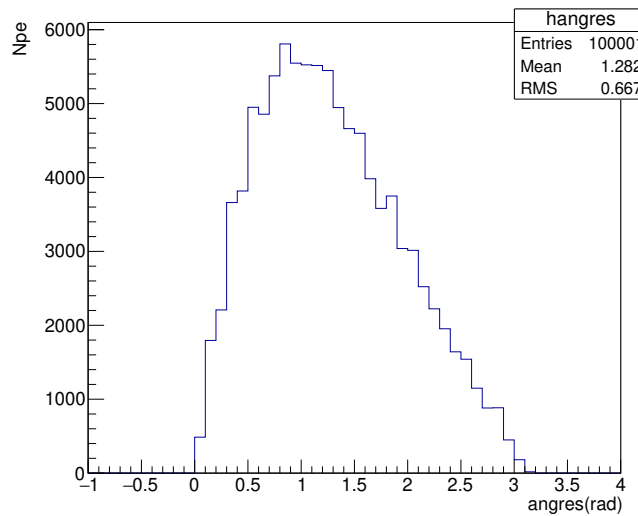


Figure 8.10: Distribution of the angular distance between the most probable direction from PMT pattern and true direction, in radians.

In conclusion, the perspective of pointing to the CCSN source using the directional information of the KM3NeT multi-PMTs gives a large angular uncertainty and is not encouraging. Even though the results are not promising, if a good background characterisation and subtraction of the baseline rates is achieved and the CCSN is close and/or energetic enough, some improvement could be possible. Moreover, the background fluctuations have been assumed to be Poissonian, with an average PMT rate of 7 kHz. However, we now know from the first data that this is optimistic, and a detailed study with a more realistic background model is needed.



## Part III

# Searching for high-energy neutrino emission from TeV gamma-ray bursts and gravitational wave sources with ANTARES



# Chapter 9

## Gamma-ray bursts as multi-messenger sources

In this chapter, the physical processes at play in gamma-ray bursts are addressed from a multi-messenger perspective. The connection between GRBs and GW sources is emphasised, highlighting the interest of the different neutrino searches that are presented in chapters 10 and 11 and have been carried out during the thesis. The different energy scales of interest are reviewed, underlining the differences with respect to MeV neutrino searches described in Part II.

### 9.1 Introduction to gamma-ray bursts

Gamma-ray bursts, introduced in section 1.5, are among the most energetic explosions in the Universe. A non-thermal electromagnetic radiation characterizes the different emission phases of GRBs. In this section, an overview on GRBs is given.

As a reminder from section 1.5, two different types of GRBs are observed, thought to correspond to different typical duration of the gamma-ray emission: short and long GRBs (see Fig. 9.1). Short and long GRBs are respectively related to the coalescence of two compact objects in a binary system and to the explosion of a single massive star. The parameter that is typically used to characterise the GRB is the time in which 90% of the gamma-ray burst luminosity is emitted, called  $T_{90}$ . The different durations, together with the fact that less and less energetic short GRBs are observed suggests that the sources are not the same and neither the mechanism driving the EM emission may be. This is illustrated in Fig. 9.1, where the number of observed event for each GRB type is shown, and Fig. 9.2, where the luminosity-redshift relation of observed GRBs is presented.

When a supernova progenitor is able to retain a significant amount of angular momentum, an accretion disk might be formed, and the stellar collapse may be accompanied by two relativistic jets launched along the rotation axis of the collapsing star [211]. In fact, a large angular momentum is required for the system to reach the huge amount of energy that is needed to launch a relativistic jet, which can be powered by accretion or rotational energy [212]. This specific subset of supernovae are thought to be connected with the emission of a long gamma-ray burst [77, 213], which represent the most energetic bursts of EM radiation observed.

Examples of the supernova subset represented by long-GRBs are the so called **collapsars**, with a high-mass progenitor that is able to sustain the energy released by the long GRB taking place with the CCSN explosion. In this case, the remnant can be a NS or a BH. The **supranova** scenario suggests that a black hole can be formed in a second step from the collapse of the neutron-star remnant left by the

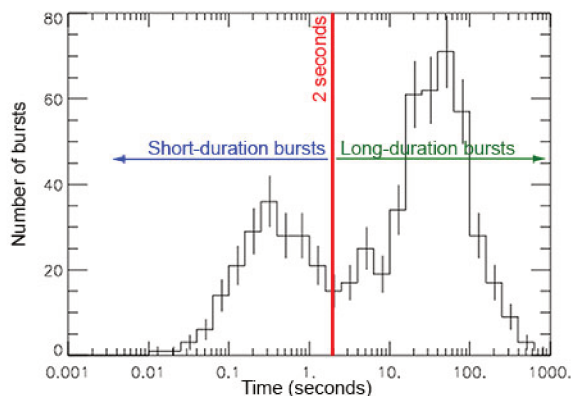


Figure 9.1: Distribution of the number of bursts as a function of time (which indicates the duration in seconds) for the gamma-ray bursts observed by the BATSE instrument on the Compton Gamma-ray Telescope. Figure from: <https://imagine.gsfc.nasa.gov/science/objects/bursts1.html>.

CCSN, in which case a relativistic outflow is also emitted with the collapse of the compact object. The collapsar and supranova models are reviewed in [214].

Short gamma-ray bursts are a second class of GRBs for which the gamma-ray emission lasts less than about  $\sim 2$  s. As for long GRBs, also a long-lived afterglow phase is observed for this kind of bursts, predominantly in radio, X-rays, optical and IR. The lower intrinsic available energy in the system leads to a weaker EM emission, which explains that less short GRBs are observed compared to long GRBs. This different energetic outputs results in such experimental bias.

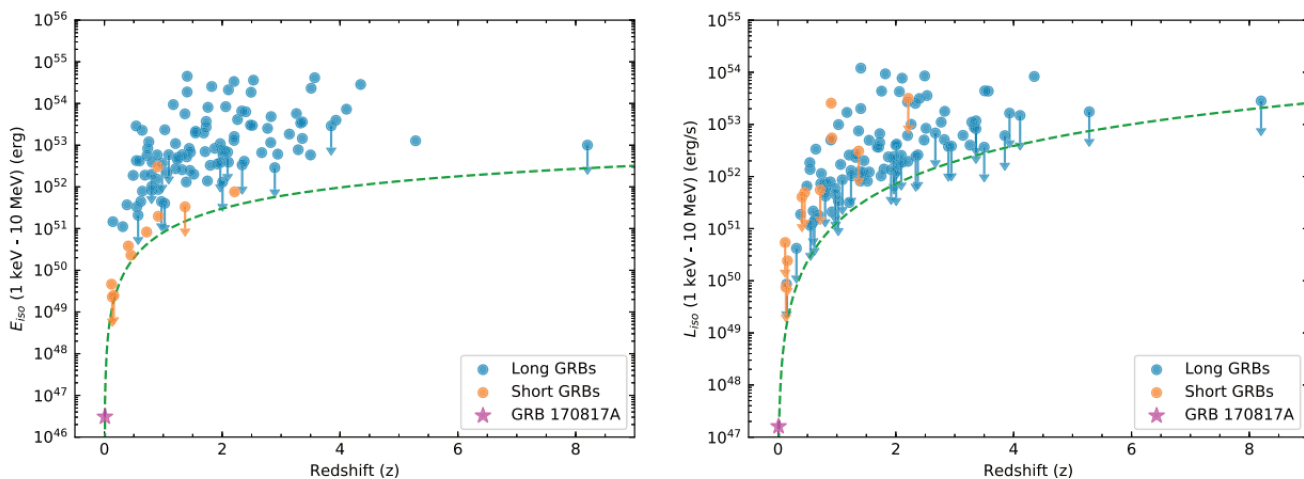


Figure 9.2: Isotropic energy (left) and luminosity (right) as a function of redshift for all GRBs detected by Fermi-GBM with measured redshifts. Redshifts are taken from GRBOX (<http://www.astro.caltech.edu/grbox/grbox.php>) and [215]. The green curve illustrates how the GBM detection threshold varies as a function of redshift in an approximate way. All quantities are calculated in the 1 keV–10 MeV energy band in which the instrument is sensitive. Figure from [216].

Neutron stars are formed after the death of a massive star (see section 4.2). Sometimes neutron stars appear gravitationally coupled in a binary system (BNS). The most common hypothesis is that the binary system is the result of the evolution of two massive stars that are formed close to each other and gravitationally attracted. However, their formation mechanism is yet under study. The evolution

of the BNS system may finish with the merging of the two neutron stars, that can lead to different remnant objects, as illustrated in Fig. 9.3: a stable NS or a black hole, depending on the initial conditions, specially the compactness and spin of the merging objects [217].

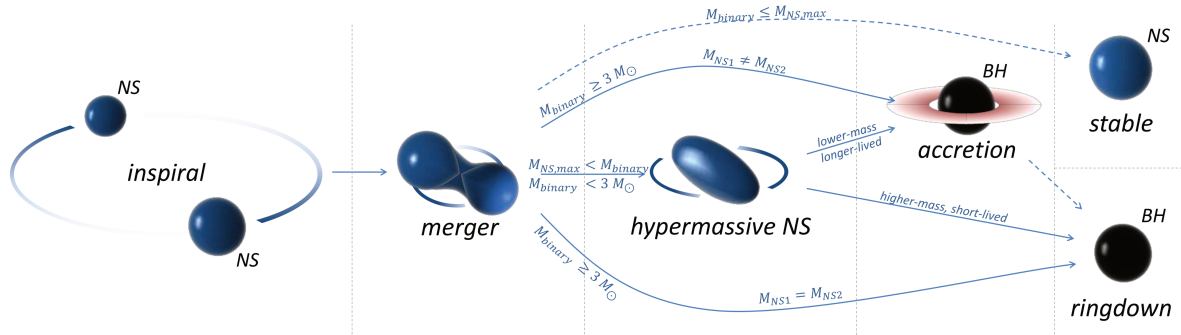


Figure 9.3: Evolution of a binary neutron star system at the coalescence. The different possible remnants are illustrated. The final state will depend on the initial masses and conditions of the merging objects. Figure adapted from [217].

For a long time, these systems have been believed to be sources of GW radiation (as predicted by General Relativity) and of gamma-ray emission. In particular, they have been thought to be the origin of short GRBs. The detection of the golden event GW170817 (see 1.4.1) both through gravitational-wave and EM radiation among all wavelengths proved Binary Neutron Star mergers as indeed the source of short GRBs, solving an old long-standing question. For what regards the source population, massive stars (giving birth to CCSN and potentially long GRB) have a shorter lifetime so they are observed from further away from us than binary systems which result from the long evolution of old stellar systems (thus observed closer).

As introduced in section 1.5, different emission phases potentially driven by different mechanisms can be identified in the observed electromagnetic time profile of gamma-ray bursts. A prompt, highly variable emission of gamma-rays produced during the expansion of the collimated outflow ejecta happens first. It is followed by a long-lived broadband afterglow emission of optical, IR radio and x-ray radiation. The first is thought to arise from internal shocks, while the second is thought to be produced by the interaction of the expanding ejecta with the surrounding medium.

## 9.2 Multi-messenger emission from GRBs

In such extreme phenomena as gamma-ray bursts, hadronic acceleration processes, leading to cosmic ray and neutrino emission, have been suggested [218, 219, 220, 221]. GRBs have several candidate sites where non-thermal particles can be accelerated: the cocoon structure that may be formed in the progenitor star by the launch of the jet, the shock breakout (in the CCSN case), internal shocks within the jet itself and interactions between the jet and the wind material from the progenitor or the interstellar medium.

In the various stages of the jet evolution, we can expect particle acceleration, which may result in not only photon emission but also neutrino and cosmic-ray production. As different mechanisms take place at each stage and dominate in different energy ranges, different energy scales for the neutrino emission are expected too, as illustrated in Fig. 9.4.

During the phase of the compact object formation at the last stage of stellar evolution followed by the gravitational collapse, MeV neutrinos may be produced in the same way as explained in section 4.2 for CCSN. In a second step, the release of a relativistic outflow in the form of a jet leads to a prompt gamma-ray emission [222, 223]. At this stage, a prompt neutrino emission with energies from TeV to PeV is expected from particle acceleration by internal shocks within the jet. This is assuming that hadrons are accelerated into the jets, which is not yet confirmed. Finally, during the afterglow phase neutrino production would be possible in the case of a dense environment that will serve as target to accelerate hadrons, subsequently producing neutrinos at PeV-EeV energies. These makes gamma-ray bursts special candidates as transient multi-energy neutrino sources.

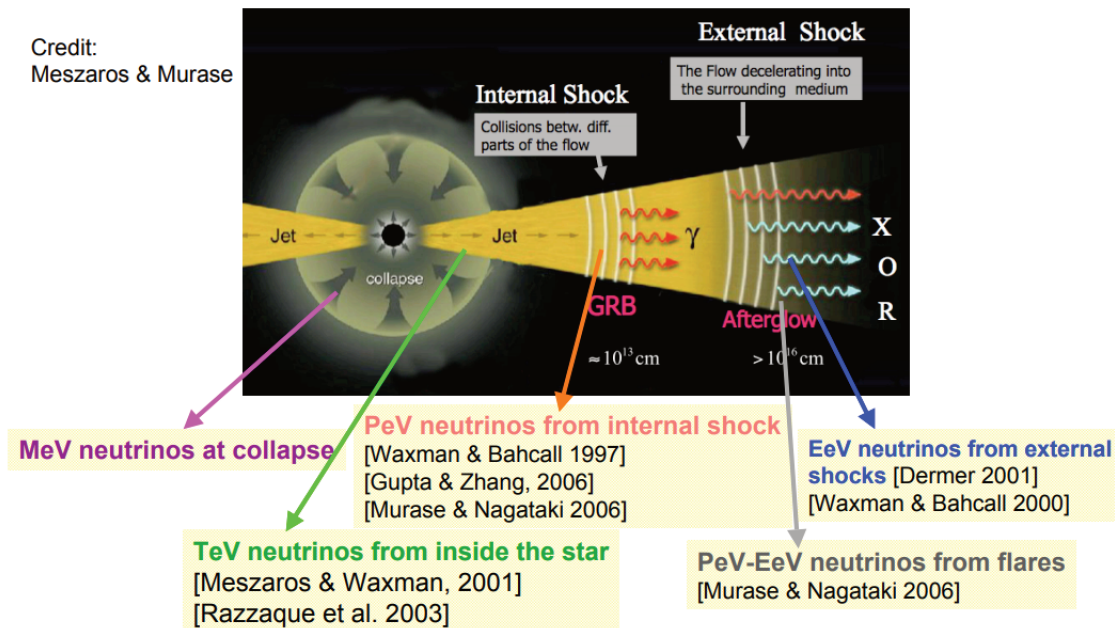


Figure 9.4: The different phases and multi-energy neutrino emission components thought to be related with a gamma-ray burst event.

In the following subsections, the focus is put on long GRBs detected at very high-energies (sub-TeV) by ground based Cherenkov Telescopes (see chapter 11) and the connection of short GRBs with compact binary mergers, motivated by the observations of GRB 170817A (see section 1.4.1).

### 9.2.1 The case of long and late very high-energy gamma-ray emission

Electromagnetic observations of gamma-ray bursts show that a complex relationship exists between the emission detected at different wavelengths. In particular, the gamma-ray data cannot be fitted by a single spectral component, and an additional power-law contribution is needed in order to accommodate data above and below 100 MeV, and reproduce the duration of the prompt and afterglow components.

The observed EM radiation requires energetic particles to be accelerated in the jet. Synchrotron processes have long been suggested as the emission mechanism driving both the prompt and afterglow phases. Multi-wavelength observations of the GRB long-lived afterglow emission evidence synchrotron radiation by shock-accelerated electrons. Some scenarios predict the synchrotron radiation to be accompanied by a Synchrotron Self-Compton (SSC) (or Inverse Compton, IC) emission, resulting in a second peak on the gamma-ray spectrum mirroring the synchrotron spectrum, but boosted in energy (see [224]). The different non-thermal spectral components are shown in Fig. 9.5.

The high-energy photons (above 100 MeV) observed by Fermi-LAT are thought to be produced in the afterglow shocks, which accelerate particles leading to synchrotron radiation. However, there is a point from the burst onset where energy losses make the acceleration process inefficient to explain a late high-energy gamma-ray emission observed in the spectrum being originated from synchrotron radiation. In fact, such synchrotron emission has a maximum energy above which this process is not enough to explain the high-energy photons, which becomes more important in the afterglow phase, where the shock is decelerated. This is called the synchrotron limit. The high-energy (95 GeV) photon detected by Fermi LAT from GRB 130427A in the early afterglow shows a violation of this maximum photon energy [225]. These apparent violations of the synchrotron limit could indicate the presence of an additional emission component, needed to model the burst.

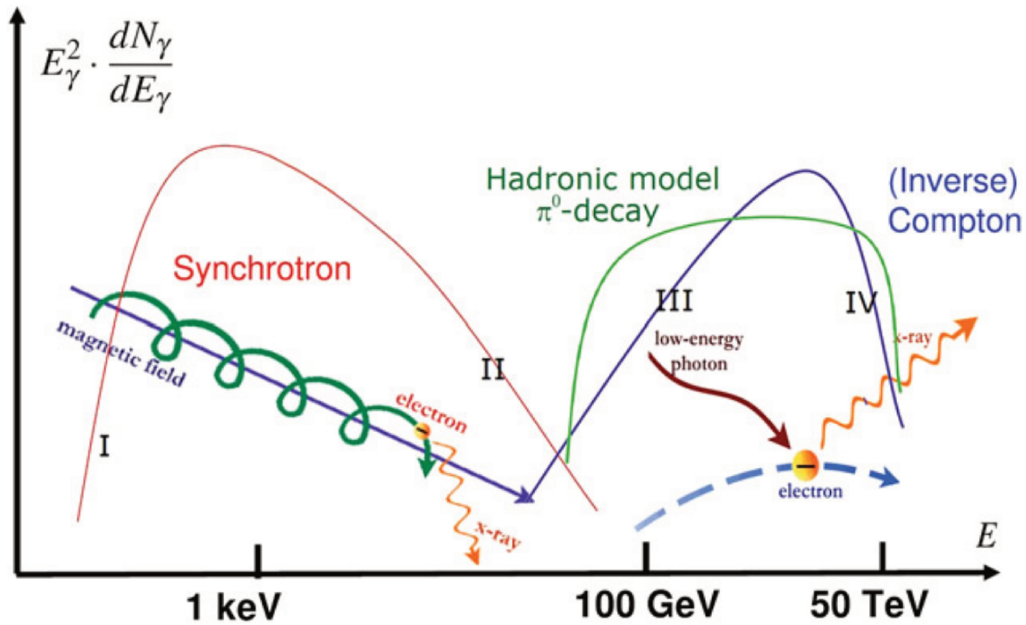


Figure 9.5: Spectral energy distribution of photons radiated by the different spectral components. Synchrotron radiation produced by relativistic electrons accelerated at the source (red line). These photons are also the target for inverse Compton scattering (or SSC) of the parent electrons (blue line). When hadrons also interact with ambient matter (or photons), gamma-rays are also produced by  $\pi^0$  decay (green line). Figure from [224].

The detection of very high energy (VHE) emission above 300 GeV by the MAGIC Cherenkov telescopes from GRB 190114, up to 1000 s after the burst, reported in [226], also presents a violation of the maximum synchrotron energy. There are different possibilities to explain the detection of high-energy photons from GRB 190114C: additional emission mechanism at high energies, a hadronic mechanism, SSC radiation, or a revision of the estimation of the maximum photon energy attainable through the synchrotron process.

After the MAGIC detection, two new observations by the H.E.S.S Telescopes of VHE gamma-rays have been reported, GRB 180720B [227] and GRB 190829A, both showing sub-TeV gamma-ray emission several hours after the prompt phase. Experimental data is in good agreement with the SSC (leptonic) scenario [228, 229, 227]. However, the presence of a subdominant hadronic component is not ruled out by the data and these GRB events remain interesting candidates as hadronic acceleration sites and thus, for high-energy neutrino emission, as shown in [230]. In chapter 11, the search for a neutrino counterpart to these events will be present as a part of this thesis work.

### 9.2.2 Neutrinos and GWs from compact binary mergers

In 1916, Einstein predicted the existence of gravitational waves 100 years before their first detection in 2015. The theory of General Relativity describes gravity as a geometric property of spacetime, governed by Einstein's equations (Eq. 9.1):

$$G_{\mu\nu} = -\frac{8\pi G}{c^4} T_{\mu\nu}. \quad (9.1)$$

This system of equations tells us that the matter-energy distribution, described by the stress-energy tensor  $T_{\mu\nu}$ , determines the space-time geometry, given by the Einstein tensor  $G_{\mu\nu}$ . The indexes  $\mu, \nu$  go through the 3 spatial and the temporal dimensions of spacetime.  $G$  and  $c$  being universal constants for the gravitational coupling and the speed of light in vacuum.

Gravitational waves, as electromagnetic waves, are predicted to travel at the speed of light. The first GW measurements are compatible with this hypothesis. Their amplitude is attenuated proportionally to the distance to the source. Therefore, gravitational-wave detectors will have to be sensitive to space distortions of the order of  $10^{-21}$  m. How to beat this challenge is described in section 10.1.

As an analogy with the electromagnetic force, that accelerates dipoles producing electromagnetic waves, the gravitational force will radiate gravitational waves when the mass-energy quadrupole moment of a system accelerates. An example of wave emitter would be therefore a binary system formed of two close compact objects orbiting around each other, as will be covered in this chapter.

Indeed, the coalescence of a compact binary system perturbs the space-time leading to GW radiation due to a high-order (quadrupolar) mass-dynamic asymmetry in the system during coalescence. Three compact binary systems can be identified by gravitational wave detectors: binary black holes (BBHs), neutron star - black hole systems (NSBHs) and binary neutron stars (BNSs).

Numerical simulations allow to reproduce the evolution of these compact binary systems very accurately, showing three different phases: the inspiral, the merger and the ringdown. Fig.9.6 shows these phases for the BBH case. The duration, amplitude and frequency of the signals and the corresponding waveforms will vary depending on the type of compact binary system as well as with the masses of the colliding objects and the distance to the source.

#### Neutrinos and GWs from binary black hole mergers

The merging of two binary black holes is believed to take place without any accretion of matter or relativistic ejecta, which means that no particle acceleration is in principle possible at these sources. Therefore, no EM or neutrino counterpart is expected to be observed.

Even though the current picture of the binary system evolution foresees no EM or neutrino emission from these objects, some scenarios predict the possible presence of an accretion disk or a relativistic jet being emitted [232, 233]. In this case, particle acceleration would take place leading to a multi-messenger production. The presence of a dense surrounding environment or a strong magnetic field from the merger remnant would be enough to motivate the search for a potential EM and/or neutrino counterpart. One of the possible scenarios is that the two low mass black-holes merging evolve in an AGN accretion disk, in which case the dense environment is procured by the amount of material known to be surrounding the central engine [234].

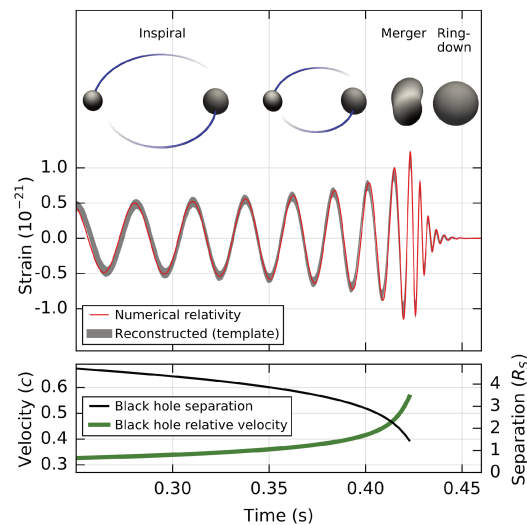


Figure 9.6: Evolution of the waveform of the GW signal from a BBH system along the three phases. The predictions for General Relativity coming from numerical simulations are compared to the reconstructed form from data, showing the good agreement between both. Figure from [231].

### Neutrinos from binary neutron stars (or short GRBs)

The coalescence of two neutron stars in a binary system with an associated short GRB observed are the most promising multi-messenger sources, and the only one observed in GWs and through electromagnetic radiation in coincidence. Different models with different predictions for the neutrino emission have been discussed since the unique observation of GW170817. The most relevant ones are discussed here.

Let's focus first on the prompt emission (few seconds). The non-thermal accelerated charged particles produced in the collimation and internal shocks might produce neutrinos through their interaction with the background photons and protons. For the collimation shock case, the accelerated protons are released with the collimated jet, which is optically thick. Therefore, only the thermal photons will be a target for meson and neutrino production, and the neutrino emission from the collimation shocks will occur at GeV-TeV energies.

From the internal shocks, two types of target photons are possible. One is the leakage photons from the collimated jet, and the other is the synchrotron radiation from the non-thermal electrons produced at the internal shock. The photomeson production is the dominant cooling process in the high-energy TeV-PeV range, where detectors like IceCube, ANTARES and ARCA are sensitive. At these energies, the contribution from the leakage photons is more important than the prompt photons.

One would expect a fraction of the energy after the front shock to be deposited into non-thermal protons if cosmic-rays are accelerated in the internal shock. These heated protons would then produce pions that decay emitting neutrinos. These are the so called trans-ejecta neutrinos from the internal shocks. For a review, see [235].

But one could also think of an extended emission (EE) that might take place over hundreds of seconds, related to the EE observed in X-rays and gamma-rays for some short GRB light-curves. In fact, the energy released in the EE can be as high as the one from the prompt phase. This extended emission is supposedly happening with a lower Lorentz factor from the decelerated shock after the prompt burst, to which the neutrino production is sensitive. In [55], it is shown that this lower Lorentz factor makes

the photomeson production more efficient, reaching the maximum values in case of extended emission. This leads to higher neutrino fluences reached in these models for energies going from 10 TeV to 10 PeV. The prompt and extended models are shown in Fig.9.7.

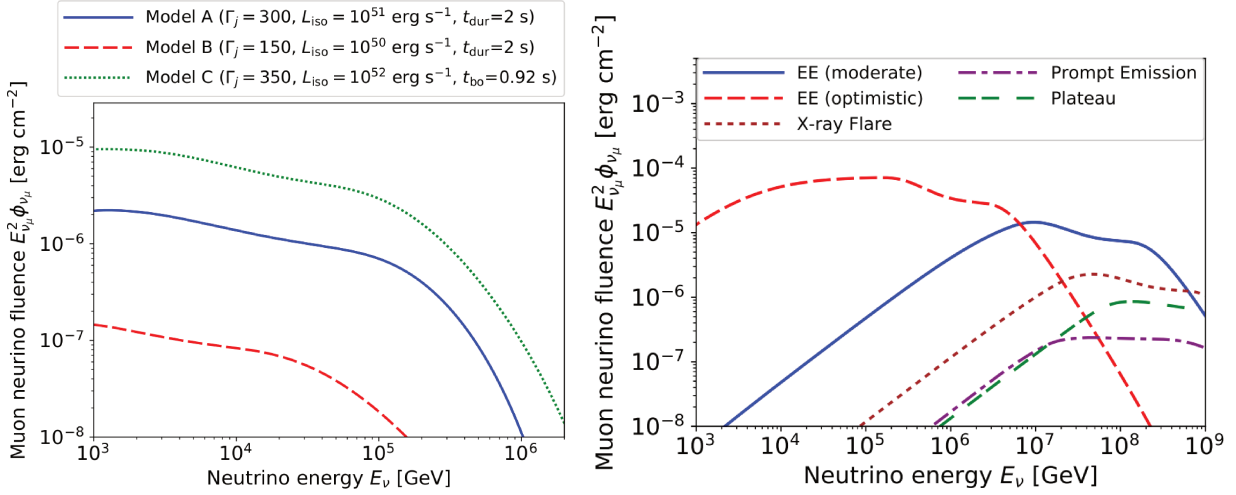


Figure 9.7: On the left, neutrino fluences from the internal shock models in [235]. On the right, the neutrino fluences at 3000 Mpc from the extended moderate and optimistic emission together with the prompt, flare and plateau emissions considered in [55].

In the afterglow phase, if the remnant has a strong magnetic field (i.e. if it is a magnetar) or there is ejected material from coalescence of the two NSs, particle acceleration might take place days after the merger, with a neutrino emission in the energy range PeV-EeV [56]. These higher energies imply a lower neutrino flux emitted, assuming the neutrino spectrum follows a power law, and thus these neutrinos will be more difficult to detect with current neutrino telescopes.

As a conclusion, more multi-messenger detections of such astrophysical sources are needed in order to completely understand the mechanisms taking place as well as to have a complete picture of GRB physics and the dynamics of the compact binary system evolution. For this reason, a future generation of neutrino telescopes, GW detectors and EM surveys of GRBs are needed.

Apart from high-energy neutrinos, thermal (MeV) neutrinos will also be produced in the compact binary system [236]. In CCSNs, the proto-neutron star is heated up by the collapse leading to a shock front. In a BNS merger, the collision of the two compact objects prior to the merger is heating up the remaining neutron star. This produces thermal neutrinos mainly through electron/positron captures on free nuclei. In CCSNs, the dominating nuclei are protons, which makes them brighter in  $\nu_e$ . In BNSs, the neutron richness results in a higher  $\bar{\nu}_e$  luminosity.

The detection of this low-energy neutrino flux from a single merger is not expected even with future detectors since the signal will be hidden by the diffuse neutrino background, coming from all CCSN explosions that have taken place through the Universe. However, the possibility of detecting one single neutrino by stacking multiple mergers ( $>2500$ ) in a long term scale ( $\sim 80$  Mt years) and with the help of GW detectors timing would allow to constrain the energy scale of the neutrino emission as well as the absolute neutrino mass.

### Neutrinos and GWs from NSBH systems

As for BNS mergers, the coalescence of a neutron star and a black hole in a compact binary system (NSBH) is believed to radiate GWs, photons and neutrinos. The characteristics of the electromagnetic light-curve may be different because of the different initial masses compared to BNS but the processes in play might be very similar, as predicted in [50]. However, the different models must be confirmed by an observations and the detection of these sources is one of the main targets of the current generation of GW interferometers.

#### 9.2.3 Observational results

Current instruments have allowed for an increased of the observational statistics, with 1-3 GRB detections per day. However, many unknowns remain concerning the theory and mechanism driving the GRB electromagnetic emission. In particular, for many GRBs, the measurement of the source distance is not possible.

A high-energy neutrino detection from a BNS would help in a multi-messenger observation. On the one hand, having the time and position of the transient event from a neutrino detection might help to detect the EM signal, that could be missed without this information due to the small field of view of these instruments. On the other hand, sub-threshold analyses between gamma-ray (or GWs) and neutrino telescopes might allow to identify faint EM (or GW) signals, for which a significant detection would not be possible in neutrinos or gamma-rays (GWs) by their own [237, 238]. For this reason, neutrino telescopes actively follow both the GW and GRB detections searching for a correlated signal.

Despite of the many improvements, only one multi-messenger detection of a binary neutron system with the GW signal and short GRB associated emission has been observed (see section 1.4.1). This event yielded no neutrino detection, which allowed IceCube to constrain an on-axis jetted emission. This was later confirmed by radio observations.

The largest operating neutrino telescopes, sensitive to high (TeV-PeV) energies, constantly perform a follow-up of the different gamma-ray burst detections, with no significant neutrino counterpart identified up to now. The dedicated analyses by the ANTARES [82] and IceCube [80, 81] collaborations cover the follow-up of  $O(1000)$  GRB events, and focus on the search for a prompt neutrino emission, i.e. they don't consider any precursor or late neutrino emission [218, 219, 220, 221]. These analyses allow to set stringent limits to the neutrino flux predicted by these models for GRBs being a population of neutrino sources. Using the available GRB catalogs, results show that these sources do not account for more than 1% of the total diffuse neutrino flux measured by IceCube (considering the source is observed in the electromagnetic spectrum).



# Chapter 10

## Neutrino follow-up of gravitational-wave sources

In this chapter, the current status of gravitational-wave (GW) astronomy is discussed, with a description of the gravitational-wave detectors and the different techniques used to analyze the gravitational-wave data. Finally, the follow-up of the GW triggers and the analysis method to search for coincident neutrinos in ANTARES data with the GW signal, is presented, showing the astrophysical constraints obtained from the analysis results.

### 10.1 Gravitational-wave interferometers

Current gravitational-wave detectors use interferometry as a detection principle. Interferometry exploits the fact that the relative spacetime deformation that is aimed to be measured can be observed as a difference in length between the two arms of a Michelson interferometer. The main working scheme is the following. A laser beam is split into two arms, placed perpendicularly one to the other, by a beam splitter. The two beams are reflected back by two mirrors, placed at the end of each arm. The light travels back through the arms and the two beams recombine at the beam splitter, leading to an interference pattern.

When a gravitational wave crosses the detector, the spacetime perturbation results into the shortening of one length with respect to the other, that is elongated, and a length difference occurs. As a consequence, there is a change of phase of the light that takes place at the recombination point, making the destructive interference become constructive. A simplified picture is given in Fig.10.1.

Up to now, four GW interferometers have been deployed. Two of  $\sim 4$  km arm length in the USA, LIGO Hanford and LIGO Livingston, which have participated in three scientific runs. They were the first to detect a GW, which deserved the Nobel Prize award in 2017. A third detector located in Italy (Pisa), Virgo, with arms of  $\sim 3$  km length, which joined LIGO detectors for data taking in August 2015 (end of run O2). A fourth detector undergoing the final stage of the commissioning phase in Japan, called KAGRA, with  $\sim 3$  km long arms, will join LIGO and Virgo in future runs.

These complex experiments are equipped with additional instruments that allow for stabilizing the detector and monitoring the different noise contributions. In particular, they host microphones and sismometers among others to identify sources that could mimic the GW signal and veto them. Fabry-Perot resonant cavities are also present, allowing to increase the effective arm length, and therefore the signal amplitude.

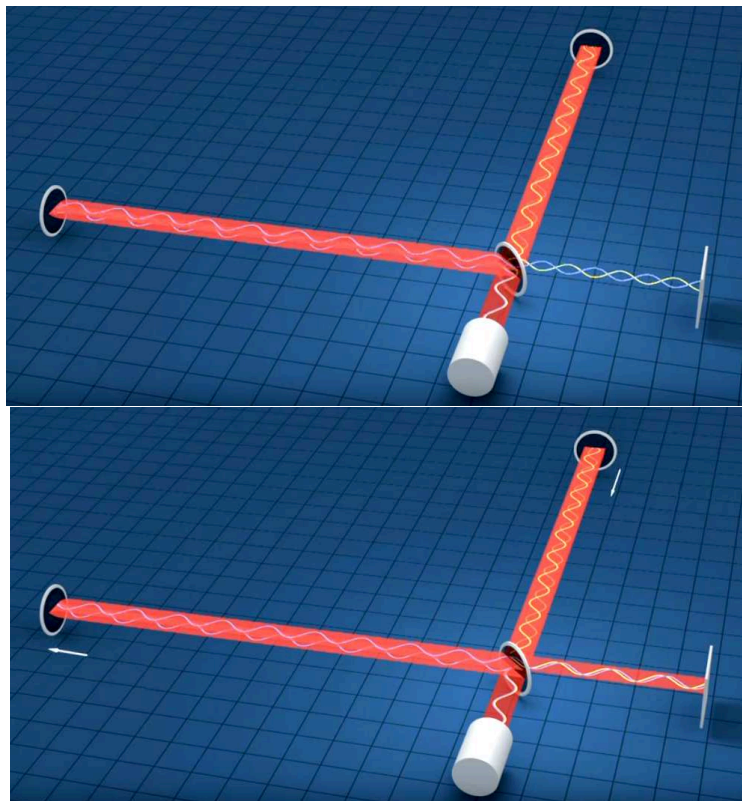


Figure 10.1: An schematic illustration of a Michelson interferometer. The main principle is drawn comparing the two Figure cases: (1) when no GW passes through the detector and a destructive interference is observed (top) and (2) when a GW crosses the detector and the interference is measured to be constructive (bottom).

### 10.1.1 Gravitational-wave searches

The search for GW events in the LIGO-Virgo detectors is done with three independent pipelines in parallel. Two of them (PyCBC [239] and GstLAL [240]) are based on Matched Filtering techniques, and are modeled searches which use templates for the signal waveform model. The range of potential merger masses they cover goes from 2 to 500(400)  $M_{\odot}$ , respectively. The main difference between them is that in the PyCBC pipeline the significance is computed from the Inverse False Alarm Rate (IFAR), which is the inverse of the number of events per unit time with a given signal to noise ratio expected from background only. GstLAL computes the significance using a log-likelihood method. The third one is Coherent Wave Burst (cWB) [241], which is an unmodelled search for transient signals based on a time frequency analysis that covers signals with duration up to 2s and frequencies up to 1 kHz.

Using time-frequency analysis and Matched Filtering techniques to filter noise, together with a good understanding of the detector, allow to reach the experimental sensitivity to observe such small signal amplitudes.

For the two modelled searches, signal waveform models (or templates) obtained from general relativity simulations are used in order to estimate the parameters of the system: component masses, chirp mass<sup>1</sup>, source location, distance, etc. In the case of an unmodelled burst, there is not existing template

<sup>1</sup>The chirp mass of a compact binary system is defined as a combination of the two merging object masses, and determines the GW signal evolution in frequency. This observable can be measured in gravitational-wave data analysis more easily and with more precision than the individual masses of the two binary components.

that can be used to infer such parameters. Even the distance can not be estimated without a multi-messenger counterpart. A coherent signature at each detector is the feature used to identify this kind of signal. The triangulation method can be applied to reconstruct the direction of the source in all the three cases.

### 10.1.2 State-of-the-art of gravitational-wave astronomy

Since 2015, the Ligo-Virgo Scientific Collaboration has completed three science runs: O1 from September 2015 until January 2016, O2 starting in November 2016 and ending up 31st August 2017, and O3 which covered the period from April 2019 until March 2020, with a month of commissioning break in the middle that divided the run into two parts, O3a and O3b.

O1 led to the first detection of a gravitational-wave signal, which originated from the merger of two black holes in a binary system, with a total of three events detected [7, 242]. During O2, the LIGO detectors started taking data, and some months later the Virgo detector joined the data taking for the first time. O2 led to the discovery of the multi-messenger signal from the coalescence of a binary neutron star system [8] (see section 1.4.1). Additionally, seven BBHs were detected during this observation run. Only three of the seven events ([243, 244, 245]) were published before the release of a final catalog [246], where four new events were announced. Finally, O3 has been a tremendous success as well as a step forward for gravitational-wave astronomy. The results coming out of this data analysis will be with no doubt a breakthrough in astroparticle physics and cosmology. The classification in terms of astrophysical origin of the 56 triggered events of O3 is given in Table 10.1.

Table 10.1: Event classification of the GW triggers during O3. Three event classes are compact binary mergers (BBH, BNS, NSBH). Terrestrial is the classification used for events with a small probability of being of astrophysical origin in the real-time analysis. Unmodelled is the label given to events that are triggered by cWB but not by the modelled pipelines. Mass Gap corresponds to events which present a reconstructed mass for one of the merging objects which is larger than the limit predicted for neutron stars and smaller than the limit predicted for stellar BHs.

Type	Terrestrial	BBH	BNS	NSBH	Mass Gap	Unmodelled
Events	3	37	6	4	5	1

## 10.2 GW events under study

In this section, some details about the six events that have been analysed as a part of this thesis work are provided. Four out of these six events were not announced as confirmed events before because, for each of them, one of the online or offline criteria failed, or all of them were satisfied but with a low signal-to-noise ratio. The two events that were already published were followed-up in real time by ANTARES, and the offline optimisation is discussed here. These two events are GW170608 [244] and GW170814 [245]. Some relevant information about the six GW events analysed:

- GW170608 is the lightest BBH observed so far. This event happened during a special period in which the LIGO-Hanford detector was going through an alignment process for angular coupling minimisation while the LIGO-Livingston detector was operating in a nominal configuration.
- GW170729 is interesting because it was found with the highest significance by the unmodelled search (cWB [241]), and one of the merging black holes presents a reconstructed mass which is

beyond the predicted limits from stellar evolution. This makes this GW source a potential candidate for being of different astrophysical origin. It was only identified in the offline search and thus, no alert was distributed to partner observatories. It is also the GW event leading to the most massive black hole remnant, the most distant source detected and the only one for which a null post-merger spin can be ruled out.

- GW170809 was found online and thus triggered an alert that was sent to electromagnetic observatories.
- GW170814 was identified as a coincident event between Livingston and Hanford detectors by GstLAL [240] when re-analyzing O2 data to incorporate an updated calibration for the Virgo detector, and additional noise subtraction applied to LIGO data. It is also well localised on the sky thanks to the non-observation by the Virgo interferometer.
- GW170818 happened just one day after the detection of the "golden" binary neutron star merger (GW170817). It was not triggered by the real-time search and thus, no alert was sent for an EM follow-up. It was only found by GstLAL in the offline analysis. It is the binary black hole merger with the best reconstructed location of the catalog.
- GW170823 was triggered by the three GW pipelines online and offline.

Table 10.2: Trigger and follow-up information of the events.

Event (GW)	LVC alert	Follow-up (TAToO)	GCN number	Event (GCN)
GW170608	YES	YES	21223	G288732
GW170729	NO	NO	-	-
GW170809	YES	YES	21433	G296853
GW170814	YES	YES	21479	G297595
GW170818	NO	NO	-	
GW170823	YES	YES	21659	G298936

Fig 10.2 (top) shows the skymap (in equatorial coordinates) containing the O2 events for which an alert was released to the electromagnetic EM community. The skymap in Fig. 10.2 (bottom) represents the events from O1 in 2015 and the two events of O2 for which no alert was sent.

In Table 10.2 we summarize the information about the GW trigger of the events and the neutrino follow-up with ANTARES, with the published GCN numbers given. ANTARES was active at the time of all GW events that triggered an alert.

In Table 10.3 the corresponding chirp mass and distance estimated for each event are shown. These parameters might be relevant in a neutrino search, as probability functions for the source being detected in neutrinos as well as for choosing the most relevant sources to be followed. The updated skymaps produced with the *LALInference* reconstruction algorithm are used for the evaluation of the 90% CL GW contour [247].

Table 10.3: Chirp mass and distance estimates for the events.

Event	GW170608	GW170729	GW170809	GW170814	GW170818	GW170823
$\mathcal{M}(M_{\odot})$	$7.9^{+0.2}_{-0.2}$	$35.7^{+6.5}_{-4.7}$	$25.0^{+2.1}_{-1.6}$	$24.2^{+1.4}_{-1.1}$	$26.7^{+2.1}_{-1.7}$	$29.3^{+4.2}_{-3.2}$
$d_L(\text{Mpc})$	$320^{+120}_{-110}$	$2750^{+1350}_{-1320}$	$990^{+320}_{-380}$	$580^{+160}_{-210}$	$1020^{+430}_{-360}$	$1850^{+840}_{-840}$

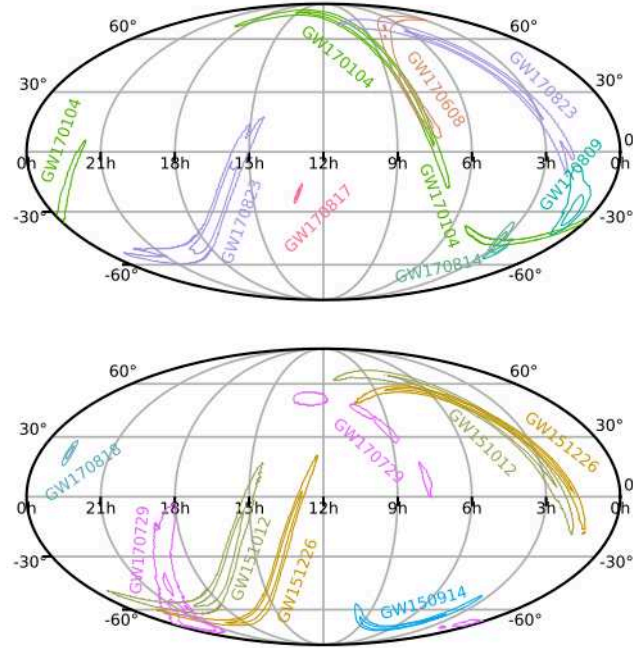


Figure 10.2: GW skymap for all the events detected during O1 and O2. Top: GW events observed during O2 for which a real-time alert was released. Bottom: GW detections from O1 and the two O2 events that were not triggered online. Figure from [246].

### 10.3 Neutrino follow-up

The ANTARES Collaboration responded to most of the GW triggers and performed a search for neutrino emission from these sources. In a first step, a real-time follow-up is done right after the reception of the alert. For this, a fixed event selection based on the quality of the reconstruction ( $\Lambda$  parameter) is applied. Later, a dedicated offline analysis is carried out for each event with refined cuts, as will be described in section 10.4.

The main difference between the two searches is that online searches only rely on upward-going muon neutrinos while offline searches have been extended to the full sky [248] and to neutrinos of all flavours [54]. Moreover, the offline analysis incorporates dedicated time and position calibrations that are not available in real-time. Results from the real-time and refined offline neutrino searches have been published for five GW signals from O1 and O2 [249, 250, 248, 54]. This leaves six GW events for which an offline search had not been performed using ANTARES data, and will be the focus of the work presented in the next sections.

#### 10.3.1 Dataset and Monte Carlo simulations

This analysis makes use of the ANTARES data set from June until September 2017, which covers all GW events that are analysed here. These data were processed using dedicated offline calibrations.

Data taking conditions during August 2017, where most of the events occurred, were quite stable and the sea current and trigger rate quite low. The information about the data quality conditions during each of the six GW runs is reported on Table 10.4. The parameter  $Q_{biolum}$  quantifies the data quality with respect to the bioluminescence conditions: the higher the value of  $Q_{biolum}$ , the lower bioluminescence and the better the conditions.

A specific high-statistics neutrino Monte Carlo simulation was generated for the 6 runs including the GW alert times with the latest run-by-run production. The time of the alerts in UTC and MJD are given in Table 10.5 together with the corresponding run number and its duration.

Table 10.4: Data quality information for each run.

GW run	Baseline (kHz)	Burst fraction (%)	Operating triggers	$Q_{biolum}$
85148	60	42	3N+2T3+K40+GC+TS0	1
85306	66	39	3N+2T3+K40+GC+TS0	3
85340	62	41	3N+2T3+K40+GC+TQ+TS0	1
85351	54	24	3N+2T3+K40+GC+TQ+TS0	3
85361	66	57	3N+2T3+K40+GC+TS0	1
85374	53	18	3N+2T3+K40+GC+TQ+TS0	4

Table 10.5: Time and run information about the events.

Event	UTC Time	MJD Time	Run number	Run duration (s)
GW170608	02:01:16.5	57912.08421875	85148	37119.20771
GW170729	18:56:29.3	57963.78922801	85306	43202.439722
GW170809	08:28:21.8	57974.35303009	85340	35947.104986
GW170814	10:30:43.5	57979.43800347	85351	29351.012496
GW170818	02:25:09.1	57983.10079977	85361	40215.559592
GW170823	13:13:58.5	57988.55137153	85374	43203.383444

### 10.3.2 Localisation of the GW events and ANTARES visibility

In this subsection, we provide the ANTARES coverage at the time of the alert, together with the localisation of the error box of each of the six GW events. The region of the GW error below (upgoing events) and above (downgoing events) is considered separately due to the different background conditions (see section 3.1). The Table 10.6 provides the size of the 90% GW CL area seen as downgoing and upgoing at the time of the GW trigger. Left plots in Figures 10.3 and 10.4 show the skymaps with the 90% confidence level (CL) GW area and the visibility of ANTARES at the time of the alert in equatorial coordinates. Right plots in Figures 10.3 and 10.4 provide the number of events in ANTARES data together with the 90% error box in local coordinates.

## 10.4 Analysis method

In this section, we focus on the strategy followed to search for a neutrino counterpart to transient sources in ANTARES. The criteria followed for the analysis optimization consists in choosing the cuts in such a way that the observation of one event in time and space coincidence with the GW trigger and

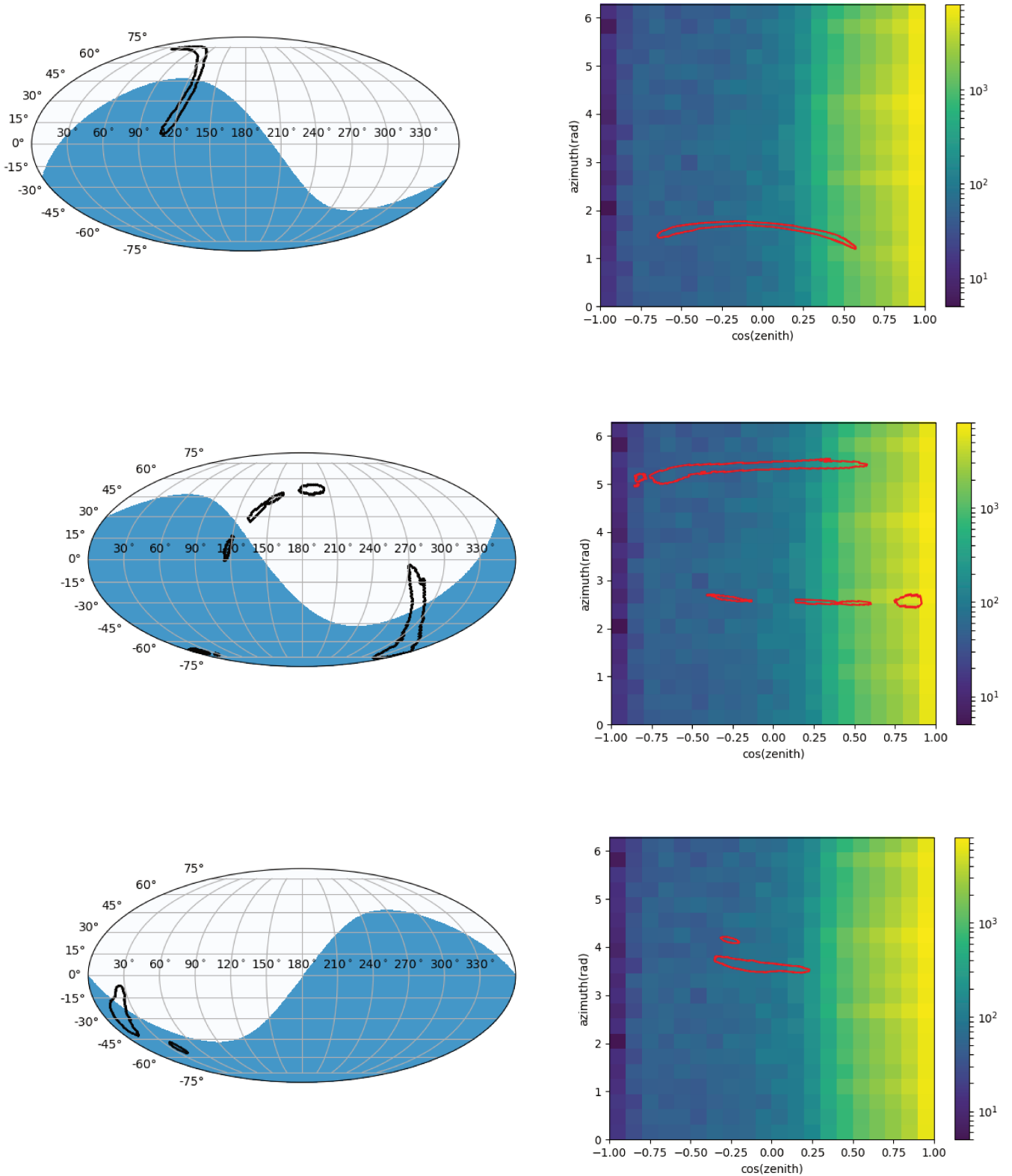


Figure 10.3: On the left, the skymaps (equatorial coordinates) with the 90% GW error box in black. The blue area corresponds to the sky region below the horizon for ANTARES at the time of the event. On the right, the number of data events over  $\sim 5$  days with  $\Lambda > -6.5$  as a function of the position on the sky (zenith, azimuth), together with the 90% GW confidence area in local coordinates in red. The skymaps are provide from top to bottom for the events: GW170608, GW170729 and GW170809.

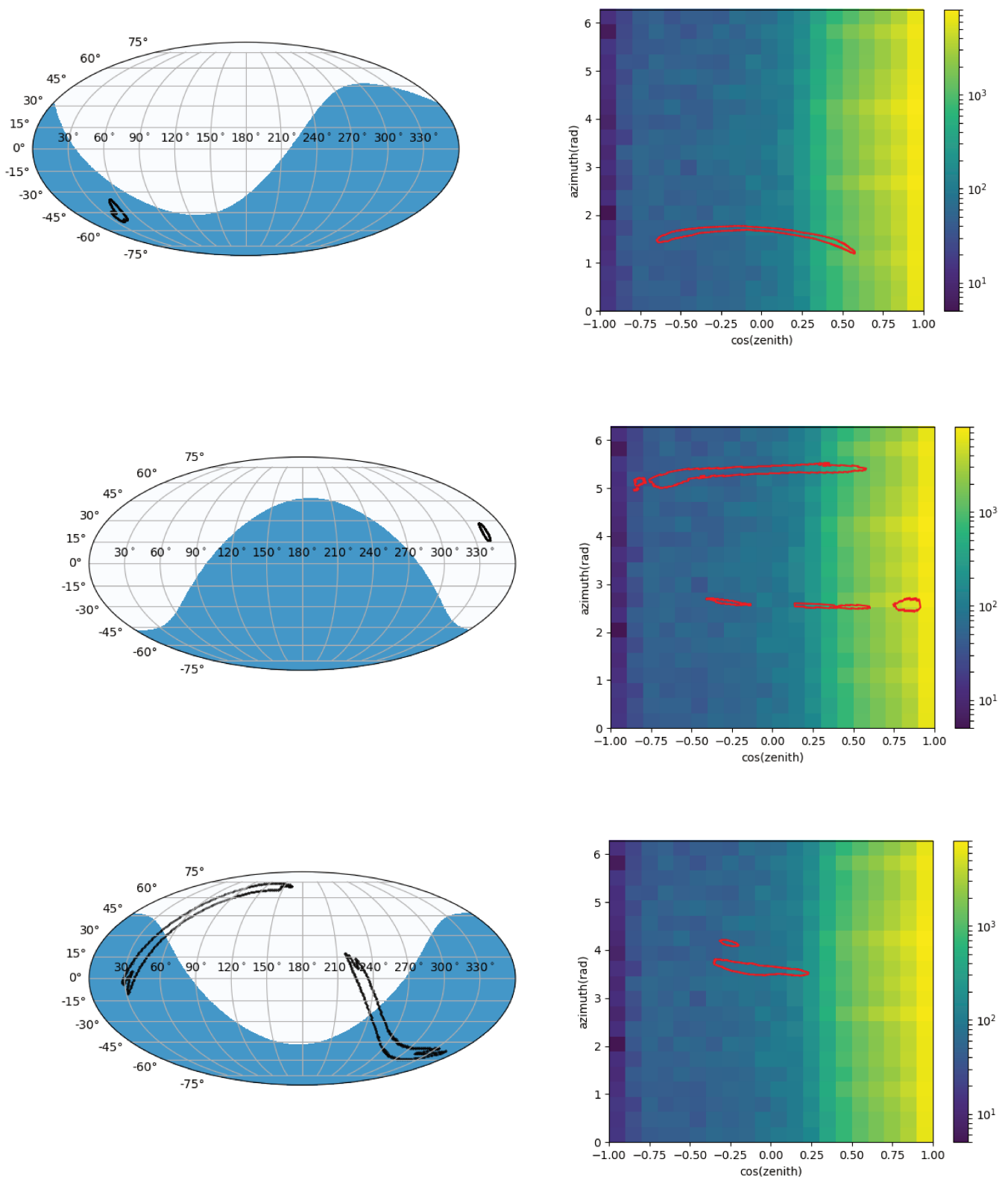


Figure 10.4: Left: skymaps in equatorial coordinates of the 90% CL GW contour in black. The region of the sky below the horizon for ANTARES at the time of the event is highlighted in blue. Right: number of events over  $\sim 5$  days with  $\Lambda > -6.5$  as a function of the position on the sky (zenith, azimuth). The GW error box in local coordinates is superimposed in red. The skymaps are provided from top to bottom for the events: GW170814, GW170818 and GW170823.

Table 10.6: Size (in deg<sup>2</sup>) of the 90% CL GW error box viewed as downgoing and upgoing events for ANTARES at the time of the alert.

Event	$A_{\text{up}}^{90\%} (\text{°})^2$	$A_{\text{down}}^{90\%} (\text{°})^2$
GW170608	226	170
GW170729	553	475
GW170809	245	95
GW170814	87	0
GW170818	0	39
GW170823	878	771

passing the selection leads to a detection significance of  $3\sigma$ .

The short time window and small region of interest for the search in case of a GW detection of a transient source allows to use time and space coincidences for a significant background reduction compared to diffuse or point-source searches, which makes possible an all-flavor search above the ANTARES horizon.

The optimization at  $3\sigma$  is chosen because on the one hand, it allows for a model independent optimization for the most sensitive channel (upgoing tracks). On the other hand, fixing the background for a  $3\sigma$  detection and maximising the signal expectation provides a good compromise between the discovery potential achieved and the obtained upper limits. In fact, this method was first proposed in [250] and has been used not only for GW-HEN analysis but also for the search of neutrino counterparts to Fast Radio Bursts [72].

It turns out that requiring that the probability of observing at least 1 event to be  $p_{3\sigma} = 2.7 \times 10^{-3}$  is equivalent to select the analysis cuts so that the background expectation is  $\mu = 2.7 \times 10^{-3}$  within the search time window and sky region, as derived in Eq. 10.1. This approximation where the probability is equal to the background expectation is only valid for small  $\mu$ .

$$\begin{aligned}
 P(n \geq 1|\mu) &= 1 - P(n = 0|\mu) = p_{3\sigma} = 2.7 \times 10^{-3} \\
 1 - e^{-\mu} &= 2.7 \times 10^{-3} \rightarrow \mu = -\ln(1 - 2.7 \times 10^{-3}) = 2.7 \times 10^{-3}
 \end{aligned}
 \tag{10.1}$$

For the analysis, four separate samples are considered taking into account the event topologies and the sky regions, dominated by a different background: upgoing tracks, upgoing showers, downgoing tracks and downgoing showers. The selection strategy and quality parameters used to set the optimal cuts is described in the following subsection for each of the samples.

To look for neutrinos in coincidence with a transient event, the data run containing the potential astrophysical signal, covering the full sky, is used to compute the number of events within the search time window and inside the region of interest in the sky where the analysis is performed, separately for the upgoing/downgoing sky coverage.

The search time window used in the analysis is  $\Delta t = \pm 500$  s, which is taken from the statistics on GRB precursors and covers the prompt GRB emission [251]. The spatial search region (RoI for Region of Interest), is defined by the area within the 90% CL contour provided by the GW reconstruction. The number of expected background events within  $\Delta t$ ,  $N_{\Delta t}$ , is computed according to Eq. 10.2.

$$N_{\Delta t} = \frac{\text{number of data events during GW event run}}{\text{run duration}} \times \Delta t
 \tag{10.2}$$

The rates are assumed not to vary significantly over the run duration. All the rates are then rescaled to get the actual number of events inside the 90% CL sky area (hereafter also referred to as error box) of the GW event, which depends on the declination of the GW event.

The background expectation inside the GW error box cannot be computed using the run of the event only because of the lack of statistics. Therefore, a larger amount of data (several months) is used to evaluate the background inside the 90% GW CL area by using the angular distance from the event position reconstruction to the source position, as stated in Eq. 10.3. Finally, one gets the total number of expected background events in the *RoI* and within  $\Delta t$ ,  $N_{\Delta t}^{RoI}$ .

$$N_{\Delta t}^{RoI} = \frac{\text{number of data events inside 90\% CL area}}{\text{total number of data events (up/down)}} \times N_{\Delta t} \quad (10.3)$$

### 10.4.1 Optimization of the track event selection

For the selection of track events, a different optimization is performed for upgoing and downgoing events, as explained below. For both, a cut on the angular reconstruction uncertainty  $\beta < 1^\circ$  is applied. The optimization is mainly based on the reconstruction quality parameter,  $\Lambda$  (see [124]), which is computed as the ratio between the likelihood of the reconstruction and the number of degrees of freedom.

The anticumulative distribution of  $N_{\Delta t}^{RoI}$  for  $\Lambda > -6.5$  is fitted to an exponential of the form  $a * \exp(-b * x)$ , with  $a$  and  $b$  the fitted parameters and  $x$  the number of events  $N_{\Delta t}^{RoI}$ . This fit is assumed to accurately describe the muon rate as a function of  $\Lambda$ . In order to estimate the number of events for high  $\Lambda$  values (where the statistics become too low), the atmospheric neutrino contribution is computed from the MC simulation and added to the exponential fit.

The optimised  $\Lambda$  cut is defined as the  $\Lambda$  value from which the number of background events  $N_{\Delta t}^{RoI}$  becomes smaller than  $p_{3\sigma} = 2.7 \times 10^{-3}$ . In this way, the optimization is done so that the Poisson probability of detecting at least one event is equal to  $p_{3\sigma}$ , as explained above. Moreover, this optimisation approach is model independent since no information about the signal is used.

For downgoing events, a cut in the energy estimate of the events is also applied to further reduce the overwhelming atmospheric muon background. This is efficient since cosmic neutrinos and atmospheric muons have a different energy spectrum. The number of hits used in the event reconstruction ( $N_{hits}$ ) is used as a proxy of the energy estimate, since they are directly correlated. The optimization for downgoing events is performed as follows:

1. The number of events remaining in the time window  $\Delta t$  and inside the 90% confidence level area is computed for different cuts in the energy-correlated variable,  $N_{hits}$ . For each value of  $N_{hits}$ , a cut on  $\Lambda$  is found to have less than  $2.7 \times 10^{-3}$  events coming from background after selection. For upgoing events, the optimisation is performed following this only step.
2. The set of cuts ( $\Lambda$ ,  $N_{hits}$ ) is optimised by comparing the number of survival signal events computed for the different combinations, assuming a signal flux  $\frac{dN}{dE} = \phi_0 E^{-2}$ , with  $\phi_0 = 10^{-8}$  GeV cm<sup>-2</sup> s<sup>-1</sup> sr<sup>-1</sup>. The set of cuts that maximizes the survival signal is applied as the final selection. In this sense, the downgoing track selection is slightly model dependent since it is optimised for a given spectrum, while for upgoing tracks it is model independent.

### 10.4.2 Optimization of the shower event selection

Once the track selection is applied, the events that do not pass the cuts are taken as shower candidates, so the two event samples are disjoint. While track-like events can start far away from the detector, shower events are required to be contained in the detector. The containment definition is given in [124]. Moreover, a pre-selection cut is applied on the output of the M-estimator value from the reconstruction fit (see section 3.4.4), based in [54]. All these conditions are summarised in Table 10.7.

Table 10.7: Pre-selection of events for the shower sample.

Criterion	Condition
Trigger	T3 or N3
Track veto	Not selected as a track
Containment	$\rho_{Sh} < 300m$ && $ z  < 250m$
M-estimator	Mest < 1000

Additional parameters are used to optimise the cuts for the shower selection. The result of a Random Decision Forest (RDF) classifier, output of the Dusj shower reconstruction [127], noted  $L_{\text{dusj}}$ , is used to distinguish track-like events from shower-like events. The RDF is trained using the information on the reconstruction parameters to identify the two topologies. In addition, an extended likelihood ratio,  $L_{\mu}$ , is also used to discriminate between cosmic showers and atmospheric muons based on the photomultiplier hits information [39], which also gives hint on the event topology.

The shower analysis for the follow-up of GW-O2 candidates uses the same optimisation procedure for upgoing and downgoing events. For each cut in the RDF output, the optimised  $L_{\mu}$  cut is obtained, using the same  $p_{3\sigma}$  criterion as for tracks. The set of cuts on  $L_{\text{dusj}}$  and  $L_{\mu}$  that maximizes the surviving signal assuming an  $E^{-2}$  neutrino spectrum while fulfilling the  $p_{3\sigma}$  condition is chosen as the final selection.

The larger angular uncertainty of shower events, which becomes comparable to the size of the 90% CL area of the GW events, needs to be taken into account. In this work, the final acceptance was corrected using the fraction of events that would be truly located and reconstructed inside the error box, using the MC information and called "good" events. In this way, the final acceptance only considers events whose angular error is smaller than the 90% GW confidence area. This uncertainty on the reconstructed direction translates, on average, into a 7% uncertainty on the final shower acceptance.

If there is no clear maximum in the number of signal events, which happens in some cases where a plateau is reached, the optimised  $L_{\text{dusj}}$  cut value is chosen in order to maximize the event statistics and reduce the uncertainty on the value  $p_{3\sigma}$  cut in the  $L_{\mu}$  parameter applied.

## 10.5 Event selection

This section will cover the results of the optimization of the cuts on the quality parameters described before for each of the events, in chronological order, following the method and selection criteria explained in section 10.4. The optimisation method is illustrated with the example of GW170814 for upgoing events and GW170818 for downgoing events.

### 10.5.1 Finding the optimal cuts: example of GW170814

Let's start with the optimisation for upgoing events. In Figure 10.5, the anticumulative distribution of the track reconstruction likelihood,  $\Lambda$  parameter, from data is shown for upgoing events. It corresponds to the expected number of background events inside the error box within  $\Delta t$ . This distribution is used to find the optimal cut: the value of  $\Lambda$  crossing the  $p_{3\sigma}$  line. The optimised value that will be applied on the analysis is  $\Lambda > -5.58$  for upgoing tracks.

The events in the GW data run that are not selected as tracks (they do not pass the optimal  $\Lambda$  cut) enter the shower selection. Table 10.8 shows the different sets of cuts for the shower sample fulfilling the  $p_{3\sigma}$  criteria. For each set of cuts, the acceptance is provided, which is the number of expected signal events passing the cuts, assuming an  $E^{-2}$  spectrum. The optimal set of cuts chosen, which maximises the acceptance, is highlighted in red. Table 10.8 also gives the fraction of shower events that have an angular resolution smaller than the error box ("good" events).

Fig. 10.6 shows the data distribution of the  $L_\mu$  likelihood value with the optimal  $L_{\text{dusj}}$  cut applied. An exponential fit is applied to the data (red line).

Table 10.8: Fraction of events generated and reconstructed inside the 90% error box for each combination of cuts and acceptance after applying the correction factor.

$L_{\text{dusj}}$ cut	$L_\mu$ up	% of "good" events up	$\text{acc}_{up}^{\text{corr}}$
0	1	<b><math>53 \pm 15\%</math></b>	<b><math>1.1 \pm 0.1</math></b>
0.1	-36	$39 \pm 12\%$	$0.90 \pm 0.08$
0.2	-52	$33 \pm 11\%$	$0.66 \pm 0.05$

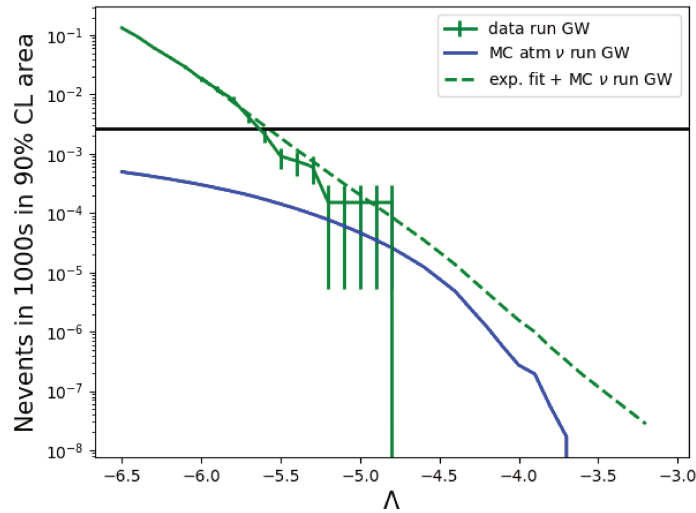


Figure 10.5: Anticumulative distribution of  $\Lambda$  after scaling to the 90% CL GW surface and the time window,  $N_{\Delta t}^{\text{ROI}}$ . Events in the corresponding data run are shown in solid green, the boosted neutrino MC of the run in blue, and the exponential fit for atmospheric muons (data) and atmospheric neutrinos (MC) is given by the dashed green line, used for finding the  $p_{3\sigma}$  cut, determined by its crossing with the black line.

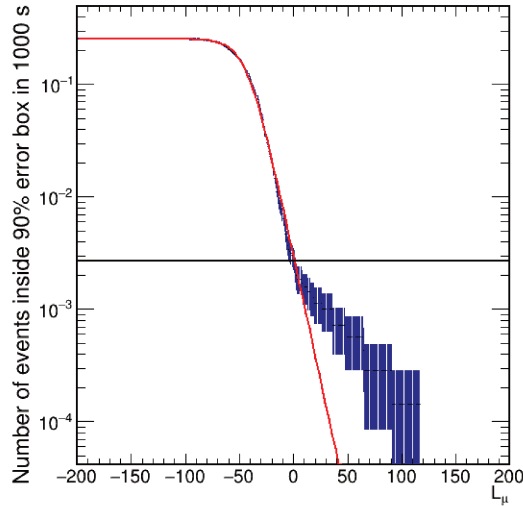


Figure 10.6: Antiumulative distribution of  $L_\mu$  of the data run after applying the pre-selection and the optimised  $L_{\text{dusj}}$  cut. The y-axis corresponds to the number of expected data events in time and space coincidence with the GW event. The GW event was inside the ANTARES detector horizon, so only upgoing events are shown.

### 10.5.2 Finding the optimal cuts: example of GW170818

Let's now move to an example of the optimisation for downgoing events. In Figure 10.7, the number of expected signal events for an  $E^{-2}$  spectrum as a function of  $\Lambda$  for the different  $N_{\text{hits}}$  cuts is shown. The red dots indicate the value of the optimal  $\Lambda$  cut, fulfilling the  $p_{3\sigma}$  condition for each  $N_{\text{hits}}$  cut. The final set of cuts ( $N_{\text{hits}}, \Lambda$ ) is chosen to maximize this signal efficiency. The corresponding optimization yields the final selection of ( $N_{\text{hits}} > 80, \Lambda > -5.4$ ).

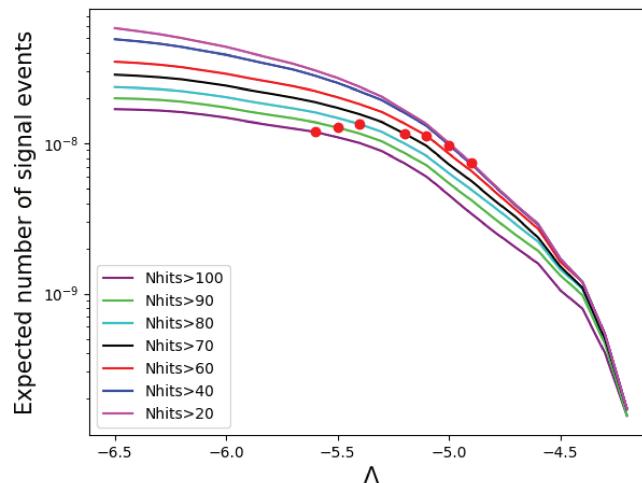


Figure 10.7: Expected number of cosmic neutrinos assuming an  $E^{-2}$  spectrum (signal efficiency) as a function of  $\Lambda$  for different cuts on the energy estimate ( $N_{\text{hits}}$ ). The red dots indicate the value of the optimised  $\Lambda$  cut in each case.

After applying the track selection and the pre-selection cut in Table 10.7, let's move to the final shower optimisation. The different sets of cuts for the shower sample fulfilling the  $p_{3\sigma}$  criteria Table 10.9, together with the number of survival signal events inside the error box (corrected acceptance) and the fraction of "good" events. The optimal set of cuts chosen is highlighted in red. Fig. 10.8 shows the  $L_\mu$  distribution for the optimal  $L_{\text{dusj}}$  cut that will be applied.

Table 10.9: Fraction of events generated and reconstructed inside the 90% error box ("good" events) for each combination of cuts, and the corresponding acceptance after applying the correction factor.

$L_{dusj}$ cut	$L_\mu$ down	% of "good" events down	$\text{acc}_{down}^{corr}$
0	3	$11 \pm 7\%$	$0.43 \pm 0.02$
0.1	-30	$13 \pm 7\%$	$0.47 \pm 0.02$
0.2	-43	$7 \pm 7\%$	$0.26 \pm 0.02$

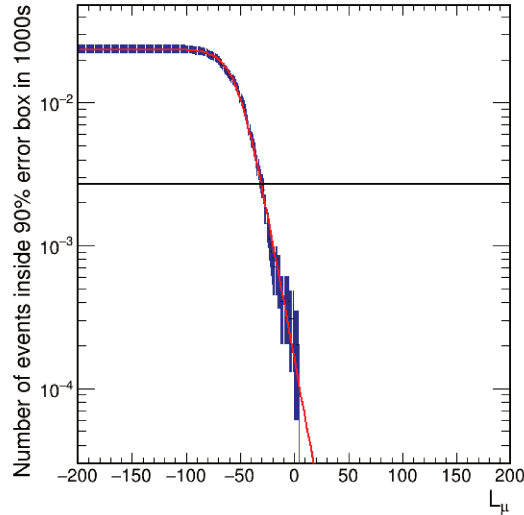


Figure 10.8: Cumulative distribution of  $L_\mu$  after applying the pre-selection and the optimised  $L_{dusj}$  cut. The y-axis corresponds to the number of events in the run containing the GW event, falling inside the 90% GW confidence area and inside the 1000 s search window. The GW event was on the ANTARES downgoing sky and only downgoing events are shown.

### 10.5.3 Summary

The search and analysis optimisation is done independently for four separate samples, defined by the event topology (tracks and showers) and the sky region (upgoing and downgoing). The final event selection cuts for each of the four samples, and for each GW event analysed are summarised in Tables 10.10 and 10.11.

Table 10.10: Final cuts obtained for each event and sample.

Event	Tracks up ( $\Lambda$ )	Tracks down ( $N_{hits}, \Lambda$ )
GW170608	-5.55	(80, -5.3)
GW170729	-5.4	(100, -5.1)
GW170809	-5.4	(40, -5.4)
GW170814	-5.6	-
GW170818	-	(80, -5.4)
GW170823	-4.9	(90, -4.85)

Table 10.11: Final cuts applied to the shower sample.

GW event	$L_{dusj}$ cut	$L_{\mu}$ down	$L_{\mu}$ up
GW170608	0.1	-31	-20
GW170729	0.1	0	-20
GW170809	0.1	no cut	-19
GW170814	0.0	-	1
GW170818	0.1	-30	-
GW170823	0.2	-16	-27

## 10.6 Analysis results

After unblinding the dataset, no neutrino was found that passed the cuts during the search window and inside the GW error box. The non-detection of neutrino events in time and space coincidence with the six analysed GW sources allows to set constraints on the neutrino emission from binary black-hole mergers.

The detector sensitivity to the searched-for signal depends on the source position and on the neutrino energy. Therefore, constraints are set as a function of the position in the sky and within the 5-95% energy range of the search. The sensitivity is given by the detector acceptance, which is defined as the expected number of signal events passing the selection cuts per given unit flux. Similarly, this sensitivity can also be characterised by the effective area; see section 3.4.5 for their relation. The ANTARES acceptance and effective area are evaluated by means of a dedicated MC simulation performed on a run-by-run basis. This accounts for the detector configuration and variable data-taking conditions for each ANTARES observing run at the time of the GW events under study, which impact the detector sensitivity.

As there is not a precise location of the GW signals, the neutrino emission is considered to come from a point-like source, with the source located at different pixels inside the error box region. The pixel size in which the detector sensitivity is computed is chosen to be large enough to avoid MC statistical fluctuations ( $18^\circ$  in sinus of the declination and  $36^\circ$  in right ascension). With these considerations, upper limits (UL) as a function of the position on the sky are presented in the form of skymaps (see Figures 10.9 and 10.10). The resulting constraints on the neutrino spectral fluence and on the total isotropic energy emitted through high-energy neutrinos (TeV-PeV range) are summarised in Tables 10.12 and 10.14.

### 10.6.1 Constraints on the neutrino spectral fluence

Upper limits at 90% CL on the neutrino spectral fluence from a point-like source located in a given position on the sky are calculated using the null result and the detector acceptance.

In the case of no signal event, a 90% CL fluence upper limit can be defined. Using Poisson statistics, this upper limit corresponds to the time-integrated flux that would produce on average  $N^{90\%}=2.3$  detected neutrino events in the pixel containing the source. The 90% UL on the number of events,  $N^{90\%}$ , is defined as:

$$N^{90\%} = \int \frac{dN}{dE_\nu}(E_\nu) A_{\text{eff}}(E_\nu, \delta) dE_\nu, \quad (10.4)$$

where  $A_{\text{eff}}(E_\nu, \delta)$  is the ANTARES effective area at the alert time, which takes into account the absorption of neutrinos by the Earth and the detector visibility. This effective area depends on the event

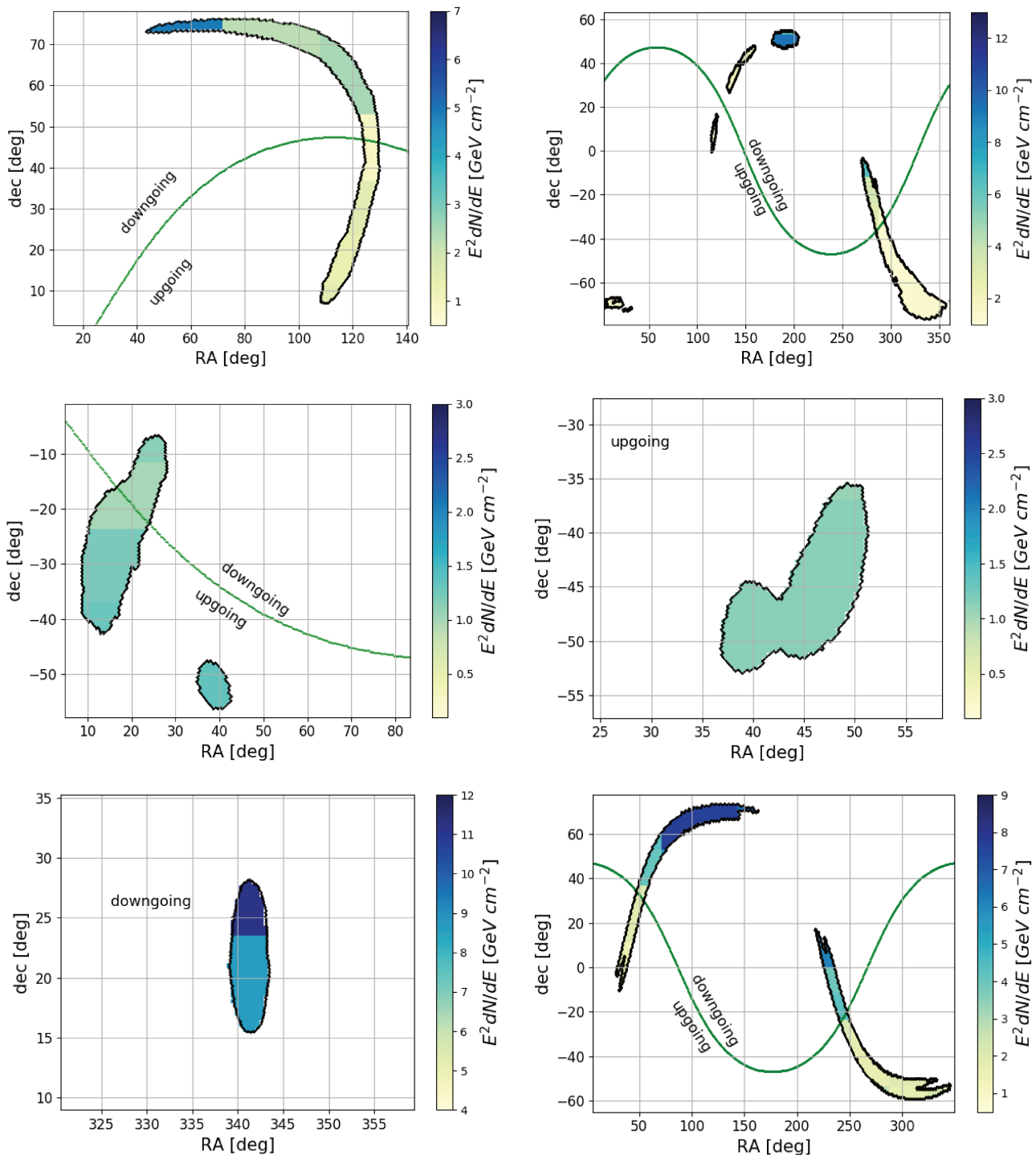


Figure 10.9: Upper limits on the neutrino spectral fluence (colored scale) as a function of the position in the sky in equatorial coordinates, computed assuming an  $E^{-2}$  neutrino spectrum. The events are shown in chronological order: GW170608 (upper left), GW170729 (upper right), GW170809 (middle left), GW170814 (middle right), GW170818 (bottom left) and GW170823 (bottom right). The 90% GW localisation contour is superimposed. The green line indicates the ANTARES horizon, below the line corresponds to upgoing events and above the line to downgoing events above the horizon.

selection cuts as well as on the neutrino energy and the position of the source. For a neutrino power-law spectrum ( $\frac{dN}{dE_\nu} \propto E^{-\gamma}$ ), the spectral fluence at the detector can be defined as:

$$E_\nu^2 \frac{dN}{dE_\nu} = \phi_0 \left( \frac{E_\nu}{1\text{GeV}} \right)^{-\gamma+2} (\text{GeV} \cdot \text{cm}^{-2}). \quad (10.5)$$

The upper limits obtained, assuming a neutrino spectrum with spectral index  $\gamma=2$  (generic model typically expected for Fermi acceleration [17]), are shown in Fig. 10.9 for the six GW events. Table 10.12 provides the average 90% CL upper limits on the neutrino spectral fluence ( $\phi_0^{90\%}$ ) inside the error box.

Table 10.12: Average 90% upper limit on the neutrino spectral fluence inside the 90% GW CL contour.

GW event	$\phi_0^{90\%}$ (GeV cm <sup>-2</sup> )	
	Upgoing	Downgoing
GW170608	1.6±0.5	2.2±0.9
GW170729	1.7±0.5	4.0±1.0
GW170809	1.1±0.3	1.2±0.5
GW170814	1.1±0.3	-
GW170818	-	9.0±4.0
GW170823	1.7±0.5	6.0±2.0

The main systematic uncertainties on the estimated fluence upper limits come from two sources. The first one is the uncertainty on the detector acceptance, which is related to the photon detection efficiency of the PMTs. It comprises an angular effect that leads to a 15% uncertainty on the flux of upgoing events [124] and a 30% uncertainty for downgoing events [252], and an overall effect due to the quantum efficiency of the PMTs and optical water properties, which results in an uncertainty of about 20% on the total acceptance [253]. The second source is related to the capability of the MC simulation to reproduce data conditions on a run-by-run basis. This effect was evaluated together for upgoing and downgoing events and amounts to  $\sim 20\%$  [248]. For the shower event topology, an additional systematic effect of  $\sim 7\%$  is introduced to account for the uncertainty on the shower position inside the GW error box. All the mentioned effects account for a total systematic uncertainty on the fluence upper limit of about  $\sim 33\%$  for upgoing and  $\sim 42\%$  for downgoing events.

Table 10.13 provides a summary of the current neutrino limits from previous GW-neutrino follow-up analyses. The first three rows in the Table are two O1 events for which the analysis was performed independently by IceCube and ANTARES telescopes [249, 250]. For these two events, the value reported in the table refers to the most sensitive detector. The third event (GW170104) is the only published event from O2 before this work. It is an ANTARES only analysis and considers events from the full sky [248]. For the second and third events, the values are extrapolated from the skymaps.

This comparison shows that IceCube limits are about one order of magnitude better than the ANTARES results presented here, both in the upgoing and downgoing respective searches. This is due to the larger size (and thus larger effective area) of the IceCube detector. The results of this work show an improvement of 15-30% for upgoing events, which becomes a factor of 2 and up to an order of magnitude improvement in the downgoing search limits obtained. This improvement comes from the addition of the shower channel and a better characterisation of the downgoing background as a function of the declination. In conclusion, in the region below the horizon for IceCube, our results are not competitive, while in the region above the horizon for IceCube, the ANTARES limits are comparable, and a combination may be of interest.

Table 10.13: Average upper limit inside the 90% CL contour for the previous GW-neutrino follow-up analyses.

GW event	sky region	$\phi_0^{90\%}$ (GeV cm <sup>-2</sup> )
GW150914	IceCube downgoing [249]	1.2±0.3
GW151226	IceCube upgoing [250]	~0.06
GW151226	IceCube downgoing [250]	~0.9
GW170104	ANTARES upgoing [248]	~2
GW170104	ANTARES downgoing [248]	~20

## 10.6.2 Constraints on the total energy

From the null detection and using the 90% CL upper limit on the neutrino spectral fluence obtained in the previous section, a constraint on the total equivalent isotropic energy ( $E_{\nu,iso}$ ) emitted by the source in high-energy neutrinos, within the sensitive energy range of the search (TeV-PeV range), can be set. The mean of the reconstructed luminosity distance ( $D_L$ ) distribution inside the error box provided by LIGO-Virgo [246] is used for the redshift estimate.

The total energy emitted in high-energy neutrinos is computed according to Eq. 10.6 by integrating the neutrino spectrum over the energy range expected to contain 5-95% of detected events (see Table 10.14) together with the measured luminosity distance and the associated redshift,

$$E_{\nu,iso} = \frac{4\pi D_L(z)^2}{1+z} \int_{E^{5\%}}^{E^{95\%}} E_\nu^{-2} \phi_0^{90\%} E_\nu dE_\nu. \quad (10.6)$$

The average 90% CL upper limits inside the error box are summarised in Table 10.14 together with the 5-95% energy range for each GW event. In Fig. 10.11, these results are shown as a function of the redshift for six GW events, separately for the upgoing (orange) and downgoing (blue) regions of the error box. These results are computed using the average limits and  $D_L$  measurements inside the 90% GW confidence regions, together with their uncertainty. In Fig. 10.10, results are provided in the form of skymaps with the 90% UL as a function of the position of the sky for the pixels inside the error box. The distance estimate at each pixel provided by the LIGO-Virgo probability map is used, as in [254, 255].

As inferred from Eq. 10.6, these limits scale with  $D_L^2$  and proportionally to the fluence limits ( $\phi_0^{90\%}$ ), which have been here obtained for a  $E^{-2}$  neutrino spectrum. While upgoing background rates are mainly isotropic in local coordinates, the downgoing rates strongly depend on the zenith angle. See for instance events GW170809 and GW170818. The GW170809 downgoing region is very close to the ANTARES horizon, where the background level is very close to the one expected when looking at events traveling through the Earth. On the other hand, GW170818 sky location was almost at the zenith of the detector at the trigger time, where the atmospheric rate becomes about two orders of magnitude higher. The different background conditions lead to the different limits as observed in Fig. 10.11.

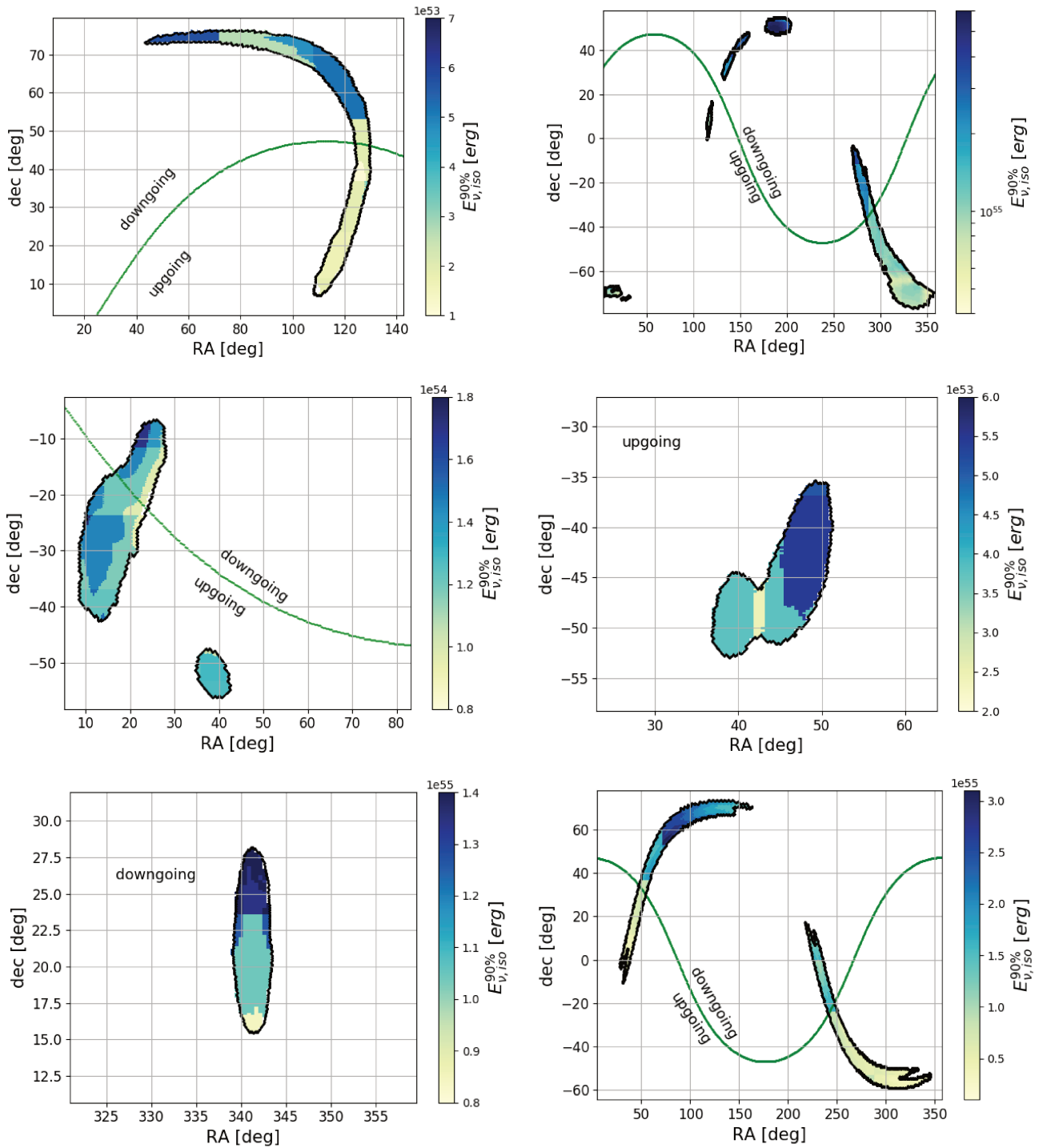


Figure 10.10: Upper limits on the total energy emitted in neutrinos within the 5-95% energy range of the analysis (colored scale) as a function of the position in the sky in equatorial coordinates, computed assuming an  $E^{-2}$  neutrino spectrum. The events are shown in chronological order: GW170608 (upper left), GW170729 (upper right), GW170809 (middle left), GW170814 (middle right), GW170818 (bottom left) and GW170823 (bottom right). The 90% GW localisation contour is superimposed. The green line indicates the ANTARES horizon, below the line corresponds to upgoing events and above the line to downgoing events.

Table 10.14: Average upper limit ( $E_{\nu,iso}^{up/down}$ ) on the total neutrino energy emitted inside the 90% confident area, computed within the 5-95% energy range of the analysis, for upgoing and downgoing events and for each GW event. The measured redshift for each event is also provided.

GW event	redshift (z)	$E_{5-95\%}^{up}$	$E_{5-95\%}^{down}$	$E_{\nu,iso}^{up}$ [erg]	$E_{\nu,iso}^{down}$ [erg]
GW170608	$0.07^{+0.02}_{-0.02}$	2.5 TeV - 4.0 PeV	20 TeV - 25 PeV	$2.2 \times 10^{53}$	$2.9 \times 10^{53}$
GW170729	$0.48^{+0.19}_{-0.20}$	3.2 TeV - 4.0 PeV	32 TeV - 25 PeV	$1.2 \times 10^{55}$	$2.6 \times 10^{55}$
GW170809	$0.20^{+0.05}_{-0.07}$	3.2 TeV - 4.0 PeV	8 TeV - 20 PeV	$1.2 \times 10^{54}$	$1.5 \times 10^{54}$
GW170814	$0.12^{+0.03}_{-0.04}$	2.5 TeV - 5.0 PeV	-	$4.8 \times 10^{53}$	-
GW170818	$0.20^{+0.07}_{-0.07}$	-	20 TeV - 32 PeV	-	$1.1 \times 10^{55}$
GW170823	$0.34^{+0.13}_{-0.14}$	4.0 TeV - 4.0 PeV	20 TeV - 25 PeV	$5.7 \times 10^{54}$	$1.9 \times 10^{55}$

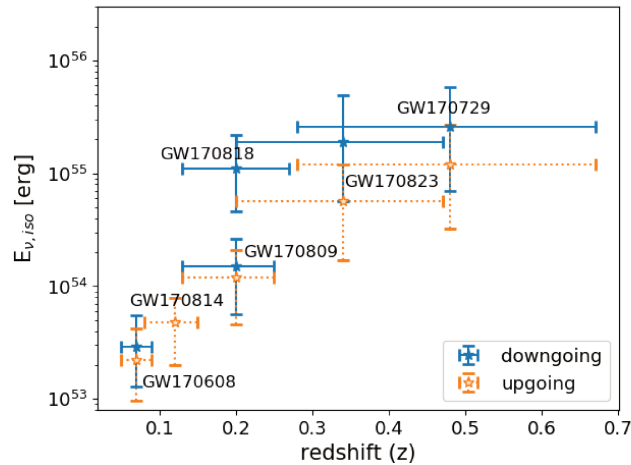


Figure 10.11: 90% CL upper limits on the total isotropic energy emitted in neutrinos within the 5-95% energy range of the search for the six GW events analysed as a function of the estimated redshift. Results are given for the ANTARES downgoing (blue) and upgoing (orange) searches. The error bars in the X-axis correspond to the uncertainty on the distance estimate. The error bars in the Y-axis indicate the maximum and minimum limits obtained within this redshift range.

# Chapter 11

## Follow-up of very high-energy gamma-ray bursts with ANTARES

In this chapter, the general context concerning the very high-energy (VHE) gamma-ray bursts detections by Imaging Air Cherenkov Telescopes (IACTs) is discussed and the results of the ANTARES follow-up of these VHE gamma-ray bursts are presented.

### 11.1 Introduction to the GRBs under study

As mentioned earlier in section 9.2, the emission of very high energy (VHE) gamma rays, in the  $O(\text{TeV})$  range during the GRB afterglow phase violates the maximum photon synchrotron energy limit. Interestingly, this could be a hint for an additional hadronic component needed to model the full EM lightcurve, motivating a high-energy neutrino search.

The detection of these  $O(\text{TeV})$  gamma rays by space instruments remains challenging due to their limited effective area. However, large ground-based Cherenkov detectors observing the showers induced in the atmosphere by high-energy gamma rays are well suited for these kind of observations. Examples of these kind of detectors are the H.E.S.S, MAGIC and VERITAS telescopes.

Three GRBs have lead to the detection of  $>300$  GeV photons in IACTs: GRB 180720B, observed by H.E.S.S, GRB 190114C, detected by MAGIC, and GRB 190829A, also detected by the H.E.S.S telescope. Even though the observed VHE photons can be explained by leptonic models and the synchrotron self-Compton (SSC) scenario [256, 257] fits the data of these observations [228, 229, 227], these sources remain of interest as potential high-energy neutrino emitters. In fact, some attempts have been made to model the data with a different hypothesis, showing that the high-energy photons could be produced in photohadronic interactions [230]. Indeed, a subdominant hadronic component is not ruled out by the available data. Therefore, a particular study is carried out for these events to investigate a possible small hadronic component that could be present in the EM data.

#### 11.1.1 GRB 180720B

The GBM (Gamma-ray Burst Monitor) instrument on board the Fermi satellite triggered the gamma-ray emission from GRB 180720B at UTC time  $T_0 = 14:21:39.65$  (GCN #22974). This event is the 6th brightest GRB observed in Fermi-GBM and the second GRB with the highest energy flux observed by Swift (GCN #22973) in the afterglow (11 h after  $T_0$ ), with a very long X-ray plateau. The source has been estimated to be at a redshift of  $z=0.653$  (measured by the VLT [227]). The time at which 90% of

the total gamma-ray luminosity is reached,  $T_{90}$ , was measured as of  $T_{90} = 48.9$  s (by Fermi-GBM [227]).

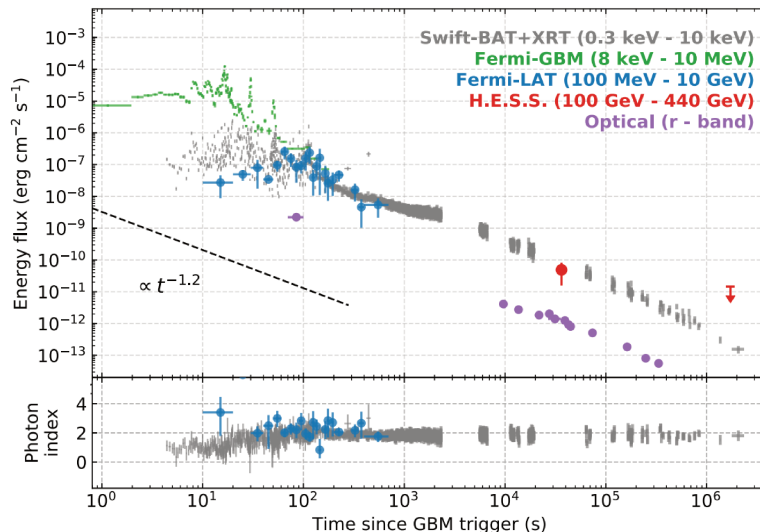


Figure 11.1: Multi-wavelength electromagnetic observations of GRB 180729. Figure from [227].

The source was located at equatorial coordinates (RA; Dec) = (0.53°; -2.93°), and entered in the H.E.S.S. field of view about 10 h after the trigger time. An observation was performed for a total of 2 h exposure, which yielded a  $5\sigma$  post-trial detection of gamma-ray emission above 300 GeV [227]. Therefore, the neutrino follow-up will cover these 12 h. The GRB lightcurve observed through the different EM wavelengths can be found in Fig. 11.1.

### 11.1.2 GRB 190114C

On January 19th 2019, the Swift satellite triggered the event GRB 190114C (GCN #23688). This burst was shortly after detected by other space instruments: Fermi-GBM (GCN #23707), Integral/SPI-ACS (GCN #23714), among others. The MAGIC telescope started the follow-up of the event about 50 seconds after the Swift trigger, and observed the source for about 20 minutes. This means, that the neutrino search will end up 1250 s after the trigger time.

MAGIC observations led to a  $20\sigma$  detection during this time exposure (GCN #23701). The source distance was estimated at a redshift of  $z=0.42$  (GCN #23708). The measured duration,  $T_{90}$ , was of 116 s by Fermi-GBM (GCN #23707) and about 362 s by Swift-BAT (GCN #23688). The GRB was identified at equatorial coordinates (RA; Dec) = (-54.51°; -26.94°).

The observation of gamma-ray photons with energies  $>300$  GeV hundreds of seconds after the trigger indicates that an additional mechanism may take place other than the non-thermal leptonic models. The SSC leptonic scenario is found to fit the data with good agreement. However, a subdominant hadronic component that would be accompanied by neutrino production, not being ruled out by the available data, remains a possible scenario. The detected EM lightcurve can be found in Fig. 11.2, including data from the different experiments sensitive at different wavelengths.

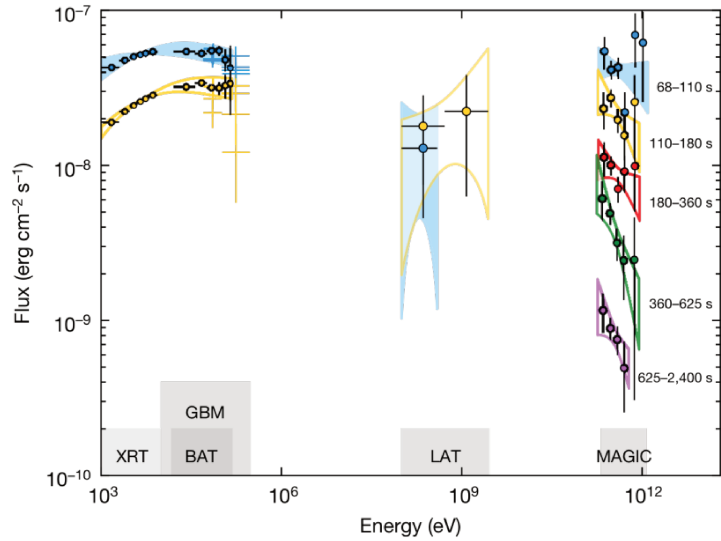


Figure 11.2: Multi-wavelength electromagnetic lightcurve of GRB 180729. Figure from [228].

### 11.1.3 GRB 190829A

The GBM instrument on board the Fermi satellite triggered the gamma-ray emission from GRB 190829A at the time  $T_0 = 19:55:53$  UTC (GCN #25551). The source has been estimated to be at a redshift of  $z=0.0785$  (GCN #25565) with a measured  $T_{90}$  of 63 s (GCN #25575). The observation of this source with the H.E.S.S. telescope started 4 h and 20 min after  $T_0$ , and the total exposure of 3h 40min led to a significant ( $>5\sigma$  excess) detection, with VHE gamma-ray emission observed during the afterglow (GCN #25566). This gives a search window for the neutrino analysis of 8 h. The position of the source is (RA; Dec) = (45.6°; -7.1°) RA=45.6 deg and DEC=-7.1 deg.

The lightcurve of GRB 190829A shows two peaks and the total isotropic energy using the best fits to the multi-wavelength spectrum is  $\sim 2.967 \times 10^{53}$  erg. The SSC scenario is able to reproduce the data at the VHE: both the non-observation by Fermi-LAT and the H.E.S.S. detection at high energies [258]. However, the H.E.S.S. analysis is not yet available and these conclusions are only based on Fermi-LAT ULs and an estimate of the H.E.S.S. sensitivity.

## 11.2 Analysis method

The analysis method for GRB events is based on the one that has been described in section 10.4.

In this case, the event rate over the time window  $\Delta t$  is computed as in Eq. 10.2. For each GRB analysed, the time window will be adjusted to cover all the EM emission observed, including the prompt and afterglow phases. The analysis is based on the information provided in the GCNs, since it was started before the publication of the final analysis.

Since these are localised sources, the spatial search region, later on called the region of interest (RoI), is optimised to take into account the ANTARES angular resolution. The RoI is taken to be a circle around the position of the GRB, whose radius ( $R_{RoI}$ ) will be optimised to maximise the signal expectation. The size of the RoI will replace the 90% GW confidence area in Eq. 10.3.

### 11.2.1 Track selection

Aside from the two differences related to the type of source described above, the track event selection is the same as for GW events, detailed in section. 10.4.1. The only exception was GRB 190114C, for which (as for GRB 170817A), no  $N_{\text{hits}}$  cut was needed due to the lower background in the short time window and small RoI considered.

### 11.2.2 Shower optimization

The first time that showers were included in a transient (GW-HEN) analysis [54], the selection was not optimised but based on what had been previously done in point-source neutrino searches [259]. In this thesis, an effort was devoted to define and optimise a shower selection for multi-messenger searches. In a first step, a dedicated optimisation was performed for GW-HEN searches (see section 10.4). For the event GRB 190114C, the same selection was applied.

As the first very-high energy,  $O(\text{TeV})$ , gamma-ray detections in the late afterglow were announced, the specific characteristics of these events (with a longer emission time and good space localisation), led to further investigation for a better performing optimisation of the shower topology cuts. Therefore, the slightly new selection used in this analysis is presented here.

As already mentioned, in the case of neutrino searches from GRBs, the spatial region of the search is optimised, and not fixed as for GW-HEN analysis. When using a large time window ( $\sim 12$  h for the two long GRBs analysis in this work) and large RoI (10-20 deg radius around the source position), the optimisation is not anymore feasible directly on data because the lower statistics in one run cannot characterise the tail of the background distribution. For this reason, a dedicated run-by-run atmospheric muon Monte Carlo simulation is used to evaluate the background. The data-MC comparisons needed in this case and the higher background rate, led to additional selection cuts in order to reach the  $p_{3\sigma}$  level.

On Fig. 11.3, we show the cumulative distribution of  $L_{\mu}$  with a cut on  $L_{\text{dusj}} > 0.3$  (typical in point source searches), for upgoing (top) and downgoing events (bottom). Both the GRB run (left) and the previous data run (right) distributions are shown. We see that indeed the statistics of one data run do not allow to set a cut using the  $3\sigma$  optimization. Therefore, the muon MC simulation must be used here to estimate the background.

First of all, one would like to discard as many mis-reconstructed muons as possible. For this, one can make use also of the track reconstruction algorithm (AAFit) for the zenith selection in the shower sample. By requiring that the event is not only reconstructed upgoing/downgoing by TANTRA, but also that it is not reconstructed in the opposite region by the AAFit reconstruction, the background is significantly reduced. Therefore, the upgoing/downgoing selection is applied simultaneously in both the track (AAFit) and shower (TANTRA) zenith reconstruction.

A further step is to use the energy estimate of the shower reconstruction to get rid of atmospheric muons (Fig. 11.4). In fact, when looking at the distribution of the reconstructed energy for muons, we see that there are many events which have no energy estimate and are given a default value of 0.1. The effect is observed both in data and the MC. Also, typical ANTARES analysis are not sensitive to energies below 100 GeV. Indeed, Fig. 11.4 shows that the signal expectation below 100 GeV is negligible, while a fraction (10-20%) of atmospheric background is discarded. Therefore, a cut is set, selecting the events with  $E_{sh} > 100$  GeV. In the same fashion, a cut on  $N_{\text{hits,sh}}$  is applied in order to further discard atmospheric muons, chosen in the same way as for downgoing tracks (see Fig. 11.5).

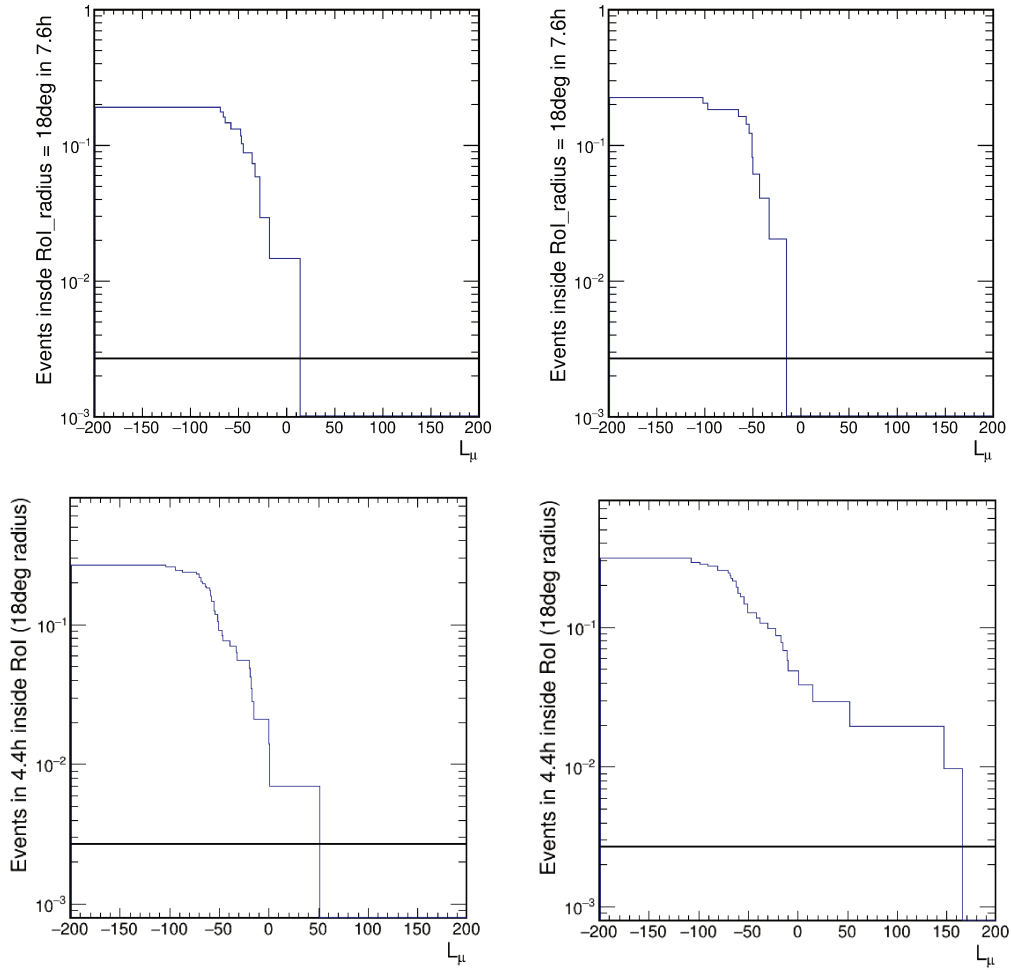


Figure 11.3: Anticumulative distribution of  $L_\mu$  with a cut in  $L_{\text{dusj}} > 0.3$ . The y axis gives the number of events inside a certain RoI and the corresponding time window search. The upgoing events are presented on the top and the downgoing events on the bottom. Both the GRB run (left) and the previous data run (right) are considered. The black line corresponds to  $p_{3\sigma}$ .

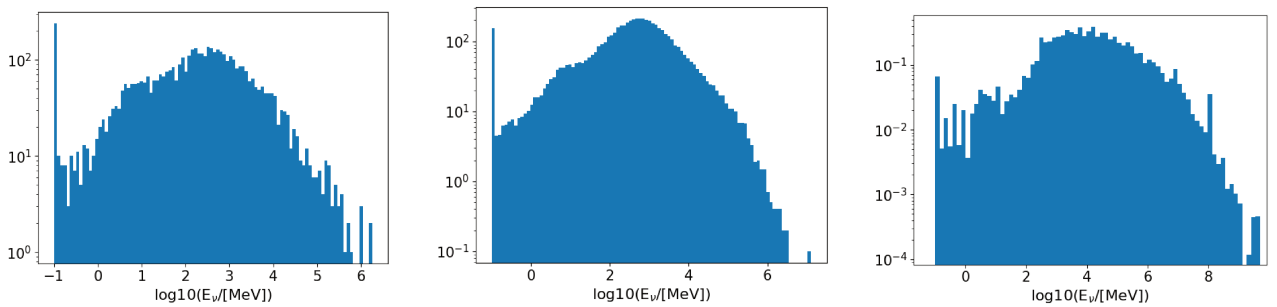


Figure 11.4: Distribution of the reconstructed energy by TANTRA, for data (left) atmospheric muons (middle) and cosmic neutrinos (right).

The shower angular error estimate,  $\beta_{sh}$ , is another parameter of interest. The corresponding distributions are shown in Fig. 11.6 for atmospheric muons (left) and signal (right). One can see a peak at  $\beta_{sh} = 99$ , which is the value assigned for the events where the reconstruction fails, for signal and background. Additionally, there is an excess of mis-reconstructed muons with  $\beta_{sh} > 70$ . Therefore, these events are removed with a pre-cut.

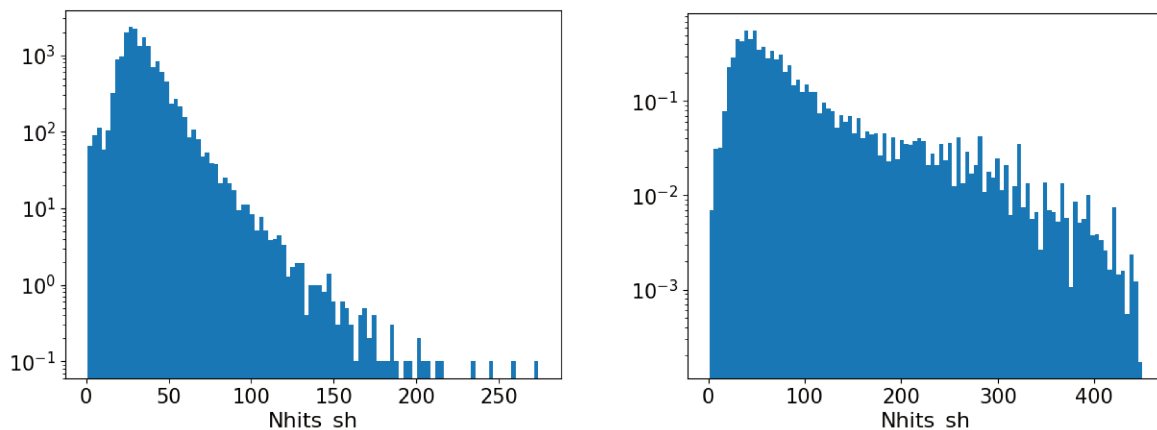


Figure 11.5: Distribution of the number of hits used by TANTRA for the event reconstruction ( $N_{hits\_sh}$ ), for atmospheric muons (left) and cosmic neutrinos (right).

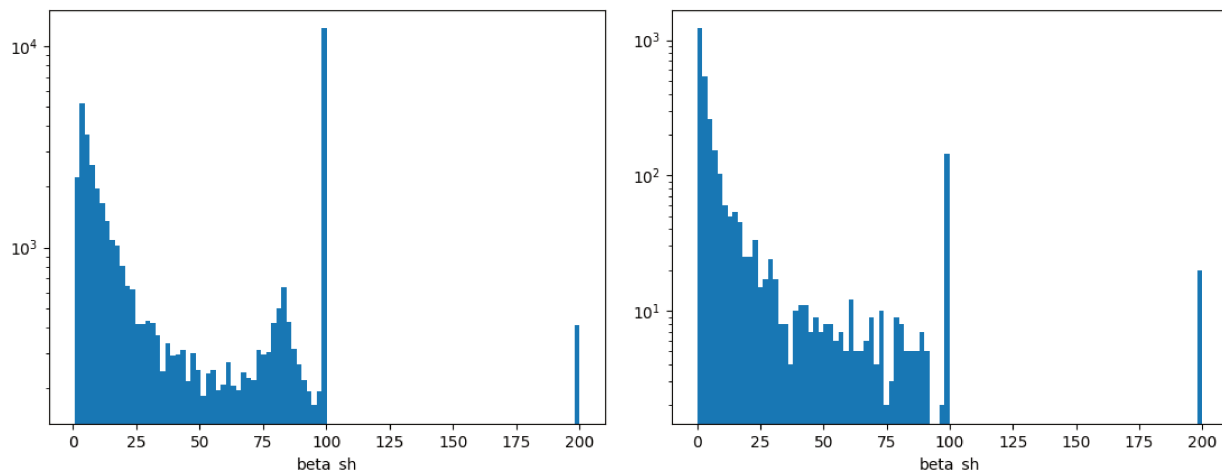


Figure 11.6: Distribution of the reconstructed angular error by TANTRA, for data atmospheric muons (left) and cosmic neutrinos (right).

These new pre-cuts that are applied in the shower sample are summarised in Table 11.1.

Table 11.1: Selection pre-cuts for downgoing shower events.

Criterion	Condition
Trigger	T3 or N3
Track veto	Not selected as a track
Containment	$\rho_{sh} < 300m$ && $ z  < 250m$
M-estimator	Mest < 1000
Down(Up)going	$\cos(\theta_{TANTRA}) < (>) 0$ && $\cos(\theta_{AAFIT}) < (>) 0$
$E_{sh}$ reco	>100 GeV
$\beta_{sh}$	< 70

After the pre-selection, two additional parameters are used to scrutinize the shower sample. One is an extended likelihood ratio,  $L_\mu$ , which is used to distinguish atmospheric muons from cosmic showers using the PMT hit information. The other is different for upgoing and downgoing events. For upgoing events, the output of the Dusj reconstruction Random Decision Forest (RDF) classifier, noted  $L_{\text{dusj}}$ , trained to distinguish between an atmospheric muon (track-like) event and a shower-like event is used. Instead, for downgoing events, the shower energy estimate ( $N_{\text{hits,sh}}$ ) is used, in a similar fashion as for downgoing tracks. In fact, the RDF was trained with upgoing events.

In summary, with these considerations and the new pre-selection, the final shower optimisation is performed on the combination of cuts:

- $L_\mu$  and  $L_{\text{dusj}}$  for upgoing events, optimised together with RoI.
- $L_\mu$  and  $N_{\text{hits,sh}}$  for downgoing events, optimised together with the RoI.

### 11.3 Data and Monte Carlo samples

The analysis makes use of the data and dedicated Monte Carlo simulations for the runs where each GRB were detected. They both incorporate dedicated calibrations and reconstruction, as well as a run-by-run reproduction of the data taking conditions. Table 11.2 provides the information about each source and data runs of the analysis.

Table 11.2: Information about the GRB event and the corresponding run.

GRB event	Run ID	MJD Time	Run duration [s]	(RA,dec) <sub>source</sub> [deg]
180720B	86371	58319.59837558	43237	(0.53, -2.9)
190114C	86915	58497.87295139	43252	(54.5, -26.9)
190829A	87564	58724.83047454	43237	(45.6, -7.1)

### 11.4 Neutrino follow-up and event selection

#### 11.4.1 GRB 180720B

For this event, the search is done over 12 h: from the trigger time until the end of the observation by H.E.S.S. Taking into account the ANTARES visibility, this corresponds to a search of 7.6 h for upgoing events covering the prompt phase, and a downgoing search of 4.4 h duration which covers the high energy observations. In fact, this event was not triggered by H.E.S.S. in the online search and the VHE emission was only identified in an offline analysis. For this reason, there was no real-time follow-up by ANTARES of this GRB.

Since the source is moving with respect to the local detector frame during the 12 h search, a full-sky MC is used to estimate the signal expectation. The angular resolution of track and shower candidate events, estimated from the MC simulation, is used to optimise the size of the RoI.

The background estimate is done using the atmospheric muon MC and thus, data-MC comparisons are done before starting the optimisation in order to check that the simulation is in good agreement with the data. Figures 11.7 and 11.8 show the data-MC comparison of the  $\Lambda$  and  $L_{\text{dusj}}$  ( $N_{\text{hits,sh}}$ ) distributions, for upgoing and downgoing events, respectively.

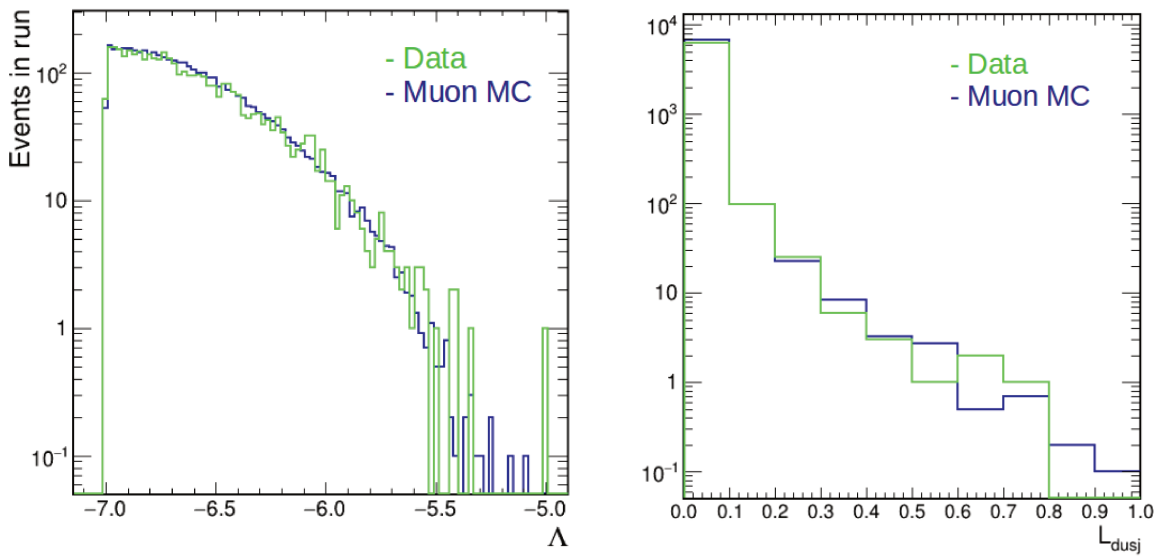


Figure 11.7: Data and MC distributions for upgoing events in the run. Left: event distribution of the  $\Lambda$  parameter, for data (green) and the boosted run-by-run muon MC (blue). Right: event distribution of the  $L_{\text{dusj}}$  parameter, for data (green) and the run-by-run muon MC (blue).

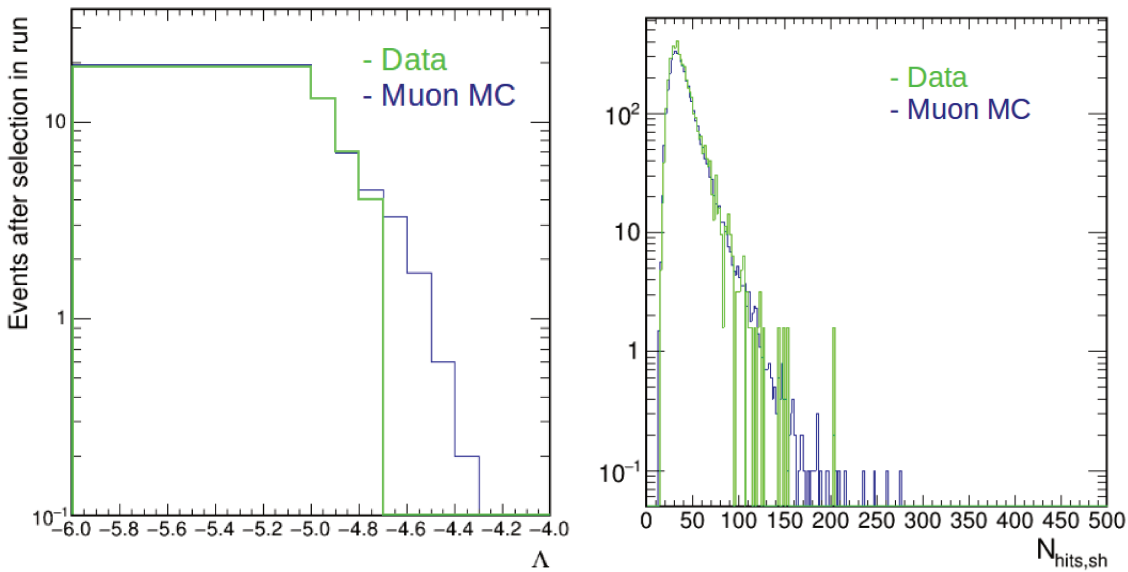


Figure 11.8: Data and MC distributions for downgoing events in the run. Left: event distribution of the  $\Lambda$  parameter from the track reconstruction, for data (green) and the boosted run-by-run muon MC (blue). Right: event distribution of the shower energy estimate ( $N_{\text{hits,sh}}$ ) for data (green) and muon MC events (blue).

### Track selection

The first step is the selection of track-like events using the  $p_{3\sigma}$  criterion to find the cuts that will be applied to the data. In Fig 11.9, the number of survival signal events assuming an  $E^{-2}$  neutrino spectrum is shown for each  $R_{\text{RoI}}$ , and for the corresponding optimal  $\Lambda$  cut. The optimal RoI radius is 2 deg for both sky region searches. The final optimised quality cuts applied are:  $\Lambda > -5.6$  for upgoing events and ( $N_{\text{hits}} > 80$ ,  $\Lambda > -5.1$ ) for downgoing events.

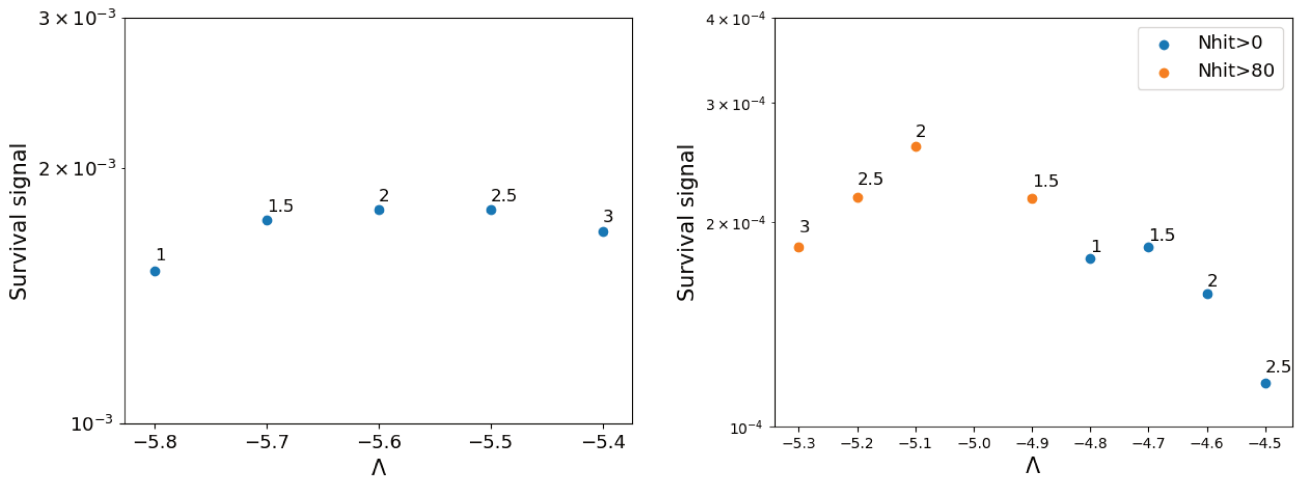


Figure 11.9: Number of survival signal events inside each RoI for an  $E^{-2}$  spectrum and the corresponding  $\Lambda$  cut for each RoI radius: on the left, for the upgoing search over 7.6 h; on the right for the downgoing search over 4.4 h, where the survival signal with or without the cut on the energy proxy ( $N_{\text{hits}}$ ), is compared (orange vs blue points).

### Shower optimisation

For upgoing showers, the event selection is the same as for GW events: we search for the optimal set of cuts in  $(L_\mu, L_{\text{dusj}})$  that maximizes the signal expectation while keeping the background below  $p_{3\sigma}$ . The only change is that in the previous analysis the optimization was done on data (since the shorter time window made it possible) and the upgoing pre-selection in Table 10.7 was applied. Here, the background needs to be reduced more severely to achieve the level of  $2.7 \times 10^{-3}$  events in 7.6 h. This is done with the new pre-selection in Table 11.1.

We find that the RoI radius that maximizes the signal expectation is  $R_{\text{RoI}}=24$  deg, and the final optimization cuts are  $(L_{\text{dusj}} > 0.2, L_\mu > 10)$ . In Fig 11.14 (left), we show the number of surviving signal events for each  $R_{\text{RoI}}$  and corresponding  $L_\mu$  cut, for  $L_{\text{dusj}} > 0.1$  (blue),  $L_{\text{dusj}} > 0.2$  (orange) and  $L_{\text{dusj}} > 0.3$  (green). In Fig 11.10 (right), we show the distribution of shower-like background events estimated from data (green) and MC (blue) as a function of  $L_\mu$ , with the optimal RDF cut  $L_{\text{dusj}} > 0.2$  applied.

For downgoing events, the shower selection strategy is somewhat different. Looking at the  $L_\mu$  anticumulative distributions after the pre-cuts (Table 11.1, Fig. 11.11), the total background needs to be reduced by almost two orders of magnitude to get to the  $p_{3\sigma}$  rate. Additionally, many atmospheric muon events remain in the tail of the  $L_\mu$  distribution, reconstructed as "good shower candidates". This makes it difficult to set a reliable cut on  $L_\mu$  and it was preferred to search for additional cuts. In fact, the strategy followed is to reduce the background by reducing the size of the RoI, and keep a simple selection, with only two parameters used (as for downgoing tracks): using the  $L_\mu$  parameter and the shower energy estimate  $N_{\text{hits,sh}}$ . The number of survival signal events assuming an  $E^{-2}$  neutrino spectrum is shown in Fig. 11.12.

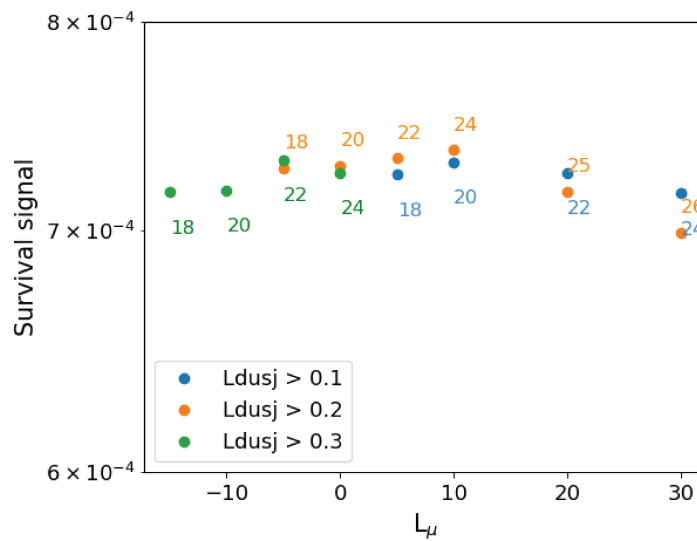


Figure 11.10: Number of survival signal events inside each RoI radius, assuming an  $E^{-2}$  spectrum. For each  $R_{RoI}$ , the corresponding optimal  $L_\mu$  cut is represented with a circle, and the  $L_{dusj}$  cut with the color as indicated in the legend.

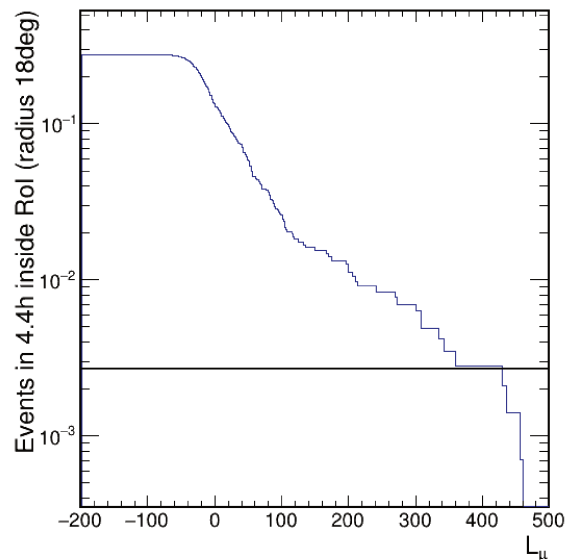


Figure 11.11: Anticumulative distribution of  $L_\mu$  for atmospheric muon events after the pre-cuts discussed above. The y-axis corresponds to the number of events expected within 4.4 h inside an RoI of 18 deg radius. The black line corresponds to  $p_{3\sigma}$ .

#### 11.4.2 GRB 190114C

The optimization approach followed for this event is based on the one used for GW170817 [54], and it is described in sections 10.4 and 11.2. The background estimate is based directly on data. As for GRB170817, the window is extended to cover potential precursors, starting 350 s before the trigger time. Thus, the time window of the search is  $[-350+T_0, T_0+1250]$  s. During this time, the source was above the ANTARES horizon (seen as downgoing). Because the event was above the ANTARES horizon at the time of the alert, an online follow-up was not possible. The results of the event selection for GRB 190114C are shown in this subsection.

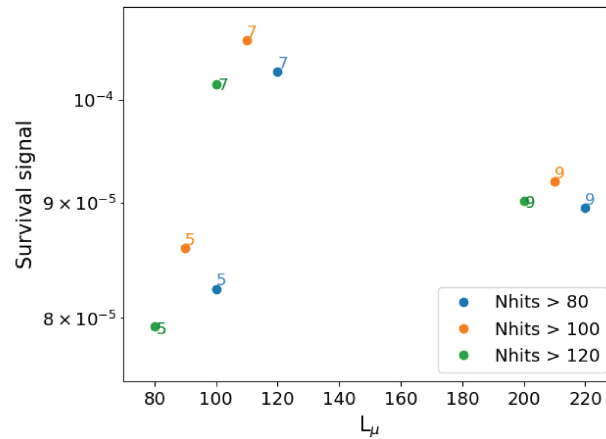


Figure 11.12: Number of survival signal events as a function of the  $L_\mu$  optimal cut, for different  $N_{\text{hits,sh}}$  cuts, and for different RoI sizes, whose radius is indicated with the numbers.

### Track optimization

For the track sample, the quality parameter of interest in the optimization is the  $\Lambda$  parameter, which provides an estimate of the goodness of the reconstruction. The low background in the small RoI and time window for the search of track-like neutrino candidates in coincidence with this GRB, does not require of an additional cut in the energy estimate to achieve the  $p_{3\sigma}$  criterion. This analysis is performed in the same way as for GW170817 [54].

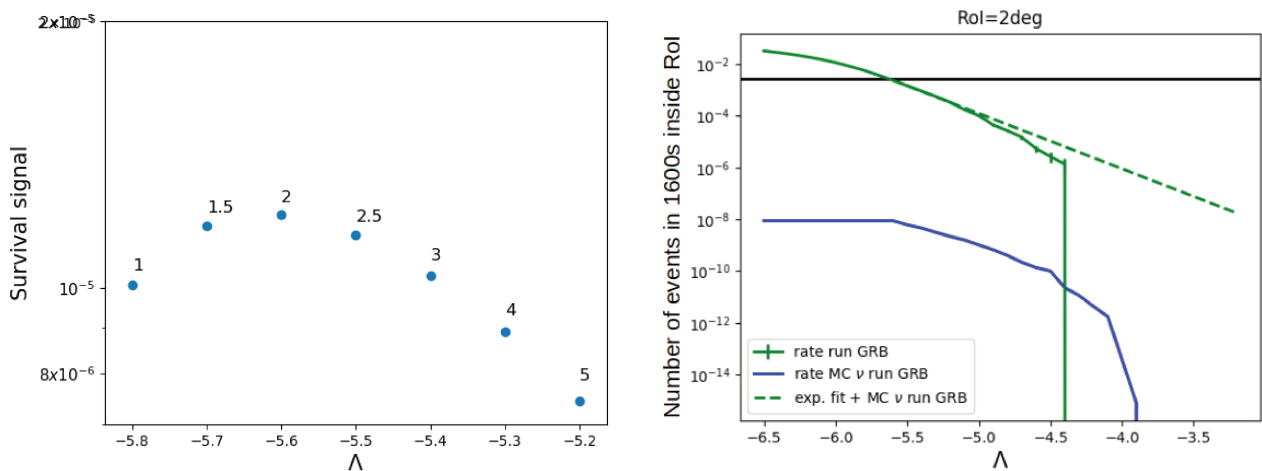


Figure 11.13: On the left, the number of survival signal events inside each RoI for an  $E^{-2}$  spectrum and the corresponding  $\Lambda$  cut for each RoI. On the right, the number of background events inside an RoI of 2 deg radius within 1600 s as a function of  $\Lambda$ . Solid green is data (atm muons), blue is atm neutrino MC. The fit accounts for the sum of the two backgrounds.

In Fig 11.13 (left), we show the number of surviving signal events for each  $R_{RoI}$  and corresponding optimal  $\Lambda$  cut. In Fig 11.13 (right), we show the distribution of background events as a function of  $\Lambda$  for the optimised  $R_{RoI}$ , allowing to maximize the signal expectation. The black line corresponds to  $p_{3\sigma}$ . A  $R_{RoI}$  of 2 deg and a quality cut of  $\Lambda > -5.6$  is the final optimised selection obtained.

### Shower optimization

For the shower sample, we start with a pre-selection of shower-like events. The different criteria used for the pre-selection are shown in Table 10.7. After the pre-selection, the optimization procedure for this event, seen as downgoing in ANTARES at the time of the alert, is done according to the reasoning in section 10.4: finding the set of cuts ( $L_{\text{dusj}}, L_{\mu}$ ) that maximises the signal inside the RoI with  $R_{\text{RoI}}$ .

We find that the best cut in the random forest score is  $L_{\text{dusj}} > 0.1$ , which appears to give the highest shower event statistics in the sample and the maximum survival signal. With this  $L_{\text{dusj}}$  cut, the RoI size that maximizes signal appears to be  $R_{\text{RoI}} = 22$  deg. The optimised cut in  $L_{\mu}$  is found to be  $L_{\mu} > -18$ .

In Fig 11.14 (left), we show the number of surviving signal events for each  $R_{\text{RoI}}$  and corresponding  $L_{\mu}$  cut, with  $L_{\text{dusj}} > 0.1$ . In Fig 11.14 (right), we show the distribution of shower-like background events as a function of  $L_{\mu}$  for the optimised  $R_{\text{RoI}}$ , allowing to maximize the signal expectation, with  $L_{\text{dusj}} > 0.1$ . The black line corresponds to  $p_{3\sigma}$ .

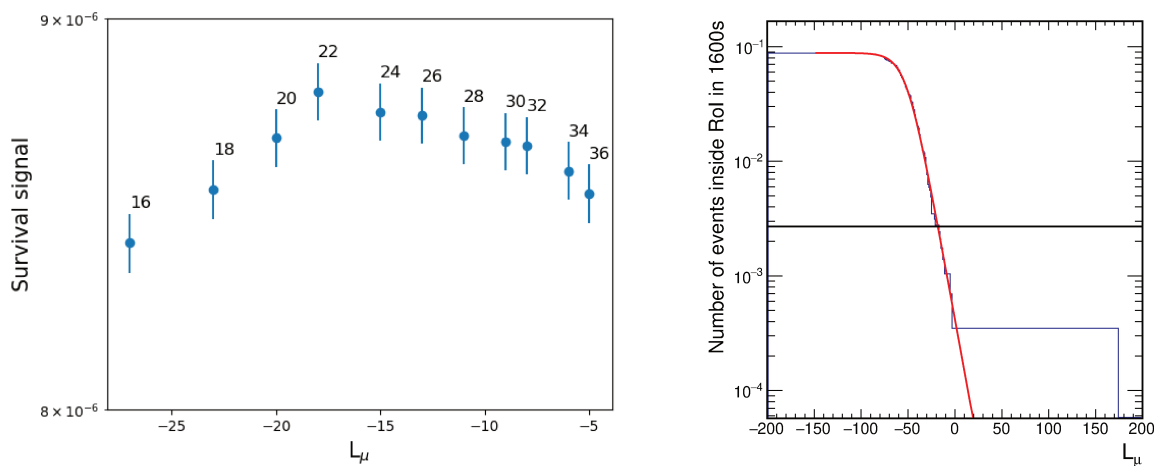


Figure 11.14: On the left, the number of survival signal events inside each RoI for an  $E^{-2}$  spectrum and the corresponding  $L_{\mu}$  cut for each RoI, with  $L_{\text{dusj}} > 0.1$ . On the right, the number of background events inside an RoI of 2 deg radius within 1600 s as a function of  $L_{\mu}$ , with  $L_{\text{dusj}} > 0.1$ . The black line corresponds to the  $p_{3\sigma}$  value.

#### 11.4.3 GRB 190829A

For this second long GRB detected by H.E.S.S, the same selection criteria as for GRB 170820B are used, previously described in section 11.2. In this case, the search window is of 8 h, covering the ensemble of the EM observations. The ANTARES visibility is used to evaluate the amount of time that the source was above and below the ANTARES horizon. This defines a search of 2.75 h for upgoing events covering the prompt phase, and a downgoing search of 5.25 h duration which covers the high energy observations. This event was detected by H.E.S.S. at  $O(\text{TeV})$  energies in real-time, which triggered an online follow-up search by ANTARES (GCN #25582).

#### Track selection

First, the track sample is determined by obtaining the  $p_{3\sigma}$  cuts and optimal  $R_{\text{RoI}}$  for the search by looking at the anticumulative data distribution of the quality parameter,  $\Lambda$  (Fig. 11.15). Once the cuts are defined for different  $R_{\text{RoI}}$ , the set of cuts leading to the maximum number of survival signal events is chosen. Fig. 11.16 shows the expected number of signal events passing the selection as a function of

the  $p_{3\sigma}$  cut, for different  $R_{RoI}$ . The optimisation defines the search region as of one and two degrees for upgoing and downgoing events, respectively. The optimal cuts to be applied are  $\Lambda > -6$  for upgoing events and ( $\Lambda > -5.4$ ,  $N_{\text{hits}} > 70$ ) for downgoing events.

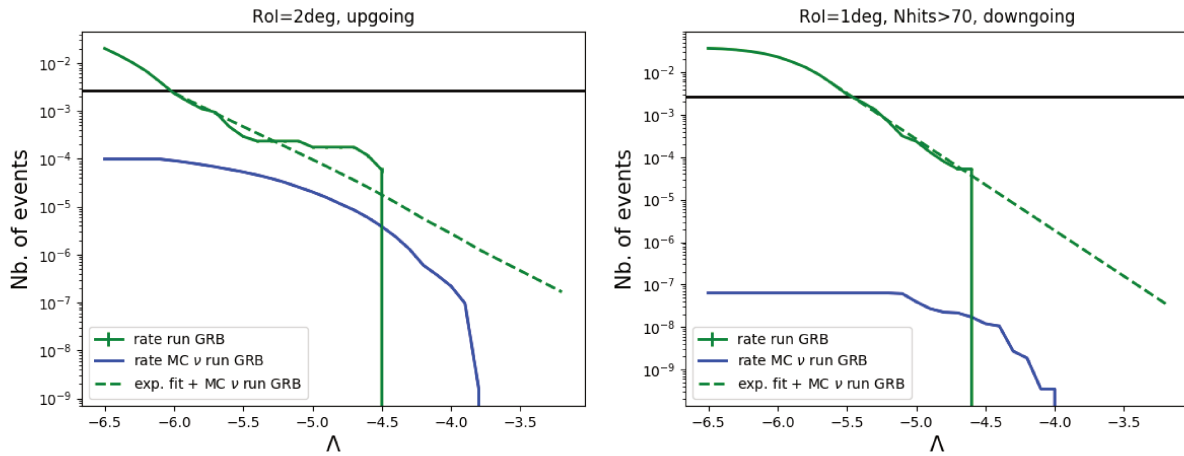


Figure 11.15: Number of background events inside the optimal RoI and within the time window as a function of  $\Lambda$ . Solid green is data (atm. muons), blue is atm. neutrino MC. The fit accounts for the addition of the two backgrounds. On the left, for upgoing events and an  $R_{RoI}$  of 2 degrees. On the right, for downgoing events inside an RoI of 1 deg radius.

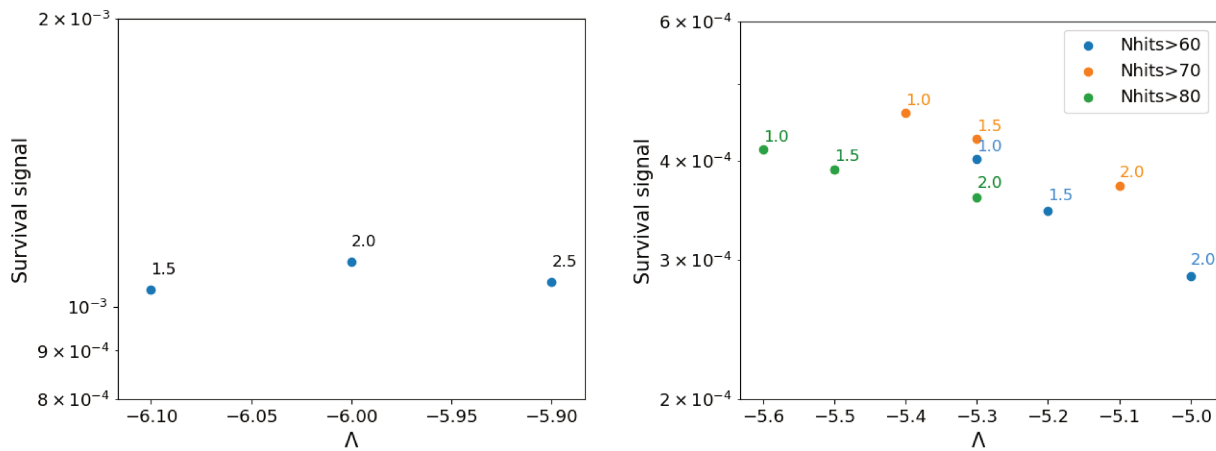


Figure 11.16: Number of survival signal events inside different RoI radius, considering an  $E^{-2}$  cosmic neutrino spectrum, as function of the  $\Lambda$  cut. Left: upgoing events selected as tracks. Right: Downgoing events selected as tracks.

### Shower selection

First, a set of pre-selection cuts is applied to the events that are not selected as tracks to define the shower sample (Table 11.1). After that, the cuts are optimised as described in section 11.2. The main parameter for the shower optimisation is the likelihood ratio  $L_\mu$ , whose anticumulative distribution is shown in Fig. 11.17 for the optimal search region, for upgoing and downgoing events. Fig. 11.18 shows the number of signal events passing the shower selection assuming an  $E^{-2}$  spectrum, as a function of the  $L_\mu$  cut and the  $R_{RoI}$ , for different and  $N_{\text{hits,sh}}$  and  $L_{\text{dusj}}$  cuts applied respectively to downgoing and upgoing events. The optimisation gives an optimal search region of 20 and 9 degrees for upgoing and

downgoing events, respectively. The optimal cuts to be applied are ( $L_\mu > -8$ ,  $L_{\text{dusj}} > 0.1$ ) for upgoing events and ( $L_\mu > 92$ ,  $N_{\text{hits,sh}} > 100$ ) for downgoing events.

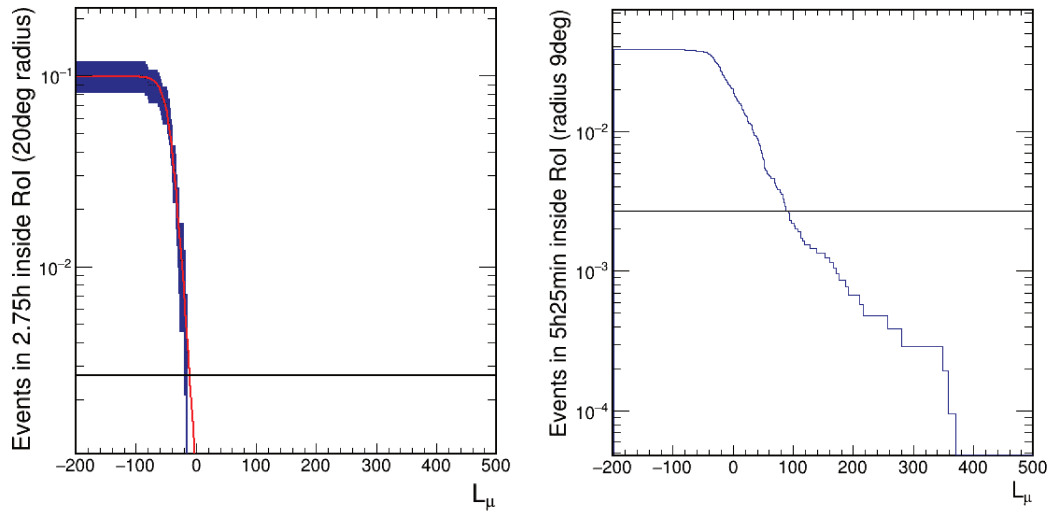


Figure 11.17: Number of background events inside the optimal RoI and within the search time window as a function of  $L_\mu$ . Left: upgoing events selected as showers, with a cut in  $L_{\text{dusj}} > 0.1$ . Right: Downgoing events selected as showers, with a cut in  $N_{\text{hits,sh}} > 100$ .

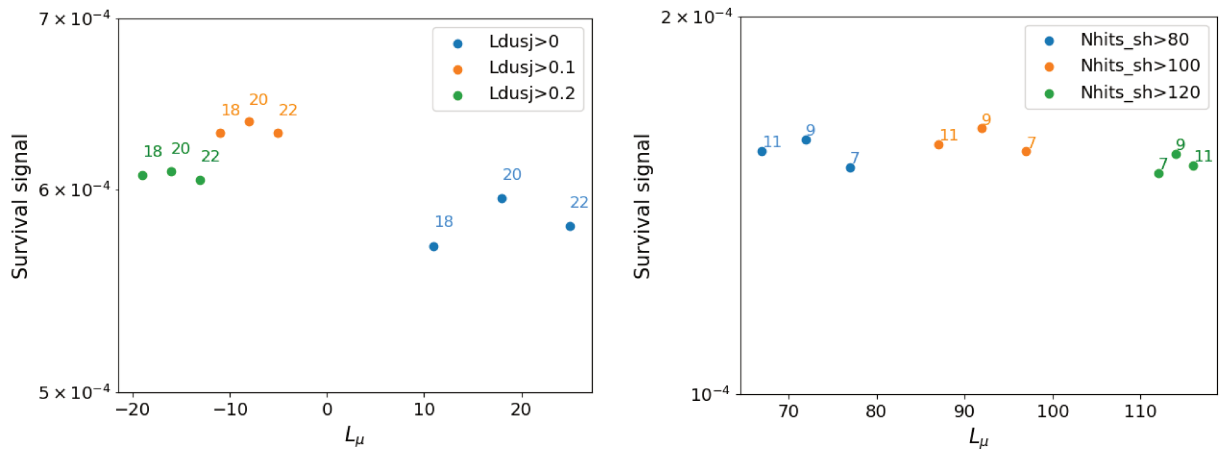


Figure 11.18: Number of survival signal events inside different RoI radius, considering an  $E^{-2}$  cosmic neutrino spectrum, as function of the  $L_\mu$  cut. Left: upgoing events selected as showers. Right: Downgoing events selected as showers.

## 11.5 Results of the ANTARES search

After unblinding the data set, the search yields no neutrino in time and space coincidence with any of the three GRBs analysed. From this non-observation, constraints are set on the potential neutrino emission.

The time-integrated neutrino flux from a given astrophysical source ( $\frac{dN}{dE_\nu}$ , in  $\text{GeV}^{-1} \text{cm}^{-2}$ ) is used to compute the expected number of neutrinos that would be observed from a source at declination  $\delta$  in a detector with effective area  $A_{\text{eff}}(E_\nu, \delta)$ , over a time window  $\Delta t$ :

$$N_\nu = \int \frac{dN}{dE_\nu}(E_\nu) A_{\text{eff}}(E_\nu, \delta) dE_\nu \quad (11.1)$$

Table 11.3: Neutrino spectral fluence upper limits ( $\phi_0^{90\%}$ ) obtained for the three VHE GRB searches, separately for upgoing and downgoing events. The search window  $\delta t$  is also given. The hyphen indicates that the corresponding GRB was not seen as upgoing during the gamma-ray emission.

Event	$\delta t$ upgoing	$\phi_0^{90\%}$ upgoing	$\delta t$ downgoing	$\phi_0^{90\%}$ downgoing
GRB180720A	7.6 h	$1.5 \pm 0.5 \text{ GeV cm}^{-2}$	4.4 h	$11 \pm 4 \text{ GeV cm}^{-2}$
GRB190114C	-	-	0.44 h	$1.6 \pm 0.7 \text{ GeV cm}^{-2}$
GRB190829B	2.75 h	$1.4 \pm 0.5 \text{ GeV cm}^{-2}$	5.25 h	$4 \pm 2 \text{ GeV cm}^{-2}$

Table 11.4: Upper limits in the total energy emitted in neutrinos ( $E_{\nu, \text{iso}}^{90\%}$ ) for the three VHE GRB searches, separately for upgoing and downgoing events. The 5-95% energy range of the analysis ( $E_{5-95\%}^{\text{up}}$  and  $E_{5-95\%}^{\text{down}}$ ) is also given. The hyphen indicates that the corresponding GRB was not seen as upgoing during the gamma-ray emission. Last column shows the isotropic photon energy measured,  $E_{\gamma, \text{iso}}$ .

Event	redshift	$E_{5-95\%}^{\text{up}}$	$E_{\nu, \text{iso}}^{90\%}$ upgoing	$E_{5-95\%}^{\text{down}}$	$E_{\nu, \text{iso}}^{90\%}$ downgoing	$E_{\gamma, \text{iso}}$
GRB180720A	0.653	2.5 TeV - 4.0 PeV	$1.8 \times 10^{55} \text{ erg}$	20 TeV - 30 PeV	$1.4 \times 10^{56} \text{ erg}$	$6 \times 10^{53} \text{ erg}$
GRB190114C	0.42	-	-	10 TeV - 20 PeV	$8.3 \times 10^{54} \text{ erg}$	$3 \times 10^{53} \text{ erg}$
GRB190829B	0.0785	2.5 TeV - 4.0 PeV	$2.3 \times 10^{53} \text{ erg}$	15 TeV - 25 PeV	$6.6 \times 10^{53} \text{ erg}$	$2.967 \times 10^{50} \text{ erg}$

Assuming that the neutrino spectrum is a power law with spectral index  $\gamma = 2$ , then the spectral fluence at the detector can be expressed as follows:

$$\phi_0 = E_\nu^2 \frac{dN}{dE_\nu} \quad [\text{GeV} \cdot \text{cm}^{-2}]. \quad (11.2)$$

Time integrated fluence upper limits can be easily be derived from Eq. 11.2, considering the Poisson 90% confidence level upper limit,  $N_\nu^{90} = 2.3$ , leading to the results shown in Table 11.3 for the three GRBs analysed. Since the redshift of the source is known, these fluence upper limits can be converted into upper limits on the total isotropic neutrino emission following:

$$E_{\nu, \text{iso}} = \frac{4\pi D_L(z)^2}{1+z} \int_{E^{5\%}}^{E^{95\%}} E_\nu^{-2} \phi_0^{90\%} E_\nu dE_\nu. \quad (11.3)$$

The results obtained are presented in Table 11.4. These neutrino limits are 2-3 orders of magnitude above to the isotropic energy inferred from electromagnetic observations:  $E_{\text{iso}, \gamma} = 6 \times 10^{53} \text{ erg}$  for GRB 180720B,  $E_{\text{iso}, \gamma} = 2-3 \times 10^{53} \text{ erg}$  for GRB 190114C according to Fermi-GVM, and  $E_{\text{iso}, \gamma} \sim 2 \times 10^{52} \text{ erg}$  as measured by MAGIC; and  $E_{\text{iso}, \gamma} = 2.967 \times 10^{50} \text{ erg}$ . Therefore, the ANTARES limits do not allow to constrain the potential hadronic component present in the EM signal. However, the next generation detectors will gain almost 2 orders of magnitude in sensitivity. Moreover, combined studies with several detectors might lead to more encouraging results. Additionally, due to the small neutrino flux expected from these sources, a stacking is appropriate in this case. However, this particular study has been done because these were the three GRBs ever detected at O(TeV) energies, after several decades of search by IACTs. For this reason, special attention was put to these sources with a dedicated search.

The results for GRB 190114C are shown in Fig. 11.19 in the form of a differential upper limit as a function of the neutrino energy. MAGIC data in [229] (Extended Data Table 1) is used to infer the differential gamma-ray fluence corresponding to the MAGIC flux over the time window  $\Delta t$  as follows:

$$E_\gamma^2 \frac{dN}{dE_\gamma} (\text{MAGIC}) = \phi_0^\gamma \times \left( \frac{E_\gamma}{E_{\text{pivot}}} \right)^{-\alpha} \times \Delta t \times E_\gamma^2, \quad (11.4)$$

where  $E_{\text{pivot}}$ ,  $\alpha$  and  $\phi_0^\gamma$  are the pivot energy, the photon index and the flux normalisation describing the spectrum from a fit to MAGIC data.  $E_\gamma$  is the photon energy, covering the range of the MAGIC observation (300 GeV-1 TeV) [228, 229].

This is done for two time windows of the MAGIC data: the first time interval of the MAGIC analysis (68-110 s from the Swift trigger), blue band in Fig. 11.19, and over the full observation window (62-2400 s), orange band in Fig. 11.19. Both are compared, including the corresponding systematical uncertainties in the spectral fit, to the ANTARES neutrino upper limit. The obtained neutrino limit is about four orders of magnitude above the MAGIC flux. Therefore, the hadronic content of the source cannot be constrained.

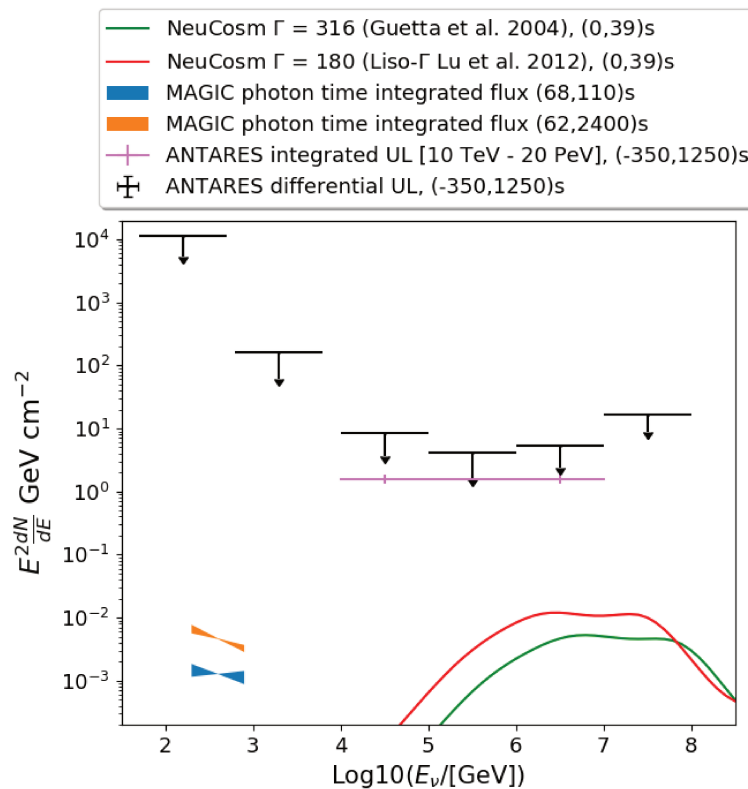


Figure 11.19: ANTARES 90% differential (black arrows) and integrated (violet line) spectral fluence upper limit as a function of the neutrino energy, considering an extended emission over 1600 s, and assuming an  $E^{-2}$  neutrino spectrum. The predicted time integrated neutrino flux for this GRB over 39 s (prompt emission) by the NeuCosm model. The parameters as measured by Fermi-GBM are used, and two different Lorentz factors considered (green and red lines), from [222, 260]. MAGIC gamma-ray spectral fluence for the first time bin of the analysis (62-110s, blue band), and for the overall time window (62-2400s, orange band).

The ANTARES 90% UL is computed assuming an  $E^{-2}$  neutrino spectrum over an extended window of 1600 s (Fig. 11.19). In order to compare this limit with theoretical predictions, the NeuCosm model [222] is used to compute the expected neutrino fluence for this specific GRB. To this aim, the GRB parameters observed by Fermi-GBM are considered, and the time variability for the model is taken to be of 0.01 s, typically assumed for long GRBs as in [222]. Predictions are provided for the time integrated flux over 39 s, that is the time window in which the Fermi-GBM instrumented measured the photon flux. Two different Lorentz factors are considered for comparison, the one predicted by the standard scenario [222] ( $\Gamma = 316$ ), and a more realistic one as presented in [260] ( $\Gamma = 180$ ). This

---

comparison is not fully accurate since this model provides the expected flux for the prompt emission, and the extended emission observed for this GRB may not be modelled in the same way. Moreover, the time variability of the GRB emission should be taken into account for a more precise calculation. However, the prompt time integrated emission already provides an estimate of the total amount of energy emitted during the GRB, and so it gives an order of magnitude for the strength of the expected flux compared to the experimental limit.



# Chapter 12

## Summary, conclusions and outlook

Neutrino astronomy is a relatively young field which was born with the observations of solar neutrinos and neutrinos from a core-collapse supernova explosion. Recently, the first detections of high-energy cosmic neutrinos and the first sources observed simultaneously through different messengers have marked a new way of conceiving astronomy which goes beyond the classical observation of electromagnetic emission from the cosmos: the era of the multi-messenger astrophysics.

Neutrinos, cosmic rays and gamma-rays can be produced in the surroundings of the same astrophysical source, where particle acceleration up to high energies is possible. However, gamma-rays can also be produced in leptonic processes, in which no neutrino or cosmic rays are produced. Therefore, detecting neutrinos from an identified source would be the proof for a site of hadron acceleration.

The fact that neutrinos interact only through the weak force makes of their detection a challenge. This same fact makes them invaluable cosmic messengers, since they are going to bring unique information and probe the astrophysical mechanisms riding the most energetic phenomena in the Universe. As of today, the blazar TXS 0506+056 is the only evidence for an astrophysical source of high-energy neutrinos. Some other sources also present an indication in the same sense. In addition, a diffuse flux of cosmic neutrinos with TeV-PeV energies has been detected, whose origin is still unknown. The search for the sources producing it should therefore continue.

Neutrinos are neutral particles that can only be detected indirectly, i.e. via the observation of their interaction products. The detection principle of neutrino telescopes is based on the detection of the charged particles produced in neutrino interactions in the detector material. In particular, in the KM3NeT and ANTARES experiments these particles are observed through the detection of the Cherenkov light induced by charged particles crossing the detector at a relativistic speed. The light is detected in the arrays of photomultipliers (PMTs) which constitute the elementary bricks of the detector. Following the amount of photons deposited and the time when they are detected in each PMT along the instrumented lines, one can reconstruct the position and direction of the particles.

In underwater Cherenkov detectors, three types of background are dominant: charged leptons produced in the interactions of cosmic-rays in the atmosphere that produce detectable light (this includes atmospheric muons and atmospheric neutrinos), bioluminescence and radioactive decays.

KM3NeT detectors ARCA and ORCA are under construction in the Mediterranean Sea, respectively offshore Sicily (Italy) and Toulon (France). The first will be dedicated to high-energy (TeV-PeV) neutrino astronomy, as ANTARES. The second has as main scientific goal the determination of the neutrino oscillation parameters and the neutrino mass ordering (GeV energies). The key component

of the KM3NeT detectors are the digital optical modules (DOMs), composed of 31 PMTs. In contrast, ANTARES has a single large photocathode PMT per optical module. Three PMTs form an ANTARES storey.

In the following, the main results and conclusions obtained during this thesis and some future prospects are presented.

## 12.1 Detection of CCSN neutrinos with KM3NeT

CCSN was the second astrophysical neutrino source identified after the Sun. In fact, the only detection of neutrinos from a CCSN event allowed to consolidate the basis of the astrophysical mechanism, showing the relevance of the role of neutrinos in such explosions. However, a single detection is not enough to constrain all the unknown parameters that allow to explain in details what happens in the different phases of the explosions, and their impact. For this reason, it is of interest to study the perspectives for a future explosion occurring in our Galaxy.

Ideally, sensitive neutrino detectors will be ready for the next Galactic explosion. In fact, current and near-future detectors will only be sensitive to CCSN events up to the Magallanic Clouds. Only one to three events are expected per century in the Galaxy, so we do not want to miss the next one.

We have seen that KM3NeT detectors are not initially designed to detect MeV neutrinos. Even though in these low energy interactions it is not possible to do an event-by-event reconstruction, a CCSN explosion may be identified as an overall increase of the detected rate over background. In fact, the large amount of neutrinos produced in these astrophysical phenomena will produce an increase not only in the total amount of detected photons (hits), but also in the amount of hits seen in coincidence between the different PMTs in a DOM. This is why both ORCA and ARCA detectors can be used for this kind of searches.

KM3NeT detectors will mainly be sensitive to the  $\bar{\nu}_e$  flux, that will interact with protons in water. Using the number of coincidences in the same DOM (called multiplicity), one can drastically reduce the background from radioactive decays and bioluminescence. Moreover, looking for spatially and temporally correlated photons through different DOMs, it is possible to filter the events produced by atmospheric muons, which show characteristic correlations. These techniques allow to optimise the KM3NeT potential to MeV neutrinos.

A detailed simulation of the KM3NeT detector response to MeV neutrinos has been developed in the framework of this thesis. From the simulation, it has been estimated that 115 KM3NeT detection lines provide an equivalent effective detector mass for MeV neutrino searches of  $\sim 50$  kton. With the multiplicity selection optimised for this kind of analysis, this effective mass is reduced to  $\sim 1$  kton. This simulation has allowed for a characterisation of the detector response at low energies, which has been implemented in the form of a parametrisation with the efficiency as a function of the neutrino energy. In this way, it allows to evaluate the KM3NeT signal expectation for any astrophysical neutrino flux with energies between 1 and 100 MeV, including all the experimental effects.

The coincidence method mentioned above has been put in place and optimised during the thesis, and it has been applied to the first KM3NeT data for the background measurement, as well as to the signal simulation. Finally, it has been used to evaluate the KM3NeT capabilities to detect CCSN neutrinos, including a detailed study of the systematic uncertainties. The results of the study are promising and show that KM3NeT will be able to detect more than 95% of the Galactic CCSN progenitors, contributing to the observation of the next Galactic explosion.

### 12.1.1 Real-time monitoring and first results

The CCSN selection has been implemented in the data acquisition system in the form of a trigger for real-time analysis, keeping the information of candidate events in a continuous way. The background stability and control achieved with this trigger have allowed the KM3NeT experiment to be part of the SNEWS network, where all the experiments sensitive to CCSN neutrinos send their alerts with a fake trigger rate which is lower than one in eight days. The interest of this network is that on the one hand it allows to lower the threshold of individual detectors by requiring a coincidence detection, and on the other hand it provides the infrastructure for sharing information between the different experiments, which may be relevant to the physics results that may be obtained from the next observation. Moreover, such network will communicate with other observatories, which might be of help for a successful multi-messenger follow-up.

KM3NeT is able to combine in real time the ORCA and ARCA data into a single trigger, with a latency below 20 s. Currently, six ORCA lines taking data can trigger an alert to SNEWS if a CCSN happens closer than 6-9 kpc, depending on the progenitor mass.

One of the main goals of the real-time searches is to be able to identify the signal through different messengers, and determining where and when the event happens. In particular, in CCSN explosions, neutrinos are expected to be detected up to several hours before photons. Moreover, CCSN are believed to be also a source of gravitational-waves. Therefore, a prompt neutrino detection may help for a multi-messenger follow-up.

During their last data taking run (O3), the gravitational-wave detectors triggered two signals, which were potentially originated from a CCSN explosion. At that moment, four ORCA lines were in operation, and a follow-up of these alerts was performed with available data, applying the CCSN analysis. No significant MeV neutrino excess was observed, which allowed to set limit on a possible CCSN emission. In particular, a CCSN source closer than 6 kpc was ruled out, and the total energy emitted in neutrinos could not be larger than  $3 \times 10^{53}$  erg if the source was at 10 kpc, corresponding to the typical energetic output expected from this kind of events. With these follow-ups, we could test the functioning and performance of the CCSN trigger in a real analysis for the first time, verifying that the analysis could be applied in a real case, and a fast response is achieved.

### 12.1.2 Study of the properties of the CCSN neutrino flux

In this work, the capability of discriminating between the different models, and determining the spectral properties of the flux has been evaluated. For this, it is crucial to estimate which are the angular, energy and time resolution of the experiment when applying the analysis to the searched signal.

In order to carry out time dependent analysis, a good time resolution is needed. In particular, a millisecond time-scale resolution is required to study fast changes in time in the neutrino flux, and to precisely determine the arrival time of the signal. To achieve this goal, the instrument must be able to detect a large number of signal events. In KM3NeT, this is possible only if all coincidences are used. The high multiplicity selection yields a better background rejection and detection sensitivity, but at the expense of losing a large amount of signal events.

The main analysis performed using the time profile (lightcurve) has been to develop a method to combine the neutrino lightcurves as detected by different experiments. The aim of this study is to determine the time delay of the arrival of the signal at the different detectors, and the uncertainty of this measurement. For this, a canonical parametrisation of the neutrino flux, and a simple detector response simulation are used to evaluate the performance and feasibility of the method. These results have been

used to infer the source localisation by triangulation of the signal at the different experiments. The analysis yields a precision of  $\sim 70 \text{ deg}^2$  in the localisation of a CCSN at 10 kpc which explodes in the direction of the Galactic Centre. The proposed approach will allow to determine the time delay between experiments in a model independent way, in contrast to the methods used in previous works. This analysis is meant as a low latency evaluation, allowing to send fast and preliminary information to other observatories. The result can be improved in a later refined analysis combining additional information and methods.

The different hydrodynamical processes and instabilities taking place during the CCSN may also impact the time evolution of the neutrino flux, in particular, by producing oscillations in the neutrino lightcurve. A spectral analysis has been carried out to evaluate the detection capability of such oscillations in KM3NeT. The results obtained conclude that KM3NeT will be able to detect this oscillatory signature (with a significance of  $3\sigma$ ) if the source is near-by (between 3 and 5 kpc distance).

Additionally, the possibility to access the neutrino spectrum information using the correlation between the neutrino energy and the multiplicity rates has been investigated. Even though the three parameters describing the CCSN neutrino spectrum are not independent in our measurement, a statistical analysis based on a  $\chi^2$  minimisation method has been performed, allowing to set confidence level intervals. In case the other two parameters are measured with an uncertainty of about 10%, KM3NeT could reach an  $\sim 0.5 \text{ MeV}$  resolution in the mean neutrino energy.

### 12.1.3 Comparison with other experiments

Table 12.1 shows the number of expected events in each detector for a CCSN explosion at 10 kpc, for three different progenitors and the two NMO hypotheses: NO on the left, IO on the right. All of the detectors in the Table will be part of SNEWS2.0, and are sensitive to a Galactic CCSN. Four of them (IceCube ICSN, Super-Kamiokande [204], Hyper-Kamiokande [206], and JUNO [197]) can reach a  $5\sigma$  detection of sources up to the Magallanic Clouds. No current or near-future detector will be sensitive to explosions further away. The currently operating KM3NeT detector, with 6 ORCA lines taking data, is already able to cover CCSN events up to  $\sim 6 \text{ kpc}$  in case of a low mass progenitor ( $11 M_{\odot}$ ) and beyond the Galactic Centre for higher-mass stellar collapse ( $27 M_{\odot}$ ).

For what concerns time-dependent analyses of the neutrino lightcurve, IceCube and Hyper-Kamiokande, provide the best opportunities. They will be the only experiments able to detect the SASI oscillations at 15-20 kpc for the  $27 M_{\odot}$  progenitor model [152, 186]. KM3NeT, Super-Kamiokande, JUNO and DUNE may contribute to close-by ( $\sim 5 \text{ kpc}$  distance) and failed CCSN explosions [154].

In terms of localisation, using the ES channel information in Super-Kamiokande with Gd doping may provide the most accurate pointing [199]. Other possibilities such as triangulation, anisotropic interactions or the first events can also be used for a fast time response involving several high-statistics detectors, which may also be helpful [198, 191, 263].

Regarding the resolution of the spectrum, scintillator detectors like JUNO will be the ones achieving the best results, with an energy resolution of the order of 1% [179]. However, the combination of various detectors may help involving more independent measurements and breaking the degeneracy between the different parameters, hence reducing the uncertainties [182, 185].

Experiments	Type	Mass [kT]	Location	11.2 $M_{\odot}$	27.0 $M_{\odot}$	40.0 $M_{\odot}$
Super-K	H <sub>2</sub> O/ $\bar{\nu}_e$	32	Japan	4053/4068	7771/7544	7597/4904
Hyper-K	H <sub>2</sub> O/ $\bar{\nu}_e$	220	Japan	28K/28K	53K/52K	52K/34K
IceCube	String/ $\bar{\nu}_e$	51600	South Pole	321K/332K	662K/659K	818K/626K
6 KM3NeT-ORCA lines	String/ $\bar{\nu}_e$	2.5	France	309/313	670/650K	834/660
KM3NeT (3 blocks)	String/ $\bar{\nu}_e$	150	Italy/France	18K/18K	38K/38K	47/38
KamLAND	C <sub>n</sub> H <sub>2n</sub> / $\bar{\nu}_e$	1	Japan	189/188	363/349	350/233
Borexino	C <sub>n</sub> H <sub>2n</sub> / $\bar{\nu}_e$	0.278	Italy	52/52	101/97	97/64
JUNO	C <sub>n</sub> H <sub>2n</sub> / $\bar{\nu}_e$	20	China	3798/3769	7276/6995	7018/4661
SNO+	C <sub>n</sub> H <sub>2n</sub> / $\bar{\nu}_e$	0.7	Canada	132/131	254/244	245/163
NO $\nu$ A	C <sub>n</sub> H <sub>2n</sub> / $\bar{\nu}_e$	15	USA	2849/2827	5457/5246	5263/3496
HALO	Pb/ $\nu_e$	0.079	Canada	4/3	9/8	10/9
HALO-1kT	Pb/ $\nu_e$	1	Italy	54/47	117/102	128/123
DUNE	Ar/ $\nu_e$	40	USA	2750/2485	5652/5133	6075/5910
MicroBooNe	Ar/ $\nu_e$	0.09	USA	6/5	12/11	13/13
DarkSide-20k	Ar/any $\nu$	0.02	Italy	100/100	300/300	400/400

Table 12.1: Estimated number of detected events in the different detectors from a CCSN at 10 kpc, for three different models, s11.2c and s27.0c from [261] that form neutron stars and s40 from [262] which forms a black hole. The two numbers given are the total events over all channels using SNOw-GLOBES [174] assuming adiabatic MSW oscillations only for the normal mass ordering (left number) and the inverted mass order (right number).

#### 12.1.4 Outlook and perspectives

At the end of this thesis, a new project has started which aims at exploiting the combination of the information coming from different experiments sensitive to different interaction channels (neutrino flavors). This is done in collaboration with theory experts and people from the DUNE and Darkside Collaborations, which are sensitive to  $\nu_e$  and all flavors, respectively, while KM3NeT is sensitive to  $\bar{\nu}_e$ . First work has been done to extend and implement the CCSN simulation for these argon detectors, in the same framework as for KM3NeT, and evaluate the expected number of events as well as the detected lightcurve for different models. In this way, the final goal is to evaluate the model discrimination power using the synergies between these experiments, and determine the flux properties thanks to this combination.

Moreover, a time-dependent analysis of the spectrum would be of interest for the discrimination between the different models. In fact, determining the spectrum at different times of the emission may reveal the time evolution of the spectral parameters.

The possibility of using machine learning techniques to achieve a better discrimination between signal and background, by identifying patterns as the signature of the bioluminescence and radioactive decay processes, is going to be studied. This could allow to enhance the sensitivity, specially in time dependent analyses.

In addition, the neutrino mass ordering, and in general neutrino flavor conversion effects, will impact the observables of the core-collapse supernova neutrino emission. Therefore, CCSN neutrinos can also provide a measurement of the neutrino mass ordering. A very preliminary study has been started on this topic, but it should be mentioned that the change in the observed neutrino flux induced by the neutrino mass ordering is a tiny effect, so the experimental systematic effects of the NMO study using the neutrino lightcurve would need to be evaluated in an accurate way. Moreover, a precise knowledge of neutrino physics in such extreme media is required for a realistic estimate of the expected signal. For

these reasons, this was kept outside of the scope of this thesis.

For what concerns the real-time analysis, there is still some work to be done/improved in the near future. As an example, defining the arrival time of the CCSN signal from the real-time trigger, implemented over 500 ms, is ongoing work. This arrival time will be part of the information to be provided in case of an alert. In particular, it is of interest also to see which is the response of the KM3NeT DAQ to a very intense flux expected from a close explosion (below one kpc), e.g. in case Betelgeuse explodes. The idea to be put in place is to inject a real simulated signal at such distance into the DAQ, and look if such high amount of data can be processed without stalling or showing problems, with a proper behavior of the filters.

Moreover, there is a plan to develop a full run-by-run simulation of the data taking conditions for the CCSN data stream, with and without an inclusion of the signal. Up to now, all the background evaluation has been done directly on data, and a separate signal simulation. The purpose is to evaluate the signal detection efficiency in a more accurate way, incorporating the varying conditions in real data.

## 12.2 ANTARES search for high-energy neutrinos in coincidence with GW events and GRBs detected at TeV energies

Cosmic neutrinos and high energy cosmic rays are expected to have a same origin, yet unknown. Among the possible source candidates, gravitational-wave and TeV gamma-ray sources may also produce high-energy neutrino emission. For this reason, we have dedicated part of the work of this PhD to the search for high-energy neutrinos observed in coincidence with EM or GW detected sources.

When looking for high-energy neutrinos in neutrino telescopes like ANTARES, space and time correlations between the detected photons are used to identify different event topologies characteristic of the interaction of charged particles in water: long tracks induced by muons produced in the atmosphere and in muon neutrino charged current interactions releasing detectable Cherenkov light, that can come from outside the detector; and quasi spherical light deposited inside the detector emitted by particles produced in neutral current interactions of all-flavor neutrinos and in charge current electron neutrino interactions (shower-like). These correlations are exploited in an optimal way and implemented in the form of triggers, which tag candidates of these particle interactions and help reducing part of the background. In fact, events marked by bioluminescence or radioactivity will not active the triggers by themselves. Thus, the dominating background component for high-energy neutrino searches is the atmospheric background.

The most usual way to get rid of the atmospheric background is to look for events that come across the Earth (seen as upgoing in the detector), since only neutrinos can travel through the Earth. Moreover, atmospheric and cosmic neutrinos are expected to have a different energy spectrum. Therefore, by selecting the most energetic events, one can filter most of the remaining miss-reconstructed muons and the atmospheric neutrino contribution.

Another possibility is to look for time and space coincidences with a confirmed detection of a transient source, observed through any messenger. This is part of the multi-messenger approach. A small space region and a short time window where to look at, allow for a significant background reduction and lead to an increase of the discovery potential. In fact, background can be reduced enough to also allow for searches above the detector horizon (downgoing events, which are most probably muons). In this way, the search can be extended to the full sky, including all neutrino flavors.

Part of the thesis work has been devoted to the development of an event selection for shower-like events to be applied to these multi-messenger/transient searches. This selection is based, as for track events, on searching for the cuts in the quality parameters of the reconstruction so that one event passing the cuts, which is found inside the search time window, and reconstructed with a position compatible with the source location, leads to a  $3\sigma$  detection. This strategy allows to keep a good sensitivity (fixed at  $3\sigma$ ) while obtaining an optimal upper limit at the same time, since the cuts are chosen to maximise the signal expectation.

This analysis has been applied during this thesis to the search for a neutrino counterpart in ANTARES data to the GW events from the O2 catalog, and to the first detection of GRB events at TeV energies. These are all-flavor and full-sky neutrino searches. Including shower events in the analysis leads to an improvement of about 30% for upgoing events, and up to 200% for downgoing searches, compared to using only tracks. However, both searches result in no neutrino detected in coincidence with any of the GW and GRB signals analysed.

### 12.2.1 Outlook and perspectives

The prospect is now to perform the analysis on the new GW candidates from run O3. For binary black-hole mergers, a stacking analysis using a more sophisticated likelihood method will be carried out, following the same strategy as for O2.

Outside of the content of the manuscript, some work has been done to evaluate the sensitivity of the future KM3NeT-ARCA detector to these same transient sources by using the same method as in ANTARES, which allows for a fast response analysis, which can be applied to the full-sky and all neutrino flavors. The conclusion of these preliminary studies is that the same method is still applicable in an efficient way to KM3NeT-ARCA, even if it is a larger detector with a higher background rate. The expected improvement compared to ANTARES is going to be evaluated.

The KM3NeT detectors will offer the opportunity of a common multi-messenger program using ORCA and ARCA, covering a large energy range that will go from  $O(\text{GeV})$  up to tens of PeV energies. Moreover, they will be operating in the same timeline as new space missions (e.g. SVOM), new Cherenkov ground-based telescopes (CTA), new GW instruments (run O4 with four GW interferometers, LISA), and the next generation neutrino detectors (IceCube-Gen2, Hyper-Kamiokande).



# Bibliography

- [1] W. Pauli, "Dear radioactive ladies and gentlemen," *Phys. Today*, vol. 31N9, p. 27, 1978.
- [2] J. Barnothy, "Solar neutrino puzzle," *Nature*, vol. 252, 1974.
- [3] M. Czakon, M. Zralek, and J. Gluza, "Are neutrinos Dirac or Majorana particles?," *Acta Phys. Polon.*, vol. B30, pp. 3121–3138, 1999.
- [4] V. F. Hess, "Über beobachtungen der durchdringenden strahlung bei sieben freiballonfahrten," *Physikalische Zeitschrift*, vol. 13, p. 1084, 1912.
- [5] The IceCube Collaboration, "Evidence for high-energy extraterrestrial neutrinos at the icecube detector," *Science*, vol. 342, p. 1242856, 2013.
- [6] The IceCube Collaboration, "Observation of high-energy astrophysical neutrinos in three years of icecube data," *Phys. Rev. Lett.*, vol. 113, p. 101101, 2014.
- [7] LIGO Scientific Collaboration and Virgo Collaboration, "Observation of gravitational waves from a binary black hole merger," *Phys. Rev. Lett.*, vol. 116, p. 061102, 2016.
- [8] LIGO Scientific Collaboration and Virgo Collaboration, "GW170817: Observation of Gravitational Waves from a Binary Neutron Star Inspiral," *Phys. Rev. Lett.*, vol. 119, p. 161101, 2017.
- [9] The IceCube Collaboration, the Fermi-LAT Collaboration, the MAGIC Collaboration, the AGILE Collaboration, ASAS-SN, the HAWC Collaboration, H.E.S.S. Collaboration, INTEGRAL Collaboration, *et al.*, "Multimessenger observations of a flaring blazar coincident with high-energy neutrino IceCube-170922A," *Science*.
- [10] The IceCube Collaboration, "Neutrino emission from the direction of the blazar TXS 0506+056 prior to the IceCube-170922A alert," *Science*, vol. 361, 2018.
- [11] Patrignani *et al.*, "Review of particle physics," *Chin. Phys.*, vol. C40.10, p. 100001, 2016.
- [12] A. M. Hillas, "The origin of ultrahigh-energy cosmic rays," *Ann. Rev. Astron. Astrophys.*, vol. 22, 1984.
- [13] J. Clay, "Penetrating radiation," *Proceedings of the Royal Academy of Sciences Amsterdam*, vol. 30, 1927.
- [14] Pierre Auger Collaboration, "The Pierre Auger Observatory: Contributions to the 36th International Cosmic Ray Conference (ICRC 2019)," 2019.
- [15] Telescope Array Collaboration *PoS ICRC 2017 515*, 2018.

- [16] A. A. Watson, "High-energy cosmic rays and the Greisen–Zatsepin–Kuz'min effect," *Rept. Prog. Phys.*, vol. 77, p. 036901, 2014.
- [17] R. A. Bell, "The acceleration of cosmic rays in shock fronts", journal =, 1978.
- [18] J. D. Raymond, "Solar Neutrinos. II. Experimental," *Phys. Rev. Lett.*, vol. 12, no. 303, 1964.
- [19] C. Patrignani *et al.*, "Review of particle physics," *Chin. Phys.*, p. C40(10):100001, 2016.
- [20] L. Wolfenstein, "Neutrino oscillations in matter," *Phys. Rev. D*, vol. 17, pp. 2369–2374, 1978.
- [21] The KM3NeT Collaboration, "Letter of intent for KM3NeT 2.0," *J of Phys. G*, vol. 43, p. 8, 2016.
- [22] L. Quinn, J. Evans, J. Koskinen, C. Diaconu, and P. Coyle, "Determining the Neutrino Mass Hierarchy with KM3NeT/ORCA," 2018.
- [23] The IceCube Collaboration, "Observation of astrophysical neutrinos in four years of icecube data," *PoS ICRC2015*, p. 1081, 2016.
- [24] The IceCube Collaboration, "Observation of astrophysical neutrinos in six years of icecube data," *Proceedings, 35th International Cosmic Ray Conference (ICRC2017)*, 2018.
- [25] The IceCube Collaboration, "A measurement of the diffuse astrophysical muon neutrino flux using eight years of icecube data," *PoS ICRC2017*, p. 1005, 2018.
- [26] The IceCube Collaboration, "Characterization of the astrophysical diffuse neutrino flux with icecube high-energy starting events," *PoS(ICRC2019)1004*.
- [27] The IceCube Collaboration, "Measurement of the diffuse astrophysical muon-neutrino spectrum with ten years of icecube data," *PoS(ICRC2019)1017*.
- [28] The IceCube Collaboration, "The IceCube Neutrino Observatory - Contributions to ICRC 2017 Part II: Properties of the Atmospheric and Astrophysical Neutrino Flux," 2017.
- [29] The IceCube Collaboration, "First double cascade tau neutrino candidates in icecube and a new measurement of the flavor composition," *PoS(ICRC2019)1015*.
- [30] G.J.Gounaris and G. Moultaqa, "The Flavor distribution of cosmic neutrinos," 2002.
- [31] The ANTARES Collaboration, "Study of the high-energy neutrino diffuse flux with the antares neutrino telescope," *PoS(ICRC2019)891*.
- [32] M. Ackermann, M. Ahlers, L. Anchordoqui, M. Bustamante, D. Grant, P. Gorham, F. Halzen, *et al.*, "Astrophysics uniquely enabled by observations of high-energy cosmic neutrinos thematic area: Multi-messenger astronomy and astrophysics," 03 2019.
- [33] The Fermi-LAT Collaboration, "The spectrum of isotropic diffuse gamma-ray emission between 100 MeV and 820 GeV," *Astrophys. J.*, vol. 799, p. 86, 2015.
- [34] The Pierre Auger Collaboration, "The flux of ultra-high energy cosmic rays after ten years of operation of the pierre auger observatory," *PoS ICRC2015*, vol. 271, 2016.
- [35] H.E.S.S. Collaboration, "Acceleration of petaelectronvolt protons in the Galactic Centre," *Nature*, vol. 531, p. 476, 2016.
- [36] T. Damour, "1974: the discovery of the first binary pulsar," *Class. Quant. Grav.*, vol. 32, no. 12, p. 124009, 2015.

- [37] LIGO Scientific Collaboration and Virgo Collaboration, "GW170817: Measurements of Neutron Star Radii and Equation of State," *LIGO-P1800115*, 2018.
- [38] LIGO Scientific Collaboration and Virgo Collaboration, "Properties of the binary neutron star merger GW170817," *LIGO-P1800061*, 2018.
- [39] G. Timothee, "Search for high-energy neutrinos from the galactic plane with the antares neutrino telescope," 2017.
- [40] LIGO Scientific Collaboration and Virgo Collaboration, "Gravitational Waves and Gamma-rays from a Binary Neutron Star Merger: GW170817 and GRB 170817A," *Astrophys. J.*, vol. 848, no. 2, p. L13, 2017.
- [41] Z. Jin, S. Covino, N. Liao, *et al.*, "A kilonova associated with GRB 070809," *Nature*, pp. 1–6, 2019.
- [42] E. Troja *et al.*, "The afterglow and kilonova of the short GRB 160821B," *Monthly Notices of the Royal Astronomical Society*, vol. 489, no. 2, pp. 2104–2116, 2019.
- [43] Fermi Collaboration, "An Ordinary Short Gamma-Ray Burst with Extraordinary Implications: Fermi-GBM Detection of GRB 170817A," *Astrophys. J.*, vol. 848, p. L14, 2017.
- [44] I. Arcavi, G. Hosseinzadeh, *et al.*, "Optical emission from a kilonova following a gravitational-wave-detected neutron-star merger," *Nature*, vol. 551, p. 64–66, 2017.
- [45] M. C. Miller, "A golden binary," *Nature*, vol. 551, 2017.
- [46] D. Kasen and B. Metzger, "Origin of the heavy elements in binary neutron-star mergers from a gravitational-wave event," *Nature*, vol. 551, pp. 80–84, 2017.
- [47] S.J. Smartt, T.W. Chen, *et al.*, "A kilonova as the electromagnetic counterpart to a gravitational-wave source," *Nature*, vol. 551.
- [48] E. Pian, P. D'Avanzo, *et al.*, "Spectroscopic identification of r-process nucleosynthesis in a double neutron-star merger," *Nature*, vol. 551.
- [49] V. A. Villar *et al.*, "The Combined Ultraviolet, Optical, and Near-Infrared Light Curves of the Kilonova Associated with the Binary Neutron Star Merger GW170817: Unified Data Set, Analytic Models, and Physical Implications," *Astrophys. J.*, vol. 851, p. L21, 2017.
- [50] C. Barbieri, O. S. Salafia, A. Perego, M. Colpi, and G. Ghirlanda, "Light-curve models of black hole – neutron star mergers: steps towards a multi-messenger parameter estimation," *Astron. Astrophys.*, vol. 625, p. A152, 2019.
- [51] E. Troja, L. Piro, *et al.*, "The X-ray counterpart to the gravitational-wave event GW170817," *Nature*, vol. 551, pp. 71–74, 2017.
- [52] G. Ghirlanda *et al.*, "Compact radio emission indicates a structured jet was produced by a binary neutron star merger," *Science*, vol. 363, p. 968, 2019.
- [53] The LIGO Scientific Collaboration, The Virgo Collaboration, The 1M2H Collaboration, The Dark Energy Camera GW-EM Collaboration, the DES Collaboration, The DLT40 Collaboration, The Las Cumbres Observatory Collaboration, The VINROUGE Collaboration, and The MASTER Collaboration, "A gravitational-wave standard siren measurement of the Hubble constant," *Nature*, vol. 551, pp. 85–88, 2017.
- [54] ANTARES, IceCube, Pierre Auger, and LIGO-Virgo Collaborations, "Search for High-energy Neutrinos from Binary Neutron Star Merger GW170817 with ANTARES, IceCube, and the Pierre Auger Observatory," *Astrophys. J.*, vol. 850, p. L35, 2017.

- [55] S. S. Kimura, K. Murase, P. Mészáros, and K. Kiuchi, “High-Energy Neutrino Emission from Short Gamma-Ray Bursts: Prospects for Coincident Detection with Gravitational Waves,” *Astrophys. J.*, vol. 848, no. 1, p. L4, 2017.
- [56] K. Fang and B. D. Metzger, “High-Energy Neutrinos from Millisecond Magnetars formed from the Merger of Binary Neutron Stars,” *Astrophys. J.*, vol. 849, no. 2, p. 153, 2017.
- [57] W. Winter, S. Gao, X. Rodrigues, A. Fedynitch, A. Palladino, and M. Pohl, “Multi-messenger interpretation of neutrinos from TXS 0506+056,” *PoS(ICRC2019)1032*, 2019.
- [58] P. Padovani, P. Giommi, E. Resconi, *et al.*, “Dissecting the region around IceCube-170922A: the blazar TXS 0506+056 as the first cosmic neutrino source,” *MNRAS*, vol. 480, p. 192, 2018.
- [59] B. T. Zhang, M. Petropoulou, K. Murase, and F. Oikonomou, “A Neutral Beam Model for High-Energy Neutrino Emission from the Blazar TXS 0506+056,” 2019.
- [60] M. Petropoulou *et al.*, “Multi-Epoch Modeling of TXS 0506+056 and Implications for Long-Term High-Energy Neutrino Emission,” 2019.
- [61] X. Rodrigues, S. Gao, A. Fedynitch, A. Palladino, and W. Winter, “Leptohadronic Blazar Models Applied to the 2014–2015 Flare of TXS 0506+056,” *Astrophys. J. Lett.*, vol. 874, no. 2, p. L29, 2019.
- [62] The ANTARES Collaboration, “The Search for Neutrinos from TXS 0506+056 with the ANTARES Telescope,” *Astrophys. J.*, vol. 863, no. 2, p. L30, 2018.
- [63] “Unified model for agns ‘zoo’.”
- [64] D. Hooper, T. Linden, and A. Viereg, “Active Galactic Nuclei and the Origin of IceCube’s Diffuse Neutrino Flux,” *JCAP*, vol. 1902, p. 012, 2019.
- [65] The IceCube Collaboration, “Search for high-energy neutrinos from agn cores,” *PoS(ICRC2019)845*.
- [66] The IceCube Collaboration, “The contribution of Fermi-2LAC blazars to the diffuse TeV-PeV neutrino flux,” *Astrophys. J.*, vol. 835, no. 1, p. 45, 2017.
- [67] The IceCube Collaboration, “Searches for steady neutrino emission from 3FHL blazars using eight years of IceCube data from the Northern hemisphere,” *PoS(ICRC2019)916*.
- [68] The ANTARES Collaboration, “Search for muon-neutrino emission from GeV and TeV gamma-ray flaring blazars using five years of data of the ANTARES telescope,” *Journal of Cosmology and Astroparticle Physics*, vol. 2015, no. 12, pp. 014–014, 2015.
- [69] M. Amiri *et al.*, “Observations of fast radio bursts at frequencies down to 400 megahertz,” *Nature*, vol. 566, p. 230–234, 2019.
- [70] V. Gajjar *et al.*, “Highest Frequency Detection of FRB 121102 at 4–8 GHz Using the Breakthrough Listen Digital Backend at the Green Bank Telescope,” *Astrophys. J.*, vol. 863, no. 1, p. 2, 2018.
- [71] D. Thornton *et al.*, “A Population of Fast Radio Bursts at Cosmological Distances,” *Science*, vol. 341, no. 6141, pp. 53–56, 2013.
- [72] E. Petroff, J.W.T. Hessels, and D.R. Lorimer, “Fast Radio Bursts,” *Astron. Astrophys. Rev.*, vol. 27, no. 1, p. 4, 2019.
- [73] The ANTARES Collaboration, “The search for high-energy neutrinos coincident with fast radio bursts with the ANTARES neutrino telescope,” *Mon. Not. Roy. Astron. Soc.*, vol. 482, no. 1, pp. 184–193, 2019.

- [74] The IceCube Collaboration, "A Search for Neutrino Emission from Fast Radio Bursts with Six Years of IceCube Data," *Astrophys. J.*, vol. 857, no. 2, p. 117, 2018.
- [75] T. Piran, "Gamma-ray bursts and the fireball model," *Phys. Rept.*, vol. 314, pp. 575–667, 1999.
- [76] D. Eichler and A. Levinson, "A compact fireball model of gamma-ray bursts," *The Astrophysical Journal*, vol. 529, no. 1, pp. 146–150, 2010.
- [77] J. Barnes, P. C. Duffell, *et al.*, "A GRB and Broad-lined Type Ic Supernova from a Single Central Engine," *Astrophys. J.*, vol. 860, no. 1, p. 38, 2018.
- [78] B. Zhang and P. Kumar, "Model-dependent high-energy neutrino flux from Gamma-Ray Bursts," *Phys. Rev. Lett.*, vol. 110, no. 12, p. 121101, 2013.
- [79] L. Becerra, C.L. Bianco, C.L. Fryer, J.A. Rueda, and R. Ruffini, "On the induced gravitational collapse scenario of gamma-ray bursts associated with supernovae," *Astrophys. J.*, vol. 833, no. 1, p. 107, 2016.
- [80] IceCube Collaboration, "An absence of neutrinos associated with cosmic-ray acceleration in gamma-ray bursts," vol. 484, pp. 351–354, 2012.
- [81] The IceCube Collaboration, "An All-Sky Search for Three Flavors of Neutrinos from Gamma-Ray Bursts with the IceCube Neutrino Observatory," *Astrophys. J.*, vol. 824, no. 2, p. 115, 2016.
- [82] The ANTARES Collaboration, "Search for muon neutrinos from gamma-ray bursts with the ANTARES neutrino telescope using 2008 to 2011 data," *Astron. Astrophys.*, vol. 559, p. A9, 2013.
- [83] H.E.S.S. Collaboration, "Gamma-Ray Burst observation at Very High Energy with H.E.S.S.," *PoS(ICRC2019)761*.
- [84] A. Kappes, J. Hinton, C. Stegmann, and A. F. Aharonian, "Potential neutrino signals from galactic gamma-ray sources," *The Astrophysical Journal*, vol. 656, no. 2, 2007.
- [85] F.L. Villante and F. Vissani, "How precisely neutrino emission from supernova remnants can be constrained by gamma ray observations?," *Phys. Rev.*, vol. D78, p. 103007, 2008.
- [86] E. Amato, D. Guetta, and P. Blasi, "Signatures of high energy protons in pulsar winds," *Astronomy and Astrophysics*, vol. 402, pp. 827–836, 2003.
- [87] H. R. Christiansen, M. Orellana, and G. E. Romero, "High-energy neutrino emission from x-ray binaries," *Phys. Rev.*, vol. D73, p. 063012, 2006.
- [88] B. Cerutti, *High-energy gamma-ray emission in compact binaries*. Theses, Université de Grenoble, June 2010. 310 pages, 113 figures, 2 tableaux.
- [89] The ANTARES Collaboration *Journal of Cosmology and Astroparticle Physics*, vol. 2017, pp. 019–019, apr 2017.
- [90] H. R. Christiansen, M. Orellana, and G. E. Romero, "High-energy neutrino emission from x-ray binaries," *Phys. Rev.*, vol. D73, p. 063012, 2006.
- [91] D. H. Perkins *Particle astrophysics*, 2003.
- [92] E. Vitagliano, J. Redondo, and G. Raffelt, "Solar neutrinos at keV energies: thermal flux," 2017.
- [93] K. Edsjo, J. Elefant, R. Enberg, and C. Niblaeus, "Neutrinos from cosmic ray interactions in the sun," *JCAP*, vol. 06, p. 033, 2017.

- [94] J. Edsjo, J. Elevant, R. Enberg, and C. Niblaeus, "Neutrinos from cosmic ray interactions in the Sun," *JCAP*, vol. 1706, no. 06, p. 033, 2017.
- [95] D. Fargion, "Detecting solar neutrino flares and flavors," *JHEP*, vol. 06, p. 45, 2004.
- [96] L.A. Fusco, "Diffuse neutrino emissions from the southern sky and mediterranean neutrino telescopes," *Eur. Phys. J.*, vol. 132, p. 353, 2017.
- [97] K. S. Cheng, D. Chernyshov, V. Dogiel, and C. Ko, "Multi-wavelength Emission from the Fermi Bubble I. Stochastic acceleration from Background Plasma," *The Astrophysical Journal*, vol. 790, 05 2014.
- [98] K.-S. Cheng, D. O. Chernyshov, V. A. Dogiel, and C.-M. Ko, "Multi-wavelength emission from the Fermi Bubble. II. Secondary electrons and the hadronic model of the bubble," *The Astrophysical Journal*, vol. 799, p. 112, jan 2015.
- [99] C. Lunardini and S. Razzaque, "High Energy Neutrinos from the Fermi Bubbles," *Phys. Rev. Lett.*, vol. 108, p. 221102, 2012.
- [100] The ANTARES Collaboration and The IceCube Collaboration, "ANTARES and IceCube Combined Search for Neutrino Point-like and Extended Sources in the Southern Sky," *The Astrophysical Journal*, vol. 892, p. 92, 2020.
- [101] The ANTARES Collaboration and The IceCube Collaboration, "Joint Constraints on Galactic Diffuse Neutrino Emission from the ANTARES and IceCube Neutrino Telescopes," *Astrophys.J.*, vol. 868, no. 2, p. L20, 2018.
- [102] The ANTARES Collaboration, "Neutrinos from the Fermi Bubbles with ANTARES," *PoS(ICRC2017)1001*.
- [103] N. Sherf, U. Keshet, and I. Gurwich, "IceCube constraints on the Fermi Bubbles," *Astrophys. J.*, vol. 847, no. 2, p. 95, 2017.
- [104] A. Esmaili and K. Murase, "Constraining high-energy neutrinos from choked-jet supernovae with IceCube high-energy starting events," *JCAP*, vol. 1812, no. 12, p. 008, 2018.
- [105] K. Murase, "New prospects for detecting high-energy neutrinos from nearby supernovae," *Phys. Rev. D*, vol. 97, p. 081301.
- [106] C. Kato, M. D. Azari, S. Yamada, K. Takahashi, H. Umeda, T. Yoshida, and K. Ishidoshiro, "Pre-supernova neutrino emissions from ONe cores in the progenitors of core-collapse supernovae: are they distinguishable from those of Fe cores?," *Astrophys. J.*, vol. 808, no. 2, p. 168, 2015.
- [107] The IceCube Collaboration, "The icecube upgrade - design and science goals," *PoS(ICRC2019)1031*.
- [108] The ANTARES Collaboration, "Time calibration of the ANTARES neutrino telescope," *Astroparticle Physics*, vol. 34, pp. 539–549, 2011.
- [109] The ANTARES Collaboration, "The positioning system of the ANTARES neutrino telescope," *Journal of Instrumentation*, vol. 7, no. 08, pp. T08002–T08002, 2012.
- [110] The ANTARES Collaboration, "Performance of the front-end electronics of the ANTARES neutrino telescope," *Nuclear Instruments and Methods in Physics Research Section A: Accelerators, Spectrometers, Detectors and Associated Equipment*, vol. 622, pp. 59–73, 2010.

- [111] The ANTARES Collaboration, "The ANTARES Detector: Electronics and Readout," *Proceedings, 30th International Cosmic Ray Conference (ICRC 2007): Merida, Yucatan, Mexico, July 3-11, 2007*, vol. 5, pp. 1609–1612, 2007.
- [112] The ANTARES Collaboration, "The antares telescope neutrino alert system," *Astroparticle Physics*, vol. 35, 2012.
- [113] C. Andreopoulos, C. Barry, S. Dytman, H. Gallagher, T. Golan, R. Hatcher, G. Perdue, and J. Yarba, "The GENIE Neutrino Monte Carlo Generator: Physics and User Manual," 2015.
- [114] The KM3NeT Collaboration, "High-energy Neutrino Event Simulation at NLO in Genie for KM3NeT and Other Observatories," *PoS(ICRC2019)895*.
- [115] T.K.Gaisser and M. Honda, "Flux of atmospheric neutrinos," *Ann. Rev. Nucl. Part. Sci.*, vol. 52, pp. 153–199, 2002.
- [116] G. Battistoni, "Extensive air showers and hadronic interactions," *Frontier Objects in Astrophysics and Particle Physics, Proceedings of the Vulcano Workshop*, vol. 57, p. 405, 1996.
- [117] Y. Becherini, A. Margiotta, M. Sioli, and M. Spurio, "A Parameterisation of single and multiple muons in the deep water or ice," *Astropart. Phys.*, vol. 25, pp. 1–13, 2006.
- [118] The ANTARES Collaboration, "Zenith distribution and flux of atmospheric muons measured with the 5-line ANTARES detector," *Astroparticle Physics*, vol. 34, 2010.
- [119] The KM3NeT Collaboration, "Dependence of atmospheric muon flux on seawater depth measured with the first KM3NeT detection units," *Eur. Phys. J. C*, vol. 80, p. 99, 2020.
- [120] D. Heck, J. Knapp, J.N.Capdevielle, G. Schatz, and T. Thouw, "CORSIKA: A Monte Carlo code to simulate extensive air showers," 1998.
- [121] M.Colomer and V. Kulikovskiy, for the KM3NeT Collaboration, "Detailed KM3NeT optical module simulation with Geant4 and supernova neutrino detection study," *PoS(ICRC2017)983*, 2017.
- [122] S. Agostinelliae, J. Allisonas, K. Amakoe, *et al.*, "Geant4—a simulation toolkit," *Nuclear Instruments and Methods in Physics Research Section A: Accelerators, Spectrometers, Detectors and Associated Equipment*, vol. 506, pp. 250–303, 2003.
- [123] A.G.Tsirigotis, G. Bourlis, A. Leisos, and S.E.Tzamarias, "Hellenic Open University Reconstruction & Simulation (HOURS) software package: User Guide & short reference of Event Generation, Cherenkov photon production and Optical Module simulation," 2017.
- [124] The ANTARES Collaboration, "Searches for Point-like and Extended Neutrino Sources Close to the Galactic Center Using the ANTARES Neutrino Telescope," *The Astrophysical Journal Letters*, vol. 786, p. L5, 2012.
- [125] The KM3NeT Collaboration, "KM3NeT/ARCA Event Reconstruction Algorithms," *PoS*, vol. ICRC2017, p. 950, 2018.
- [126] The ANTARES Collaboration, "An Algorithm for the Reconstruction of Neutrino-induced Showers in the ANTARES Neutrino Telescope," *Astron. J.*, vol. 154, p. 275, 2017.
- [127] The ANTARES Collaboration, "An algorithm for the reconstruction of high-energy neutrino-induced particle showers and its application to the ANTARES neutrino telescope," *Eur. Phys. J.*, vol. 77, p. 419, 2017.

- [128] L. Lista, "Statistical methods for data analysis in particle physics," *Lecture notes in Physics*, vol. 909, 2016.
- [129] R. D. Cousins, "Annotated bibliography of some papers on combining significances or p-values," *arXiv:0705.2209 [physics.data-an]*, 2008.
- [130] R. A. Fisher, "Statistical methods for research workers," 1932.
- [131] A. Roodman, "Blind analysis in particle physics," *eConf*, vol. C030908, 2003.
- [132] W. Baade and F. Zwicky, "On super-novae," *Proc Natl Acad Sci USA*, vol. 20, 1934.
- [133] W. Baade and F. Zwicky, "Cosmic rays from super-novae," *Proc Natl Acad Sci USA*, vol. 20, 1934.
- [134] W. Baade and F. Zwicky, "Remarks on super-novae and cosmic rays," *Physical Review Letters*, vol. 46, 1934.
- [135] A. Burrows and J. M. Lattimer, "Neutrinos from SN 1987A," *Astrophysical Journal, Part 2 - Letters to the Editor (ISSN 0004-637X)*, vol. 318, 1987.
- [136] K.S.Hirata *et al.*, "Observation in the Kamiokande-II Detector of the Neutrino Burst from Supernova SN1987A," *Phys. Rev. D*, vol. 38.2, p. 448–458, 1988.
- [137] T. Haines *et al.*, "Neutrinos from SN1987a in the IMB Detector. In: Nucl. Instrum. Methods," *Phys. Res. Sect. A*, vol. 264.1, p. 28–31, 1988.
- [138] E. N. Alekseev, L. N. Alekseeva, I. V. Krivosheina, and V.I.Volchenko, "Detection of the neutrino signal from SN 1987A using the INR Baksan underground scintillation telescope," *ESO Workshop on the SN 1987A, Proceedings (A88-35301 14-90)*, 1987.
- [139] The IceCube Collaboration, "Eleven Year Search for Supernovae with the IceCube Neutrino Observatory," *PoS*, vol. ICRC2019, p. 889, 2020.
- [140] Super-Kamiokande Collaboration, "Search for Supernova Neutrino Bursts at Super-Kamiokande," *Astrophys. J.*, vol. 669, pp. 519–524, 2007.
- [141] Hyper-Kamiokande Collaboration, "Neutrino astrophysics with Hyper-Kamiokande," *Journal of Physics: Conference Series*, vol. 718, p. 062071, 2016.
- [142] S. M. Adams, C. S. Kochanek, J. F. Beacom, M. R. Vagins, and K. Z. Stanek, "OBSERVING THE NEXT GALACTIC SUPERNOVA," *The Astrophysical Journal*, vol. 778, p. 164, nov 2013.
- [143] J. R. Wilson, "Supernovae and Post-Collapse Behavior in Numerical Astrophysics," pp. 422–434, 1985.
- [144] H. A. Bethe and J. R. Wilson, "Revival of a stalled supernova shock by neutrino heating," *Astrophys. J.*, vol. 295, p. 14, 1985.
- [145] H.-T. Janka, T. Melson, and A. Summa, "Physics of core-collapse supernovae in three dimensions: A sneak preview," *Annual Review of Nuclear and Particle Science*, vol. 66, no. 1, pp. 341–375, 2016.
- [146] B. Peres, "Transport de neutrinos dans les supernovas gravitationnelles.," *PhD thesis. Astrophysique stellaire et solaire [astro-ph.SR]. Observatoire de Paris.*, 2013.
- [147] H.T.Janka, "Neutrino driven explosions," *Alsabti A., Murdin P. (eds) Handbook of Supernovae. Springer, Cham*, 2017.

- [148] I. Tamborra, G. Raffelt, F. Hanke, H.-T. Janka, and B. Müller, “Neutrino emission characteristics and detection opportunities based on three-dimensional supernova simulations,” *Phys. Rev. D*, vol. 90, p. 045032, 2014.
- [149] L. Hüdepohl, B. Müller, H.-T. Janka, A. Marek, and G. G. Raffelt, “Neutrino signal of electron-capture supernovae from core collapse to cooling,” *Phys. Rev. Lett.*, vol. 104, p. 251101, 2010.
- [150] E. R. Valentim, J. E. Horvath, “Evidence for Two Neutrino Bursts from SN1987A,” *International Journal of Modern Physics*, vol. 45, 2017.
- [151] Rampp, M. and Janka, H.-T., “Radiation hydrodynamics with neutrinos\* - variable eddington factor method for core-collapse supernova simulations,” *A&A*, vol. 396, pp. 361–392, 2002.
- [152] I. Tamborra, F. Hanke, B. Müller, H.-T. Janka, and G. Raffelt, “Neutrino signature of supernova hydrodynamical instabilities in three dimensions,” *Phys. Rev. Lett.*, vol. 111, p. 121104, 2013.
- [153] “<http://wwwmpa.mpa-garching.mpg.de/ccsnarchive/data/tamborra2014/>,”
- [154] L. Walk, I. Tamborra, H.-T. Janka, and A. Summa, “Neutrino emission characteristics of black hole formation in three-dimensional simulations of stellar collapse,” 2019.
- [155] F. Hanke, B. Müller, A. Wongwathanarat, A. Marek, and H.-T. Janka, “SASI Activity in Three-dimensional Neutrino-hydrodynamics Simulations of Supernova Cores,” *The Astrophysical Journal*, vol. 770, p. 16, 2013.
- [156] C. Volpe, “Neutrino Astrophysics,” *Acta Phys. Polon. Supp.*, vol. 9, p. 769, 2016.
- [157] S. Mikheyev and A. Smirnov, “Resonance Amplification of Oscillations in Matter and Spectroscopy of Solar Neutrinos,” *Sov. J. Nucl. Phys.*, vol. 42, pp. 913–917, 1985.
- [158] A. S. Dighe and A. Y. Smirnov, “Identifying the neutrino mass spectrum from the neutrino burst from a supernova,” *Phys. Rev. D*, vol. 62, p. 033007, 2000.
- [159] K. Takahashi and K. Sato, “Effects of Neutrino Oscillation on Supernova Neutrino: Inverted Mass Hierarchy,” *Progress of Theoretical Physics*, vol. 109, pp. 919–931, 06 2003.
- [160] E. Müller, H.-T. Janka, and A. Wongwathanarat *Astron. Astrophys.*, vol. 537, p. A63, 2012.
- [161] S. Scheidegger, R. Käppeli, S. C. Whitehouse, T. Fischer, and M. Liebendörfer *Astron. Astrophys.*, vol. 514, p. A51, 2010.
- [162] T. Kuroda, K. Kotake, and T. Takiwaki *Astrophys. J. Lett.*, vol. 829, p. L14, 2016.
- [163] H. Andresen, B. Müller, E. Müller, and H.-T. Janka *Mon. Not. R. Astron. Soc.*, vol. 468, p. 2032, 2017.
- [164] V. Roma, J. Powell, I. S. Heng, and R. Frey, “Astrophysics with core-collapse supernova gravitational wave signals in the next generation of gravitational wave detectors,” *Phys. Rev.*, vol. D99, no. 6, p. 063018, 2019.
- [165] K. Nakamura, S. Horiuchi, M. Tanaka, K. Hayama, T. Takiwaki, and K. Kotake, “Multimessenger signals of long-term core-collapse supernova simulations: synergetic observation strategies,” *Mon. Not. Roy. Astron. Soc.*, vol. 461, no. 3, pp. 3296–3313, 2016.
- [166] L. S. Finn, C. R. Evans *ApJ*, vol. 351, p. 588, 1990.

- [167] B. Mueller, H.-T. Janka, and A. Marek, "A New Multi-Dimensional General Relativistic Neutrino Hydrodynamics Code of Core-Collapse Supernovae III. Gravitational Wave Signals from Supernova Explosion Models," *Astrophys. J.*, vol. 766, p. 43, 2013.
- [168] A. Odrzywolek, M. Misiaszek, and M. Kutschera, "Detection possibility of the pair - annihilation neutrinos from the neutrino - cooled pre-supernova star," *Astropart. Phys.*, vol. 21, pp. 303–313, 2004.
- [169] K. Scholberg, "Supernova Neutrino Detection," *Ann. Rev. Nucl. Part. Sci.*, vol. 62, pp. 81–103, 2012.
- [170] The IceCube Collaboration, "Icecube sensitivity for low-energy neutrinos from nearby supernovae," *A&A*, vol. 535, p. A109, 2011.
- [171] The ANTARES Collaboration *Proceedings of ICRC2011*, 2011.
- [172] F. A. Strumia, "Precise quasielastic neutrino/nucleon cross-section," *Physics Letters B*, vol. 564, pp. 42–54, 2003.
- [173] G. Radel and R. Beyer, "Neutrino electron scattering," *Mod. Phys. Lett.*, vol. A8, 1993.
- [174] A. Beck *et al.*, "SNOwGLOBES: SuperNova Observatories with GLOBES," 2011.
- [175] M. De Jong *et al.*, *Jpp - Documentation*.
- [176] G. Cowan, K. Cranmer, E. Gross, and O. Vitells, "Asymptotic formulae for likelihood-based tests of new physics," *Eur. Phys. J.*, vol. C71, p. 1554, 2011.
- [177] G. J. Feldman and R. D. Cousins, "A Unified approach to the classical statistical analysis of small signals," *Phys. Rev. D*, vol. 57, pp. 3873–3889, 1998.
- [178] T. M. Karbach, "Feldman-Cousins Confidence Levels - Toy MC Method," 2011.
- [179] J.-S. Lu, Y.-F. Li, and S. Zhou, "Getting the most from the detection of Galactic supernova neutrinos in future large liquid-scintillator detectors," *Phys. Rev. D*, vol. 94, no. 2, p. 023006, 2016.
- [180] V. Kulikovskiy, "Km3net sensitivity estimation to supernova detection," *KM3NeT Internal Note*, 2017.
- [181] Y. Avni, "Energy spectra of X-ray clusters of galaxies," *Astrophys. J.*, vol. 210, pp. 642–646, 1976.
- [182] A. Gallo Rosso, F. Vissani, and M. C. Volpe, "What can we learn on supernova neutrino spectra with water Cherenkov detectors?," *JCAP*, vol. 1804, no. 04, p. 040, 2018.
- [183] C. Martellini, S. M. Mari, P. Montini, and G. Settanta, "Towards a reconstruction of Supernova Neutrino Spectra in JUNO," *EPJ Web Conf.*, vol. 209, p. 01012, 2019.
- [184] D. Vaananen and C. Volpe, "The neutrino signal at HALO: learning about the primary supernova neutrino fluxes and neutrino properties," *JCAP*, vol. 1110, p. 019, 2011.
- [185] L. Köpke, "Improved Detection of Supernovae with the IceCube Observatory," *J. Phys. Conf. Ser.*, vol. 1029, no. 1, p. 012001, 2018.
- [186] J. Migenda, "Detecting Fast Time Variations in the Supernova Neutrino Flux with Hyper-Kamiokande," *eprint arXiv:1609.04286*, 2015.
- [187] A. Burrows, D. Klein, and R. Gandhi *Phys. Rev. D*, vol. 45, p. 3361, 1992.

- [188] J.F. Beacom and P. Vogel, "Can a supernova be located by its neutrinos?," *Phys.Rev. D*, vol. 60, p. 033007, 1999.
- [189] T. Mühlbeier, H. Nunokawa, and R. Zukanovich Funchal, "Revisiting the triangulation method for pointing to supernova and failed supernova with neutrinos," *Phys.Rev. D*, p. 88, 2013.
- [190] V. Brdar, M. Lindner, and X.-J. Xu, "Neutrino astronomy with supernova neutrinos," *JCAP*, vol. 4, no. 1804, p. 25, 2018.
- [191] N.B. Linzer and K. Scholberg, "Triangulation pointing to core-collapse supernovae with next-generation neutrino detectors," *Phys. Rev. D*, vol. 100, no. 10, p. 103005, 2019.
- [192] R.S.L. Hansen, M. Lindner, and O. Scholer, "Timing the neutrino signal of a galactic supernova," *eprint arXiv:1904.11461*, 2019.
- [193] K. Scholberg, "The SuperNova Early Warning System," *Astron. Nachr.*, vol. 329, pp. 337–339, 2008.
- [194] Super-Kamiokande Collaboration, "The Super-Kamiokande detector," *Nucl. Instr. and Meth. A*, vol. 501, pp. 418–462, 2003.
- [195] Hyper-Kamiokande Proto-Collaboration, "Hyper-Kamiokande Design Report," *eprint arXiv:1805.04163*, 2018.
- [196] The IceCube Collaboration, "The IceCube Neutrino Observatory: instrumentation and online systems," *J of Inst.*, vol. 12, p. P03012, 2017.
- [197] JUNO Collaboration, "Neutrino physics with JUNO," *J. Phys. G*, vol. 43, p. 030401, 2016.
- [198] P. Vogel and J. F. Beacom, "The angular distribution of the reaction:  $\bar{\nu}_e + p \rightarrow e^+ + n$ ," *Phys. Rev. D*, vol. 60, p. 053003, 1999.
- [199] R. Tomàs *et al.*, "Supernova pointing with low- and high-energy neutrino detectors," *Phys.Rev. D*, vol. 68, p. 093013, 2003.
- [200] A. Coleiro, M. Colomer Molla, D. Dornic, M. Lincetto, and V. Kulikovskiy, "Combining neutrino experimental light-curves for pointing to the next Galactic Core-Collapse Supernova," 2020.
- [201] E. Nardina and I. Zuluaga *Nuclear Physics B*, vol. 731, pp. 140–163, 2005.
- [202] I. Tamborra, B. Müller, L. Hüdepohl, H.-T. Janka, and G. Raffelt, "High-resolution supernova neutrino spectra represented by a simple fit," *Phys. Rev. D*, vol. 86, p. 125031, 2012.
- [203] M. Colomer and M. Lincetto, for the KM3NeT Collaboration *PoS(ICRC2019)857*, 2019.
- [204] Super-Kamiokande Collaboration, "Search for Supernova Neutrino Bursts at Super-Kamiokande," *Astrophys. J*, vol. 669, pp. 519–524.
- [205] Super-Kamiokande Collaboration *Astropart. Phys.*, vol. 81, p. 39, 2016.
- [206] Hyper-Kamiokande Collaboration *J. Phys. Conf. Ser.*, vol. 718, p. 062071, 2016.
- [207] L. Larsson, "Statistical analysis of multiwavelength light curves," *eprint arXiv:1207.1459*, 2012.
- [208] E.D. Feigelson and G. Jogesh Babu *Modern Statistical Methods for Astronomy*, Cambridge University Press, 2012.

- [209] K. Gorski, E. Hivon, A. Banday, B. Wandelt, F. Hansen, M. Reinecke, and M. Bartelman, "HEALPix - A Framework for high resolution discretization, and fast analysis of data distributed on the sphere," *Astrophys. J.*, vol. 622, pp. 759–771, 2005.
- [210] T. Hanka *et al.*, "Neutrino signal of electron-capture supernovae from core collapse to cooling," *Physical Review Letters*, vol. 104, p. 251101, 2010.
- [211] R. V. Lovelace, P. Gandhi, and M. Romanova, "Relativistic jets from accretion disks," *Astrophys. Space Sci.*, vol. 298, pp. 115–120, 2005.
- [212] M. Livio, N. Panagia, and K. Sahu, "Supernovae and Gamma-Ray bursts: The greatest explosions since the Big Bang," *Space Telescope Science Institute Symposium*, 2001.
- [213] C. D. Matzner, "Supernova hosts for gamma-ray burst jets: dynamical constraints," *Monthly Notices of the Royal Astronomical Society*, vol. 345, pp. 575–589, 2003.
- [214] C. D. Dermer, "The Collapsar and supranova models," *On recent developments in theoretical and experimental general relativity, gravitation, and relativistic field theories. Proceedings, 10th Marcel Grossmann Meeting, MG10, Rio de Janeiro, Brazil, July 20-26, 2003. Pt. A-C*, pp. 461–482, 2004.
- [215] W. Fong, En Berger, R. Margutti, and B. A. Zauderer, "A decade of short-duration gamma-ray burst broadband afterglows: Energetics, circumburst densities, and jet opening angles," *The Astrophysical Journal*, vol. 815, p. 102, 2015.
- [216] LIGO Scientific, VIRGO, and Fermi Collaborations, "Gravitational Waves and Gamma-Rays from a Binary Neutron Star Merger: GW170817 and GRB 170817A," *The Astrophysical Journal*, vol. 848, p. L13, oct 2017.
- [217] I. Bartos, P. Brady, and S. Marka, "How Gravitational-wave Observations Can Shape the Gamma-ray Burst Paradigm," *Class. Quant. Grav.*, vol. 30, p. 123001, 2013.
- [218] E. Waxman, "Cosmological gamma-ray bursts and the highest energy cosmic rays," *Physical Review Letters*, vol. 75, p. 386–389, 1995.
- [219] M. Vietri, "The acceleration of ultra-high-energy cosmic rays in gamma-ray bursts," *Astrophysical Journal Letters*, vol. 453, p. 883–889, 1995.
- [220] B. Paczynski and G. Xu, "Neutrino bursts from gamma-ray bursts," *The Astrophysical Journal*, vol. 427, p. 708–713.
- [221] E. Waxman and J. Bahcall, "High energy neutrinos from cosmological gamma-ray burst fireballs," *Physical Review Letters*, vol. 78, p. 2292–2295, 1997.
- [222] D. Guetta, D. Hooper, J. Alvarez-Muniz, F. Halzen, and E. Reuveni, "Neutrinos from individual gamma-ray bursts in the BATSE catalog," *Astropart. Phys.*, vol. 20, pp. 429–455, 2004.
- [223] B. Zhang and P. Kumar, "Model-dependent high-energy neutrino flux from Gamma-Ray Bursts," *Phys. Rev. Lett.*, vol. 110, no. 12, p. 121101, 2013.
- [224] S. Maurizio, "Particles and astrophysics," *Springer*, p. 249, 2016.
- [225] Fermi Collaboration, "Fermi-LAT Observations of the Gamma-ray Burst GRB 130427A," *Science*, vol. 343, p. 42, 2014.
- [226] R. Mirzoyan, K. Noda, *et al.* *GRB Coordinates Network Circular Service*, no. 23701, 2019.
- [227] H.E.S.S. Collaboration, "A very-high-energy component deep in the  $\gamma$ -ray burst afterglow," *Nature*, vol. 575, no. 7783, pp. 464–467, 2019.

- [228] MAGIC Collaboration, "Teraelectronvolt emission from the gamma-ray burst GRB 190114C," *Nature*, vol. 575, pp. 455–458, 2019.
- [229] MAGIC Collaboration, "Observation of inverse Compton emission from a long gamma-ray burst," *Nature*, vol. 575, pp. 459–463, 2019.
- [230] S. Sahu and C. E. L. Fortin, "Origin of sub-TeV afterglow emission from gamma-ray bursts GRB 190114C and GRB 180720B," *Astrophys. J.*, vol. 895, no. 2, p. L41, 2020.
- [231] "Observation of gravitational waves from a binary black hole merger,"
- [232] K. Kotera and J. Silk, "Ultrahigh energy cosmic rays and black hole mergers," *Astrophys. J.*, vol. 823, p. L29, 2016.
- [233] R. Perna, D. Lazzati, and B. Giacomazzo, "Short gamma-ray bursts from the merger of two black holes," *Astrophys. J.*, vol. 821, p. L18, 2016.
- [234] I. Bartos *et al.*, "Rapid and Bright Stellar-mass Binary Black Hole Mergers in Active Galactic Nuclei," *The Astrophysical Journal*, vol. 835, p. 165, 2017.
- [235] S. S. Kimura, K. Murase, I. Bartos, K. Ioka, I. S. Heng, and P. Mészáros, "Transejecta high-energy neutrino emission from binary neutron star mergers," *Phys. Rev.*, vol. D98, no. 4, p. 043020, 2018.
- [236] K. Kyutoku and K. Kashiyama, "Detectability of thermal neutrinos from binary-neutron-star mergers and implication to neutrino physics," *Phys. Rev.*, vol. D97, no. 10, p. 103001, 2018.
- [237] ANTARES and AMON Collaborations, "A Search for Cosmic Neutrino and Gamma-Ray Emitting Transients in 7.3 Years of ANTARES and Fermi LAT Data," *Astrophys. J.*, vol. 886, p. 98, 2019.
- [238] ANTARES, IceCube, LIGO Scientific, and Virgo Collaborations, "Search for Multimessenger Sources of Gravitational Waves and High-energy Neutrinos with Advanced LIGO during Its First Observing Run, ANTARES, and IceCube," *Astrophys. J.*, vol. 870, no. 2, p. 134, 2019.
- [239] LIGO Scientific and Virgo Collaboration *Class. Quant. Grav.*, vol. 33, no. 21, p. 215004, 2016.
- [240] S. Sachdev *et al.* *e-Print: arXiv:1901.08580*, 2019.
- [241] S. Klimenko, I. Yakushin, *et al.*, "Coherent method for detection of gravitational wave bursts," *Class. Quant. Grav.*, p. 114029, 2008.
- [242] LIGO Scientific and Virgo Collaboration, "GW151226: Observation of Gravitational Waves from a 22-Solar-Mass Binary Black Hole Coalescence," *Phys. Rev. Lett.*, vol. 116, p. 241103, 2016.
- [243] LIGO Scientific and Virgo Collaboration, "GW170104: Observation of a 50-Solar-Mass Binary Black Hole Coalescence at Redshift 0.2," *Phys. Rev. Lett.*, vol. 118, p. 221101, 2016.
- [244] LIGO Scientific and Virgo Collaboration *ApJL*, vol. 851, p. 2, 2017.
- [245] LIGO Scientific and Virgo Collaboration, "GW170814: A Three-Detector Observation of Gravitational Waves from a Binary Black Hole Coalescence," *Phys. Rev. Lett.*, vol. 119, p. 141101, 2017.
- [246] LIGO Scientific and Virgo Collaboration, "GWTC-1: A Gravitational-Wave Transient Catalog of Compact Binary Mergers Observed by LIGO and Virgo during the First and Second Observing Runs," *Phys. Rev. X*, vol. 9, p. 031040, 2019.
- [247] J. Veitch and others, "Parameter estimation for compact binaries with ground-based gravitational-wave observations using the LALInference software library," *Phys. Rev. D*, vol. 91, p. 042003, 2015.

- [248] The ANTARES Collaboration, "All-sky search for high-energy neutrinos from gravitational wave event GW170104 with the ANTARES neutrino telescope," *Eur. Phys. J. C*, vol. 911, p. 77, 2017.
- [249] ANTARES, IceCube, and LIGO-Virgo Collaborations, "High-energy Neutrino follow-up search of Gravitational Wave Event GW150914 with ANTARES and IceCube," *Phys.Rev. D*, vol. 93, p. 122010, 2016.
- [250] ANTARES, IceCube, and LIGO-Virgo Collaborations, "Search for High-energy Neutrinos from Gravitational Wave Event GW151226 and Candidate LVT151012 with ANTARES and IceCube," *Phys.Rev. D*, vol. 96, p. 022005, 2017.
- [251] B. Baret *et al.*, "Bounding the time delay between high-energy neutrinos and gravitational-wave transients from gamma-ray bursts," *Astropart. Phys.*, vol. 35, 2011.
- [252] J.A. Aguilar *et al.*, "Zenith distribution and flux of atmospheric muons measured with the 5-line antares detector," *PhD Thesis, Astropar. Physics*, vol. 34(3), 2010.
- [253] The ANTARES Collaboration, "Measurement of the atmospheric muon flux with a 4 GeV threshold in the ANTARES neutrino telescope," *Astropart. Phys.*, vol. 33, p. 86, 2010.
- [254] Leo P. Singer, "Going the Distance: Mapping Host Galaxies of LIGO and Virgo Sources in Three Dimensions Using Local Cosmography and Targeted Follow-up," *Astrophys. J. Lett*, vol. 829, p. L15, 2016.
- [255] Leo P. Singer, "Supplement: Going the Distance: Mapping Host Galaxies of LIGO and Virgo Sources in Three Dimensions Using Local Cosmography and Targeted Follow-up," *Astrophys. J. Lett supplement*, vol. 829, p. L15, 2016.
- [256] Xiang-Yu Wang *et al.*, "Synchrotron self-Compton emission from external shocks as the origin of the sub-TeV emission in GRB 180720B and GRB 190114C," *arXiv:1905.11312*, 2019.
- [257] N. Fraija *et al.*, "Modeling the observations of GRB 180720B: From radio to sub-TeV gamma-rays," *arXiv:1905.13572*, 2019.
- [258] N. Fraija *et al.*, "On the origin of the multi-GeV photons from the closest burst with intermediate luminosity: GRB 190829A," *arXiv:2003.11252*, 2020.
- [259] The ANTARES Collaboration, "First all-flavor neutrino pointlike source search with the ANTARES neutrino telescope," *Phys. Rev. D*, vol. 96, no. 8, p. 082001, 2017.
- [260] J. Lu and others, "LORENTZ-FACTOR-ISOTROPIC-LUMINOSITY/ENERGY CORRELATIONS OF GAMMA-RAY BURSTS AND THEIR INTERPRETATION," *the Astrophys. J.*, vol. 751, p. 49, 2012.
- [261] A. Mirizzi, I. Tamborra, H.-T. Janka, N. Saviano, K. Scholberg, R. Bollig, L. Hudepohl, and S. Chakraborty, "Supernova neutrinos: production, oscillations and detection," *String Theory*, vol. 39, no. 1-2, pp. 1-112, 2016.
- [262] E. O'Connor, "An Open-Source Neutrino Radiation Hydrodynamics Code for Core-Collapse Supernovae," *Astrophys. J. Suppl.*, vol. 219, no. 2, p. 24, 2015.
- [263] A. Coleiro, M. Colomer Molla, D. Dornic, M. Lincetto, and V. Kulikovskiy, "Combining neutrino experimental light-curves for pointing to the next Galactic Core-Collapse Supernova," 2020.